Petrogenesis of the Moose Lake Area of the Acasta Gneiss Complex, Slave Craton, Northwest Territories, Canada

by

Michael Bradley Koop Belosevic

A thesis submitted in partial fulfillment of the requirements for the degree of

Master of Science

Department of Earth and Atmospheric Sciences

University of Alberta

Abstract

The Acasta Gneiss Complex (AGC) is a late Hadean to early Archean terrane in northwestern Canada known to contain the oldest evolved rocks on Earth. However, only a small portion of the AGC has been studied in detail. This study aims to explore one of the poorly explored portions of the AGC, the Moose Lake area, using a combination of bedrock mapping, petrographic analysis, whole-rock geochemistry, U-Pb geochronology, and isotope tracer analysis.

Bedrock mapping indicates that the Moose Lake area can be divided by a gradational contact into a higher-strain western domain, and a lower-strain eastern domain. The area has undergone multiple phases of deformation in which the regional gneissosity has been folded in a later deformational event into map-scale folds with fold axes shallowly plunging to the southwest. Like at the original discovery site of the AGC at the Acasta River, the Moose Lake area is composed primarily of tonalitic-granodioritic gneisses, containing variable size layers and boudins of metagabbro and amphibolite. The bulk of the area is made up of tonalitic – granodioritic gneisses that formed during two main pulses of magmatism: one at 3.72 – 3.68 Ga, and the other at 3.60 – 3.55 Ga. In contrast to previous work, a significant portion of the Moose Lake area is composed of a large homogeneous pluton of foliated granite which was emplaced at 3374.6 ± 8.5 Ma. The oldest felsic rock at Moose Lake (~3700 Ma) has strong heavy rare earth element depletion, which indicates magma formation at great depths. In turn, this suggests that the transition from shallow- to deep-level melt-generation processes, which had previously been proposed to have occurred at ~ 3.6 Ga, may have happened ~100 Myr earlier. Unlike all the other 3.70-3.55 Ga granitoid gneisses at

Moose Lake, one of the ~3.6 Ga tonalites has geochemical signatures indicative of shallow melt generation similar to the oldest lithologies in the AGC.

Many of the 'metamorphic' zircons found in the Moose Lake area record an age of ~ 3.30 Ga, which does not coincide with the age of any known age of plutonic activity in the AGC. Thus, 3.30 Ga may represent the time of regional metamorphism or regional hydrothermal activity in the AGC which led to subsolidus zircon growth.

Mafic rocks, which are widespread in the AGC, are generally not well dated because of the absence or poor quality of zircon in these rocks. However, two of the metagabbro samples of my study contain abundant, good-quality zircon. On the basis of their zoning patterns and Th/U ratios, most of these zircons are interpreted to be of igneous origin and record a robust age of 3740.7 ± 2.3 Ma. These zircons also record an initial epsilon hafnium isotope value (εHf_i) of -4.7 ± 0.24, a surprisingly unradiogenic value for a mafic rock. Assimilation-fractional crystallization (AFC) modelling suggests that it is difficult for a primary mafic magma with an initial chondritic Hf isotope composition to acquire such a negative εHf value through assimilation of known felsic- or intermediate-composition rocks in the AGC, without also increasing the magma SiO_2 content above that observed in the metagabbro. Alternative models for generating this Hf isotope composition in the metagabbro include partial melting of an enriched mantle that had a long-term (Hadean) history of low Lu/Hf or assimilation of enriched, early Hadean-age mafic rocks that had evolved to strongly negative εHf by 3.74 Ga.

To Priscilla

“Believe you can and you’re halfway there.”

- Theodore Roosevelt

Acknowledgments

Funding was provided by the Northern Scientific Training Program, the University of Alberta Northern Research Awards and by an NSERC grant to Dr. Tom Chacko. I would like to thank Dr. Chacko for his eternal patience, cultivating guidance and deep well of knowledge over the course of this program, including a (somewhat) miserable trip to maybe the buggiest place on Earth. I would also like to thank Dr. Larry Heaman for the training and use of his laboratory facilities; Dr. Graham Pearson for the use of his high-precision instruments, and Drs. Andrew Dufrane and Andrew Locock for the use and assistance with the use of their analytical instruments. A special thanks is also due to Dr. Jesse Reimink, Dr. John Ketchum and Scott Cairns for their specialized expertise in the area. Without them I wouldn't even know where to start with Acasta. I would also like to thank (and apologize to) Dr. Matt Hardman, Madisen Sagan, Alix Osinchuk, Dr. Janina Czas, Dr. Rasmus Haugaard, Dr. Alberto Reyes, Serhiy Buryak and Grayson Bilak for their sympathetic ears, academic advice, and company through what seemed like an endless process. Finally, I would like to thank my parents Dr. Mike Belosevic and Dr. Priscilla Koop as well as my faithful partner Brittany Bilida. If not for them, I doubt I would have been able to make it through to the finish line in one piece.

Table of Contents

List of Tables

List of Figures

Chapter 1. Introduction

One of the most challenging questions in earth science revolves around how the planet developed during the first billion years of its existence. This challenge arises in part because there are only a few terranes from this time period that survive today. Most of our information about the 4.6 to 3.6 Ga time period on Earth comes from Isua supracrustal belt and associated Itsaq Gneiss Complex of Greenland (e.g., Nutman et al., 1986), the Saglek block of northern Labrador (e.g., Komiya et al., 2015), the Jack Hills detrital zircons of western Australia (e.g., Compston and Pidgeon, 1986), the Nuvvuagittuq greenstone belt of Quebec (e.g., O'Neil et al., 2008), and the Acasta Gneiss Complex of the Northwest Territories (e.g., Bowring et al., 1989)). There is evidence that Eoarchean rocks show the geochemical input of pre-existing Hadean crustal material sourced from heterogeneous mantle reservoirs (Bennet et al., 2007; O'Neil et al., 2008, 2010; Guitreau et al., 2013; Bauer et al., 2020) as well as other evidence that suggests that the Hadean "proto-crust" was different from modern-day continental crust (Reimink et al., 2014; 2016b).

Due to the geologically active nature of our planet and the extent of time being explored, only a few localities may contain the critical evidence that is needed to elucidate Earth's early history (e.g., Hartlaub et al., 2006; Condie, 2007). Another drawback of having a geologically active planet is that most of these ancient pieces of crust have undergone extensive deformation, metamorphism, later intrusion and partial melting where the provenance of components of these rocks can be complex (Mojzsis et al., 2014; Reimink et al., 2014, 2016a, 2016b). External forces may have also played a role, where the inner planets of the solar system may have undergone the Late Heavy Bombardment by meteorites at the Hadean-Archean boundary (Chapman et al., 2007); the effects of which have been recorded in some Hadean material (Trail et al., 2007) which could further reduce the preservation potential of early Earth material (Mojzsis et al., 2014). While certain components of these terranes are focused on for being exceptionally ancient (O'Neil et al., 2008; Reimink et al., 2014), understanding how a terrane evolved over time is also vitally important (e.g., Iizuka et al., 2007; Reimink et al., 2016a).

Some of the > 4.0 Ga Jack Hills zircons have oxygen isotope signatures that indicate crystallization from a melt whose source(s) had interacted with surface waters, which in turn

suggests that, at this time, the Earth already had an operating hydrosphere and potentially even oceans (Wilde et al., 2001). In addition, on the basis of their trace-element composition and inclusion mineral assemblages, some have suggested that the Jack Hills zircons crystallized from a granitic melt (Harrison, 2009), implying that the first continental crust on Earth was granitic in composition. In contrast, later work on the Lu-Hf systematics of Jack Hills zircons suggest they evolved along the same Hf isotope trajectory as evolved lunar crustal rocks, the so-called lunar KREEP (Kemp et al., 2010). This observation opens the possibility that the Jack Hills zircons were not derived from granitic continental crust but incompatible-element-enriched mafic rocks. If correct, there would be no requirement for the operation of modern-style plate tectonics in the early Earth.

The composition of the first crust on Earth is a contentious issue, however, recent studies support an ultramafic or mafic crust being the likely scenario. The Ujaraaluk amphibolite in the Nuvvuagittuq greenstone belt of Quebec is one such example of mafic crust of possible Hadean age and includes mafic/ultramafic rocks of both tholeiitic and calc-alkaline affinity (O'Neil et al., 2008, 2009, 2011, 2012). Reimink et al. (2014) suggested that the 4.02 Ga Idiwhaa unit of the Acasta Gneiss Complex, an iron-rich, mafic tonalite gneiss, was produced by shallow-level fractionation of basaltic magma accompanied by assimilation of surface water-altered crust. They also proposed that the processes that formed the Idiwhaa unit magmas were broadly similar to those currently producing evolved crust in modern-day Iceland.

1.1 Objectives of this Thesis

Given the scarcity of ancient rock localities worldwide, it is essential that as much information as possible be gleaned from those few localities that have been identified. In the case of the Acasta Gneiss Complex (AGC), the vast majority of the ~ 2400 km^2 extent of the complex has been mapped only at a 1:125000 scale by the Geological Survey of Canada (St-Onge, 1989). Prior to the present study, the only part of the AGC that had been mapped and indeed studied in significant detail is an ~ 35 km^2 area surrounding the original site where ca. 4 Ga rocks were first discovered (Bowring et al., 1989; Stern and Bleeker, 1998; Bowring

and Williams, 1999; Iizuka et al., 2007). Thus, there is a great deal of the AGC that is essentially unexplored.

In this thesis, I use bedrock mapping, lithological characterization, uranium-lead geochronology, whole-rock major- and trace-element geochemistry and tracer-isotope geochemistry to document one of the underexplored parts of the AGC. The first objective of this thesis is to provide a detailed (1:5000-scale) bedrock geological map of an area in the AGC separate from the original discovery area. The second objective is to characterize the lithological units of this new area in terms of their petrography, crystallization ages and chemical composition. These data, in combination with the bedrock mapping, will enable an assessment of whether the rock types, proportions and ages reported in the original discovery area of the AGC are typical of the complex as a whole. The third objective of the thesis is to characterize a metagabbro lithology that is widespread in the present mapping area and also in the original discovery area. A great deal of the previous work in the AGC has focused on geochronology and, in particular, the geochronology of zircon-bearing felsic to intermediate units. By comparison, the age(s) of mafic lithologies, many of which are not zircon bearing, are not as well documented. The discovery of some zircon-rich mafic rocks in the present study area provides the opportunity to obtain precise age constraints on one of the important mafic rock units of the AGC. In addition, the Lu-Hf systematics of these primary magmatic zircons from mafic rocks can offer insights into the nature of the early Archean mantle unavailable in more differentiated lithologies.

Chapter 2. Geological Setting

2.1 Regional Geology of the Slave Craton

The Slave craton is a well-exposed, small- to medium-sized Archean craton that occupies parts of two Canadian territories, Nunavut and the Northwest Territories (Hoffman, 1989; Padgham and Fyson, 1992; Bleeker and Hall, 2007). The craton (Fig. 2.1) is bounded to the west by the 1.9 – 1.8 Ga Wopmay Orogen (Hoffman and Bowring, 1984), and to the south and east by the 2.0 – 1.9 Ga Taltson-Thelon Magmatic Zone (van Breemen et al., 1987a,b; Hoffman, 1989). It is composed primarily of four main rock packages, which include pre-2.9 Ga basement granitoids and gneisses of the Central Slave Basement Complex and a ~2.9 – 2.8 Ga cover sequence known as the Central Slave Cover Group (Bleeker and Davis, 1999; Sircombe et al., 2001; Ketchum et al., 2004). These older rocks are uncomformably overlain by a thick sequence of ~2.75-2.60 Ga supracrustal rocks, the Yellowknife Supergroup (Green et al., 1968; Jenner et al., 1981; Bleeker and Hall, 2007), which are in turn intruded by ~2.70 – 2.58 Ga plutons (van Breemen et al., 1992; Bleeker and Hall, 2007). The Central Slave Cover Group is composed of fuchsitic quartzites and iron formations overlain by basalts and intercalated rhyolitic volcanic sequences (Bleeker and Davis, 1999; Bleeker et al., 2011). The Yellowknife Supergroup is composed of a mafic-felsic volcanic sequence and overlying turbiditic sedimentary rocks, all of which are intruded by syn- to post-depositional plutonic rocks (Jenner et al., 1981; Sircombe et al., 2001). The last sequence of 2.62 – 2.58 Ga plutons make up a large portion of the exposed crust in the Slave craton (Padgham and Fyson, 1992). Most of the craton has undergone regional greenschist- to granulite-facies metamorphism (Thompson, 1978; Henderson, 1981; Pehrsson et al., 2000). The Slave craton can be further subdivided into western and eastern sections on the basis of the Nd isotope compositions of granitoid and supracrustal rocks. These isotopic data show that the western part of the craton is underlain by significantly older crust than the eastern part (Davis and Hegner, 1992).

2.2 Regional Geology of Acasta Gneiss Complex

The Acasta Gneiss Complex (AGC) is an approximately 2400 km^2 exposure of > 2.9 Ga basement rocks at the western margin of the Slave craton, exposed within a tectonic window through the Wopmay Orogen (St Onge et al., 1988; Stubley, 2005). It is a variably deformed package of granitic, intermediate and mafic meta-igneous rocks metamorphosed at broadly amphibolite-facies conditions (Bowring and Williams, 1999; Iizuka et al., 2007; Reimink et al., 2016a). The complex has undergone multiple phases of folding and now displays a dominantly steeply dipping N-S foliation (St Onge et al., 1988; Bowring et al., 1989; Iizuka et al., 2007; Reimink et al., 2014). The AGC has been previously divided into a lower strain eastern domain, and a higher strain western domain (Iizuka et al., 2007). The igneous crystallization ages of zircon reported from both domains are similar, although the relatively lower strain eastern domain allows for more straightforward geochronological interpretation (Stern and Bleeker, 1998; Bowring and Williams, 1999; Iizuka et al., 2007; Reimink et al., 2014, 2016a).

Upon discovery of very old (3.96 Ga) rocks on an island in the Acasta River (Bowring et al., 1989), there was considerable interest in exploring the AGC. As a consequence, rocks of the complex have been extensively studied over the past three decades by several different research groups (e.g., Bowring et al., 1989; Bowring and Housh, 1995; Iizuka et al., 2007, 2010; Guitreau et al., 2014; Mojzsis et al., 2014; Reimink et al., 2014, 2016a,b, 2018; Bauer et al., 2017). However, all of these studies focused on an ~30 km^2 area surrounding the original discovery site (Fig. 2.1). Due to the remote location of the AGC and the generally lichen-covered and lithologically and structurally complex nature of its outcrops, more regional-scale investigation of the complex has proven challenging. As a result, most of the 2400 km^2 of the AGC remains unexplored.

2.3 Previous Geochronological and Geochemical Studies in the AGC

Most geochronological studies of the AGC have focused on the U-Pb isotope systematics of zircon. These studies reveal that the AGC experienced several major tectonothermal events which extended from ~ 4.03 to 2.9 Ga. The oldest rocks at Acasta

crystallized between 4.03 and 4.02 Ga (Stern and Bleeker, 1998; Bowring and Williams, 1999; Reimink et al., 2014, 2016b) and are broadly tonalitic in composition. Reimink et al. (2014) found these ancient rocks are geochemically and isotopically similar to intermediate-composition rocks on modern-day Iceland, commonly referred to as icelandites. Like icelandites, the oldest AGC rocks have anomalously high FeO, low magnesium numbers, flat whole-rock REE patterns (low La/Yb), and zircon $\delta^{18}O$ values similar to or lower than those found in the mantle. A second major pulse of magmatic activity in the AGC occurred at ~3.75 Ga (Bowring and Housh, 1995; Iizuka et al., 2007; Reimink et al., 2016a). This second episode of magmatism includes tonalitic rocks and possibly also some mafic plutons, although the latter are not yet well dated (see below). The ~3.7 Ga tonalitic rocks have slightly steeper REE patterns than the 4.02 Ga rocks but patterns that are still much flatter than those of typical Archean tonalite-trondhjemite-granodiorite (TTG)-suite rocks (Moyen and Martin, 2012; Reimink et al., 2016a).

Studies in the original discovery area suggest that the most regionally extensive granitoid rock unit in the AGC intruded between 3.55 and 3.6 Ga (Iizuka et al., 2007; Reimink et al., 2016a). These rocks display many of the geochemical characteristics of typical Archean TTGs such as elevated SiO_2 and steep REE patterns characterized by pronounced Yb depletion, which is indicative of partial melting at considerable depth where significant garnet was present in the magma source region (Moyen and Martin, 2012; Reimink et al., 2016a). Younger rocks have also been reported in the AGC, including granitoids with crystallization ages of ~ 3.37 Ga and 2.94 Ga (Reimink et al., 2016a), but their regional extent has not yet been well documented.

The mafic rocks of the AGC have generally been under-studied and are not well dated. Until the present study, the mafic bodies found on the Iizuka et al. (2007) map (referred to as the quartz diorite unit in that study and as metagabbro in this study) had only had minimum crystallization ages assigned them of 3.58 Ga in the western zone and 3.69 Ga in the eastern zone. These minimum ages are based on the ages of cross-cutting granitic rocks or the interpretation that some of the zircons contained therein grew because of partial melting of the unit during later metamorphism (Iizuka et al., 2007). The most extensive geochemical study of mafic rocks in the AGC is that of Koshida et al. (2016) who defined

three main mafic lithologies, which they termed weakly foliated amphibolite (metagabbro in the present study), amphibolite, and hornblendite. On the basis of their geochemical study of these mafic units, Koshida et al (2016) posit that the least-modified amphibolite unit initially crystallized from a basaltic composition magma that was generated through the partial melting of a Nb-Ta depleted primitive mantle.

In addition to U-Pb zircon, several other geochronological methods have been applied to AGC rocks, including U-Pb Apatite and Titanite (Davidek et al., 1997; Sano et al., 1999) and Ar/Ar of hornblende and biotite (Hodges et al., 1995). These studies show that Wopmay-aged (ca. 1.8-1.9 Ga) thermal disturbances affected the rocks of the AGC. Whole-rock Sm-Nd isotope studies have also been conducted on AGC rocks, initially as a tracer of magma sources (Bowring and Housh, 1995) and later for the purpose of geochronology (Moorbath et al., 1997; Roth et al., 2014). Moorbath et al. found that the isotopic data from diverse samples fall along a broadly linear data array whose slope corresponds to an age of 3371 ± 59 Ma (MSWD = 9.2). Notably, many of the samples plotting on this data array have zircons recording U-Pb ages that are much older. Thus, either the data array record extensive whole-rock resetting of the Sm-Nd system at ca. 3370 Ma or the array is a mixing line of unrelated samples that has no age significance (Bowring and Williams, 1999; Reimink et al., 2018).

2.4 Description of the Moose Lake Study Area

My study area in the AGC is centered around a lake we have unofficially named Moose Lake after its moose head-like shape. It is located in the southern portion of the AGC approximately 9 km southwest of the original discovery site (Fig 2.1). The study area was chosen due to some relatively recent forest fires, which has provided many lichen-free outcrops suitable for detailed investigation. The landscape is hummocky, with large outcrops of glacially polished basement rock. There are several small eskers in the study area generally oriented east-west. In some of the lees of the larger hummocks in this area, glacial till can be found under moss mats and in swamps. The area is generally flat, with no more than 60 m of topographic relief across the area. The map area can be roughly divided into two parts: a western higher-strain domain and an eastern lower-strain domain similar to what was described in the original discovery area to the northeast.

I mapped a 3 x 5 km area surrounding Moose Lake at approximately a 1:5000 scale. The resulting geological map is presented in Fig. 2.2. The map area is dominated by variably deformed granitoids, felsic to intermediate orthogneiss containing small enclaves and layers of fine-grained amphibolite gneiss, larger domains of coarser-grained amphibolite (metagabbro) and a few zones of garnet-bearing biotite gneiss. In addition, there are numerous small intrusions of little deformed to undeformed leucocratic coarse-grained pink granites as well as a smaller number of undeformed mafic dykes found throughout the study area. The pink felsic granites crosscut every other unit present including some of the mafic dykes. These mafic dykes are generally oriented NE-SW. There is a strong steeply dipping foliation trending NE-SW with accompanying SW-trending folding patterns. This foliation is expressed in every lithology in the study area except for the late-stage pink granites and the mafic dykes.

2.4.1 Foliated Granite Suite

The foliated granite suite comprises a large segment of the western part of the Moose Lake study area (orange shade in Fig. 2.2). In contrast to most of the other units, it is relatively homogeneous in both composition and texture. This unit is in contact with the felsic-intermediate gneiss suite, the metagabbro as well as the amphibolite units. These contacts typically run along frost-heaved areas where the rock is heavily stockwork-veined indicating that there was some late-stage fluid movement along the contact. The foliated granite is composed primarily of quartz, K-feldspar, plagioclase and biotite ± hornblende. Accessory minerals include magnetite and ilmenite, with trace zircon, titanite, and apatite. Like the other units in the area, the foliated granites display a dominant NE-SW foliation defined primarily by the alignment of biotite crystals (Fig 2.3A). The foliation present in this unit is somewhat weaker than in other felsic units and does not display any of the parasitic folding found in the surrounding area.

2.4.2 Felsic-Intermediate Gneiss Suite

This unit, which is found on the western half of the map area, primarily comprises tonalitic, granodioritic and granitic gneisses banded on the centimeter to decimeter scale and intercalated with small bands and lenses of metagabbro. The foliation in this unit, similar to that in the foliated granite, is defined by steeply-dipping, NE-SW gneissic banding as well as shallow southwest-plunging folds. This highly strained package, appropriately named zebra gneiss (Fig. 2.3B,D) may also contain small (decimeter-sized) augen of hornblendite primarily found in the hinges of folds. In some of the tonalitic-granodioritic gneisses with higher biotite and hornblende content, small augen of K-feldspar are present as well as mm- to cm-scale bands of leucosome. Throughout this package are numerous intrusions of co-deformed white granitic gneisses that crosscut the intermediate gneisses but have also undergone some deformation. Another rock type within this package are pink granites. Although ubiquitous, these granites are not resolvable at the map scale. The pink granites are very coarse-grained to pegmatitic and are composed primarily of quartz and K-feldspar. They are undeformed and crosscut nearly every unit in the study area (Fig. 4D). These are particularly common along contacts between lithologies as well as across gneissic banding. Notably, stockwork quartz veining is common in the larger bodies of pegmatitic granite.

2.4.3 Mixed Felsic-Mafic Gneiss Suite

This package of gneisses is composed primarily of tonalitic to granodioritic orthogneisses with a high proportion of coarse-grained amphibolite (metagabbro) bodies ranging in size from decimeters to hundreds of meters. The eastern gneiss suite is more lithologically heterogeneous on the outcrop scale and exhibits a lower overall level of strain than the felsic-intermediate gneiss suite to the west. The lower strain in the eastern gneiss package is manifested by the presence of discrete isoclinal folds in relatively homogeneous tonalitic gneiss (Fig. 2.3C) compared to the straight banding that is common in the western gneiss package (Fig. 2.3B). Similarly, highly stretched felsic and mafic lithologies are interbanded at the centimetre to decimetre scale in the western gneiss package (Fig. 2.3D,E) whereas mafic to ultramafic lithologies (metagabbro, hornblendite) in the eastern gneiss package typically occur as lenses and lozenges of varying sizes (Fig 2.3F) within less competent felsic gneisses. Notably this strain gradient can be seen at map-scale, with the

presence of ovoid-shaped metagabbro bodies, some of which are several hundred meters in diameter (Fig. 2.4E new). As in the case of the western package, there is extensive intrusion of the eastern gneiss package by deformed white to gray tonalite to grandiorite and pink granite.

2.4.4 Metagabbro

The rock unit termed metagabbro is presently an amphibolite composed primarily of hornblende and plagioclase ± minor biotite, along with trace apatite, titanite, ilmenite and locally zircon. On the basis of its coarse-grained, equigranular texture (Fig. 2.4E), which is common in many unmetamorphosed gabbros, I infer that the amphibole presently in the unit is of metamorphic origin and replaced original igneous pyroxene. I therefore refer to the unit as metagabbro. This interpretation is in contrast to Iizuka et al. (2007, 2009, 2010) who refer to a similar unit in the discovery area as diorite or diorite gneiss. That name would imply that the amphibole in the unit is of igneous rather than metamorphic origin.

The grain size of the metagabbro varies with the degree of strain, with the more highly strained areas characterized by a finer grain size. Compared with the felsic to intermediate units, the metagabbro is resistant to deformation and commonly occurs as less internally deformed augen within the felsic-intermediate units. In addition, in the lower-strain eastern part of the map area, the metagabbro in part occurs as large, relatively homogeneous, ovoid-shaped bodies that resemble plutons but are more likely larger-scale enclaves within the gneiss package.

The metagabbro does vary somewhat in its mineral proportions, primarily in terms of its amphibole to plagioclase ratio. In general, the more leucocratic parts of the metagabbro correspond to the presence of biotite and an increase in the amount of zircon.

2.4.5 Amphibolite

The amphibolite unit is mineralogically similar to but generally finer grained than the metagabbro. This unit only occurs as a dominant rock type at the outcrop scale in the

southwest portion of the Moose Lake study area. A common feature of this unit, which is not seen in the surrounding lithologies, is the presence of mm-scale folded quartz veins. The fold axes of these veins align with the dominant foliation of the area. There are some sections of amphibolite that show distinct compositional banding with alternations of amphibole-rich and plagioclase-rich layers (Fig 2.4A). The origin of this layering is not entirely clear but may be a vestige of primary magmatic pyroxene-plagioclase layering. This amphibolite unit, while typically homogeneous is locally intruded by white or pink granitoids, with the former being co-deformed with the amphibolite. The orientation of foliation and fold axes in the amphibolite unit is similar to that present in the other units of the study area.

2.4.6 Biotite Gneisses

There are four areas in the eastern portion of the map area underlain by biotite gneiss, all of which extend on strike along a synclinal trough. The biotite gneiss unit is characterized by layers of biotite ± garnet ± hornblende intercalated with layers of quartz and plagioclase (Fig. 2.4C). The parts of this unit that are hornblende bearing are devoid of garnet. The biotite gneisses are also relatively rich in zircon, apatite, allanite and monazite. At the outcrop-scale, layers and boudins of white granitoid commonly occur within the biotite gneisses (Fig 2.4C). This unit is infolded not only with the white granitoids but also with the granodioritic gneisses and metagabbro. Similar to the other major units in the area, the biotite gneisses are cross-cut by the late-stage pink granites (Fig 2.4D)

2.4.7 Iron Formation

One location in the eastern part of the map area (Station 116) contains a ~ 10 m-thick layered package of rocks. The majority of this package comprises iron formation consisting mainly of magnetite and quartz along with small amounts of amphibole. Intercalated with the iron formation is a narrow ultramafic layer rich in amphibole and chlorite and ~ 0.5 m thick garnetite layer consisting mainly of garnet along with subordinate biotite and titanite (Fig. 2.5). This layered package extends for ~ 25 m along strike but, as it was only noted at this one location, its relationship to the other rocks of the AGC is not known. Unfortunately,

no zircon was found in either the iron formation or the garnetite with which to date either the depositional or metamorphic age of this package.

2.5 Structure of the Moose Lake Study Area

The rocks of the Moose Lake area have undergone a complex tectonic history that included multiple deformation events. The most regionally extensive structural characteristic is the subdivision of the Moose Lake area into a more highly strained western half and a lower strain eastern half. Such a west to east strain gradient has also been reported in the discovery area to the north. The most widely used geological map for that area (Iizuka et al., 2007) represents the boundary between the higher and lower strain areas as a discrete fault. However, at Moose Lake, that boundary is better characterized as a gradational transition in the overall degree of strain.

At the outcrop scale, the structure of the area is defined by a steeply-dipping, NE-SW striking penetrative foliation that is found in all units except the late-stage pink granitoid and the mafic dykes. There is evidence for at least three fold hinges present in this area, where the locus of each is defined by various features at the 1-100 meter scale. For example, the western synclinal axial trace is defined by the fold closure in the amphibolite unit. The eastern synclinal trace is the only place where rocks of possible supracrustal origin, the biotite gneiss unit and the iron formation-garnetite layered package, are preserved in a synclinal trough. The central anticlinal axial trace is defined primarily by the change in strike of the steeply-dipping planar fabric. As with most fold domains, these axial traces are not the only ones present. There are numerous parasitic traces not visible at the scale of this map.

When plotted on a stereonet, measurements of foliation planes and fold axis lineations taken across the Moose Lake study area show a rather interesting pattern (Fig. 2.6). The fold hinges cluster in the southwest and the foliation planes for the most part intersect that cluster indicating folds plunging at an average of 33° to the southwest. Stereonet data arrays like this are typical in folded sedimentary basins where bedding planes are folded and have a variety of orientations, yet the measured fold hinges are uniform. The Moose Lake

study area likely went through several major deformation events, where one or more of the earlier events deformed these igneous plutons into bands and layers that approximate sedimentary bedding. A later deformation event then folded these planar surfaces, leading to the simple folding pattern shown in the stereonet.

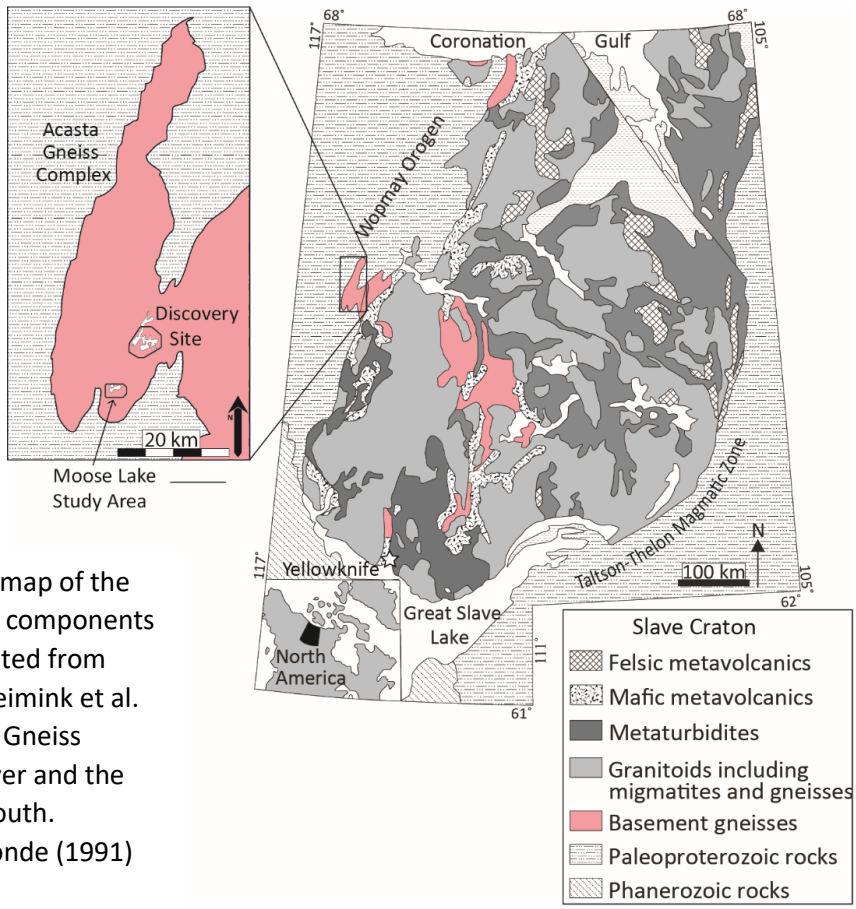

Fig. 2.1. Generalized geological map of the Slave craton showing the major components and surrounding features. Adapted from Bleeker and Davis (1999) and Reimink et al. (2014). Left: Inset of the Acasta Gneiss Complex showing the Acasta river and the Moose Lake study area in the south. Adapted from St. Onge and Lalonde (1991)

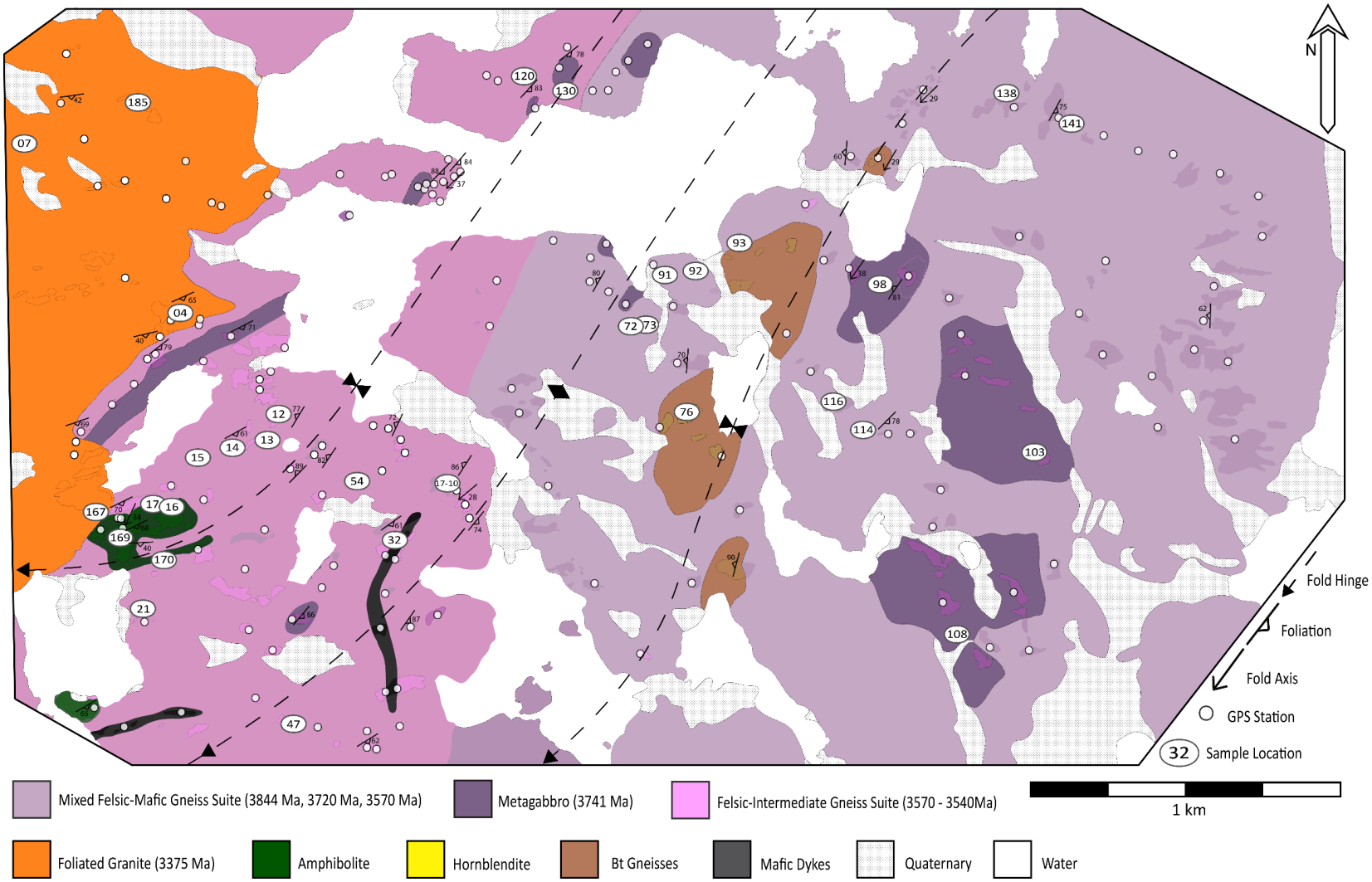

Fig. 2.2. Geological Map of the Moose Lake area of the Acasta Gneiss Complex. It is primarily made up of felsic, intermediate and mafic gneisses with intrusive granitic and mafic dykes. Foliation is steeply-dipping and trends northeast to southwest and fold hinges and stretch lineations trend to the southwest. The area can be divided into a western higher-strain and eastern lower-strain portion separated by a strain gradient. The geochronology is from this study and can be found in chapter 5.

Fig. 2.3. **A**. Foliated Granite showing lower levels of deformation defined primarily by the alignment of biotite crystals. **B**. High-strain Tonalitic-Granodioritic Gneiss showing centimeter-decimeter scale gneissic banding. **C**. Lower-strain tonalitic gneiss showing folding in the gneissic banding. **D**. High-strain steeply-dipping straight gneisses showing cm-decimeter banding of metagabbro, granodioritic-tonalitic gneiss, late-stage intrusive and co-deformed white granitic gneisses. **E**. High-strain finer-grained metagabbro gneiss showing intrusive white granitic gneisses and normal faulting. **F**. Coarse-grained Metagabbro “augen” within granitic gneisses. Common in the eastern half of the study area.

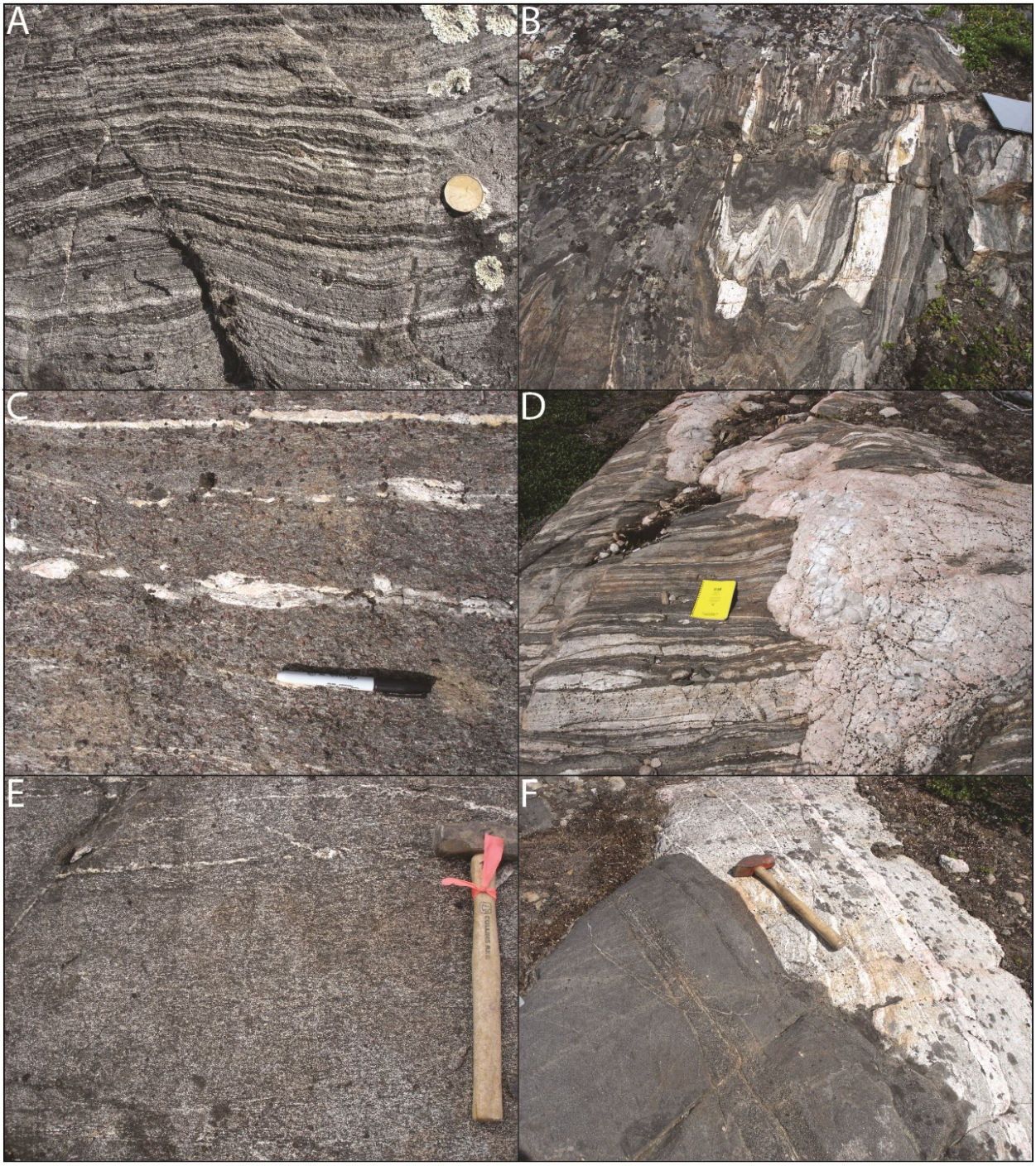

Fig. 2.4. **A**. Compositional banding in the fine-grained amphibolite unit. Visible white quartz-veining is common in this unit. **B**. Co-folded tonalitic gneiss with amphibolite and white co-deformed intrusive granitic gneisses. **C**. Garnet-biotite gneiss with boudinaged gneissic layers. **D**. Banded and boudinaged granodioritic-tonalitic gneisses within the garnet-biotite gneiss cross cut by coarse-grained pink granite. **E**. Typical Metagabbro outcrop in the eastern portion of the map area showing low-strain coarser-grained metagabbro. **F**. Granodioritic Gneiss with intrusive white granitic gneiss cross cut by one of the common mafic dykes. This mafic dyke shows grain size variation.

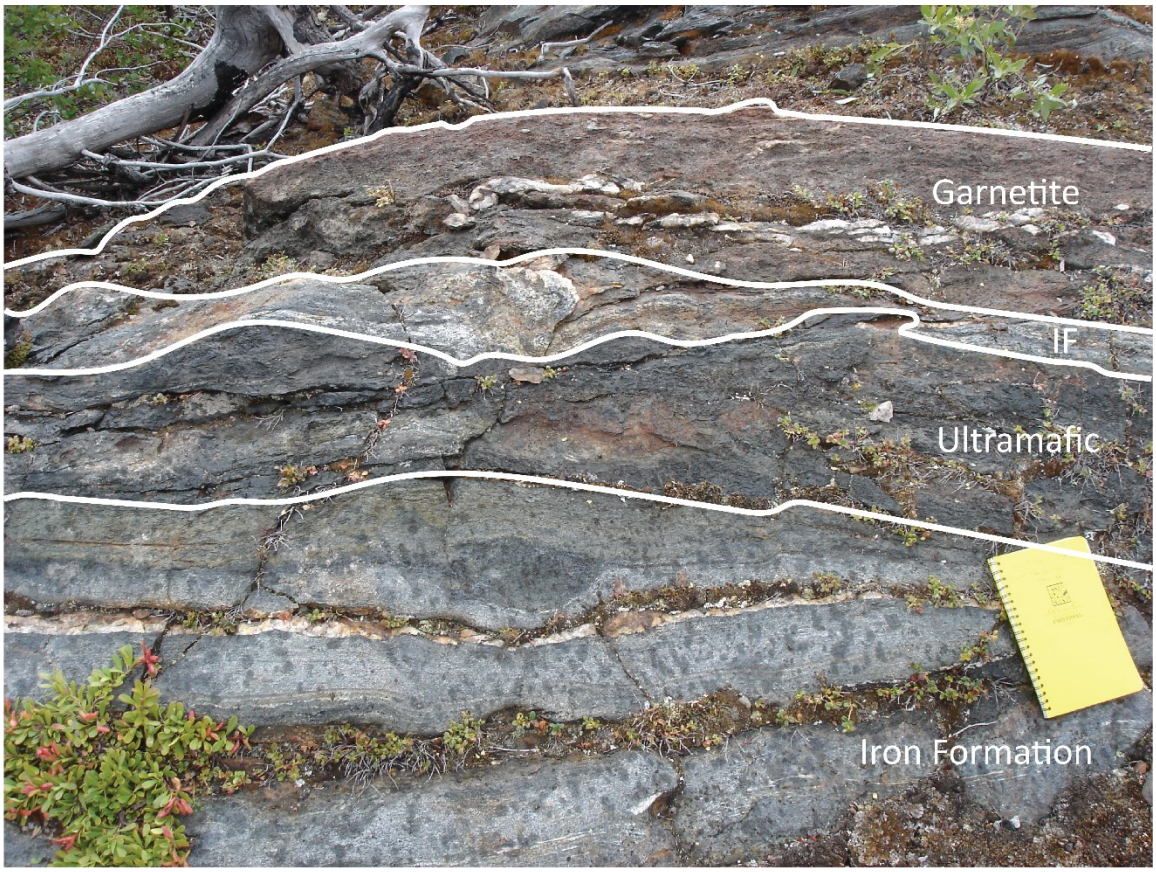

Fig. 2.5. Supracrustal package found in the Eastern trough of the Moose Lake area. From the bottom, a weakly banded iron formation, an ultramafic layer, another thin weakly banded iron formation, and a layer of Garnetite.

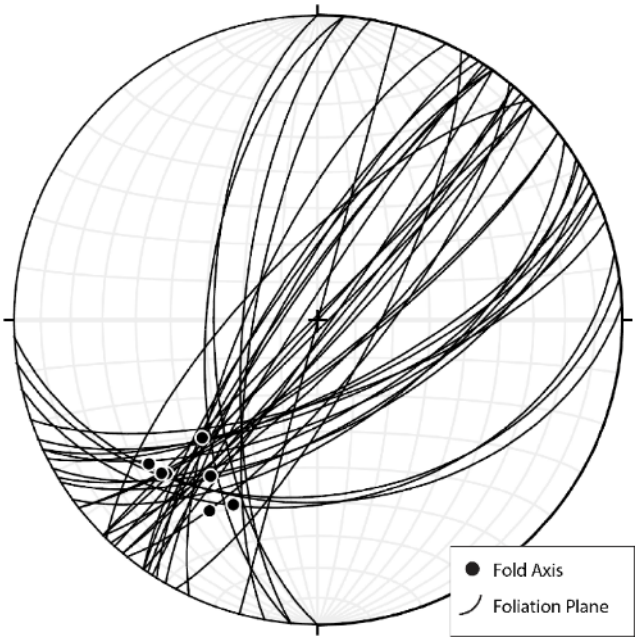

Fig. 2.6. Equal-area stereonet plot of the measured foliation and fold axis lineations of the Moose Lake study area. The plot shows that the regional foliation has been folded and the folds plunge to the SW at an average of 33°. Stereonet plot produced and analyzed using software after Allmendinger et al. (2011) and Cardozo et al. (2013).

Chapter 3. Methods

3.1 Whole-Rock Geochemistry

Representative samples were collected during the 2016 and 2017 field seasons. A table of sample locations is available in appendix 6. Care was taken to collect samples for geochemical or isotopic analysis consisting of only a single lithological component rather than more highly-strained samples that may contain multiple lithological components interlayered at the centimeter scale. A table of sample locations is available in appendix 6. Altered rocks were excluded from analysis. The samples were further prepared by removing weathering, alteration crusts/haloes and veining with a rock saw. The samples were then washed, allowed to dry and were wrapped in plastic and crushed into <5 mm diameter pieces. Further crushing was done using an alumina shatterbox, which was precleaned with silica chips. Each prepared sample resulted in 15-30 g of very fine-grained (< 20 μm) powder. Twenty-four powdered samples were analyzed for their whole-rock major- and trace-element composition at Washington State University in their GeoAnalytical Laboratory. The powders were analyzed by X-ray fluorescence (XRF) spectrometry (Johnson, et al., 1999) for major and some trace elements (Ni, Cr, Sc, V, Ba, Rb, Sr, Zr, Y, Nb, Ga, Cu, Zn, Pb, La, Ce, Th, Nd, U) and inductively coupled mass spectrometry (ICP-MS) (Knaack, et al., 1994) for most of the trace elements. The limits of detection for the XRF analyses is < 0.2 wt % for the major elements and < 4 ppm for the trace elements. The uncertainties in the ICP-MS analyses are ≤ 5 % relative for the rare earth elements (REE) and ≤ 10 % relative for the other trace elements.

3.2 Zircon Identification, Separation and Mounting

A suite of 58 polished petrographic thin sections were prepared from each of the samples obtained from fieldwork at the Thin Section Laboratory at the University of Alberta. Suitably-sized zircons were located in these thin sections using a petrographic microscope and then submitted for in-situ U-Pb isotope analysis.

Samples chosen for more extensive geochronological analysis were processed for zircon separation. The samples were trimmed of alteration and veining and washed and left

to dry. They were then wrapped in plastic and crushed into < 1 cm chips. These chips were then crushed to < 300 μm particle size using a tungsten carbide disc mill. To separate the zircon crystals, the sample powder was processed through a Wilfley table. The heavy mineral fraction was further passed through a Frantz Isodynamic Separator to remove magnetic phases from the powder. The resulting powder was then processed by methylene iodide heavy liquid separation to further separate the phases based on density. Zircons were then picked from the dense fraction for quality, avoiding cloudy and inclusion-rich crystals, and mounted in epoxy.

Zircons in thin section targeted for in-situ U-Pb dating were imaged using a JEOL JXA-8900R electron probe microanalyzer (EPMA) at the Electron Microprobe Laboratory at the University of Alberta. Specifically, the EPMA was used to obtain back scatter electron images of zircon to investigate the internal structure of individual grains. The zircon epoxy mounts were imaged using a Zeiss EVO LS15 EP-scanning electron microscope (SEM) with both BSE and cathodoluminescence (CL) imaging capabilities at the Scanning Electron Microscope Laboratory at the University of Alberta.

Each zircon image was evaluated based on its internal zoning characteristics and degree of radiation damage. Zircon grains or parts of grains were separated into three categories: 1) Grains with oscillatory, sector, or coarse-scale zoning interpreted to be of igneous origin. 2) Unzoned zircon commonly occurring as rims around igneous zircon grains or the interior part of igneous grains that have undergone internal recrystallization. These types of unzoned zircon are interpreted to be of metamorphic origin. 3) Zircon, which due to lack of distinctive features in CL or BSE images, was unable to be categorized into either of the first two categories with certainty. I refer to this latter category as ‘ambiguous’ zircon in terms of its mode of origin.

3.3 LA-MC-ICP-MS

Zircons in thin section and a portion of the mounted zircon separates were analyzed using laser ablation-multi-collector inductively couple mass spectrometry (LA-ICP-MS) following the procedure outlined in Simonetti et al. (2006). Both igneous and metamorphic

parts of zircon grains were targeted for age dating. I used a New Wave Research 213 nm laser for ablating the zircon grains, utilizing a 25 μm spot size, 1.5-2.5 J/cm^2 fluence and 30 one-second integrations for each analysis. The ablated zircon material was then carried to a Nu Plasma MC-ICP-MS for ionization and isotopic analysis. Wherever possible, we avoided performing analyses on visible cracks and in metamict zones. In addition, certain analyses showed multiple plateaus in lead isotope ratios and lead counts, which indicate different zircon growth zones were being sampled during a single analysis as ablation penetrated deeper into the zircon. Data from integration cycles showing this behaviour were either edited to remove the influence of these zones or culled entirely if they were too short to be statistically viable. In processing these data, I did not make common lead (^{204}Pb) corrections but instead, screened out analyses with measured ^{206}Pb/^{204}Pb ratios lower than 500. In addition, using the isotopic data in conjunction with CL and BSE imaging, I identified a number of analyses where the laser spot appears to have straddled two different growth zones. These analyses were removed from further consideration. In total, 307 out of 345 analyses were kept after these initial screens. Concordia plots, weighted averages and probability density plots were constructed using Isoplot 4.15 (Ludwig, 2004) and all analytical data points are plotted at and ages reported at the 2σ or 95 % confidence level.

Zircon standards were analyzed before and after the analysis of each sample and after every 10 unknown analyses. A primary standard, LH94-15 (Ashton et al., 1999; Simonetti et al., 2006), was used to determine normalization factors so that the measured ^{207}Pb/^{206}Pb and ^{206}Pb/^{238}U ratios for this zircon would correspond to the ratios determined by isotope dilution thermal ionization mass spectrometry (ID-TIMS). A secondary zircon standard, OG1 (Stern et al., 2009), was used to check the accuracy of the analyses. A total of 75 analyses of OG1 were obtained over 6 separate analytical sessions. One of these analyses was culled due to high levels of ^{204}Pb and 3 more were omitted from the calculation due to discordancy. The remaining 71 analyses yielded a weighted ^{207}Pb/^{206}Pb average of 3462.1 ± 1.9 Ma with an MSWD of 0.82, which is very similar to the accepted age of this zircon of 3465.4 ±0.6 Ma, determined by ID-TIMS (Stern et al., 2009). More information on the results obtained on the OG1 standard are provided in Appendix 2.

3.4 LASS

Laser ablation split-stream (LASS) analyses of zircon in one metagabbro sample (MB108A) were performed at the Arctic Resources Laboratory at the University of Alberta using the methods detailed in Fisher et al. (2014). Ablation was performed by a Resonetics Excimer 193 nm laser using a 33 μm laser spot size at 10 Hz and operating with a 5 J/cm^2 energy fluence. The ablated zircon material was analyzed simultaneously for both its U-Pb and Hf isotope compositions using the split-stream technique. The U-Pb analyses were done with a Thermo Element-XR mass spectrometer using a Secondary Electron Multiplier (SEM) detector in peak-hopping mode. The hafnium isotope analysis was done with a Thermo Neptune Plus mass-spectrometer with multiple Faraday detectors. Every analysis consisted of 20 seconds of background (blank) measurement, followed by 40 seconds of sample ablation and then 30 seconds of blank again (to wash out the carrier tubes of material) for a total of 90 seconds per analytical spot. The data reduction was done using Iolite v3 software where signal integrations of U-Pb, Hf and Pb-Pb were compared in order to determine uniform sample composition and ensure that only one component of complex zircons was sampled. Isotopic data integrations in which multiple sources of zircon domains were sampled, were trimmed where appropriate or discarded if integration time was too short. No screens were used in these data. Initial $^{176}Hf/^{177}Hf$ and εHf values were calculated using a crystallization age of 3740.4Ma ± 2.4 Ma obtained using a weighted average of the oldest 40 analyses of samples MB108A and MB103 using both LA-ICP-MS as well as LASS. Both initial εHf values and propagated uncertainties associated with those values were calculated using the formulas given in Ickert (2013). The ^{176}Lu decay constant and CHUR values used for the initial $^{176}Hf/^{177}Hf$ and εHf calculations were taken from from Scherer et al. (2001) and Soderlund et al. (2004) and Bouvier et al. (2008), respectively. Concordia plots, weighted averages and probability density plots were constructed using Isoplot 4.15 (Ludwig, 2004). Thorium – Uranium ratios were measured using ^{232}Th and ^{238}U and processed through Iolite v3 software to report the elemental ratios.

Plešovice (Sláma et al., 2008) and LH94-15 (Ashton et al., 1999) zircons were used as the primary standards for Hf and U-Pb isotope analyses by LASS, respectively. In

addition, the Yb-doped standards MUN1 and MUN 3 (Fisher et al., 2011) were used to calibrate the corrections for isobaric interference of ^{176}Yb on ^{176}Hf after the methods outlined in Fisher et al. (2011; 2014). The secondary standards used in the LASS analyses were zircons OG1 (U-Pb) (Stern et al., 2009), R33 (U-Pb and Hf) (Black et al., 2004; Vervoort, 2010), and 91500 (U-Pb and Hf) (Wiedenbeck et al., 1995; Woodhead and Hergt, 2005). The LASS analyses of the secondary standards yielded Hf isotope ratios and their measured and model Th/U ratios that are, within analytical uncertainty, in agreement with the accepted values for these standards. Some reverse discordance was recorded in the analysis of several sample zircons, which suggests small inaccuracies in the U/Pb normalization; however, this reverse discordancy is quite low (< 3.5 %) and has a negligible affect on the dataset as a whole. The LASS analyses of secondary standards for their U-Pb isotopic character agreed within error of accepted ID-TIMS values. Despite the large Yb interference correction required, the ^{176}Hf/^{177}Hf ratio determined for the secondary standard MUN-3 is within the uncertainty of the accepted isotope ratio as measured by Fisher et al. (2011).

Each primary standard was measured twice, while each secondary standard was measured once before and after every 10 unknown sample analyses. Data obtained for the LASS reference materials are presented in Appendix 4. Concordia plots and Hf results figures from the secondary standards are found in Appendix 4.1.

Chapter 4. Results

4.1 Zircon U-Pb isotope data

The full U-Pb isotope dataset is given in Appendix 1. Representative zircon images from each sample are found in Appendix 5.

4.1.1 Foliated Granite Suite

MB07

The zircons from this sample are generally well preserved; most show clear oscillatory zoned cores and large metamorphic rims and include some grains that exhibit internal metamorphic recrystallization. These zircons have undergone variable amounts of single-stage, recent lead-loss in both igneous and metamorphic parts of grains (Fig. 4.1A). In total, I performed 19 analyses on 14 zircon crystals. Fifteen of these analyses were of igneous zircon, 13 of which define a discordia array that returned an upper intercept date of 3379 ± 6.0 Ma (MSWD = 1.7). I interpret this date to be good estimate of the igneous crystallization age of this sample. The metamorphic zircons in the sample also show simple recent lead loss and 3 analyses fall along a single, somewhat scattered discordia array with an upper intercept date of 3307 ± 17 Ma (MSWD = 0.091), including one concordant analysis that yields a $^{207}Pb/^{206}Pb$ date of 3308 ± 18 Ma.

MB167

Zircons from this sample typically show faint oscillatory zoning with small metamorphic rims. There is some internal metamorphic recrystallization and a number of these zircons show radiation damage leading to lead loss. In total, 7 spots were analyzed in 6 zircon grains. The igneous crystallization age of this sample was determined to be 3370 ± 100 Ma (MSWD = 5.8) using the upper intercept of a discordia array with the lower intercept representing recent lead loss (Fig. 4.1B). The metamorphic analyses were mostly obtained from parts of grains showing internal recrystallization rather than on metamorphic rims.

These yield an approximate upper intercept age of 3300 Ma, similar to that obtained for sample MB07.

MB185

Sample MB185 has a similar number of zircon grains as MB167. Unfortunately, these grains are structurally more complex, which made it more difficult to isolate zircon growth zones as effectively with a 25 μm laser spot size. In this sample, I analyzed 4 spots in 3 zircons, all of which were of igneous origin. These analyses all plotted along a discordia array, similar to the other foliated granite samples. This discordia array has an upper intercept of 3355 ± 19 Ma (MSWD = 0.70), again with the lower intercept representing recent lead loss (Fig. 4.1C).

Combined Foliated Granite Dataset

The combined dataset for this lithology strongly highlights the similarities between these analyzed samples. The sample localities were widespread across the pluton, yet highlight the relatively homogeneous nature of this lithology. The igneous analyses fall along a well-defined discordia array with a significant portion on the curve itself. The igneous age of this rock is 3374.6 ± 8.5 Ma (defined by the upper intercept of the discordia array). The metamorphic age of this sample is also defined by a discordia array with an upper intercept of 3332 ± 49 Ma (MSWD: 7.3, n= 7).

4.1.2 Felsic-Intermediate Gneiss Suite

MB12

This sample was relatively zircon rich, particularly for a thin section. I analyzed 14 spots on 8 different zircons. There was a variation in zoning appearance, with some grains displaying obvious igneous oscillatory zoning, whereas other grains showed coarse zonation of uncertain origin (ambiguous). No grains of metamorphic origin could be dated. A

regression line fit to data obtained from zircon in this sample of clear igneous origin and which were < ± 10 % discordant yield upper and lower intercept dates of 3623 ± 35 Ma (MSWD = 1.3) and 1843 ± 480 Ma, respectively (Fig. 4.2A). One of the analyses in this data array is concordant and yields a $^{207}Pb/^{206}Pb$ date of 3609 ± 17 Ma. Thus, I interpret the igneous crystallization of this sample to be broadly between 3610 and 3630 Ma. In addition, this sample also contains 2 inherited zircons, with a weighted mean $^{207}Pb/^{206}Pb$ date of 3958 ± 11 Ma.

MB21B

This sample provided few zircons large enough to analyse by LA-ICP-MS. In total, I conducted 5 analyses of 4 zircons found in thin section. In general, the zoning in these zircons is interpreted to be igneous with some coarsely zoned cores and one grain with clear oscillatory zoning. These analyses fall along a discordia array yields an upper intercept date of 3546 ± 38 Ma (MSWD = 3.3) and a broadly Neoproterozoic (587 ± 280 Ma) lower intercept. One concordant analysis in the data array yields a $^{207}Pb/^{206}Pb$ date of 3541 ± 17 Ma, which I interpret to be the approximate igneous crystallization age of the sample.

MB47B

This sample had relatively abundant zircon, which allowed me to perform 14 analyses on 9 zircons. Most of these zircons display oscillatory zonation as well as some showing irregular metamorphic rims and metamorphic recrystallization. The zircons were generally large, more euhedral and more radiation damaged than those from most other samples from this granitoid suite. A regression line fit to data obtained from zircon in this sample interpreted to be of igneous origin and which were < ± 11 % discordant yield upper and lower intercept dates of 3593 ± 55 Ma (MSWD = 3.9) and 1840 ± 610 Ma, respectively (Fig. 4.2C). Two additional analyses of igneous zircon do not fit this discordia array suggesting the rock experienced a multi-stage lead loss history. Three recrystallized zones were targeted for analysis and provided an age of approximately 3400 Ma, indicating secondary zircon growth occurred at this time.

MB54B

This sample, like MB21B, is not rich in zircons, however unambiguous igneous zonation was visible in every zircon grain found. In addition, these zircons are commonly heavily fractured, likely making them more susceptible to lead loss. I was able to conduct 7 analyses of 6 zircons that all plotted along a discordia array, with the upper intercept plotting at 3578 ± 35 Ma (MSWD = 3.0) and a broadly Mesoproterozoic (927 ± 350 Ma) lower intercept (Fig. 4.2D).

MB120

This sample is of interest as it shares some key mineralogical and geochemical characteristics with some of the oldest rocks yet discovered in the Acasta Gneiss Complex, the ~ 4020 Ma Idiwhaa tonalitic gneiss (Reimink et al., 2014). Unfortunately, sample MB120 is quite zircon-poor and most of the zircons present are of low quality or too small to be analyzed by LA-ICP-MS. I examined several thin sections as well as performed traditional zircon extraction of this sample, which ultimately yielded 27 analyses on 17 zircon grains (Fig. 4.2E). The zircons from this sample show a variety of growth textures including oscillatory zoning, metamorphic recrystallization and metamorphic rim growth. A small group of concordant or near concordant analyses of igneous grains give a range of $^{207}Pb/^{206}Pb$ dates between 3550 – 3600 Ma. Six concordant (≤±2% discordance) analyses returned a weighted average of 3565 ± 13 Ma (MSWD = 13) which is likely the crystallization age of the rock. I also identified what appears to be two separate resolvable metamorphic growth events in this sample. One at 3315 ± 7.8 Ma as well as one at 3240 ± 13 Ma. This secondary zircon growth occurred between 3240 – 3315 Ma.

Combined Felsic-Intermediate Gneiss Suite Dataset

The combined dataset highlights several shared features between the zircons in these samples. The clearest comparison is the large cluster of analyses with $^{207}Pb/^{206}Pb$ ages of between 3550-3600 Ma. A weighted average of this combined dataset with ≤3% discordance

gives an age of 3570 ± 12 Ma (MSWD = 4.9, n = 10) which agrees with each igneous age in this lithology. In addition, both metamorphic age arrays are discernable. Like other units in the area, the ambiguous zircon is similar in age to the clearly igneous zircon material. Recent lead-loss is apparent in its effect on the discordance of these analyses, pulling many of them towards the origin, though there is some 'smearing' of these analyses along the concordia curve which is likely caused by some degree of ancient lead-loss as well.

4.1.3 Mixed Felsic-Mafic Gneiss Suite

MB73A1

Sample MB73A1 was analyzed in-situ and was found to have few zircons. One of the grains shows metamorphic recrystallization whereas the other three display weak oscillatory zoning. Six analyses were obtained on these grains including one analysis of the recrystallized grain (Fig. 4.3A). The zircon grains from this sample have extensive radiation damage but the degree of lead loss is relatively minor. Regression of the 4 igneous analyses yield an upper intercept date of 3546 ± 22 Ma, which is the identical to the $^{207}Pb/^{206}Pb$ age of the one concordant analysis in this array. I interpret this date to be igneous crystallization age of the sample.

MB138B2

This sample shows a variety of interesting zircon textures, including fine-scale oscillatory zoning, metamorphic rims, metamorphically recrystallized cores, and radiation-damaged zones. Unfortunately, this variety of textures means that interpreting its geochronological data is difficult. I obtained 11 analyses of 8 zircons (Fig. 4.3B). Analysis of 2 oscillatory-zoned zircon cores yielded concordant $^{207}Pb/^{206}Pb$ dates of 3844 ± 14 Ma and 3829 ± 15 Ma. Two other analyses of zircon of uncertain paragenesis yielded concordant $^{207}Pb/^{206}Pb$ dates of 3550 and 3589 Ma and a third analysis of inferred metamorphic zircon yielded a concordant date of 3400 Ma. In addition to the concordant analyses, there are also 6 strongly discordant analyses of radiation-damaged igneous zircon. This complex dataset can

be interpreted in at least two possible ways: (1) The igneous crystallization age of this rock is ~3835 Ma with some of the metamict igneous grains having undergone extensive lead loss (Fig. 4.3B). In this interpretation, the concordant analyses at ~3560 and ~3400 Ma are attributed to two episodes of metamorphic zircon growth. (2) The zircons that gave ~3835 Ma dates are of xenocrystic origin and the actual igneous crystallization age of this sample is ~ 3560 Ma, the date recorded in zircons of texturally uncertain origin. The rock then experienced a single episode of metamorphic zircon growth at ~3400 Ma.

MB108B1

The zircons in this sample generally have homogeneous, unzoned inner cores and faintly oscillatory-zoned outer cores, some of which are surrounded by metamorphic rims. These zircon grains were analyzed both in thin section and in grain mount. In total, I performed 93 spot analyses on 69 grains. The zircons in this sample, like many others in this area, have a complex lead loss history that included both ancient (Archean or Paleoproterozoic) and more recent lead loss. The metamorphic analyses fall along a single discordia array yielding an upper intercept date of 3300 ± 28 Ma (MSWD = 5.7) and a broadly Neoproterozoic lower intercept (Fig. 4.3C). I interpret the upper intercept date to be a reasonable estimate of the time of metamorphic zircon growth in this sample. Analyses of zircons classified texturally as being of igneous or uncertain paragenesis overlap on the concordia diagram, which suggests that the 'ambiguous' grains are most likely of igneous origin. Thus, for the purposes of age interpretation, I treat the ambiguous analyses as being of magmatic origin. Collectively, the great majority of these analyses yield $^{207}Pb/^{206}Pb$ dates between ~3600 and 3720 Ma. When plotting analyses with < ± 5 % discordancy on a probability density plot (Fig. 4.3D), the main age peak is at 3680 Ma, which indicates that the age of this rock is likely between 3680 – 3720 Ma. Unfortunately, I was unable to determine a precise crystallization age due to the complex lead-loss history. However, even with this large age uncertainty, this sample is clearly older than the 3550-3600 Ma tonalitic-granodioritic gneisses found in the rest of the area.

4.1.4 Metagabbro

MB103

The zircons in this sample are relatively large (60 – 350 μm long), which when combined with their abundance allowed for the acquisition of a large number of analyses, particularly for a single thin section. The zircons display a variety of morphological and zoning characteristics, from euhedral crystals with patchy zoning, to crystals with coarse-scale banding, which is typical of zircons in mafic to intermediate rocks (Corfu et al., 2003). I analyzed a total of 32 spots on 9 zircons (Fig. 4.5C). Aside from 3 younger possible metamorphic analyses, which indicate new zircon growth between 3280 – 3380 Ma, the older igneous-origin analyses plot as an array subparallel to the concordia curve between ~3580 and 3750 Ma. Typically, analyses that plot along a discordia array would be interpreted as having undergone single-stage lead-loss and a regression line would be fitted to the data array. In this sample, such a regression line indicates upper and lower intercept dates of 3808 ± 72 and 2708 ± 420 Ma, respectively. These intercepts dates are unlikely to have geological significance for two reasons: (1) If the igneous crystallization age of the sample was in fact ~ 3800 Ma as suggested by the discordia array, one would expect, given the large number of analyses conducted, to see at least some of these analyses plot close to or directly on the upper intercept as well as other analyses that plot further down the array reflecting greater lead loss. Instead, there are no analyses with $^{207}Pb/^{206}Pb$ dates older than 3754 Ma. (2) The analyses are not uniformly distributed along discordia array but concentrated between 3710 and 3754 Ma. Specifically, the majority of igneous analyses (17 of 29) yield $^{207}Pb/^{206}Pb$ dates in that range, with the oldest 10 analyses indicating a weighted average $^{207}Pb/^{206}Pb$ date of 3737.7 ± 5.5 Ma (MSWD = 0.91). It is likely, therefore that this sample crystallized at ~3740 Ma, and has undergone subsequent complex lead loss, including ancient lead loss sometime in the Meso-Paleoarchean as well as additional lead loss taking place in the (relatively) recent past. In this scenario, the analyses would first be pulled along the concordia due to ancient lead-loss event(s), then towards the origin due to more recent lead-loss event(s).

MB108A

This sample yielded a significant number of large zircons (50 -700 μm long) providing a large number of analyses both in thin section and grain mount. The zoning patterns of zircons (Fig 4.4) in this sample are similar to those of MB103, were but also include some grains displaying patchy sector zoning. There are also a small number of zircons showing metamorphic rims or metamorphic recrystallization. Zircons from this sample were analyzed both in thin section by conventional, single-stream LA-ICP-MS for their U-Pb isotope compositions and also in a grain mount by split-stream LA-ICP-MS (LASS) for both U-Pb and Hf isotope compositions. Both U-Pb data sets are combined here since there are minimal differences between them. The chief differences seen are a higher proportion of concordant analyses and even a small number of analyses exhibiting reverse discordance with LASS. Overall, I analyzed 58 spots in 31 zircons by the LASS method and 55 spots on 18 zircons by the conventional method (Fig. 4.5A and 4.5B). Similar to MB103, the igneous zircon U-Pb isotopic data from this sample plots sub-parallel to the concordia curve and is interpreted to have the same origin. Therefore, the oldest 31 analyses from this sample likely represent the true crystallization age of this sample and produce a weighted average of 3741.2 ± 2.6 Ma (MSWD = 0.82) which agrees within-error of MB103 (3737.4 ± 5.5 Ma) resulting in an overall date of this unit obtained by a weighted average of the oldest 40 analyses of 3740.7 ± 2.3 Ma (MSWD = 0.80) (Fig. 4.5D). I interpret this date to reflect the crystallization age of the gabbroic magma that formed the protolith of the metagabbro.

4.1.5 Biotite Gneisses

MB76C

This sample was analyzed in thin section and provided 11 analyses from 7 zircons that range from 30 – 120 μm in length. The zircons in this sample are universally of uncertain origin, lacking textures clearly diagnostic of either an igneous or metamorphic paragenesis. Most of the zircons have undergone significant radiation damage, are intensely fractured and contain numerous mineral inclusions. The U-Pb isotope data from this sample are equally unclear, with no concordant analyses and a large spread in $^{207}Pb/^{206}Pb$ dates

between 3241 ± 31 Ma and 3682 ± 25 Ma (Fig. 4.6). If the protolith of this sample was a granitoid, the scattered nature of the U-Pb isotope systematics would require a complex, multi-stage lead loss history. Alternatively, if the protolith of the sample was a clastic sediment, the zircons would be of detrital origin and therefore may reflect the broad ranges of ages of the sediment sources.

4.2 Whole-Rock Geochemistry

I collected major-, minor-, and trace-element geochemical data for 24 samples encompassing every major lithology from the Moose Lake study area. These data are reported in Table 4.2. Whole-rock geochemical data was normalized on a volatile-free basis. The key geochemical characteristics of these samples are reported below, subdivided by lithology and age.

4.2.1 Foliated Granite Suite

Two samples were analyzed from this suite; MB04 and MB185, which are granite and monzogranite, respectively, in the Q vs ANOR classification scheme of Streckeisen and LeMaitre (1979. These samples are characterized by high silica (> 74 wt. %), low FeO (< 1.2 wt. %) and MgO (< 0.30 wt. %) and relatively high Na_2O (> 3.9 wt. %) and K_2O (> 3.1 wt. %). The notable trace-element features of this suite are fractionated rare-earth-element (REE) patterns with distinctly low heavy REE (HREE) contents, similar to average low HREE Archean tonalite-trondhjemite-granodiorite (TTG) suite rocks (Moyen and Martin, 2012) (Fig. 4.7). These rocks have a high normalized La/Yb value (average = 26) and they both contain pronounced negative Nb and Ti anomalies (Fig. 4.7). Sample MB185 has a positive Eu anomaly whereas MB04 has a slightly negative Eu anomaly. Both samples are peraluminous based on the Aluminum Saturation Index (ASI) (Shand, 1927, Frost et al., 2001) with ASI values of 1.09 and 1.10 for MB04 and MB07, respectively.

4.2.2 Tonalitic-Granodioritic Gneisses

These samples were found across two of the map units, the Felsic-Intermediate Gneisses as well as the Mixed Gneiss Suite. All 6 analyzed samples from these two suites have similar crystallization ages (see previous section) and, with one exception (sample MB120), display similar geochemical traits. Most of the samples are high in silica (66 - 74 wt. %), low in FeO (< 4.2 wt. %) and have relatively high magnesium numbers (Mg# = molar MgO/(MgO + FeO) = 23 - 37). These samples also display the trace-element characteristics of typical Archean TTGs including very high normalized La/Yb (34 - 230), high Na_2O (> 4.3 wt. %), generally weak to absent Eu anomalies and marked negative Nb and Ti anomalies (Fig. 4.7). Sample MB120 differs significantly from the others. It has distinctly lower SiO_2 contents (59.3 wt. %), high FeO (12.3 wt. %), low Mg# (14), a relatively flat REE pattern (La/Yb = 2.9) and a much smaller negative Ti anomaly (Fig. 4.7). It also shows a significantly lower ASI value of 0.83, which makes this sample metaluminous, whereas the rest of the rocks in this suite are peraluminous. Many of the geochemical characteristics of MB120 (low Mg#, flat REE pattern) are similar to those of the 4.02 Ga Idiwhaa tonalitic gneiss (Reimink et al., 2014; 2016) though the latter has distinctly higher Zr and total REE contents.

4.2.3 Metagabbro

Five metagabbro samples were analyzed from both the western and eastern portion of the mapping area. All the samples have low to intermediate silica contents (52 - 57 wt. %) and moderate to high FeO (7 - 11.5 wt. %) and MgO (4 - 8 wt. %) contents. Samples MB98A2 and MB114 have lower FeO contents than the others and thus higher Mg# (52 and 44, respectively). These two samples also have higher Ni and Cr and lower Zr than the rest of the samples. In contrast, MB108A and MB103 both have very high Zr contents (399 - 163 ppm, respectively) for mafic samples. The REE pattern of these samples are generally shallow (La_N/Yb_N = 2 - 10) and exhibit variable Eu anomalies (Eu/Eu* of 0.68 – 1.65) (Fig. 4.8A). All of the metagabbro samples show negative Nb and Ti anomalies with the strongest negative anomalies in samples MB17-10B and 98A2 (Fig. 4.8B). The latter two samples also have strong positive Pb anomalies.

4.2.4 Amphibolite

The two analyzed amphibolite samples have similar compositions. Both have low-silica (51 - 52 wt. %), moderate FeO (~10 wt. %) and relatively high MgO (8-9 wt. %) contents. The amphibolites have higher Mg#s (58 - 62) and lower alkali contents than the metagabbros. These samples also have moderate Cr (113-119 ppm), high Ni (352 - 396 ppm), low Zr (34 - 70 ppm) and relatively flat REE pattern (La_N/Yb_N = 0.8 - 1.8) (Fig. 4.8A). The extended trace-element signatures of these rocks are characterized by small to absent negative Ti anomalies and marked positive Pb anomalies (Fig. 4.8B).

4.2.5 Hornblendite

The hornblendite unit is found throughout the map area, typically in smaller enclaves within other units. It is represented in the geochemical dataset by sample MB141, which has low SiO_2 (51.4 wt. %), and Al_2O_3 (5.5 wt. %), moderate FeO (11.6 wt. %), high CaO (10 wt. %) and very high MgO (18.8 wt. %). It has some geochemical similarities to the amphibolite unit, although it has lower Al_2O_3 and much higher MgO (Mg# 62.6). The hornblendite also deviates from the amphibolites and gabbros in its trace-element composition, with a large positive Th anomaly and a moderate negative Sr anomaly (Fig. 4.8F). In contrast with the rest of the samples of this study, there is no notable Pb anomaly present and much a lower Rb content. The REE signature is flat, with a slight positive Eu anomaly (Fig. 4.8E).

4.2.6 Biotite Gneisses and Supracrustal Rocks

Compared with the tonalite-granodioritic gneisses, the biotite gneisses have a broadly similar range of SiO_2 contents (65 – 69 wt. %), lower Al_2O_3 (10 - 13 wt. %), and much higher FeO (10.9 – 13.6 wt. %). They also have lower Na_2O (0.98 and 2.34 wt. %) and similar K_2O (1.6 – 2.5 wt. %). The alumina saturation index (ASI) of these rocks is very high (1.3 and 2.1). Both biotite gneiss samples contain high Zr (276 - 356 ppm) and low Ni and Cr (≤ 1.5 ppm). The REE patterns of these gneisses are similar to those of sample MB120, flat (La_N/Yb_N = 1.8 - 2.8) with minor negative Eu anomalies (Fig 4.6).

Along strike with the biotite gneisses is a small suite of supracrustal rocks, including an iron formation and a garnetite rock. The iron formation made up a small outcrop towards the center of the map area. It is a strong departure geochemically and mineralogically from the rest of the rocks from this study. It has moderate silica (61.5 wt. %), and unsurprisingly, very high FeO (53.4 wt. %). The remaining oxides are anomalously low, with low MgO and CaO (1.5 wt. % and 1.3 wt. %). The rock also has low levels of trace elements with the total detected trace elements about one order of magnitude lower than the rest of the samples analyzed in this area (~128 ppm vs ~1578 ppm on average), which is not surprising given that this sample is almost entirely magnetite and quartz. The REE pattern of this sample is relatively flat ($La_N/Yb_N = 1.7$) with a slight positive Eu anomaly, with a slight concave-upwards pattern.

4.3 Zircon Hf Isotope Data

The LASS isotopic (U-Pb and Hf) and trace-element (Th, U) data for zircons for MB-108A are presented in appendix 3 while the CL zircon images are shown in appendix 5. A small selection of CL zircon images can be found in figure 4.5. As noted above, the inferred igneous crystallization age of the metagabbro is 3740.7 ± 2.3 Ma. Therefore, this single age was used to calculate the initial $^{176}Hf/^{177}Hf$ ratios and εHf values of all analyses rather than the measured $^{207}Pb/^{206}Pb$ ages of individual analyes. On the basis of 55 analyses, the weighted average initial $^{176}Hf/^{177}Hf$ ratio of the Igneous zircons in this sample is 0.280295 ± 0.000009 (MSWD = 1.9) resulting in average εHf_i value of -4.7 ± 0.24 (MSWD = 0.81) for the metagabbro (Fig. 4.11). In addition, the Th/U ratios of this sample were lower than that of typical mafic zircon (Heaman et al., 1990) and highly variable, where igneous and ambiguous zircon have average Th/U of 0.59 with a median of 0.62 (Fig. 4.11). These ratios are in between the accepted 'typical' averages for granitic (0.52) and mafic zircon (0.81) as discussed in Wang et al. (2011). Overall, these are well within the range for igneous zircon of 0.1 - 1.0 (Belousova et al., 2002) and generally close to the loosely defined igneous cutoff of ≥ 0.5 suggested by Hoskin and Schaltegger (2003), as well as the large database of igneous and metamorphic zircon collected by Yakymchuk et al. (2017). The metamorphic zircons in this sample have distinctly lower Th/U ratios that average 0.20 with a median of 0.15.

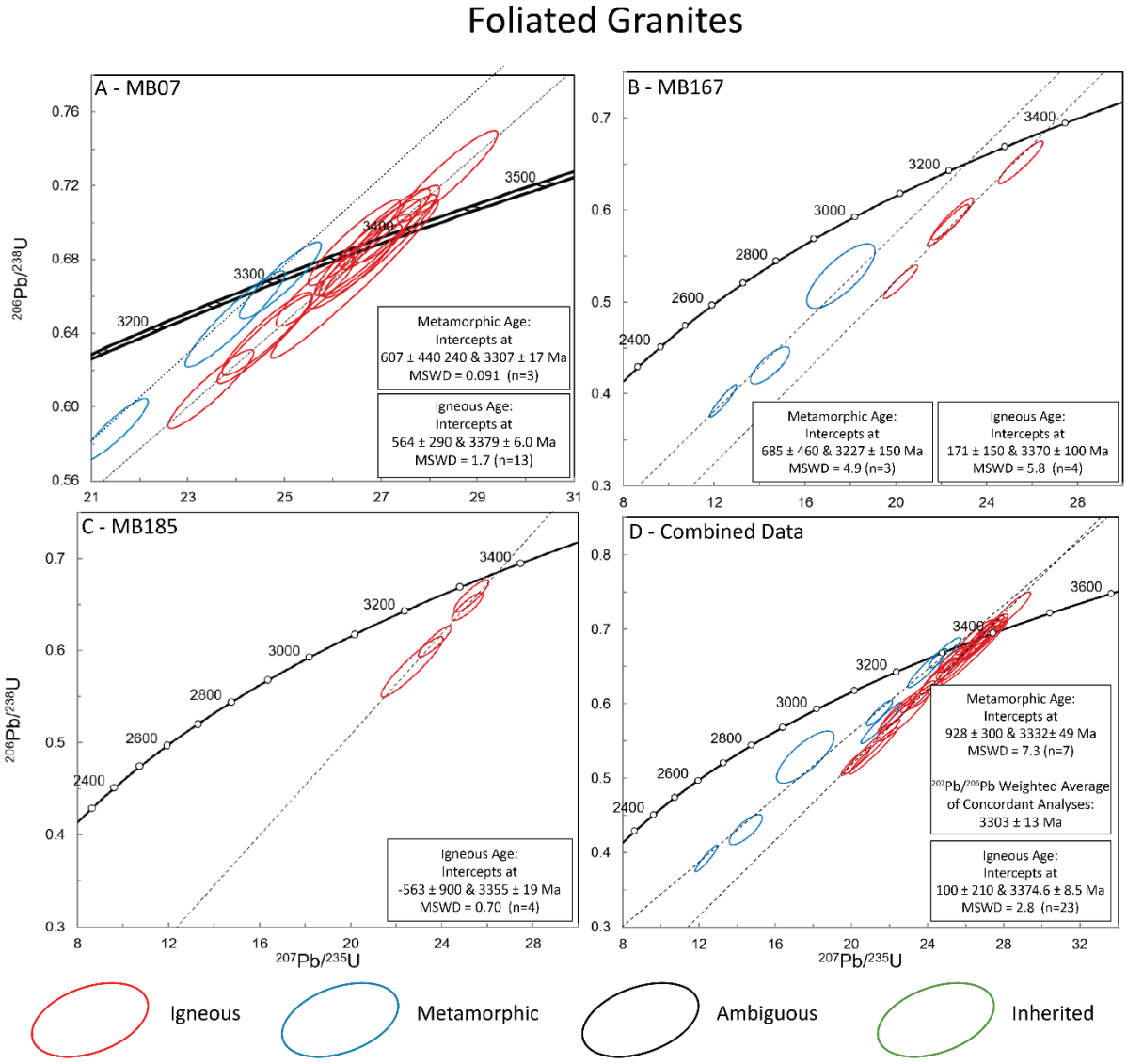

Fig. 4.1. Wetherill U-Pb concordia plots for the Foliated Granite suite. Ellipses represent 2σ errors. Interpreted ages for each of these samples agree within error with the age derived from the combined data set. **A.** MB07, **B.** MB167, **C.** MB185).

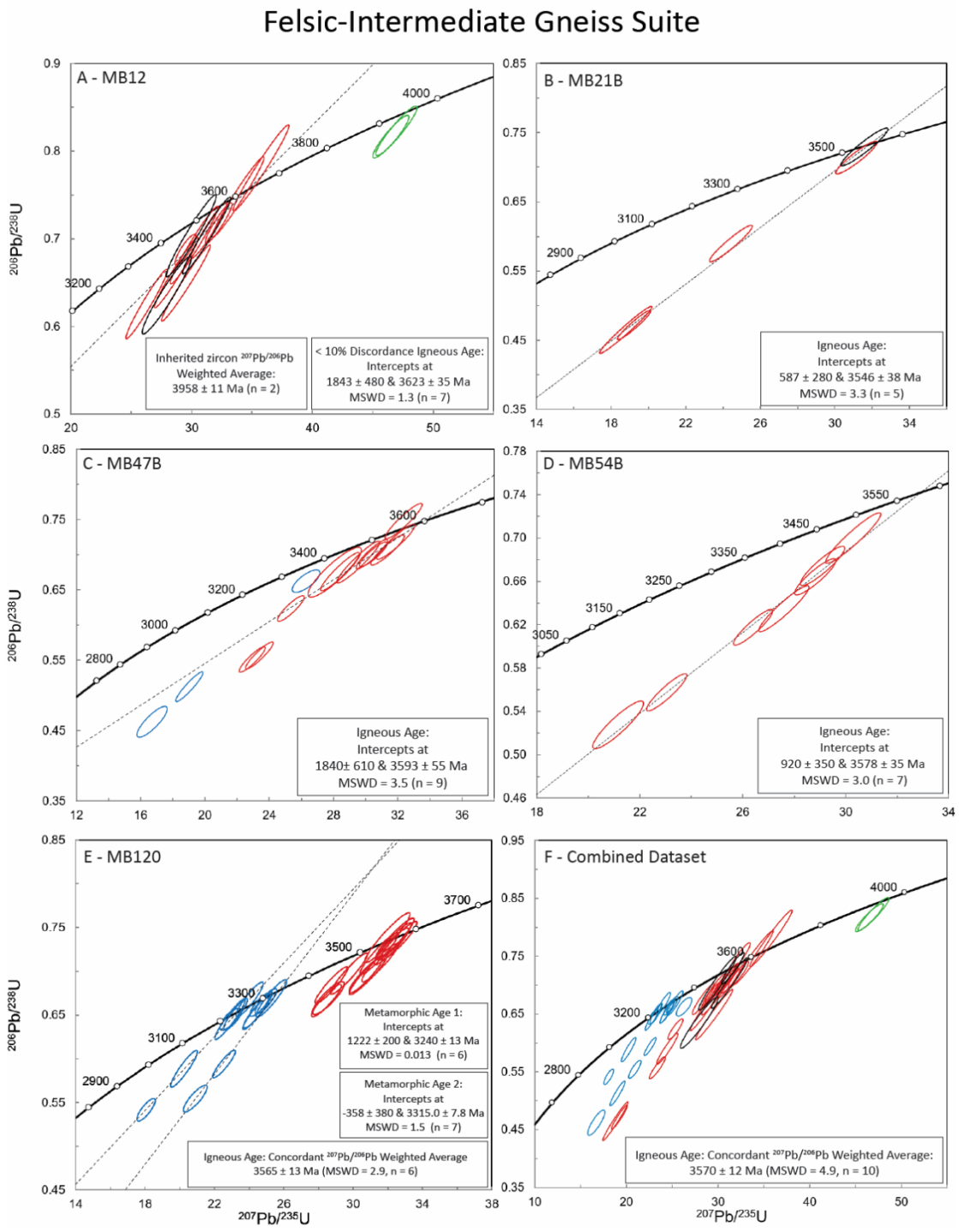

Fig. 4.2. Concordia plots for the Felsic-Intermediate Gneiss suite. These samples range from tonalite to monzogranite in composition. Ellipses represent 2σ errors. Ellipse colours as in Fig. 4.1. **A.** MB12, **B.** MB21B, **C.** MB47B, **D.** MB54B, **E.** MB120.

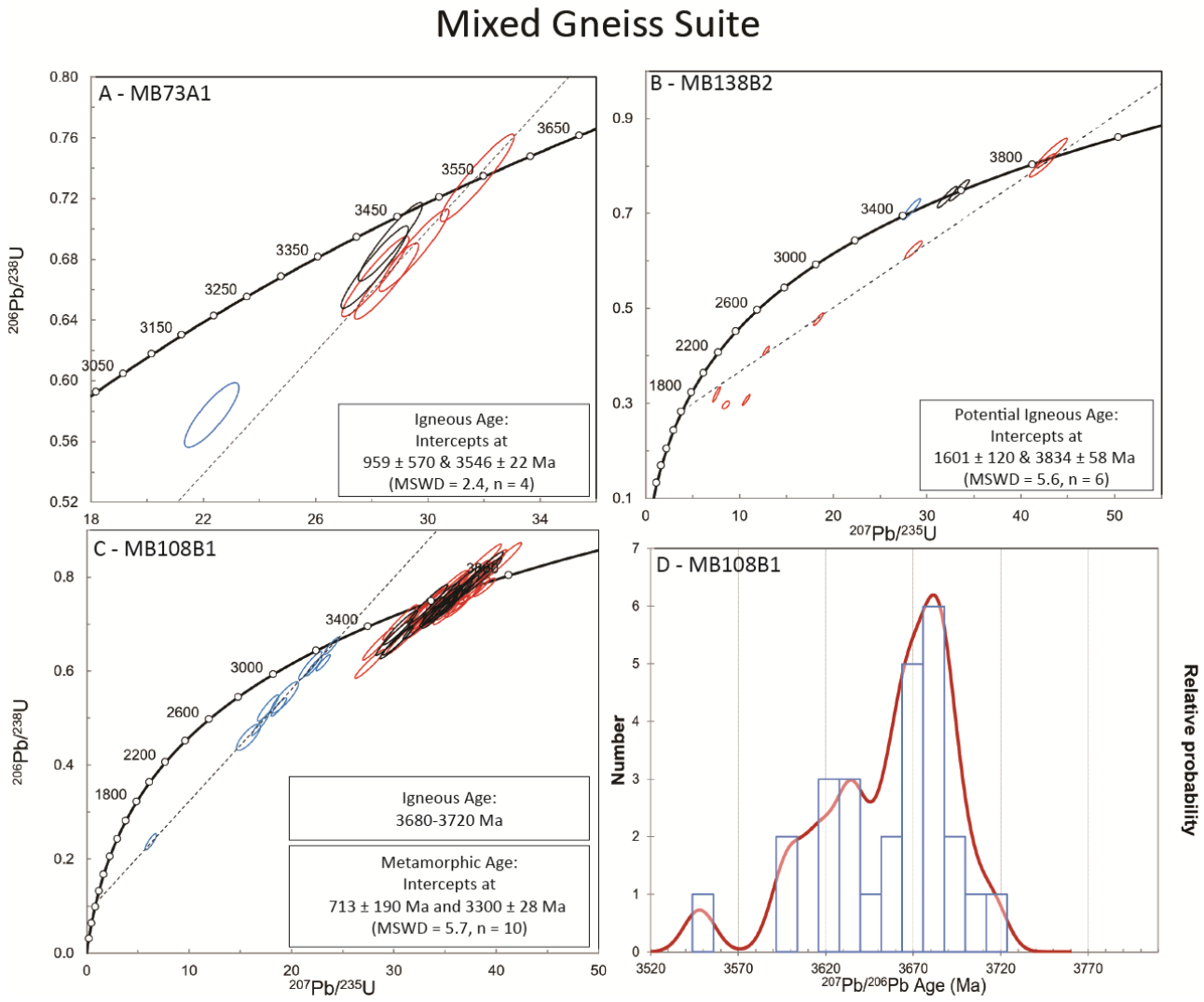

Fig. 4.3. Three concordia plots and one probability density plot for the Mixed Gneiss suite samples. Ellipses represent 2σ errors. Ellipse colours as in Fig. 4.1. **A.** MB73A1, **B.** MB138B2, **C, D.** MB108B1.

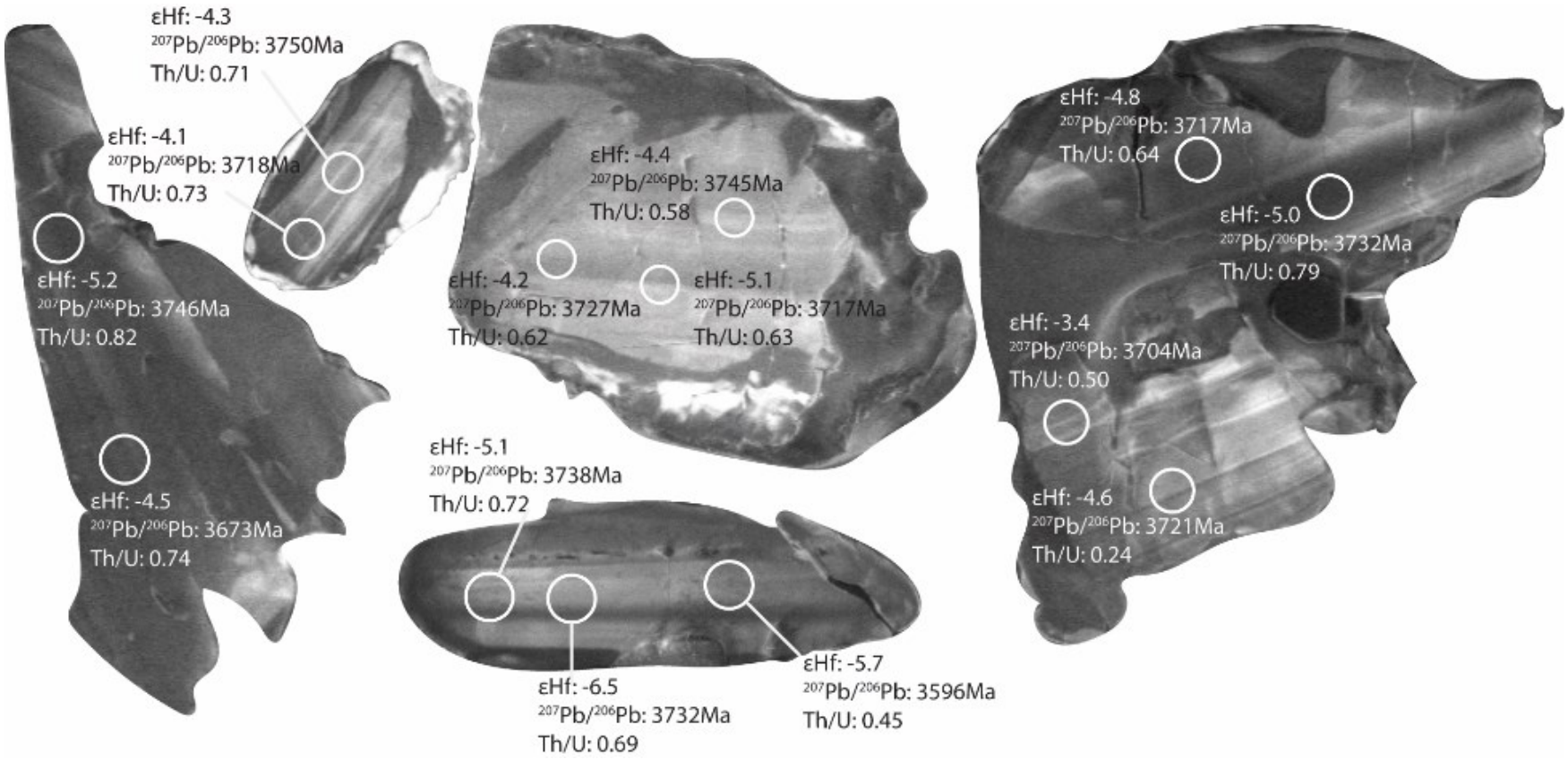

Fig. 4.4. Selection of CL zircon images from sample MB108A showing igneous coarse-scale banding with some small spread in $^{207}Pb/^{206}Pb$ ages as well as Th/U. Spot size is 33µm.

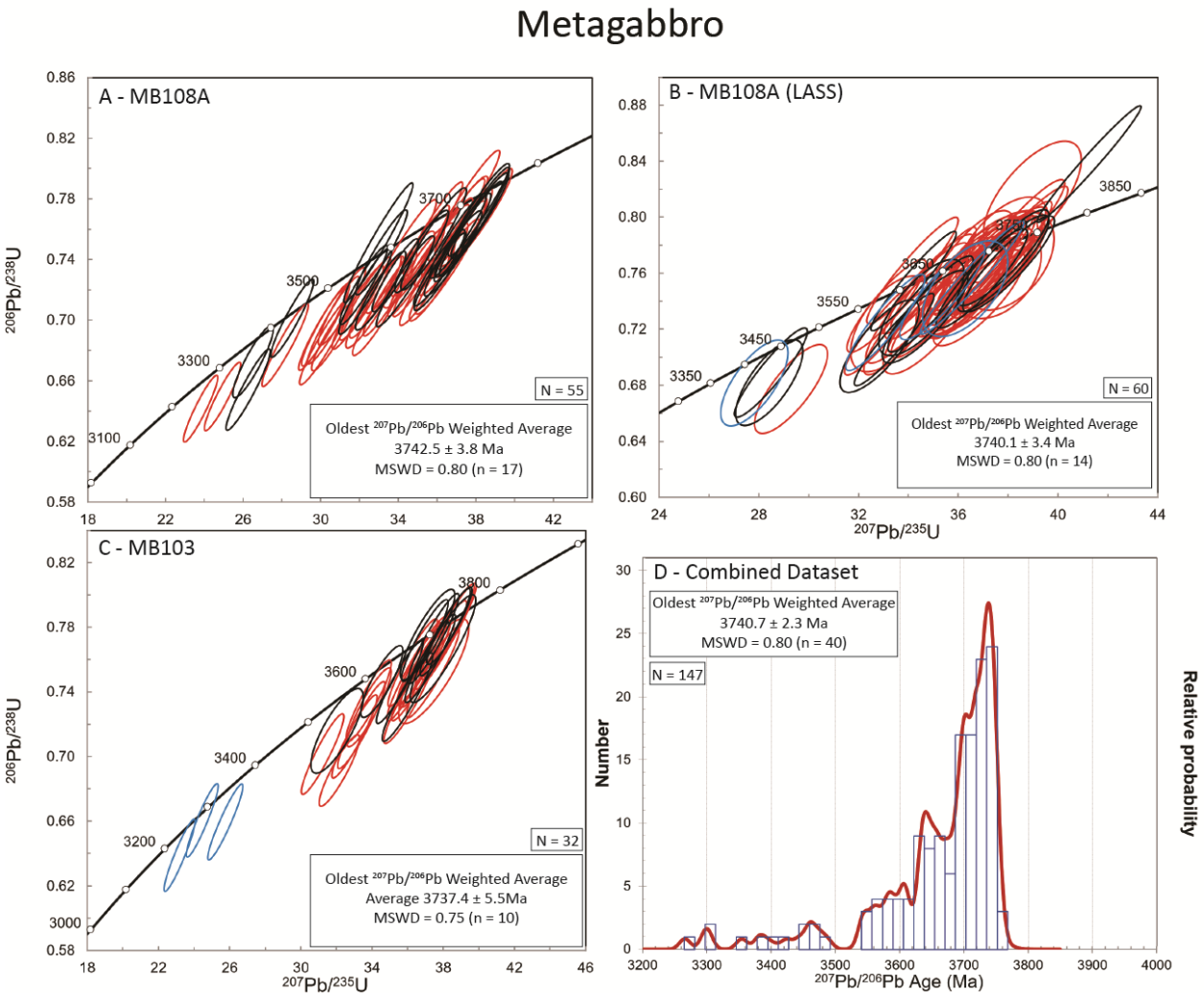

Fig. 4.5. Three concordia and one probability density plots of the metagabbro lithology. Sample MB108A was analyzed by both LA-ICP-MS as well as LASS. MB103 was analyzed by LA-ICP-MS. Error ellipses represent 2σ errors. Ellipse colours as in Fig. 4.1. **A.** MB108A LA-ICP-MS, **B.** MB108A LASS, **C.** MB103 LA-ICP-MS.

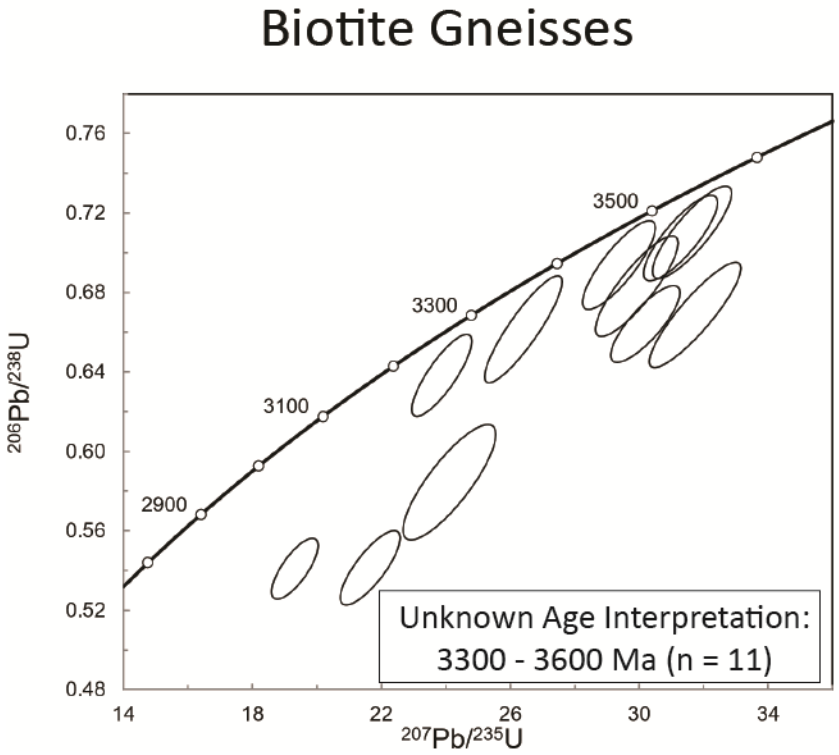

Fig. 4.6. Concordia plot of biotite gneiss sample MB76C. Error ellipses represent 2σ errors. Ellipse colours after fig. 4.1.

Table 4.1. Summary table of sample ages

Sample	Rock Type	Map Unit	Method	Age (Ma)	Age Type	Interpretation	n	MSWD
MB07	Bt-Hbl Foliated Granite	Foliated Granite	TS	3379 ± 6.0	Upper Intercept	Igneous	13	1.7
				3307 ± 17	Upper Intercept	Metamorphic	3	0.091
MB12	Bt Granodioritic Gneiss	Felsic-Intermediate Suite	TS	3623 ± 35	Upper Intercept	Igneous	7	1.3
				3958 ± 11	$^{207}Pb/^{206}Pb$ Weighted Average	Inherited	2	0.047
MB21B	Hbl Granodioritic Gneiss	Felsic-Intermediate Suite	TS	3546 ± 38	Upper Intercept	Igneous	5	3.3
MB47B	Msc-Bt Granitic Gneiss	Felsic-Intermediate Suite	TS	3593 ± 55	Upper Intercept	Igneous	9	3.5
MB54B	Bt Granodioritic Gneiss	Felsic-Intermediate Suite	TS	3578 ± 35	Upper Intercept	Igneous	7	3
MB73A1	Bt Granodioritic Gneiss	Mixed Gneiss Suite	TS	3546 ± 22	Upper Intercept	Igneous	4	2.4
MB76C	Ap-Hbl-Bt Gneiss	Biotite Gneisses	TS	3300 - 3600	$^{207}Pb/^{206}Pb$	?	11	
MB103	Tit-Bt Amphibolite	Metagabbro	TS	3737.4 ± 5.5	Oldest $^{207}Pb/^{206}Pb$ Weighted Average	Igneous	10/29	0.75
				~3300	$^{207}Pb/^{206}Pb$	Metamorphic	3	
MB108A	Tit-Bt Amphibolite	Metagabbro	TS	3741.2 ± 2.6	Oldest $^{207}Pb/^{206}Pb$ Weighted Average	Igneous	31/110	0.85
				~3450 - 3700Ma	$^{207}Pb/^{206}Pb$	Metamorphic	5	
MB108B1	Bt Granodioritic-Tonalitic Gneiss	Mixed Gneiss Suite	TS+Mount	3680 - 3720	Probability Density Plot Peak	Igneous	27	
				3300 ± 28	Upper Intercept	Metamorphic	10	5.7
MB120	Grt-Hbl-Bt Tonalitic Gneiss	Felsic-Intermediate Suite	TS+Mount	3565 ± 13	Concordant $^{207}Pb/^{206}Pb$ Weighted Average	Igneous	6	2.9
				3315 ± 7.8	Upper Intercept	Metamorphic	7	1.5
				3240 ± 13	Upper Intercept	Metamorphic	6	0.013
MB138B2	Bt Tonalitic Gneiss	Mixed Gneiss Suite	TS	3834 ± 58	Upper Intercept	Igneous	6	5.6
				3417 - 3590	$^{207}Pb/^{206}Pb$	Metamorphic	3	
MB167	Bt Foliated Granite	Foliated Granite	TS	3370 ± 100	Upper Intercept	Igneous	4	5.8
				~3300	$^{207}Pb/^{206}Pb$	Metamorphic	3	
MB185	Bt Foliated Granite	Foliated Granite	TS	3355 ± 19	Upper Intercept	Igneous	4	0.7

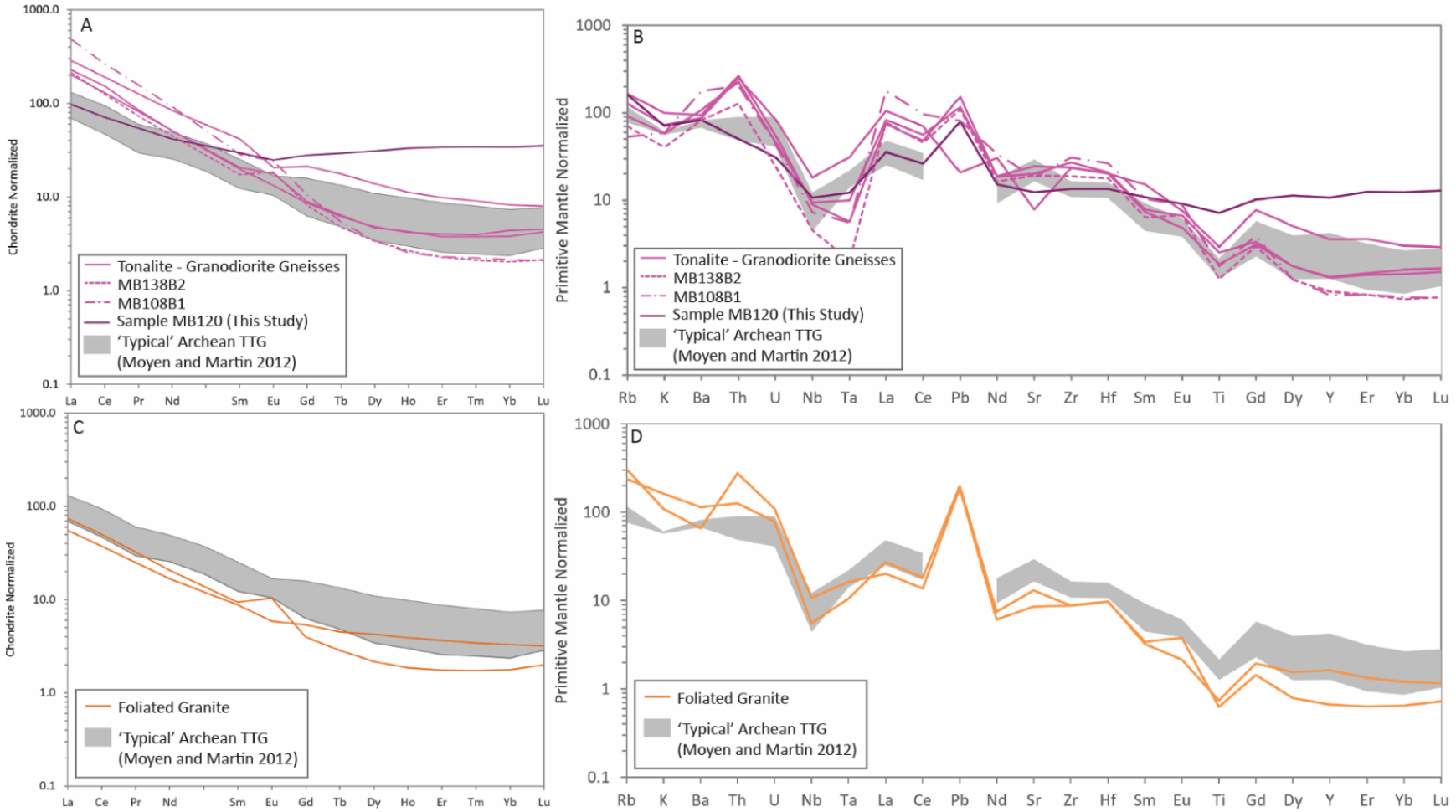

Fig. 4.7. Chondrite-normalized (McDonough and Sun, 1995) REE Patterns and Primitive Mantle normalized (McDonough and Sun, 1995) trace element diagrams of select felsic-intermediate lithologies of the Moose Lake study area. The grey area represents typical Archean TTG's as reported by Moyen and Martin (2012). These are also arranged from oldest (Top) to youngest (Bottom) highlighting a change in the trace element geochemistry of the felsic parts of the AGC over time.

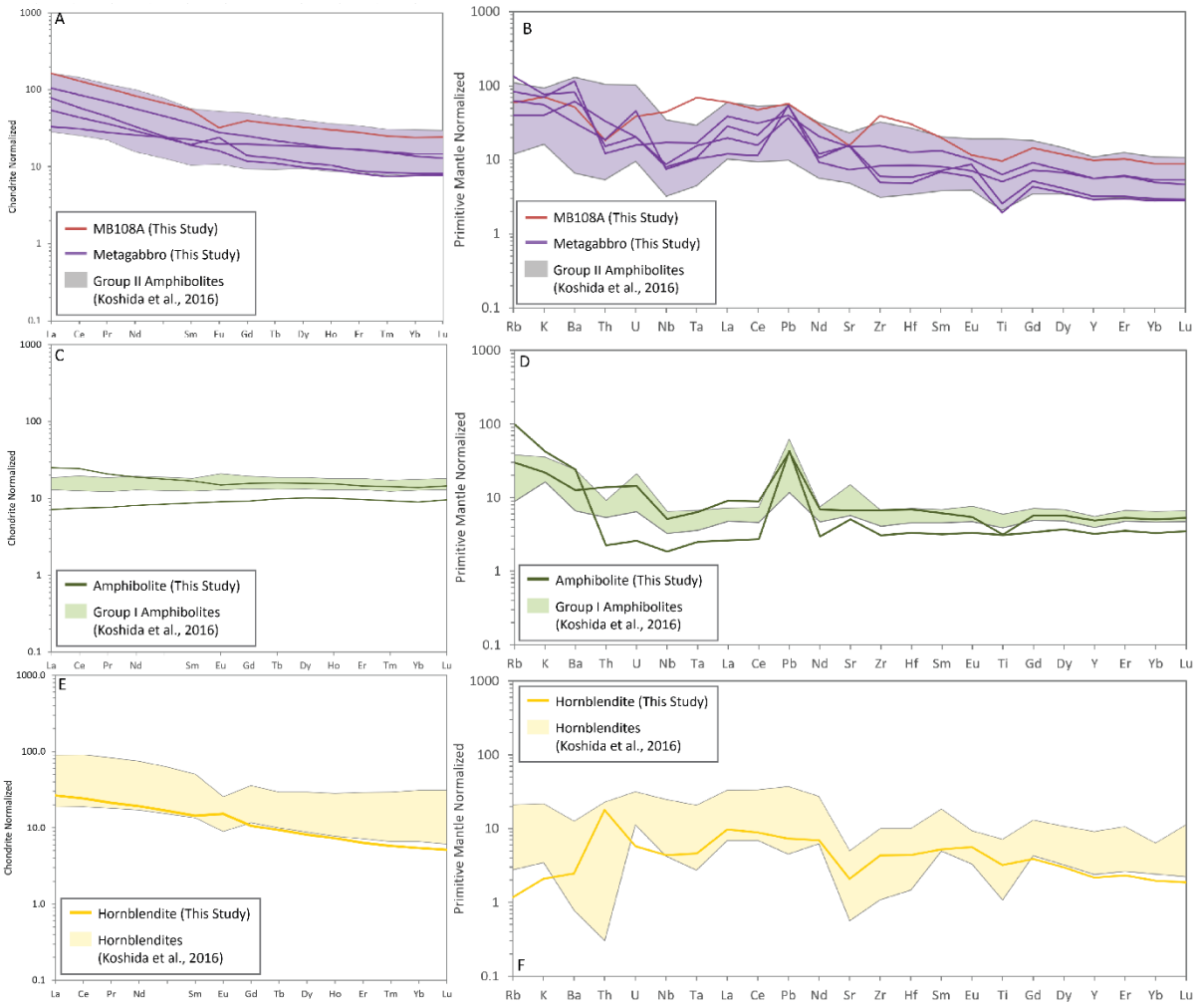

Fig. 4.8. Chondrite-normalized (McDonough and Sun, 1995) REE Patterns and Primitive mantle-normalized (McDonough and Sun, 1995) trace element patterns for the mafic lithologies of the Moose Lake study area. The shaded areas represent geochemical ranges found in similar lithologies from the Acasta discovery site as reported in Koshida et al. (2016).

Table 4.2 Whole-Rock Geochemistry Tables

	Foliated Granite		Tonalite-Granite Suites						Metagabbro					Amphibolite	
	MB04	MB185	MB14	MB21A	MB54B	MB120	MB138B2	MB-108B1	MB98A2	MB108A	MB114	MB17-10B	MB-103	MB17	MB169
SiO2 (wt.%)	74.71	74.39	67.17	67.95	71.91	60.11	73.96	72.47	53.66	52.23	56.82	53.39	52.22	51.20	51.99
TiO2	0.146	0.123	0.496	0.570	0.362	1.401	0.246	0.345	0.379	1.896	0.507	0.997	1.246	0.613	0.608
Al2O3	14.51	14.63	17.13	16.49	15.49	13.43	14.87	15.38	18.36	16.63	16.81	14.74	16.91	15.40	14.23
FeO*	1.21	1.04	3.02	4.24	2.52	12.43	1.71	2.05	7.14	11.25	7.32	11.05	10.24	9.91	9.79
MnO	0.027	0.015	0.046	0.108	0.030	0.332	0.024	0.023	0.148	0.195	0.132	0.196	0.220	0.200	0.253
MgO	0.29	0.21	1.73	1.89	0.77	1.96	0.61	0.87	7.79	4.21	5.70	6.37	5.65	8.93	7.68
CaO	1.23	0.95	2.93	0.57	2.77	5.35	2.63	2.63	6.57	7.69	7.76	8.40	7.86	10.24	13.11
Na2O	4.71	3.94	4.47	5.93	4.39	2.80	4.73	4.47	3.67	3.38	3.71	3.15	3.41	2.82	1.09
K2O	3.15	4.68	2.88	2.09	1.68	2.04	1.16	1.71	2.23	2.04	1.17	1.60	2.02	0.63	1.22
P2O5	0.02	0.02	0.12	0.15	0.09	0.13	0.07	0.04	0.05	0.47	0.06	0.10	0.23	0.06	0.04
Total	100.00	100.00	100.00	100.00	100.00	100.00	100.00	100.00	100.00	100.00	100.00	100.00	100.00	100.00	100.00
LOI %	0.64	0.56	0.64	1.91	0.82	0.63	0.55	0.63	2.19	0.95	1.32	0.91	1.81	1.23	1.91
Mg#*	30	26	51	44	35	22	39	43	66	40	58	51	50	62	58
XRF															
Ni (ppm)	2	6	7	11	6	26	7	13	133	31	80	44	69	113	119
Cr	6	5	9	14	6	19	10	15	434	9	216	53	156	352	396
Sc	3	1	5	6	2	55	3	3	17	22	17	29	21	33	45
V	9	10	37	42	25	429	14	23	96	241	112	247	161	217	262
Ba	431	753	619	563	707	558	544	1113	537	347	403	218	771	86	162
Rb	184	142	100	78	57	96	43	34	81	37	25	39	51	18	58
Sr	171	267	402	160	493	240	385	375	313	307	318	146	299	131	100
Zr	92	89	280	245	248	140	195	328	53	399	63	85	163	70	35
Y	6	3	5	16	5	45	3	4	13	41	14	24	24	21	15
Nb	6.9	4.2	5.8	12.3	6.2	7.3	2.9	3.9	5.3	29.7	4.9	4.7	10.7	2.4	0.3
Ga	19	17	17	22	19	18	17	16	18	23	18	16	18	15	12
Cu	6	3	22	8	34	59	6	8	5	54	7	27	40	67	61
Zn	20	24	35	73	30	141	31	34	103	118	87	102	119	94	97
Pb	30	31	22	4	16	12	16	12	7	10	5	9	6	7	7
La	11	18	45	66	51	25	46	105	20	39	12	3	22	3	2
Ce	20	33	79	111	87	50	73	157	36	80	30	21	54	17	8
Th	22	10	22	20	18	5	10	15	1	1	3	2	2	2	BD
Nd	6	9	19	34	21	21	20	40	15	39	13	12	24	9	4
U	2	1	1	1	1	1	1	2	1	2	2	1	1	1	2
ICP-MS															
La (ppm)	13.08	17.55	48.02	68.07	53.66	22.98	50.39	115.29	18.46	39.06	12.78	7.80	25.03	5.92	1.69
Ce	22.86	30.54	80.85	117.16	94.12	43.64	76.23	162.05	35.74	79.44	26.63	19.10	52.54	14.89	4.57
Pr	2.32	3.00	7.79	11.71	7.84	5.05	6.76	14.60	4.19	9.72	3.35	2.61	6.51	1.92	0.71
Nd	7.62	9.41	23.28	38.36	23.41	18.95	20.54	42.06	15.12	37.97	13.44	11.75	26.01	8.67	3.70
Sm	1.30	1.38	3.19	6.14	2.96	4.40	2.56	4.23	2.81	8.11	2.87	3.34	5.44	2.48	1.28
Eu	0.33	0.58	1.02	1.17	0.75	1.40	1.04	1.36	0.91	1.80	1.34	1.10	1.57	0.84	0.51
Gd	1.06	0.78	1.81	4.22	1.70	5.58	1.62	2.11	2.37	7.97	2.80	3.91	4.99	3.10	1.84
Tb	0.16	0.10	0.22	0.64	0.22	1.06	0.17	0.20	0.40	1.29	0.46	0.69	0.79	0.58	0.35
Dy	1.05	0.53	1.19	3.43	1.19	7.60	0.83	0.84	2.43	8.00	2.78	4.54	4.85	3.83	2.49
Ho	0.21	0.10	0.23	0.61	0.23	1.80	0.15	0.14	0.50	1.66	0.57	0.95	0.96	0.85	0.54
Er	0.58	0.28	0.61	1.58	0.64	5.45	0.37	0.37	1.31	4.51	1.41	2.68	2.65	2.32	1.55
Tm	0.08	0.04	0.09	0.22	0.10	0.85	0.05	0.06	0.18	0.62	0.21	0.38	0.38	0.35	0.23
Yb	0.53	0.29	0.64	1.32	0.71	5.45	0.33	0.34	1.24	3.89	1.31	2.36	2.21	2.23	1.44
Lu	0.08	0.05	0.10	0.20	0.11	0.87	0.05	0.05	0.19	0.60	0.20	0.36	0.32	0.36	0.23
Ba	443	767	625	575	713	547	548	1168	542	342	406	210	766	83	158
Th	22.27	10.26	21.11	19.90	18.03	4.00	10.11	16.24	1.22	1.46	2.64	1.49	0.98	1.09	0.18
Nb	7.07	3.64	5.86	11.93	6.23	7.03	2.99	4.74	5.32	29.51	5.72	4.96	11.40	3.37	1.21
Y	6.95	2.87	5.57	15.31	5.74	45.76	3.89	3.54	12.51	42.22	13.71	24.35	24.12	20.95	13.84
Hf	2.76	2.73	5.83	5.67	5.74	3.82	5.09	7.52	1.36	8.65	1.65	2.37	3.60	1.96	0.94
Ta	0.60	0.39	0.21	1.16	0.37	0.45	0.07	0.21	0.39	2.55	0.58	0.38	0.63	0.23	0.09
U	2.23	1.60	1.12	1.71	0.94	0.63	0.49	0.89	0.41	0.79	0.42	0.94	0.32	0.29	0.05
Pb	27.89	29.62	22.94	3.10	17.59	11.90	16.43	12.10	8.02	8.66	5.55	8.19	6.01	6.20	6.50
Rb	184.5	141.3	98.5	76.4	55.0	96.9	42.2	31.8	81.2	35.8	24.3	37.8	50.0	17.9	59.1
Cs	5.85	2.25	1.72	0.36	1.41	4.02	1.49	0.71	1.09	0.91	0.55	1.91	0.33	0.48	1.72
Sr	169.8	261.0	398.2	156.4	487.5	243.8	380.9	366.2	309.5	309.5	317.2	146.4	300.5	132.6	101.0
Sc	2.3	0.9	3.6	5.3	1.9	55.6	1.5	1.8	16.2	21.8	16.6	30.6	21.0	33.3	45.6
Zr	92	92	283	245	250	142	196	325	53	413	63	87	163	71	32
La_N/Yb_N**	16.81	41.80	51.33	34.91	51.40	2.86	104.54	228.50	10.13	6.82	6.61	2.24	7.68	1.80	0.80
Eu/Eu***	0.86	1.71	1.29	0.70	1.02	0.86	1.55	1.39	1.08	0.68	1.45	0.93	0.92	0.92	1.01
ASI****	1.09	1.10	1.10	1.30	1.12	0.83	1.09	1.11	0.91	0.81	0.79	0.67	0.79	0.65	0.53

All analyses done at the Geoanalytical Laboratory at Washington State University.

Major and certain trace elements were analyzed using XRF (Johnson et al., 1999).

Most trace elements were analyzed by ICP-MS (Knaack et al., 1994)

Major element analyses were normalized to 100% without including Loss-on-Ignition

*** Mg# calculated as 100* [MgO/(Feo+MgO)] calculated on a molar basis**

**** Normalization factors after McDonough and Sun, 1995**

***** $Eu/Eu = Eu_N/sqrt[\{Sm_N*Gd_N\}]$, normalization factors after McDonough and Sun, 1995**

****** After Shand, 1927 and Frost et al., 2001**

*******BD: Below Detection Limit**

Table 4.2 Whole-Rock Geochemistry Tables (Continued)

	Hornblendite	Pegmatitic Granites		Leucocratic Granites			Biotite Gneisses		Supracrustals
	MB141	MB47A	MB93	MB92	MB138A	MB170B	MB76B1	MB91	MB116A
SiO2 (wt.%)	51.35	75.53	74.20	74.57	75.32	76.08	68.62	65.72	61.49
TiO2	0.624	0.028	0.035	0.037	0.064	0.010	0.674	1.179	0.005
Al2O3	5.54	13.98	15.12	15.89	14.20	14.90	10.52	12.84	0.14
FeO*	11.63	0.52	0.59	0.49	0.66	0.26	13.55	10.91	35.41
MnO	0.256	0.008	0.008	0.013	0.012	0.044	0.144	0.216	0.071
MgO	19.45	0.07	0.18	0.19	0.16	0.09	2.53	2.20	1.53
CaO	10.49	0.73	0.66	1.67	0.97	2.14	0.47	2.69	1.31
Na2O	0.55	3.17	5.23	6.19	3.27	5.55	0.98	2.34	0.00
K2O	0.06	5.97	3.98	0.96	5.34	0.91	2.47	1.59	0.00
P2O5	0.04	0.00	0.00	0.00	0.01	0.01	0.05	0.32	0.05
Total	100.00	100.00	100.00	100.00	100.00	100.00	100.00	100.00	100.00
LOI %	1.78	0.46	0.58	0.73	0.54	0.86	0.40	1.63	0.00
Mg#*	75	19	36	41	30	38	25	26	7
XRF									
Ni (ppm)	994	3	2	4	4	7	2	1	23
Cr	3722	4	3	3	4	3	1	1	5
Sc	25	1	3	2	2	3	19	35	BD
V	158	3	5	10	4	1	4	9	4
Ba	16	373	207	712	629	365	402	317	10
Rb	1	158	137	17	93	22	77	42	1
Sr	40	107	59	289	130	248	40	117	2
Zr	47	63	62	64	68	27	356	276	15
Y	10	7	17	2	16	17	75	73	5
Nb	2.6	12.6	16.3	1.1	12.2	3.4	16.7	13.8	BD
Ga	9	16	25	17	20	14	17	19	1
Cu	22	2	5	3	4	6	33	129	22
Zn	101	8	6	8	13	2	73	89	38
Pb	BD	39	67	21	36	37	11	13	1
La	6	7	3	5	14	4	35	22	1
Ce	17	12	2	5	21	5	74	41	BD
Th	1	15	17	2	13	5	13	8	BD
Nd	9	4	1	1	8	2	38	20	BD
U	BD	5	8	2	3	4	3	3	BD
ICP-MS									
La (ppm)	6.27	4.20	1.07	6.17	14.32	4.68	35.71	20.60	1.30
Ce	14.84	8.64	2.56	9.27	23.87	7.08	71.69	42.30	2.14
Pr	1.98	0.76	0.32	0.91	2.32	0.74	8.90	5.38	0.25
Nd	8.74	2.57	1.46	2.88	7.81	2.54	37.43	22.62	1.14
Sm	2.13	0.82	0.90	0.54	2.01	0.86	9.62	6.57	0.32
Eu	0.86	0.23	0.20	0.68	0.42	0.20	2.39	2.01	0.18
Gd	2.12	1.00	1.46	0.47	2.25	1.09	11.03	8.78	0.48
Tb	0.34	0.22	0.35	0.06	0.43	0.26	2.00	1.81	0.09
Dy	2.00	1.42	2.40	0.33	2.77	2.13	13.36	12.87	0.66
Ho	0.40	0.28	0.52	0.06	0.55	0.56	2.98	2.86	0.16
Er	1.02	0.75	1.53	0.16	1.51	1.88	8.60	8.04	0.48
Tm	0.14	0.11	0.26	0.02	0.22	0.34	1.31	1.21	0.07
Yb	0.87	0.69	1.77	0.16	1.42	2.57	8.43	7.67	0.52
Lu	0.13	0.11	0.28	0.03	0.20	0.44	1.35	1.21	0.09
Ba	8	383	210	725	638	366	394	318	1
Th	0.71	15.06	18.48	1.99	13.83	5.38	12.26	7.40	0.09
Nb	2.86	12.41	16.04	0.88	12.08	3.28	16.31	14.15	0.17
Y	9.26	7.35	15.89	2.07	15.76	16.22	76.19	72.61	5.90
Hf	1.23	2.41	2.87	2.02	2.53	1.14	9.79	7.70	0.03
Ta	0.17	1.83	2.63	0.06	2.03	0.43	1.03	1.13	0.01
U	0.12	4.49	8.95	0.57	3.98	3.20	2.64	2.03	0.05
Pb	1.10	37.17	60.29	19.60	34.69	30.64	11.11	12.84	0.27
Rb	0.7	153.3	134.0	16.8	92.3	20.8	76.4	40.9	0.2
Cs	0.04	0.98	0.76	0.26	0.62	0.30	3.85	1.12	0.00
Sr	41.5	103.2	56.7	280.7	128.9	246.5	40.3	118.3	3.0
Sc	24.5	1.7	3.7	0.6	1.8	1.9	18.5	34.3	0.4
Zr	45	63	62	64	71	26	366	285	2
La_N/Yb_N**	4.90	4.14	0.41	26.01	6.84	1.24	2.88	1.82	1.70
Eu/Eu***	1.24	0.77	0.52	4.10	0.60	0.62	0.71	0.81	1.38
ASI****	0.28	1.08	1.07	1.11	1.10	1.06	2.10	1.33	0.06

All analyses done at the Geoanalytical Laboratory at Washington State University.
Major and certain trace elements were analyzed using XRF (Johnson et al., 1999).
Most trace elements were analyzed by ICP-MS (Knaack et al., 1994)
Major element analyses were normalized to 100% without including Loss-on-Ignition
*** Mg# calculated as 100* [MgO/(Feo+MgO)] calculated on a molar basis**
**** Normalization factors after McDonough and Sun, 1995**
***** Eu/Eu = $Eu_N/sqrt[(Sm_N*Gd_N)]$, normalization factors after McDonough and Sun, 1995**
****** After Shand, 1927 and Frost et al., 2001**
*******BD: Below Detection Limit**

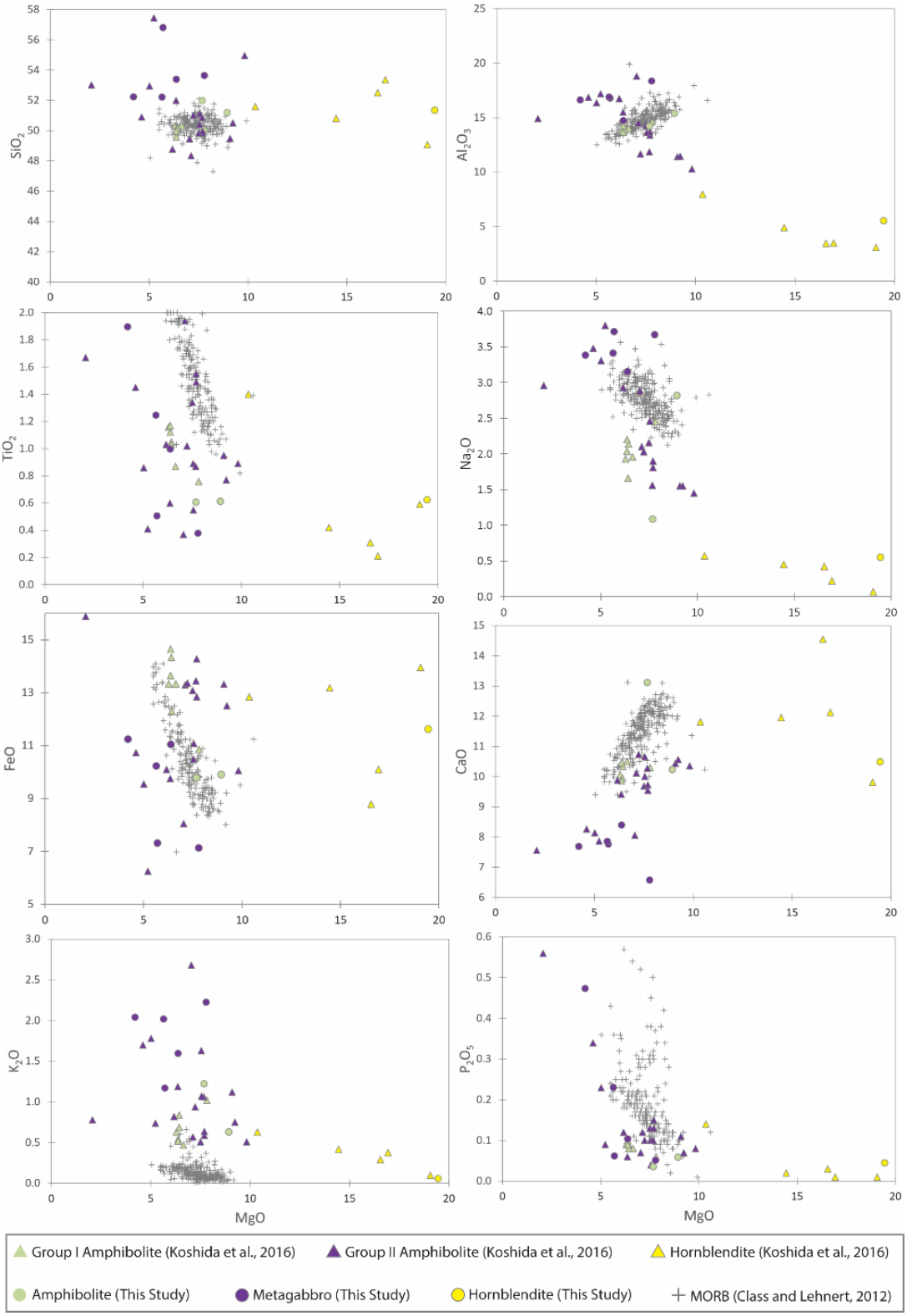

Fig. 4.9. Major elements discrimination diagrams of the mafic rocks of the Moose Lake study area compared to the mafic rocks in Koshida et al. (2016) and with MORB (Class and Lehnert, 2012)

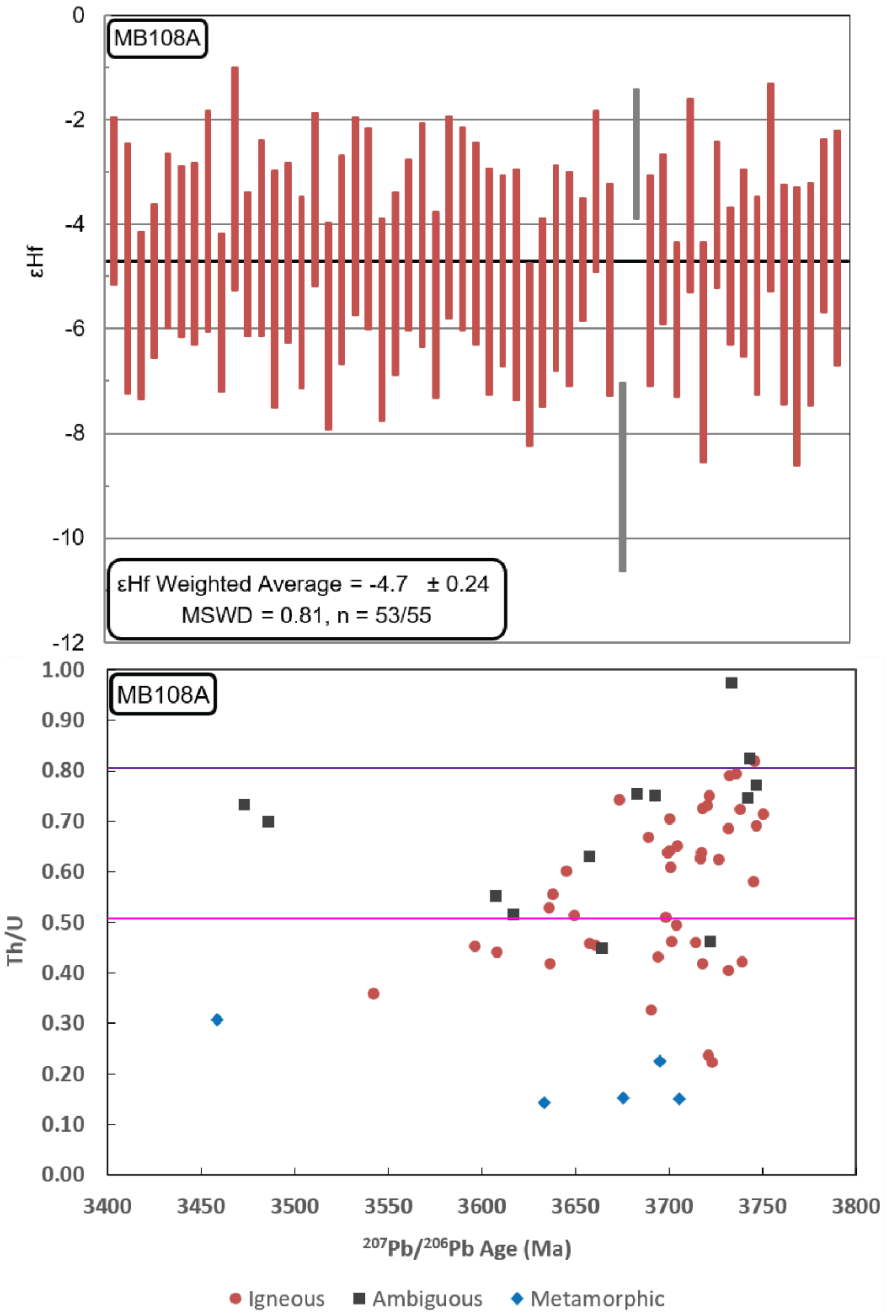

Fig. 4.10. A) Weighted average of zircon $\varepsilon Hf_{initial}$ values of igneous and ambiguous zircons for sample MB108A calculated assuming an igneous crystallization age of 3740 Ma. Two analyses falling more than 2σ outside of the mean were excluded. B) Th-U ratio vs $^{207}Pb/^{206}Pb$ age showing analyses of grains texturally inferred to be of igneous, metamorphic, and uncertain (ambiguous) origin. This plot shows a general grouping, where metamorphic zircon by-and-large has low Th/U values relative to igneous zircon. While the spread of the ages in this sample is likely due to complex multi-stage lead loss, they were nonetheless included in this plot to highlight that there are no clear trends between Th/U and Age in this sample. The pink line represents the average granitic zircon Th/U and the purple line represents the average mafic zircon Th/U (Wang et al., 2011)

Chapter 5. Discussion

5.1. Structural and Lithological Comparison of the Moose Lake and 'Discovery' Study Areas

There are several salient features of the general geology of the Moose Lake area that are distinct from the original AGC discovery area. These differences are listed and discussed in point format below.

(1) Although the geological structure of the Moose Lake area is generally similar to the discovery area, there are also a few differences. In both areas, the dominant foliation, defined by gneissic banding and alignment of platy minerals, is steeply dipping and aligned NE-SW. The orientation of fold hinges in both areas are also similar, plunging shallowly to the SW. The structure of the Moose Lake area can be explained by multi-stage deformation, whereby an earlier deformation event that generated a regional gneissosity was refolded by later event(s), forming a map pattern commonly seen in simple single-event folding of sedimentary rocks. Like in the discovery area (Bowring and Williams, 1999; Iizuka et al., 2007), there is a structural division of the Moose Lake area into western and eastern portions, where the west is higher strain and the east is lower strain. This division between the eastern and western halves of the Moose Lake area is better characterized as a strain gradient, rather than as a sharp fault contact as shown in the map of Iizuka et al. (2007) for the discovery area.

(2) The foliated granite lithology makes up a significant portion (~ 15 %) of the Moose Lake area but is not present as large, continuous bodies in the discovery map area of the AGC. This granite body has a pervasive foliation but lacks the gneissic banding that characterizes many of the other rocks of the area. There are two possible causes for the difference in strain: (a) the presence of a large homogeneous pluton partitioned the strain into surrounding more heterogeneous lithologies, or (b), the emplacement of the foliated granite post-dates the deformation event that generated gneissic banding in the rest of the area.

(3) Biotite ± garnet ± amphibole gneisses are a minor lithological component in the Moose Lake area that have not been reported in the discovery area. These rocks are strongly peraluminous (ASI values of 1.3 and 2.1), which suggests either that the

rocks are deformed S-type granites that were derived by melting metasedimentary rocks or more likely, that the rocks themselves are metamorphosed clastic sedimentary rocks. If the latter interpretation is correct, some or most of the zircons in these rocks may be of detrital origin. Unfortunately, due to the high U content of the zircons and the associated radiation damage, all the analyzed grains have undergone significant lead loss, which in turn leads to considerable uncertainty in interpreting these ages. A probability density plot of $^{207}Pb/^{206}Pb$ ages of the least discordant analyses (< 10% discordant) reveal a cluster of ~ 3600 Ma ages (Fig 4.6). Assuming these are analyses of detrital zircon, the sedimentary protolith of these rocks would have been deposited sometime after 3.6 Ga.

5.2. Geochemical Character of the Moose Lake study area

5.2.1. Sample MB108B1: 3.70 Ga Magmatism

The 3700 Ma granodioritic gneiss (MB108B1) is the oldest well-dated felsic rock in the Moose Lake area but would be considered "middle - aged" in terms of the 4.0 - 2.9 Ga AGC as a whole (e.g. Iizuka et al., 2007; Reimink et al., 2016a). This rock is strongly enriched in LREE, reflecting the presence of abundant allanite in the sample. The rock is also depleted in HREE, Nb and Ta (Fig. 4.7). The very steep REE pattern (La_N/Yb_N = ~ 230), pronounced negative Nb anomaly and high Nb/Ta (23) indicate the presence of abundant garnet (Arth and Hanson, 1972) and rutile (Foley et al., 2002; Moyen and Stephens, 2006) in the melt residue, which in turn imply melt generation at great depth in the eclogite stability field. Somewhat surprisingly, this rock also has a significant positive Eu anomaly (Eu/Eu* = 1.4), indicating the involvement of the lower-pressure mineral plagioclase in magma evolution. The positive Eu anomaly may represent plagioclase accumulation at shallower levels during final magma emplacement.

Working on rocks from the AGC discovery area, Reimink et al. (2016a) documented a shallow to deep progression with age in the depth of melt generation. They noted that steep REE patterns (La_N/Yb_N > 25), which are characteristic of many Archean TTG rocks worldwide (Moyen and Martin, 2012) and indicative of deep-seated melting, were only observed in AGC rocks younger than ~ 3600 Ma. In combination with zircon oxygen isotope

data, which indicated that the mafic source rocks of these granitoid magmas had interacted with surface waters, they further proposed that this shift to strongly fractionated REE patterns in the AGC granitoids reflects the onset of a subduction-like process in the area, beginning at ~ 3600 Ma (see also Reimink et al., 2019). My results for the granodioritic gneiss sample from Moose Lake (MB108B1) indicate that the transition from shallow- to deep-level melting may have started ~ 100 Myr earlier, at ~ 3700 rather than 3600 Ma.

5.2.2. 3.55 – 3.60 Ga Felsic - Intermediate Suite

As in the discovery area, granitoids yielding 3550 - 3600 Ma ages are volumetrically the most abundant magmatic suite at Moose Lake. The two well-dated rocks (MB21A, MB54B) and one undated rock (MB14) thought to belong to this suite and for which I have major- and trace-element data are similar in many respects to the 3700 Ma granodiorite gneiss sample discussed above. Sample MB138B2, which could have an igneous crystallization age of either 3844 or 3560 Ma (Fig. 4.3), is also geochemically similar to the rocks of this suite. All these samples have fractionated REE patterns (La_N/Yb_N = 38 - 104) and variable Eu anomalies (Eu/Eu* = 0.7 - 1.6) and Nb/Ta ratios (10 – 43). The method of Nair and Chacko (2008) uses La_N/Yb_N and the degree of Yb depletion in the TTG to estimate the proportion of garnet remaining in the melt residue during partial melting of a mafic source with MORB-like Yb contents. Application of the method to this suite of ~ 3600 Ma granitoids indicates at least 20% garnet is required in the melt residue to generate the degree of HREE depletion, which in turn suggests that melting took place at a pressure > 14 kbar. The range of Nb/Ta ratios observed in this suite of granitoids implies a range of melting pressures according to the modeling of Moyen and Stephens (2006), from > ~10 kbar for sample MB21 (Nb/Ta = 10) to > ~15 kbar for MB54 (Nb/Ta = 17). As suggested by Reimink et al. (2016a, 2019), these high melting pressures in combination with the oxygen isotope evidence for interaction of the source rocks with surface waters are more in line with tectonic burial of mafic source rocks to depth in a subduction-like process than melting at the base of a thick mafic plateau. The latter scenario would generally have melting occur at pressures ≤ 10 kbar (Nair and Chacko, 2008) and no evidence that the source rocks had interacted with surface waters.

5.2.3. Sample MB120: Enigmatic 3565 Ma Tonalitic Gneiss

One tonalitic sample that I investigated (MB120), yielded a crystallization age (3565 Ma) in the same range as others from the 3550-3600 Ma suite of rocks but, unlike those rocks, is garnet-bearing and relatively melanocratic. This sample is broadly similar both petrographically and geochemically to the oldest lithology found in the AGC discovery area, the 4.02 Ga Idiwhaa tonalitic gneiss (Reimink et al., 2014). Specifically, both of these tonalitic rocks are garnet bearing and have a high mafic mineral content, which includes a large proportion of hornblende. In addition, both of these rocks are relatively low in silica and alumina, very high in iron and have relatively flat REE patterns with a small to moderate negative Eu anomaly (Fig 4.8). Reimink et al. (2014) proposed that these geochemical traits are also present in some modern-day Icelandic rocks (icelandites) and were generated by shallow-level fractional crystallization of a mafic magma, in a process that involved plagioclase fractionation and produced an iron enrichment trend. Although there are many similarities, it should be noted that there are also some significant differences between Idiwhaa unit and sample MB120, including distinctly lower P, Zr, Nb and Ta and higher Pb and Sc in the latter.

The flat REE pattern and lack of HREE depletion in MB120 is unusual among Archean TTGs (Moyen and Martin, 2012) and indicates that the magma that formed this rock was generated at relatively shallow depth where garnet was not a major phase in the melt residue. The small negative europium anomaly also suggests that plagioclase was either left in the residue or was fractionated from the melt during magma evolution. It is unclear how the geochemical features in MB120, indicative of shallow-level melt generation, can be reconciled with those of many other broadly coeval (3550 - 3600 Ma) rocks in the Moose Lake area and elsewhere in the AGC (Reimink et al., 2016a) whose compositions clearly indicate deep-seated melt generation. One possibility is that the relatively shallow-level magmatic processes that appear to have dominated the AGC from 4.02 to 3.75 Ga (Reimink et al., 2016a) persisted to a small degree until ca. 3550 Ma and partially overlapped in time with deep-seated, possibly subduction-related, melt-generation processes that characterized most of the AGC after ca. 3700 – 3600 Ma.

5.2.4. 3.37 Ga Foliated Granite

The ~ 3.37 Ga foliated granite, which is a significant unit in the Moose Lake area, is not well described in previous studies. Thus far, only Reimink et al. (2016a) and Bauer et al. (2017) have documented rocks of this age from the AGC but the reported ages are not on samples obtained from well-mapped plutonic bodies. Several studies (Williams et al., 1992; Williams and Bowring, 1997; Stern and Bleeker, 1998; Reimink et al., 2014) have dated metamorphic zircon growth near this age. The present study yielded a robust age of 3374.6 ± 8.5 Ma for this unit (Fig. 4.1), agreeing with the dating done by previous studies in the discovery area. Notably, detrital zircons of this age feature prominently in eskers that transect the AGC (Bilak et al., 2019). Collectively, these observations suggest that 3.37 Ga granitoids make up a significantly larger proportion of the AGC than previously known. Given the size of the foliated granite intrusion and its widespread occurrences in the AGC, it is reasonable to posit that the ~3.37 Ga metamorphism (Stern and Bleeker, 1998) and resetting of Sm-Nd isochrons documented in the AGC discovery area (Moorbath et al., 1997; Roth et al., 2014) may be related to intrusion of this suite of granitoids.

The chemical composition of this unit is like the 3550 – 3700 Ma suite granitoids described by Reimink et al. (2016a) and in the present study, albeit with somewhat lower La_N/Yb_N (17-41) and Nb/Ta (9-12) on average than those rocks. These compositions suggest melt generation at relatively high pressures but not as high as those associated with melt generation in the preceding ~3.6 Ga magmatic episode. Bauer et al. (2017) have studied the Lu-Hf systematics of zircons from ~ 3.37 Ga granitoids (εHf_i = -4.6 to -1.4) and conclude that they were likely formed by partial melting of juvenile ~3.6 Ga AGC crust rather than by reworking of older (> 3.7 Ga) AGC rocks, which would have had significantly more negative εHf values by 3.4 Ga. The relatively elevated K_2O contents of these 3.37 Ga granitoids suggests their derivation by partial melting of intermediate or felsic rather than mafic source rocks. If the Hf isotope data reported by Bauer et al. (2017) for 3.37 Ga rocks from the discovery area also apply to granitoids of this age from the Moose Lake area, the crustal source rocks for these granitoids must have been extracted from the mantle at or after 3.6 Ga.

5.2.5. 3.30 Ga Zircon Growth/Metamorphism

An important finding of the present study is the occurrence of zircon, interpreted to be of non-igneous and possibly metamorphic origin, recording U-Pb ages of ~ 3.30 Ga. Zircons of this age were found in at least some samples of all three of the major rock units of the Moose Lake area and include data from both concordant or near-concordant analyses (MB07; Fig. 4.1, MB108B1; Fig. 4.3, MB120; Fig. 4.2) and upper intercepts of discordia arrays obtained on these 'metamorphic' grains (MB108B1; Fig. 4.3, MB120; Fig. 4.2). In one sample (MB120), there are two discrete populations of these concordant 'metamorphic' analyses, one at ~3315 Ma and another at ~3240 Ma. A compilation of all zircon analyses inferred to be of 'metamorphic' origin is shown in Figure 5.1.

The significant geographic separation of the rock units from which these zircons were derived as well as their disparate chemical compositions and strain characteristics suggests that this 'metamorphic' zircon growth event at 3.30 Ga must have been regional in scale. Notably, an ID-TIMS study of igneous zircons from 4.02 Ga Idiwhaa unit of the discovery area show a discordia array with a lower intercept of 3290 ± 16 Ma (Reimink et al., 2016b). This finding suggests that ~3.30 Ga represents not only a time of new zircon growth across the AGC but also a time of Pb loss from earlier-formed igneous zircon. While ages reported on other non-igneous zircon from the AGC, like those at ~3.6 Ga (e.g., Iizuka et al., 2007; Reimink et al., 2016a) and ~3.36 Ga (e.g., Bleeker and Stern, 1997), coincide with known episodes of plutonic activity, this 3.30 Ga zircon growth event does not correspond to any hitherto reported age of igneous intrusion in the AGC. As such, zircon growth at ~3.30 Ga reflects either regional metamorphism or regional-scale hydrothermal activity that took place in the AGC at this time and which was not directly related to plutonism.

5.3. Mafic suites and their comparison to the discovery area

Most of the work done in the AGC has been focused on traditionally zircon - bearing lithologies, which are generally felsic to intermediate in composition. Mafic rocks in the discovery area, including metagabbro, amphibolite and hornblendite are comparatively not well dated due to the general paucity of zircon in these rocks.

5.3.1. Age and Origin of the Metagabbro Unit

In the Moose Lake area, I collected two samples of homogeneous metagabbro from the lower - strain eastern portion of the map area that contain a large number of zircon grains, and which yielded a robust igneous crystallization age of 3740.7 ± 2.3 Ma. Given the paucity of age data for mafic lithologies in the AGC (e.g. Iizuka et al., 2007; Mojzsis et al., 2014; Reimink et al., 2016a), having relatively well - behaved U - Pb data from zircons obtained from mafic rocks is valuable.

Considering the lack of clearly igneous zircon material in other areas of the AGC, the origin of the zircons in the Moose Lake metagabbros must be established. In Figure 4.5, a typical selection of zircons from sample MB108A are highlighted showing distinct coarse-scale banding. It is highly unlikely that these zircons are xenocrysts derived from older felsic rocks because high-temperature mafic melts readily dissolve xenocrystic zircon (Boehnke et al., 2013). Additionally, the banding found in the metagabbro zircons is coarse scale, in contrast to the fine-scale oscillatory zoning typically found in zircons crystallized from felsic magmas (Hoskin, 2000). Finally, the Th/U ratio of zircon interpreted on textural grounds to be of magmatic origin is mostly between 0.4 and 0.8, which is at the lower end of the range of those reported from mafic to intermediate composition igneous rocks (Wang et al., 2011). Thus, it is reasonable to posit that the zircons from the metagabbro are of igneous origin.

Geochemically, zircon - rich metagabbro such as samples MB108A and MB103 are distinct from the non - zircon bearing mafic lithologies; both have high Zr content, as well as moderately LREE-enriched patterns with moderate (MB108A) to very weak (MB103) negative Eu anomalies. The Hf and La contents of these two samples differ somewhat, though both are elevated in Hf compared with average N-MORB and E-MORB (Gale et al., 2013). As noted above, the zircons present in the metagabbro have textures consistent with igneous crystallization and, apart from some ancient lead - loss, appear to have retained their U-Pb isotopic composition. The initial εHf values (εHf_i) of the zircons in the metagabbro unit (-4.7 ± 0.24) is within error of those reported from some similarly-aged but generally more evolved AGC rocks (εHf_i = -3.8 to -5.9; Bauer et al., 2017). Zircon Hf isotope data from the younger 3.55 - 3.60 Ga suite of AGC granitoids have less strongly negative εHf_i values (Amelin et al., 1999; Iizuka et al., 2009; Bauer et al., 2017; 2019). Previous work done by

Bauer et al (2017) has highlighted that these younger granitic suites have markedly different Hf isotope compositions, potentially due to a shift in the tectonic setting in the AGC after 3.7 Ga, as originally postulated by Reimink et al. (2016a).

Metagabbro sample MB108A, for which I have both U-Pb and Hf isotope data, is mafic in composition (~ 52 wt. % SiO_2). Given its little-evolved major-element composition, the relatively negative εHf_i value (-4.7) of this rock is somewhat surprising. This low value could imply either derivation of the primary gabbro magma from an enriched mantle source (ancient mantle source with long-term low Lu/Hf) or derivation of the magma from a more normal (chondritic) mantle source, followed by extensive assimilation by this magma of older crust with a negative εHf value. To evaluate the latter possibility, I performed some assimilation-fractional crystallization (AFC) calculations using the equations developed by Taylor (1980) and DePaolo (1981). Two main sets of scenarios were modelled, one involving a primary magma with N-MORB-like and the other with E-MORB-like trace-element characteristics (Gale et al, 2013). These primary magmas were assumed to have a chondritic Hf isotope composition at the time of intrusion ($\varepsilon Hf_{3.74\ Ga} = 0$). Three different assimilants were also considered in the modelling: 1) The intermediate-composition Idiwhaa tonalitic gneiss (Remink et al., 2014; 2016b), which would have had $\varepsilon Hf_{3.74\ Ga} = -5.6$. 2) A more felsic 3.94 Ga tonalitic gneiss reported by Reimink et al. (2016a) with an unusually high Hf content (12.6 ppm Hf; sample JR13-206)). 3) A felsic rock with average upper crustal Hf content (5.3 ppm; Rudnick and Gao, 2003). The $\varepsilon Hf_{3.74\ Ga}$ value of the latter two possible assimilants was assumed to be -7, the most negative value that earlier-formed AGC rocks are inferred to have evolved to by 3.74 Ga (Bauer et al. 2017). Following Reimink et al. (2016b), I assumed that the minerals fractionating from the primary magma comprised 10 % olivine, 60 % clinopyroxene and 30 % plagioclase. The calculations also implicitly assume that the measured composition of the metagabbro reflects a liquid composition rather than that of a cumulate. The bulk mineral-melt partition coefficients (D values) for Hf, La and Yb with this fractionating assemblage are 0.14, 0.11 and 0.32, respectively (Reimink et al. 2016b). The rare-earth elements were also included in the modelling to investigate the degree of LREE to HREE fractionation that might be induced in the magma by the AFC process.

Another important input parameter in the AFC calculations is the r-value (DePaolo, 1981), which is the ratio of country rock assimilated to cumulates fractionated from the magma ($r=Mass_{assimilants}/Mass_{cumulates}$). The r-value relates to the amount of fractional crystallization the magma must undergo to generate the thermal energy required to heat up and assimilate country rocks; a low r-value means the magma must undergo a higher degree of crystallization and visa-versa. I assume a relatively high r-value (0.67) in the calculations, which implies that the rocks being assimilated were already at near-melting temperatures prior to intrusion of the mafic magma. In turn, with this high r-value, a smaller amount of fractional crystallization is needed to achieve the same degree of change in the trace-element and isotopic composition of the magma. Thus, assuming a high r-value is a best-case scenario for shifting the Hf isotope composition of a primary mafic magma by an AFC process without greatly affecting its major-element composition.

A summary of input parameters used in the AFC calculations is given in Table 5.1. Figures 5.2A and 5.2B show the results of the modelling for the N-MORB and E-MORB primary magma scenarios, respectively, with the results plotted as εHf vs La_N/Yb_N. With an N-MORB composition primary magma, incorporation of the three potential assimilants result in the evolving magma approaching the composition of metagabbro sample MB108A at varying degrees of magma fractionation. The amount of fractionation required ranges from < 90% crystallization (i.e., < 10 % liquid remaining) in the case of an Idiwhaa gneiss-like assimilant to ~ 50 % crystallization for an assimilant with a composition like average upper continental crust to ~ 35 % crystallization if the assimilant has both a high Hf content and a strongly negative εHf value like the felsic gneiss modelled. For an E-MORB composition primary magma, the required degrees of fractionation are somewhat less, ranging from slightly greater 90 % crystallization for an Idiwhaa-like assimilant to ~ 20 % crystallization for a high Hf content, low εHf assimilant.

The amount of magma crystallization required to reproduce the trace-element and initial Hf isotope composition of the metagabbro is important in that it is one of the two factors that will determine the degree to which the major-element composition (e.g. SiO_2 content) of the magma is affected by the assimilation process. The other factor affecting major-element composition during assimilation will be the difference in concentration of a

particular element between the primary magma and the assimilant; the larger the difference, the more the magma's composition will be affected for a given degree of magma crystallization and assimilation. Given that the SiO_2 content of the metagabbro (~ 52 wt. %) is only slightly higher than that of primary magmas considered here (~ 50 wt. %), this major-element parameter provides a stringent constraint with which to evaluate the viability of the different AFC scenarios considered in my modelling.

Calculations by Spera and Scruggs (2016) using the MELTS thermodynamic software indicate that pure fractional crystallization of basaltic magma with no assimilation will cause very little increase in the SiO_2 content of residual magma in the first 40 % of magma crystallization (i.e., 60 % of original liquid remaining). Thus, one can reasonably assume that any significant increase in SiO_2 content that occurs over that initial 40 % crystallization interval in an AFC process will be due to assimilation rather than to pure fractional crystallization. The r-value dictates how much country rock is assimilated for a given amount of magma crystallization. For example, for the r-value assumed in my calculations (0.67), 40 % magma crystallization (i.e., 0.4 g of cumulates have formed from 1 g of original magma) results in 0.4 g x 0. 67 = 0.268 g of country rock assimilated per gram of original magma. If the assimilant is higher in SiO_2 than the primary magma, this assimilation process will result in an increase in the SiO_2 content of the magma. More generally, the change in the SiO_2 content of the magma ($\Delta(SiO_2)_{magma}$) caused by country rock assimilation can be approximated by the following equation:

$$\Delta(SiO_2)_{magma} = \{[SiO_2]_{assimilant} - [SiO_2]_{primary\ magma}\} * f * r$$

where f is the fraction of magma crystallized and r is the r-value ($Mass_{assimilants}/Mass_{cumulates}$) used as input in the AFC calculations.

Notably, for nearly all the scenarios considered in my AFC modelling, the degree of magma fractionation required to generate the observed εHf and La_N/Yb_N of the metagabbro sample would result in a > 4 wt. % increase in the SiO_2 content of the magma, which is more than double the difference between the SiO_2 content of the modelled MORB-like primary magma and that of the metagabbro. The only modelled AFC scenario in which the calculated $\Delta(SiO_2)_{magma}$ approaches the observed value is the case where an E-MORB-like primary magma assimilates a high Hf content, low εHf rock. Even here, the calculated increase in

magma silica content (2.9 wt. %) is larger than the observed increase in SiO_2 in the metagabbro relative to the modelled primary magma (1.6 wt. %).

The modelling reveals that although some AFC scenarios considered here come close to explaining the composition of the metagabbro, it is difficult to rigorously account for both the isotopic/trace-element and major-element characteristics of the metagabbro by assimilation of known rocks in the AGC. Therefore, alternative models need to be considered to explain the strongly negative εHf of the metagabbro. There are at least three possible scenarios that could account for these major element, trace element, and isotopic characteristics: 1) This metagabbro lithology formed from a melt generated from an enriched mantle source; 2) Assimilation of an enriched ancient (> 4.2 Ga) mafic crust which could modify trace element and Hf isotopic signatures without significantly changing major element geochemistry, or 3) a combination of derivation from a slightly enriched source with a small enough degree of assimilation of felsic crust to not modify the major elements significantly.

5.3.2. Amphibolites

These samples have relatively flat REE and PM normalized trace element patterns indicating not much of a deviation from its original melt composition. It is possible, as suggested by Koshida et al. (2016) that these rocks were generated from partially melting a primitive mantle - like source. Unfortunately, due to the lack of reliable age information and the lack of definitive field relationships due to the deformation, it is impossible to determine the absolute or relative age of this unit. The Moose Lake amphibolite suite, like the group I Koshida et al. (2016) amphibolites, is the closest, geochemically, to modern MORB compositions in both major and trace elements. It is a likely scenario that the amphibolite unit does represent some of the most primitive mafic material at the AGC and is potentially some of the most ancient.

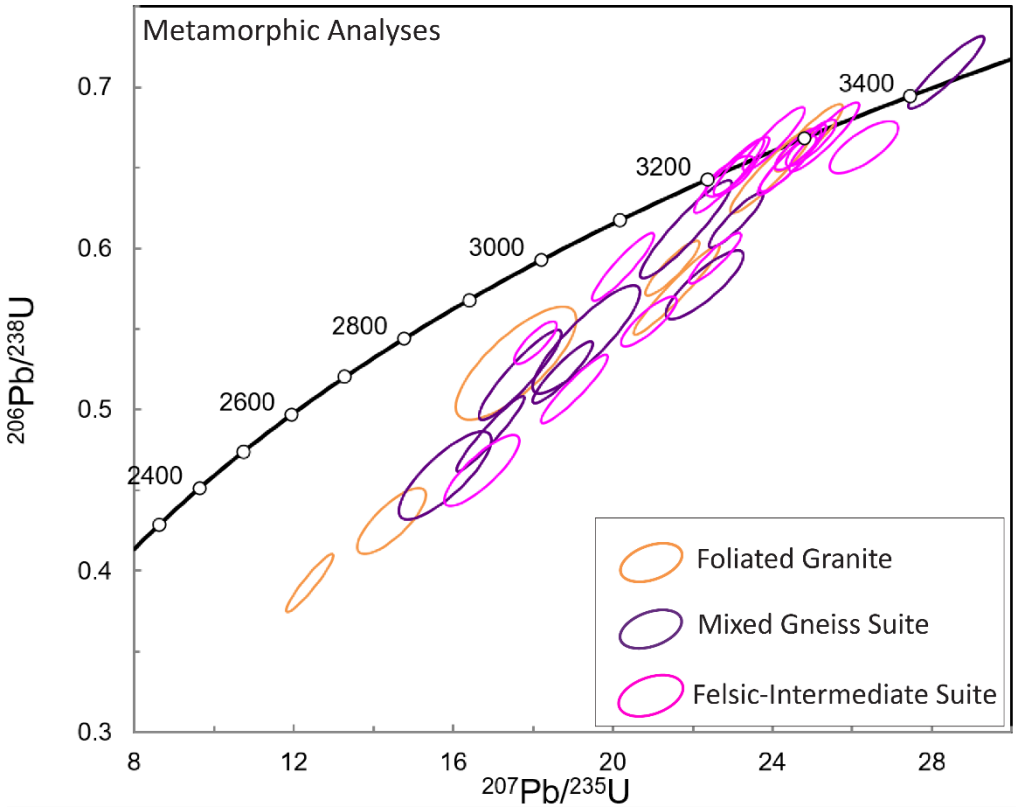

Fig 5.1. Wetherill U-Pb concordia plot for metamorphic zircon analyses from the Foliated Granite suite (Orange), the Mixed Gneiss Suite (Purple) and the Felsic-Intermediate Suite (Pink). This plot highlights the ubiquitous nature of the ~3.3Ga zircon growth event throughout the Moose Lake study area. Ellipses represent 2σ errors.

Table 5.1. Input Parameters for AFC Calculations

Rock Type	La (ppm)	Yb (ppm)	Hf (ppm)	εHf(3.74 Ga)	r-value	SiO2 (wt. %)
N-MORB	4.19	3.28	2.46	0	0.67	50.42
E-MORB	12.02	2.59	2.54	0	0.67	50.58
Idiwhaa intermediate gneiss	27.15	6.65	8.02	-5.6	0.67	57.94
3.94 Ga felsic gneiss	42.90	1.55	12.56	-7	0.67	72.41
Average Upper Crust	31	2.0	5.3	-7	0.67	66.6

Trace-element (TE) data for MORB from Gale et al. (2013). TE data for 3.94 Ga gneiss from Reimink et al. (2016a).

TE and εHf data for Idiwhaa gneiss from Reimink et al. (2014; 2016b). TE data: average upper crust-Rudnick and Gao (2003).

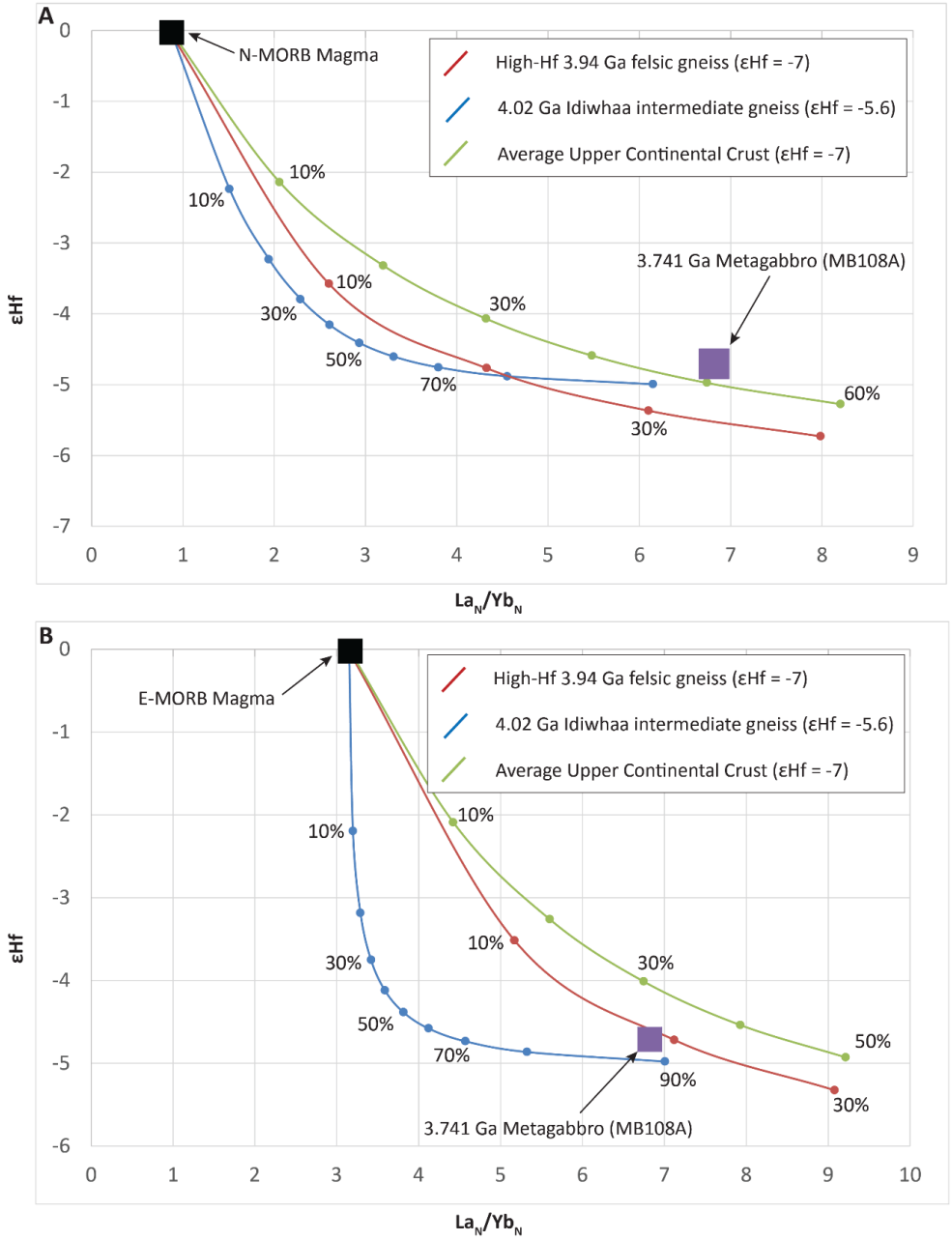

Fig 5.2. AFC Modelling of three potential crustal assimilants during the emplacement of the metagabbro unit (MB108A) using formulas from Taylor (1980) and Depaolo (1981). Starting melt composition trace elements are from N-MORB (**A**) and E-MORB (**B**) (Gale et al., 2013), with bulk distribution coefficients for 10% Olivine, 30% Plagioclase, and 60% Clinopyroxene, using formulas from Rollinson (1993). Percentages are the amount of crystallization taken place. This plot compares the assimilation required in order to generate an εHf and LaN/YbN signature present in the metagabbro, using an expected scenario (Idiwhaa), an idealized scenario (~3.94 Ga Tonalite), and an average upper crustal scenario (Rudnick and Gao, 2003). Under idealized circumstances, it is possible to produce these trace element and isotopic signatures using only (relatively) low levels of assimilation during fractional crystallization of a high-Hf, strongly-negative εHf 3.94 Ga felsic gneiss geochemically similar to JR13-206 (Reimink et al., 2016a)

Chapter 6. Conclusions and Future Work

In this thesis, I present the results of a field-based geochronological and geochemical study of a 3 x 5 km portion of the Acasta Gneiss Complex informally named the "Moose Lake" area. The study includes the preparation of a bedrock geological map of the area at the 1:5000 scale. This map and its associated laboratory data provide valuable insight into an unexplored region of the AGC approximately 9 km away from the well-trodden discovery site on the Acasta River. Similar to the discovery site, the Moose Lake area can be divided into two principal domains: (1) A western domain generally characterized by higher-strain banded felsic to intermediate gneisses, with entrained elongate bodies of metagabbro and amphibolite, capped at its western margin by a large homogeneous pluton of foliated granite, and (2) an eastern domain characterized by lower-strain chaotically folded and deformed mixed felsic to mafic gneisses including small bodies of metagabbro and subordinate ultramafic lithologies. These two domains have similar rock units and are separated by what is best characterized as a strain gradient. Both domains have been intruded by numerous small felsic and mafic dykes that range in width from the centimeter to the meter scale. Also present are several small areas of garnet - bearing biotite gneisses, which are potentially sedimentary in origin, within a structural trough in the east-central portion of the map area. One outcrop in that same general area contains interlayered magnetite-rich iron formation, amphibolitite and garnetite (a grt-rich, grt-bt rock). This package of rocks is also likely of supracrustal origin.

The deformational fabric of the Moose Lake area is consistent and pervasive, with a steeply-dipping NE-SW foliation defined by gneissosity and mineral alignment. This penetrative deformational fabric has been folded into map-scale folds with fold hinges and mineral lineations indicating that the fold axes plunge shallowly to the SW. Three major axial traces were identified in the area, which were defined by field relationships, structural measurements, and appearances of certain lithologies.

Given the inherent complexity of interpreting age-relationships in highly deformed gneiss terranes, I established the ages of most of the lithologies present in the Moose Lake area through LA-ICP-MS U-Pb zircon geochronology. In particular, I identified two main

"pulses" of the older felsic- intermediate magmatic activity in the Moose Lake area, one at 3.72 – 3.68 Ga and a second at 3.60 – 3.55 Ga. The 3.72-3.68 Ga aged rocks are only found in the mixed gneiss suite, whereas the 3.60 – 3.55 Ga rocks are found in both the mixed gneiss suite and the felsic – intermediate suite. With the exception of sample MB120, which has a distinctive composition, all other samples from both age pulses share similar geochemical and geological characteristics. They range from granodioritic to tonalitic in composition, with a distinct HREE depletion and a pronounced negative Nb anomaly indicating melt generation at depths corresponding to > 14 kbar. The one exception, sample MB120, yielded an age of 3565 ± 13 Ma but is similar to the 4.02 Ga Idiwhaa tonalitic gneiss (Reimink et al., 2014) in terms of its intermediate, iron-rich major-element composition and lack of HREE depletion. These compositional characteristics indicate a shallow depth of formation in contrast to roughly contemporaneous deep-seated rocks from the area. This unit, which was only noted in one area, does not appear to be regionally extensive in the Moose Lake area

Another igneous rock unit that has been noted elsewhere in the AGC but which had not previously been described in any detail is the foliated granite unit. This unit comprises a significant portion of the Moose Lake area. It is more homogeneous at the outcrop scale than most other rock units in the AGC and has a well-defined crystallization age of 3374.6 ± 8.5 Ma, which corresponds closely to the Sm-Nd resetting date of the AGC (Moorbath et al., 1997) and some metamorphic zircon rim analyses performed by Bleeker and Stern (1998). The deformational fabric in this unit is generally weaker than the surrounding gneisses while still following the orientation of the regional fabric. There are two potential explanations for the less pronounced deformational fabric in this unit: (1) this large granite pluton was able to partition strain and decrease the intensity of deformation within the body itself during the event(s) that generated the fabric in the rest of the complex or, (2) the intrusion of this granite occurred late in the deformational event(s) that generated this regional fabric.

In addition to documenting the igneous crystallization age of the main rock units in the Moose Lake area, I also investigated the U-Pb isotope systematics of zircon interpreted on textural grounds to be of non-igneous and possibly metamorphic origin. Interestingly, many of the zircon-bearing rock units from across the study area record a period of

'metamorphic' zircon growth and recrystallization at ~3.30 Ga, which is notable due to a lack of plutonism in the Moose Lake area or elsewhere in the AGC during this time. This is unique in the AGC in that other reported ages of 'metamorphic' zircon growth, including those at ~ 3.7-3.8 Ga, ~3.6 Ga and ~ 3.37 Ga (Bleeker and Stern, 1998; Bowring and Williams, 1999; Iizuka et al., 2007; Reimink et al., 2014;2016a), coincide with known episodes of plutonic activity. This suggests that the AGC may have experienced regional metamorphism or regional-scale fluid flow at ~ 3.30 Ga, which led to the growth of non-igneous zircon.

A final important discovery of the present study relates to mafic rocks in the study area, in particular the metagabbro unit. The mafic rocks of the AGC are less well understood than the felsic and intermediate rocks, in part due to significant uncertainty regarding their ages. Many of these rocks do not contain zircon and, in the few that do, the zircon is commonly of uncertain paragenesis. Thus, it is significant that two of the metagabbro samples of my study, MB103 and MB108A, which were collected from a relatively large metagabbro body, contain abundant, well-preserved zircon. Detailed investigation of the U-Pb isotope systematics of these zircons showed a consistent pattern, which included some degree of Pb loss in nearly all the analyses but also a pronounced peak of $^{207}Pb/^{206}Pb$ ages in the near-concordant analyses, corresponding to a weighted mean date of 3740.7 ± 2.3 Ma. The internal zoning characteristics and Th/U of the zircons on which this weighted mean date is based are more typical of igneous than metamorphic zircon. Therefore, I interpret this date to be the intrusion age of the gabbro magma. This represents what is likely the most robust igneous crystallization age estimate that has yet been reported for any mafic rocks of the AGC.

To investigate the petrogenesis of this metagabbro unit, I conducted both whole-rock major- and trace-element analyses and zircon Hf isotope analyses of the unit. The metagabbro has a low Mg# (40-50), is relatively enriched in incompatible elements (La_N/Yb_N = 6.8-7.6) and has a distinctly unradiogenic initial εHf value (-4.7 ± 0.24). Calculations were carried out to evaluate if an assimilation-fractional crystallization (AFC) process could account for this combination of geochemical and isotopic characteristics. The AFC calculations assumed a primary magma with MORB-like major- and trace-element

characteristics and a chondritic Hf isotope composition (εHf = 0) and considered three different potential intermediate- to felsic-composition assimilants, which broadly correspond to older (> 3.8 Ga) rock types present in the AGC. For the modelling scenarios considered, the degree of magma crystallization and associated assimilation that would be required to generate the strongly negative εHf value of the metagabbro unit was too great to retain the observed mafic (low SiO_2) character of the metagabbro. This finding suggests that assimilation of known older intermediate- and felsic-composition rocks from the AGC is unlikely to account for the distinctive Hf isotope composition of the gabbro. Other models to explain the observations include derivation of the gabbro magma from an enriched mantle that had acquired a low Lu/Hf early in the planet's history and had therefore evolved to a strongly negative εHf value by 3.74 Ga. Alternatively, assimilation of early- to mid-Hadean mafic crustal rocks by a chondritic Hf isotope composition primary magma could generate the requisite negative εHf value without greatly affecting the major-element characteristics of the magma. The existence of Hadean-age mafic crust in the AGC has in fact been suggested in some earlier studies (Reimink et al., 2016a; 2018).

Future Work

While much is known about the felsic and intermediate lithologies from the AGC, less is understood about the mafic lithologies. Due to the absence of zircon, the absolute age of the amphibolite unit is unknown. From field and textural relationships as well as its primitive geochemical signatures, it could potentially be one of the oldest components of the AGC. I recommend that future study examines alternative geochronological approaches to dating this unit, two such approaches that could work are 1) Re - Os dating of sulfides such as pyrite, or 2) whole – rock Lu-Hf.

One of the rock units that I characterized in this study is the garnet-bearing biotite gneiss, which may be of supracrustal origin. Due to their elevated uranium contents, the zircons analyzed from these rocks are highly radiation damaged, which made it impossible to establish an absolute age or even a maximum depositional age for this rock. Considering the impact that the discovery of an ancient package of supracrustal rocks at Acasta would have, I recommend that more of the samples I collected from this lithology be processed for zircon

and monazite. A larger sample size of zircons and monazites may allow both a maximum depositional age (zircon) and a metamorphic age (monazite) to be established for this unit.

Finally, due to time and scope restraints, I did not perform any oxygen isotope analysis of the zircons from this study. These analyses would provide an additional tracer for understanding the petrogenesis of the metaigneous rocks investigated herein. This is particularly true of the metagabbro, where zircon oxygen isotope analysis could clarify the nature of the assimilant that interacted with the parental mafic magma to produce the strong negative initial εHf values of the metagabbro. Specifically, as documented by Reimink et al. (2016b), many of the zircons derived from the felsic lithologies of the AGC have $\delta^{18}O$ values above the mantle value (5.3 ± 0.6 ‰). As such, assimilation of these rocks by the primary magma should lead to above-mantle $\delta^{18}O$ values in the metagabbro zircons. Alternatively, assimilation of Hadean-age mafic crust, such as has been suggested for the 4.02 Ga Idiwhaa tonalitic gneiss (Reimink et al., 2016a), may not lead to elevated $\delta^{18}O$ values if that crust had never interacted with surface waters.

Bibliography

Allmendinger, R.W., Cardozo, N., Fisher, D.M., 2011. Structural geology algorithms: Vectors and tensors, Structural Geology Algorithms: Vectors and Tensors. https://doi.org/10.1017/CBO9780511920202

Arth, J.G., Hanson, G.N., 1972. Quartz diorites derived by partial melting of eclogite or amphibolite at mantle depths. Contrib. to Mineral. Petrol. 37, 161–174. https://doi.org/10.1007/BF00371074

Ashton, K.E., Heaman, L.M., Lewry, J.F., Hartlaub, R.P., Shi, R., 1999. Age and origin of the Jan Lake Complex: a glimpse at the buried Archean craton of the Trans-Hudson Orogen. Can. J. Earth Sci. 36, 185–208.

Barker, F., Arth, J.G., 1976. Generation of trondhjemitic-tonalitic liquids and Archean bimodal trondhjemite-basalt suites. Geology 4, 596–600. https://doi.org/10.1130/0091-7613(1976)4<596:GOTLAA>2.0.CO;2

Bauer, A.M., Fisher, C.M., Vervoort, J.D., Bowring, S.A., 2017. Coupled zircon Lu–Hf and U–Pb isotopic analyses of the oldest terrestrial crust, the >4.03 Ga Acasta Gneiss Complex. Earth Planet. Sci. Lett. 458, 37–48. https://doi.org/10.1016/j.epsl.2016.10.036

Bauer, A.M., Vervoort, J.D., Fisher, C.M., 2020. Unraveling the complexity of zircons from the 4.0–2.9 Ga Acasta Gneiss Complex. Geochim. Cosmochim. Acta 283, 85–102. https://doi.org/10.1016/j.gca.2020.05.023

Belousova, E.A., Griffin, W.L., O'Reilly, S.Y., Fisher, N.I., 2002. Igneous zircon: Trace element composition as an indicator of source rock type. Contrib. to Mineral. Petrol. 143, 602–622. https://doi.org/10.1007/s00410-002-0364-7

Bennett, V.C., Brandon, A.D., Nutman, A.P., 2007. Coupled 142Nd-143Nd isotopic evidence for hadean mantle dynamics. Science (80-.). 318, 1907–1910. https://doi.org/10.1126/science.1145928

Bilak, G.S., Reyes, A. V, Chacko, T., Reimink, J.R., Belosevic, M.B.K., Niemetz, K., Ketchum, J.W.F., Dufrane, S.A., 2019. New insights into the Acasta Gneiss Complex using detrital zircon in Pleistocene esker systems. 21st EGU Gen. Assem. 21, 1.

Black, L.P., Kamo, S.L., Allen, C.M., Davis, D.W., Aleinikoff, J.N., Valley, J.W., Mundil, R., Campbell, I.H., Korsch, R.J., Williams, I.S., Foudoulis, C., 2004. Improved 206Pb/238U microprobe geochronology by the monitoring of a trace-element-related matrix effect; SHRIMP, ID-TIMS, ELA-ICP-MS and oxygen isotope documentation for a series of zircon standards. Chem. Geol. 205, 115–140. https://doi.org/10.1016/j.chemgeo.2004.01.003

Black, L.P., Williams, I.S., Compston, W., 1986. Four zircon ages from one rock: the history of a 3930 Ma-old granulite from Mount Sones, Enderby Land, Antarctica. Contrib. to Mineral. Petrol. 94, 427–437. https://doi.org/10.1007/BF00376336

Bleeker, W., Davis, W.J., 1999. The 1991-1996 NATMAP Slave Province Project: Introduction. Can. J. Earth Sci. 36, 1033–1042.

Bleeker, W., Hall, B., 2007. The Slave Craton: geology and metallogenic evolution, in: Goodfellow, W.D. (Ed.), Mineral Deposits of Canada: A Synthesis of Major Deposit-Types, District Metallogeny, the Evolution of Geological Provinces, and Exploration Methods. Geological Association of Canada, Mineral Deposits Division, pp. 849–879.

Bleeker, W., Ketchum, J.W.F., Davis, B., Sircombe, K.N., 2004. The Slave Craton From On Top: The Crustal View, in: From Parameters to Processes Revealing the Evolution of a Continent. pp. 1–5.

Bleeker, W., Ketchum, J.W.F., Davis, W.J., 2011. The Central Slave Basement Complex, Part II: age and tectonic significance of high-strain zones along the basement-cover contact. Can. J. Earth Sci. 36, 1111–1130. https://doi.org/10.1139/e99-007

Bleeker, W., Stern, R.A., 1997. The Acasta Gneisses: An imperfect sample of Earth's oldest crust. LITHOPROBE Rep. 56, 32–35.

Bleeker, W., Stern, R.A., Sircombe, K.N., 2000. Why the Slave Province, Northwest Territories, got a little bigger. Geol. Surv. Canada, Curr. Res. 2000-C2, 9.

Boehnke, P., Watson, E.B., Trail, D., Harrison, T.M., Schmitt, A.K., 2013. Zircon saturation re-revisited. Chem. Geol. 351, 324–334. https://doi.org/10.1016/j.chemgeo.2013.05.028

Bouvier, A., Vervoort, J.D., Patchett, P.J., 2008. The Lu-Hf and Sm-Nd isotopic composition of CHUR: Constraints from unequilibrated chondrites and implications for the bulk composition of terrestrial planets. Earth Planet. Sci. Lett. 273, 48–57. https://doi.org/10.1016/j.epsl.2008.06.010

Bowring, S.A., Housh, T., 1995. The Earth's Early Evolution. Science (80-.). 269, 1535–1540.

Bowring, S.A., Williams, I.S., 1999. Priscoan (4.00-4.03 Ga) orthogneisses from northwestern Canada. Contrib. to Mineral. Petrol. 134, 3–16. https://doi.org/10.1007/s004100050465

Bowring, S.A., Williams, I.S., Compston, W., 1989. 3.96 Ga gneisses from the Slave province, Northwest Territories, Canada. Geology 17, 971–975. https://doi.org/10.1130/0091-7613(1989)017<0971:GGFTSP>2.3.CO;2

Cardozo, N., Allmendinger, R.W., 2013. Spherical projections with OSXStereonet. Comput. Geosci. 51, 193–205. https://doi.org/10.1016/j.cageo.2012.07.021

Chapman, C.R., Cohen, B.A., Grinspoon, D.H., 2007. What are the real constraints on the existence and magnitude of the late heavy bombardment? Icarus 189, 233–245. https://doi.org/10.1016/j.icarus.2006.12.020

Class, C., Lehnert, K., 2012. PetDB Expert MORB (Mid-Ocean Ridge Basalt) Compilation. Integrated Earth Data Applications (IEDA). https://doi.org/10.1594/IEDA/100060

Compston, W., Pidgeon, R.T., 1986. Jack Hills, evidence of more very old detrital zircons in Western Australia. Nature 321, 766–769. https://doi.org/10.1038/321766a0

Condie, K., 2007. The Distribution of Paleoarchean Crust, in: Developments in Precambrian Geology. pp. 9–18. https://doi.org/10.1016/S0166-2635(07)15012-X

Corfu, F., Hanchar, J.M., Hoskin, P.W.O., Kinny, P.D., 2003. Atlas of Zircon Textures. Rev. Mineral. Geochemistry 53, 469–500. https://doi.org/10.2113/0530469

Davidek, K.L., Martin, M.W., Bowring, S.A., Williams, I.S., 1997. Conventional U-Pb geochronology of the Acasta gneisses using single crystal fragmentation technique, in: Geological Association of Canada/Mineralogical Association of Canada Annual Meeting. p. A-75.

Davis, W.J., Hegner, E., 1992. Neodymium isotopic evidence for the tectonic assembly of Late Archean crust in the Slave Province, northwest Canada. Contrib. to Mineral. Petrol. 111, 493–504. https://doi.org/10.1007/BF00320904

DePaolo, D.J., 1981. Trace Element and Isotopic Effects of Combined Wallrock Assimilation and Fractional Crystallization. Earth Planet. Sci. Lett. 53, 189–202.

Fisher, C.M., Hanchar, J.M., Samson, S.D., Dhuime, B., Blichert-Toft, J., Vervoort, J.D., Lam, R., 2011. Synthetic zircon doped with hafnium and rare earth elements: A reference material for in situ hafnium isotope analysis. Chem. Geol. 286, 32–47. https://doi.org/10.1016/j.chemgeo.2011.04.013

Fisher, C.M., Vervoort, J.D., Dufrane, S.A., 2014. Accurate Hf isotope determinations of complex zircons using the “laser ablation split stream” method. Geochemistry, Geophys. Geosystems 15, 121–139. https://doi.org/10.1002/2013GC004962

Foley, S., Tiepolo, M., Vannucci, R., 2002. Growth of early continental crust controlled by melting of amphibolite in subduction zones. Nature 417, 837–840. https://doi.org/10.1038/nature00799

Frost, B.R., Barnes, C.G., Collins, W.J., Arculus, R.J., Ellis, D.J., Frost, C.D., 2001. A geochemical classification for granitic rocks. J. Petrol. 42, 2033–2048. https://doi.org/10.1093/petrology/42.11.2033

Froude, D.O., Ireland, T.R., Kinny, P.D., Williams, I.S., Compston, W., Myers, J.S., 1983. Ion microprobe identification of 4,100-4,200 Myr-old terrestrial zircons. Nature 304, 616–618. https://doi.org/10.1038/304616a0

Gale, A., Dalton, C.A., Langmuir, C.H., Su, Y., Schilling, J.G., 2013. The mean composition of ocean ridge basalts. Geochemistry, Geophys. Geosystems 14, 489–518. https://doi.org/10.1029/2012GC004334

Green, D.C., Baadsgaard, H., Cumming, G.L., 1968. Geochronology of the Yellowknife area, Northwest Territories, Canada. Can. J. Earth Sci. 5, 725–735. https://doi.org/10.1139/e68-071

Guitreau, M., Blichert-Toft, J., Mojzsis, S.J., Roth, A.S.G., Bourdon, B., Cates, N.L., Bleeker, W., 2014. Lu-Hf isotope systematics of the Hadean-Eoarchean Acasta Gneiss Complex (Northwest Territories, Canada). Geochim. Cosmochim. Acta 135, 251–269. https://doi.org/10.1016/j.gca.2014.03.039

Hanson, G.N., 1980. Rare Earth Elements in petrogenetic studies of igneous systems. Annu. Rev. Earth Planet. Sci. 8, 371–406.

Harrison, T.M., 2009. The Hadean Crust: Evidence from greater than 4 Ga Zircons. Annu. Rev. Earth Planet. Sci. 37, 479–505. https://doi.org/10.1146/annurev.earth.031208.100151

Heaman, L.M., Bowins, R., Crocket, J., 1990. The chemical composition of igneous zircon suites: implications for geochemical tracer studies. Geochim. Cosmochim. Acta 54, 1597–1607. https://doi.org/10.1016/0016-7037(90)90394-Z

Henderson, J.B., 1981. Archaean basin evolution in the slave province, Canada, in: Developments in Precambrian Geology. pp. 213–235. https://doi.org/10.1016/S0166-2635(08)70014-8

Hoffman, P.F., 1989. Precambrian geology and tectonic history of North America, in: The Geology of North America. The Geological Society of America, pp. 447–512.

Hoffman, P.F., Bowring, S.A., 1984. Short-lived 1.9 Ga continental margin and its destruction, Wopmay orogen, northwest Canada. Geology 12, 68–72. https://doi.org/10.1130/0091-7613(1985)13<83a:carosg>2.0.co;2

Hollocher, K., 2004. CIPW Norm Calculation Program.

Hoskin, P.W.O., Schaltegger, U., 2003. The Composition of Zircon and Igneous and Metamorphic Petrogenesis, in: Zircon. pp. 27–62. https://doi.org/10.2113/0530027

Ickert, R.B., 2013. Algorithms for estimating uncertainties in initial radiogenic isotope ratios and model ages. Chem. Geol. 340, 131–138. https://doi.org/10.1016/j.chemgeo.2013.01.001

Iizuka, T., Komiya, T., Johnson, S.P., Kon, Y., Maruyama, S., Hirata, T., 2009. Reworking of Hadean crust in the Acasta gneisses, northwestern Canada: Evidence from in-situ Lu-Hf isotope analysis of zircon. Chem. Geol. 259, 230–239. https://doi.org/10.1016/j.chemgeo.2008.11.007

Iizuka, T., Komiya, T., Ueno, Y., Katayama, I., Uehara, Y., Maruyama, S., Hirata, T., Johnson, S.P., Dunkley, D.J., 2007. Geology and zircon geochronology of the Acasta Gneiss Complex, northwestern Canada: New constraints on its tectonothermal history. Precambrian Res. 153, 179–208. https://doi.org/10.1016/j.precamres.2006.11.017

Iizuka, T., Nakai, S., Sahoo, Y.V., Takamasa, A., Hirata, T., Maruyama, S., 2010. The tungsten isotopic composition of Eoarchean rocks: Implications for early silicate differentiation and core-mantle interaction on Earth. Earth Planet. Sci. Lett. 291, 189–200. https://doi.org/10.1016/j.epsl.2010.01.012

Jenner, G.A., Fryer, B.J., McLennan, S.M., 1981. Geochemistry of the Archean Yellowknife Supergroup. Geochim. Cosmochim. Acta 45, 1111–1129. https://doi.org/10.1016/0016-7037(81)90135-6

Johnson, D.M., Hooper, P.R., Conrey, R.M., 1999. XRF Analysis of Rocks and Minerals for Major and Trace Elements on a Single Low Dilution Li-tetraborate Fused Bead. Adv. X-Ray Anal. 4, 843–867.

Kamber, B.S., Collerson, K.D., Moorbath, S., Whitehouse, M.J., 2003. Inheritance of early archaean Pb-isotope variability from long-lived hadean protocrust. Contrib. to Mineral. Petrol. 145, 25–46. https://doi.org/10.1007/s00410-002-0429-7

Ketchum, J.W.F., Bleeker, W., Stern, R.A., 2004. Evolution of an Archean basement complex and its autochthonous cover, southern Slave Province, Canada. Precambrian Res. 135, 149–176. https://doi.org/10.1016/j.precamres.2004.08.005

Knaack, C., Cornelius, S., Hooper, P.R., 1994. Trace element analyses of rocks and minerals by ICP-MS. Washingt. State Univ. Dep. Geol. Open File Rep. 4.

Koshida, K., Ishikawa, A., Iwamori, H., Komiya, T., 2016. Petrology and geochemistry of mafic rocks in the Acasta Gneiss Complex: Implications for the oldest mafic rocks and their origin. Precambrian Res. 283, 190–207. https://doi.org/10.1016/j.precamres.2016.07.004

Ludwig, K.R., 2004. Isoplot 4.15: A Geochronological Toolkit for Microsoft Excel [WWW Document]. BGC Spec. Publ. 5.

Martin, H., 1999. Adakitic magmas: Modern analogues of Archaean granitoids. Lithos 46, 411–429. https://doi.org/10.1016/S0024-4937(98)00076-0

McDonough, W.F., Sun, S. s, 1995. The composition of the Earth. Chem. Geol. 120, 223–253. https://doi.org/10.1016/0009-2541(94)00140-4

Mojzsis, S.J., Cates, N.L., Caro, G., Trail, D., Abramov, O., Guitreau, M., Blichert-Toft, J., Hopkins, M.D., Bleeker, W., 2014. Component geochronology in the polyphase ca. 3920Ma Acasta Gneiss. Geochim. Cosmochim. Acta 133, 68–96. https://doi.org/10.1016/j.gca.2014.02.019

Moorbath, S., Whitehouse, M.J., 1996. Sm-Nd isotopic data and earth's evolution. Science (80-.). 273, 1878–1879. https://doi.org/10.1126/science.273.5283.1878a

Moorbath, S., Whitehouse, M.J., Kamber, B.S., 1997. Extreme Nd-isotope heterogeneity in the early Archaean—fact or fiction? Case histories from northern Canada and West Greenland. Chem. Geol. 148, 219–224. https://doi.org/10.1016/s0009-2541(98)00032-1

Moyen, J.-F., Martin, H., 2012. Forty years of TTG research. Lithos 148, 312–336. https://doi.org/10.1016/j.lithos.2012.06.010

Moyen, J.-F., Stevens, G., 2006. Experimental Constraints on TTG Petrogenesis: Implications for Archean Geodynamics. Geophys. Monogr. Geophys. Union 164, 149–175.

Nair, R., Chacko, T., 2008. Role of oceanic plateaus in the initiation of subduction and origin of continental crust. Geology 36, 583–586. https://doi.org/10.1130/G24773A.1

Nicholls, I.A., Harris, K.L., 1980. Experimental rare earth element partition coefficients for garnet, clinopyroxene and amphibole coexisting with andesitic and basaltic liquids. Geochim. Cosmochim. Acta 44, 287–308. https://doi.org/10.1016/0016-7037(80)90138-6

Nicholson, H., Condomines, M., Fitton, J.G., Fallick, A.E., Grönvold, K., Rogers, G., 1991. Geochemical and isotopic evidence for crustal assimilation beneath krafla, Iceland. J. Petrol. 32, 1005–1020. https://doi.org/10.1093/petrology/32.5.1005

Nutman, A.P., McGregor, V.R., Friend, C.R.L., Bennett, V.C., Kinny, P.D., 1996. The Itsaq Gneiss Complex of southern West Greenland; the world's most extensive record of early crustal evolution (3900-3600 Ma). Precambrian Res. 78, 1–39. https://doi.org/10.1016/0301-9268(95)00066-6

O'Neil, J., Carlson, R.W., Francis, D., Stevenson, R.K., 2008. Neodymium-142 Evidence for Hadean Mafic Crust. Science (80-.). 321, 1828–1831.

Padgham, W.A., Fyson, W.K., 1992. The Slave Province: a distinct Archean craton. Can. J. Earth Sci. 29, 2072–2086. https://doi.org/10.1139/e92-165

Pehrsson, S.J., Chacko, T., Pilkington, M., Villeneuve, M.E., Bethune, K.M., 2000. Anton terrane revisited: Late Archean exhumation of a moderate pressure granulite terranc in the Western Slave Province. Geology 28, 1075–1078. https://doi.org/10.1130/0091-7613(2000)28<1075:ATRLAE>2.0.CO;2

Reimink, J.R., 2015. Petrogenesis of the Acasta Gneiss Complex, Northwest Territories, Canada. University of Alberta. PhD Thesis. 1-320.

Reimink, J.R., Chacko, T., Stern, R.A., Heaman, L.M., 2016a. The birth of a cratonic nucleus: Lithogeochemical evolution of the 4.02-2.94 Ga Acasta Gneiss Complex. Precambrian Res. 281, 453–472. https://doi.org/10.1016/j.precamres.2016.06.007

Reimink, J.R., Chacko, T., Stern, R.A., Heaman, L.M., 2014. Earth's earliest evolved crust generated in an Iceland-like setting. Nat. Geosci. 7, 529–533. https://doi.org/10.1038/ngeo2170

Reimink, J.R., Davies, J.H.F.L., Chacko, T., Stern, R.A., Heaman, L.M., Sarkar, C., Schaltegger, U., Creaser, R.A., Pearson, D.G., 2016b. No evidence for Hadean continental crust within Earth's oldest evolved rock unit. Nat. Geosci. 9, 777–780. https://doi.org/10.1038/ngeo2786

Reimink, J.R., Pearson, D.G., Shirey, S.B., Carlson, R.W., Ketchum, J.W.F., 2019. Onset of new, progressive crustal growth in the central Slave craton at 3.55 Ga. Geochemical Perspect. Lett. 10, 8–13. https://doi.org/10.7185/geochemlet.1907

Reimink, J.R., Bauer, A.M., Chacko, T., 2019. The Acasta Gneiss Complex. In: Van Kranendonk, M.J., Bennett, V.C., Hoffman, J.E. (Eds.) Earth's Oldest Rocks. Second Edition, Elsevier, Cambridge, 329-347.

Rollinson, H.R., 1993. Using Geochemical Data: Evaluation, Presentation, Interpretation. Longman Scientific & Technical.

Roth, A.S.G., Bourdon, B., Mojzsis, S.J., Rudge, J.F., Guitreau, M., Blichert-Toft, J., 2014. Combined 147,146Sm-143,142Nd constraints on the longevity and residence time of early terrestrial crust. Geochemistry, Geophys. Geosystems 15, 2329–2345. https://doi.org/10.1002/2014GC005313

Rudnick, R.L., Gao, S., 2003. Composition of the Continental Crust. Treatise on Geochemistry 3, 1–64.

Sano, Y., Terada, K., Hidaka, H., Yokoyama, K., Nutman, A.P., 1999. Palaeoproterozoic thermal events recorded in the ~4.0 Ga Acasta gneiss, Canada: Evidence from SHRIMP U-Pb dating of apatite and zircon. Geochim. Cosmochim. Acta 63, 899–905. https://doi.org/10.1016/S0016-7037(98)00303-2

Saunders, A.D., Tarney, J., Weaver, S.D., 1980. Transverse geochemical variations across the Antarctic Peninsula: Implications for the genesis of calc-alkaline magmas. Earth Planet. Sci. Lett. 46, 344–360. https://doi.org/10.1016/0012-821X(80)90050-3

Scherer, E., Munker, C., Mezger, K., 2001. Calibration of the Lutetium-Hafnium Clock. Science (80-.). 293, 683–688.

Shand, S.J., 1927. Eruptive Rocks, Their Genesis, Composition, Classification, and Their Relation to Ore-deposits, with a Chapter on Meteorites. Murby, London.

Simonetti, A., Heaman, L.M., Chacko, T., Banerjee, N.R., 2006. In situ petrographic thin section U-Pb dating of zircon, monazite, and titanite using laser ablation-MC-ICP-MS. Int. J. Mass Spectrom. 253, 87–97. https://doi.org/10.1016/j.ijms.2006.03.003

Sircombe, K.N., Bleeker, W., Stern, R.A., 2001. Detrital zircon geochronology and grain-size analysis of a ~ 2800 Ma Mesoarchean proto-cratonic cover succession, Slave

Province, Canada. Earth Planet. Sci. Lett. 189, 207–220. https://doi.org/10.1016/S0012-821X(01)00363-6

Sláma, J., Košler, J., Condon, D.J., Crowley, J.L., Gerdes, A., Hanchar, J.M., Horstwood, M.S.A., Morris, G.A., Nasdala, L., Norberg, N., Schaltegger, U., Schoene, B., Tubrett, M.N., Whitehouse, M.J., 2008. Plešovice zircon - A new natural reference material for U-Pb and Hf isotopic microanalysis. Chem. Geol. 249, 1–35. https://doi.org/10.1016/j.chemgeo.2007.11.005

Söderlund, U., Patchett, P.J., Vervoort, J.D., Isachsen, C.E., 2004. The 176Lu decay constant determined by Lu-Hf and U-Pb isotope systematics of Precambrian mafic intrusions. Earth Planet. Sci. Lett. 219, 311–324. https://doi.org/10.1016/S0012-821X(04)00012-3

Spera, F., Scruggs, M., 2018. Fractional crystallization and assimilation. Encycl. Earth Sci. Ser. 513–518. https://doi.org/10.1007/978-3-319-39312-4_285

St-Onge, M.R., King, J.E., Lalonde, A.E., 1991. St. Onge - 1991 - Geology, east-central Wopmay Orogen, District of Mackenzie, Northwest Territories Geological Survey of Canada, Map 1754A.

Stern, R.A., Bleeker, W., 1998. Age of the world's oldest rocks refined using Canada's SHRIMP: the Acasta Gneiss Complex, Northwest Territories, Canada. Geosci. Canada 25, 27–31.

Stern, R.A., Bodorkos, S., Kamo, S.L., Hickman, A.H., Corfu, F., 2009. Measurement of SIMS Instrumental Mass Fractionation of Pb isotopes during Zircon dating. Geostand. Geoanalytical Res. 33, 145–168.

Streckeisen, A., Le Maitre, R.W., 1979. A chemical approximation to the modal QAPF classification of the igneous rocks. Neues Jahrb. fuer Mineral. Abhandlungen 136, 169–206.

Stubley, M.P., Irwin, D., 2019. Bedrock Geology of the Slave Craton , Northwest Territories and Nunavut;Northwest Territories Geological Survey, NWT Open File 2019-01.

Taylor, H.P., 1980. The Effects of Assimilation of Country Rocks by Magmas on 18O/16O and 87Sr/86Sr Systematics in Igneous Rocks. Earth Planet. Sci. Lett. 47, 243–254.

Thirlwall, M.F., Smith, T.E., Graham, A.M., Theodorou, N., Hollings, P., Davidson, J.P., Arculus, R.J., 1994. High field strength element anomalies in arc lavas: Source or process? J. Petrol. 35, 819–838. https://doi.org/10.1093/petrology/35.3.819

Thompson, P.H., 1978. Archean regional metamorphism in the Slave Structural Province, Geological Survey of Canada, Paper. https://doi.org/10.4095/104514

Trail, D., Mojzsis, S.J., Harrison, T.M., 2007. Thermal events documented in Hadean zircons by ion microprobe depth profiles. Geochim. Cosmochim. Acta 71, 4044–4065. https://doi.org/10.1016/j.gca.2007.06.003

Van Breemen, O., Davis, W.J., King, J.E., 1992. Temporal distribution of granitoid plutonic rocks in the Archean Slave Province, northwest Canadian Shield. Can. J. Earth Sci. 29, 2186–2199. https://doi.org/10.1139/e92-173

Van Breemen, O., Henderson, J.B., Loveridge, W.D., Thompson, P.H., 1987a. U-Pb zircon and monazite geochronology and zircon morphology of granulites and granite from the Thelon Tectonic Zone, Healey Lake and Artillery Lake map areas, N.W.T.

Van Breemen, O., Thompson, P.H., Bostock, H.H., Loveridge, W.D., 1987b. Timing of plutonism in the northern Thelon tectonic zone and Taltson magmatic zone, in: Geological Association of Canada. p. 98.

Vervoort, J.D., 2010. Hf analyses in zircon by LA-MC-ICPMS: promise and pitfalls. Am. Geophys. Union 42, 667.

Wang, X., Griffin, W.L., Jie, C., Pinyun, H., Xiang, L., 2011. U and Th Contents and Th/U Ratios of Zircon in Felsic and Mafic Magmatic Rocks: Improved Zircon-Melt Distribution Coefficients. Acta Geol. Sin. - English Ed. 85, 164–174. https://doi.org/10.1111/j.1755-6724.2011.00387.x

Wiedenbeck, M., Alle, P., Corfu, F., Griffin, W.L., Meier, M., Oberli, F., Quadt, A. von, Roddick, J.C., Spiegel, W., 1995. Three Natural Zircon Standards for U-Th-Pb, Lu-Hf, Trace Element and Ree Analyses. Geostand. Newsl. 19, 1–23. https://doi.org/10.1111/j.1751-908X.1995.tb00147.x

Williams, I.S., Compston, W., Bowring, S.A., Housh, T., 1992. The age and history of the Acasta Gneisses, Canada: an ion microprobe zircon study. Am. Geophys. Union 73, 324.

Wood, D.A., 1978. Major and trace element variations in the tertiary lavas of eastern Iceland and their significance with respect to the Iceland geochemical anomaly. J. Petrol. 19, 393–436. https://doi.org/10.1093/petrology/19.3.393

Woodhead, J.D., Hergt, J.M., 2005. A Preliminary Appraisal of Seven Natural Zircon Reference Materials for In Situ Hf Isotope Determination. Geostand. Geoanalytical Res. 29, 183–195. https://doi.org/10.1111/j.1751-908x.2005.tb00891.x

Woodhead, J.D., Hergt, J.M., Shelley, M., Eggins, S., Kemp, R., 2004. Three Natural Zircon Standards For U-Th-Pb, Lu-Hf, Trace Element and REE Analysis. Chem. Geol. 209, 121–135. https://doi.org/10.1016/j.chemgeo.2004.04.026

Yakymchuk, C., Kirkland, C.L., Clark, C., 2018. Th/U ratios in metamorphic zircon. J. Metamorph. Geol. 36, 715–737. https://doi.org/10.1111/jmg.12307

Appendix 1. LA-ICP-MS U-Pb Zircon Data

Sample Name	Zircon Phase	Format	^{206}Pb (cps)	^{204}Pb (cps)	$^{206}Pb/^{204}Pb$	$^{207}Pb/^{206}Pb$	2σ	$^{207}Pb/^{235}U$	2σ	$^{206}Pb/^{238}U$	2σ	ρ
MB07-A	Ign (Core)	TS	533024	194	2742	0.28232	0.00338	26.72380	0.89152	0.68653	0.02137	0.933
MB07-B1	Ign (Core)	TS	1105019	409	2703	0.28197	0.00317	21.08344	1.19153	0.54229	0.03003	0.980
MB07-B2	Ign (Osc)	TS	957334	25	38005	0.28010	0.00310	24.59259	0.80819	0.63678	0.01971	0.942
MB07-C3-1A	Ign (Osc)	TS	349841	3	104184	0.28356	0.00313	26.67469	0.77416	0.68226	0.01831	0.925
MB07-C3-1B	Ign (Core)	TS	666535	204	3273	0.28594	0.00321	21.16605	1.03890	0.53687	0.02565	0.973
MB07-D1	Metamorphic	TS	801867	19	41954	0.27274	0.00306	21.59023	0.88079	0.57414	0.02252	0.961
MB07-D2	Ign (Core)	TS	760701	2	502901	0.28066	0.00312	25.64996	0.66882	0.66283	0.01564	0.905
MB07-C	Ign (Osc)	TS	1296165	21	63080	0.28389	0.00315	28.38126	0.85231	0.72507	0.02024	0.929
MB07-I1	Metamorphic	TS	1249272	127	9875	0.26845	0.00326	23.97954	0.84117	0.64785	0.02132	0.938
MB07-I2	Ign (Core)	TS	190065	6	30045	0.28384	0.00323	26.46585	0.78671	0.67626	0.01857	0.924
MB07-J	Ign (Core)	TS	634798	17	36773	0.27928	0.00315	23.48011	0.72410	0.60976	0.01750	0.931
MB07-K	Ign (Core)	TS	1021217	1	909548	0.27830	0.00307	26.44656	0.78439	0.68920	0.01897	0.928
MB07-O	Metamorphic	TS	1013505	11	93381	0.27031	0.00304	24.91629	0.69239	0.66854	0.01699	0.914
MB07-C6-1B	Ign (Core)	TS	815343	7	123439	0.28201	0.00316	27.08907	0.75915	0.69668	0.01789	0.916
MB07-U1	Ign (Core)	TS	1100140	3	399622	0.28336	0.00313	27.31685	0.74028	0.69919	0.01730	0.913
MB07-C10-1A	Metamorphic	TS	1423777	35	40421	0.26512	0.00293	21.48496	0.55932	0.58774	0.01385	0.905
MB07-C10-1B	Ign (Core)	TS	288946	52	5568	0.28474	0.00316	26.98240	0.94974	0.68726	0.02296	0.949
MB07-C9-1	Ign (Osc)	TS	718651	231	3112	0.28658	0.00322	26.45685	1.41901	0.66956	0.03512	0.978
MB07-S	Ign (Core)	TS	798299	114	7023	0.27942	0.00333	24.64381	0.76877	0.63965	0.01844	0.924
MB12S1-C2-Z2-1	Ign (Osc)	TS	1117838	305	3663	0.33007	0.00362	29.54493	1.65422	0.64919	0.03565	0.981
MB12S1-C6-Z1-1	Ign (Core)	TS	1387143	128	10879	0.32571	0.00340	32.23584	0.91915	0.71781	0.01904	0.930
MB12S1-C6-Z1-2	Ign (Core)	TS	1623978	547	2969	0.32118	0.00360	31.42526	1.20426	0.70962	0.02600	0.956
MB12S1-C7-Z2-1	Ign (Osc)	TS	1094870	12	90962	0.31099	0.00373	29.46540	0.71342	0.68717	0.01445	0.869
MB12S1-C7-Z1-1	Inherited (Core)	TS	2151406	0	5211688	0.41372	0.00432	46.95061	1.40273	0.82307	0.02304	0.937

Appendix 1. LA-ICP-MS U-Pb Zircon Data

Sample Name	Zircon Phase	Format	^{206}Pb (cps)	^{204}Pb (cps)	$^{206}Pb/^{204}Pb$	$^{207}Pb/^{206}Pb$	2σ	$^{207}Pb/^{235}U$	2σ	$^{206}Pb/^{238}U$	2σ	ρ
MB12S1-C14-Z1-1	Inherited (Core)	TS	1197641	5	221854	0.41305	0.00434	46.50382	1.23415	0.81655	0.01990	0.918
MB12S2-C1Z1A	Ign (Core)	TS	1205470	187	6453	0.30453	0.00386	26.26563	1.39393	0.62554	0.03224	0.971
MB12S2-C1Z1B	Amb	TS	503892	42	11893	0.30884	0.00438	29.94630	1.68728	0.70325	0.03835	0.968
MB12S2-C1Z1C	Amb (Recryst)	TS	902499	196	4616	0.31897	0.00569	27.94379	1.66703	0.63539	0.03617	0.954
MB12S2-C3Z1A	Ign (Osc)	TS	884386	45	19775	0.31606	0.00381	30.18736	1.61801	0.69271	0.03618	0.974
MB12S2-C3Z2A	Ign (Osc)	TS	910801	163	5595	0.31515	0.00351	28.73780	1.46391	0.66135	0.03287	0.976
MB12S2-C14Z1A	Amb	TS	1052897	244	4321	0.32209	0.00381	31.25146	1.62898	0.70371	0.03572	0.974
MB12S2-C15Z1A	Ign (Osc)	TS	569724	46	12485	0.32823	0.00365	33.83901	1.74529	0.74773	0.03766	0.976
MB12S2-C15Z1B	Ign (Osc)	TS	543346	207	2627	0.33210	0.00367	35.76088	1.88933	0.78098	0.04035	0.978
MB21B-C8Z1	Ign (Core)	TS	1183843	19	61817	0.31656	0.00337	31.15693	0.90345	0.71382	0.01926	0.930
MB21B-C1Z1	Amb	TS	1106605	7	154101	0.31408	0.00340	31.58996	1.02469	0.72947	0.02231	0.943
MB21B-C4Z1A	Ign (Core)	TS	883043	771	1145	0.29318	0.00378	18.79337	1.14251	0.46492	0.02762	0.977
MB21B-C4Z1B	Ign (Osc)	TS	1056560	981	1077	0.30045	0.00366	24.42657	0.94980	0.58965	0.02177	0.950
MB21B-C6Z1	Ign (Core)	TS	1426933	256	5573	0.29590	0.00330	19.24587	0.73087	0.47173	0.01712	0.956
MB47B-C2Z1A	Ign (Osc)	TS	1146487	223	5133	0.32165	0.00345	31.36236	0.85269	0.70717	0.01767	0.919
MB47B-C2Z1B	Ign (Osc)	TS	1277191	56	22714	0.31368	0.00336	32.35435	0.95157	0.74808	0.02049	0.931
MB47B-C2Z1C	Ign (Osc)	TS	1574398	74	21399	0.31426	0.00337	30.37381	0.79845	0.70098	0.01683	0.913
MB47B-C4Z1A	Metamorphic	TS	657797	44	14786	0.28785	0.00520	26.29113	0.70705	0.66242	0.01320	0.741
MB47B-C4Z2A	Ign (Osc)	TS	1532065	67	22867	0.30446	0.00369	28.38410	0.98472	0.67616	0.02198	0.937
MB47B-C5Z1A	Ign (Osc)	TS	790184	118	6715	0.31542	0.00338	30.47564	0.71002	0.70074	0.01449	0.888
MB47B-C8Z1A	Ign (Osc)	TS	1465035	1062	1380	0.30439	0.00358	23.38064	0.71151	0.55710	0.01564	0.922
MB47B-C10Z1A	Ign (Osc)	TS	1373692	151	9124	0.31051	0.00375	29.54348	1.09522	0.69005	0.02419	0.945
MB47B-C11Z1A	Ign (Core)	TS	1460684	484	3019	0.29462	0.00351	25.34371	0.66852	0.62389	0.01469	0.892
MB47B-C13Z1B	Ign (Osc)	TS	900616	427	2107	0.30173	0.00366	22.94259	0.67449	0.55147	0.01477	0.911

Appendix 1. LA-ICP-MS U-Pb Zircon Data

Sample Name	Zircon Phase	Format	^{206}Pb (cps)	^{204}Pb (cps)	$^{206}Pb/^{204}Pb$	$^{207}Pb/^{206}Pb$	2σ	$^{207}Pb/^{235}U$	2σ	$^{206}Pb/^{238}U$	2σ	ρ
MB47B-C13Z1C	Ign (Core)	TS	627919	90	7001	0.32166	0.00354	31.86830	0.97011	0.71855	0.02039	0.932
MB47B-C15Z1A	Metamorphic	TS	1626925	318	5123	0.26915	0.00340	19.03195	0.68342	0.51284	0.01724	0.936
MB47B-C15Z1B	Ign (Osc)	TS	879921	188	4669	0.30139	0.00677	28.06420	1.36071	0.67534	0.02902	0.886
MB47B-C16Z1A	Metamorphic	TS	2216787	321	6912	0.26216	0.00667	16.71226	0.77835	0.46234	0.01804	0.838
MB54B-4	Ign (Core)	TS	2078814	344	6046	0.31523	0.00316	27.59841	0.80301	0.63498	0.01735	0.939
MB54B-12	Metamict	TS	1713853	171	10024	0.29091	0.00476	21.16220	0.79869	0.52759	0.01794	0.901
MB54B-18	Ign (Core)	TS	1677806	151	11132	0.31297	0.00321	29.10013	0.70671	0.67435	0.01485	0.907
MB54B-25	Ign (Core)	TS	1313052	85	15412	0.31383	0.00301	30.28888	0.87714	0.69998	0.01913	0.944
MB54B-26	Ign (Core)	TS	1485994	85	17506	0.31470	0.00312	28.81663	0.65527	0.66412	0.01359	0.900
MB54B-32A	Ign (Osc)	TS	1530160	137	11139	0.29975	0.00331	23.04641	0.63690	0.55763	0.01412	0.916
MB54B-32B	Ign (Osc)	TS	1294538	114	11324	0.30998	0.00303	26.40120	0.62809	0.61771	0.01339	0.911
MB73A1-C2Z1A	Ign (Core)	TS	293360	46	6389	0.31087	0.00367	28.52663	0.93898	0.66554	0.02045	0.933
MB73A1-C2Z1B	Ign (Core)	TS	687431	79	8754	0.31387	0.00348	31.75644	1.07658	0.73381	0.02351	0.945
MB73A1-C4Z1A	Metamorphic	TS	914722	273	3356	0.28015	0.00524	22.30280	0.79443	0.57740	0.01751	0.851
MB73A1-C4Z2A	Ign (Osc)	TS	1535183	207	7399	0.30506	0.00366	28.12734	0.97275	0.66871	0.02169	0.938
MB73A1-C8Z1A	Ign (Sector)	TS	631811	154	4112	0.31185	0.00350	29.50527	1.00994	0.68620	0.02219	0.945
MB73A1-C8Z1B	Amb (Recryst)	TS	1223336	72	17058	0.30212	0.00361	28.11137	0.98011	0.67484	0.02210	0.939
MB73A1-C8Z1C	Amb (Recryst)	TS	1031270	110	9391	0.30064	0.00336	28.66756	0.93538	0.69157	0.02120	0.940
MB76C-C1-Z1-1	Metamict	TS	3006735	2226	1351	0.25907	0.00517	19.31661	0.59024	0.54077	0.01251	0.757
MB76C-C2-Z1-1	Amb	TS	2207105	262	8421	0.29924	0.00814	24.11238	1.17471	0.58442	0.02362	0.830
MB76C-C4-Z1-1	Metamict	TS	1306445	297	4398	0.34430	0.00578	31.74071	1.15692	0.66862	0.02163	0.888
MB76C-C5-Z1	Amb	TS	1962233	159	12371	0.31774	0.00571	29.92825	1.05002	0.68314	0.02059	0.859
MB76C-C7-Z1	Amb	TS	2639235	181	14575	0.29024	0.00607	21.65997	0.76141	0.54125	0.01529	0.803
MB76C-C10-Z3-1	Amb	TS	2856730	93	30873	0.32301	0.00542	31.63584	0.99735	0.71033	0.01895	0.846

Appendix 1. LA-ICP-MS U-Pb Zircon Data

Sample Name	Zircon Phase	Format	^{206}Pb (cps)	^{204}Pb (cps)	$^{206}Pb/^{204}Pb$	$^{207}Pb/^{206}Pb$	2σ	$^{207}Pb/^{235}U$	2σ	$^{206}Pb/^{238}U$	2σ	ρ
MB76C-C10-Z3-2	Amb	TS	1646876	96	17089	0.32073	0.00537	31.27955	0.93325	0.70733	0.01747	0.828
MB76C-C10-Z3-3	Amb	TS	1915554	208	9221	0.32970	0.00553	30.19223	0.87789	0.66417	0.01578	0.817
MB76C-C111-Z1-1	Amb	TS	2210307	124	17861	0.30715	0.00526	29.37749	0.92244	0.69368	0.01825	0.838
MB76C-C111-Z1-2	Amb	TS	1913673	167	11476	0.27133	0.00478	23.87802	0.75697	0.63827	0.01682	0.831
MB76C-C111-Z1-3	Amb	TS	2297289	97	23735	0.28950	0.00494	26.40083	0.98485	0.66140	0.02194	0.889
MB103-C0Z1-1	Ign (Core)	TS	189664	45	4226	0.35149	0.00379	36.80950	1.14103	0.75952	0.02207	0.938
MB103-C0Z1-2	Ign (Core)	TS	142450	33	4335	0.34714	0.00386	36.28217	1.13690	0.75804	0.02221	0.935
MB103-C1Z1-1	Amb	TS	166945	53	3148	0.34562	0.00371	35.55085	1.07167	0.74603	0.02102	0.935
MB103-C1Z1-2	Ign (Osc)	TS	79341	30	2613	0.35714	0.00396	37.87115	1.18346	0.76907	0.02247	0.935
MB103-C1Z1-3	Ign (Sector)	TS	127100	49	2586	0.33390	0.00405	33.80930	1.03492	0.73438	0.02064	0.918
MB103-C1Z1-4	Amb	TS	423073	67	6280	0.34739	0.00395	36.96872	1.07432	0.77181	0.02064	0.920
MB103-C1Z1-5	Amb	TS	122179	75	1627	0.35127	0.00380	37.43601	1.17563	0.77294	0.02278	0.939
MB103-C2Z1-1	Amb	TS	155333	106	1459	0.34712	0.00572	37.11554	1.25244	0.77549	0.02283	0.873
MB103-C2Z1-2	Amb	TS	216348	63	3456	0.32447	0.00735	32.03044	1.20260	0.71595	0.02143	0.797
MB103-C3Z1-1	Metamorphic	TS	224654	41	5513	0.28331	0.00305	25.76099	0.80201	0.65947	0.01927	0.938
MB103-C3Z1-2	Metamorphic	TS	246371	8	30986	0.26857	0.00288	24.45709	0.73685	0.66046	0.01859	0.934
MB103-C5Z1-1	Amb (Patchy)	TS	123362	21	5953	0.35932	0.00624	37.99323	1.50214	0.76687	0.02724	0.898
MB103-C5Z1-2	Amb (Patchy)	TS	60344	13	4813	0.35436	0.00411	35.99505	1.17130	0.73671	0.02240	0.934
MB103-C5Z1-3	Amb (Patchy)	TS	532785	18	29872	0.35622	0.00376	38.35009	1.03844	0.78081	0.01947	0.921
MB103-C5Z1-4	Amb (Patchy)	TS	228483	40	5673	0.33566	0.00483	34.54677	0.97415	0.74647	0.01810	0.860
MB103-C5Z1-5	Amb (Patchy)	TS	166954	35	4772	0.35579	0.00377	38.12157	1.15174	0.77709	0.02199	0.937
MB103-C5Z1-6	Amb (Patchy)	TS	128845	29	4373	0.35541	0.00383	37.27600	1.16448	0.76068	0.02230	0.939
MB103-C7Z1-1	Ign (Osc)	TS	142949	26	5478	0.33746	0.00419	32.16590	0.93220	0.69130	0.01811	0.904
MB103-C7Z1-2	Ign (Sector)	TS	119612	32	3713	0.33588	0.00438	33.82590	1.02459	0.73041	0.01997	0.903

Appendix 1. LA-ICP-MS U-Pb Zircon Data

Sample Name	Zircon Phase	Format	^{206}Pb (cps)	^{204}Pb (cps)	$^{206}Pb/^{204}Pb$	$^{207}Pb/^{206}Pb$	2σ	$^{207}Pb/^{235}U$	2σ	$^{206}Pb/^{238}U$	2σ	ρ
MB103-C7Z1-3	Ign (Mixed)	TS	103323	28	3634	0.32276	0.00372	31.21553	0.97311	0.70145	0.02032	0.929
MB103-C7Z1-4	Ign (Sector)	TS	114191	55	2063	0.33627	0.00364	33.02653	1.03935	0.71231	0.02105	0.939
MB103-C7Z1-5	Ign (Sector)	TS	77039	24	3198	0.33672	0.00387	33.40513	1.09071	0.71952	0.02199	0.936
MB103-C8Z1-1	Ign (Osc)	TS	279224	28	10119	0.35060	0.00389	36.37706	1.26904	0.75252	0.02489	0.948
MB103-C8Z1-2	Ign (Osc)	TS	481119	33	14747	0.35648	0.00377	38.23360	1.22095	0.77788	0.02344	0.944
MB103-C8Z1-3	Ign (Osc)	TS	366730	25	14875	0.35424	0.00377	36.99395	1.14783	0.75741	0.02207	0.939
MB103-C8Z1-5	Ign (Osc)	TS	290577	14	21484	0.35344	0.00381	36.57620	1.19797	0.75056	0.02321	0.944
MB103-C9Z1-1	Ign (Osc)	TS	92055	66	1391	0.36089	0.00406	37.41479	1.20930	0.75192	0.02278	0.938
MB103-C9Z1-2	Ign (Osc)	TS	81081	11	7118	0.35731	0.00392	38.30347	1.26799	0.77748	0.02428	0.943
MB103-C9Z1-3	Ign (Osc)	TS	156924	12	13068	0.36100	0.00893	37.46726	1.61100	0.75274	0.02648	0.818
MB103-C10Z1-1	Ign (Sector)	TS	115431	21	5397	0.35598	0.00413	36.04315	1.13181	0.73434	0.02143	0.929
MB103-C10Z1-2	Ign (Sector)	TS	144952	23	6192	0.35194	0.00384	36.73976	1.08359	0.75713	0.02074	0.929
MB103-C10Z1-3	Metamorphic	TS	353050	28	12660	0.26315	0.00285	23.17726	0.70671	0.63880	0.01821	0.935
MB108A-C1-Z2-1	Amb	TS	363559	79	4604	0.36030	0.00380	38.20717	1.21344	0.76909	0.02304	0.943
MB108A-C1-Z2-2	Amb	TS	501358	25	19712	0.35807	0.00378	38.15029	1.29679	0.77274	0.02497	0.951
MB108A-C1-Z2-3	Amb	TS	118554	45	2664	0.35913	0.00398	36.83642	1.21447	0.74392	0.02310	0.942
MB108A-C1-Z2-4	Amb	TS	124598	24	5149	0.34340	0.00390	34.35730	1.22221	0.72563	0.02446	0.948
MB108A-C1-Z1-1	Amb	TS	502277	60	8427	0.32275	0.00343	33.13307	1.08033	0.74455	0.02295	0.945
MB108A-C1-Z1-2	Amb	TS	555465	51	10982	0.32311	0.00348	32.21385	1.01161	0.72308	0.02133	0.939
MB108A-C1-Z1-3	Amb	TS	591020	45	13120	0.31850	0.00343	32.98656	1.46006	0.75116	0.03225	0.970
MB108A-C1-Z1-4	Amb	TS	414871	59	7047	0.29509	0.00315	28.53204	0.90462	0.70125	0.02094	0.942
MB108A-C1-Z3-1	Ign (Osc)	TS	298413	69	4319	0.32809	0.00347	32.30678	1.07069	0.71417	0.02243	0.948
MB108A-C1-Z3-2	Ign (Osc)	TS	206277	41	4982	0.31764	0.00348	30.65329	1.08630	0.69990	0.02359	0.951
MB108A-C1-Z3-3	Ign (Osc)	TS	539089	65	8328	0.31811	0.00378	31.09379	0.99191	0.70892	0.02099	0.928

Appendix 1. LA-ICP-MS U-Pb Zircon Data

Sample Name	Zircon Phase	Format	^{206}Pb (cps)	^{204}Pb (cps)	$^{206}Pb/^{204}Pb$	$^{207}Pb/^{206}Pb$	2σ	$^{207}Pb/^{235}U$	2σ	$^{206}Pb/^{238}U$	2σ	ρ
MB108A-C1-Z4-1	Ign (Osc)	TS	315834	57	5586	0.31485	0.00343	30.25665	1.01905	0.69697	0.02221	0.946
MB108A-C1-Z4-2	Ign (Osc)	TS	196574	46	4264	0.32667	0.00360	31.91323	1.07637	0.70853	0.02259	0.945
MB108A-C2-Z1-1	Amb	TS	297695	37	8013	0.32569	0.00370	32.30988	1.11836	0.71949	0.02353	0.945
MB108A-C2-Z1-2	Ign (Osc)	TS	429282	55	7751	0.34181	0.00361	35.14479	1.21058	0.74572	0.02445	0.952
MB108A-C2-Z1-3	Ign (Osc)	TS	600465	51	11721	0.34607	0.00364	34.91357	1.19653	0.73169	0.02386	0.952
MB108A-C2-Z1-4	Ign (Osc)	TS	1366070	51	26983	0.34154	0.00359	35.79257	1.25020	0.76006	0.02532	0.954
MB108A-C2-Z2-1	Amb	TS	445292	54	8235	0.34480	0.00443	35.82771	1.38651	0.75361	0.02751	0.943
MB108A-C3-Z1-1	Ign (Osc)	TS	269867	78	3482	0.34984	0.00389	37.39587	1.50533	0.77528	0.02999	0.961
MB108A-C3-Z1-2	Ign (Osc)	TS	1174261	99	11856	0.33392	0.00414	34.16353	1.47615	0.74202	0.03071	0.958
MB108A-C3-Z1-3	Ign (Osc)	TS	156286	66	2373	0.35098	0.00379	36.84382	1.32848	0.76135	0.02619	0.954
MB108A-C3-Z2-1	Ign (Osc)	TS	457203	80	5735	0.27845	0.00309	24.94275	0.76053	0.64968	0.01845	0.931
MB108A-C3-Z2-2	Ign (Osc)	TS	243398	62	3953	0.29881	0.00328	28.16867	0.97109	0.68370	0.02234	0.948
MB108A-C3-Z2-3	Ign (Osc)	TS	499662	74	6781	0.26920	0.00290	23.81804	0.71509	0.64170	0.01798	0.933
MB108A-C4-Z1-1	Ign (Sector)	TS	567642	34	16756	0.33418	0.00437	32.79707	1.21674	0.71179	0.02471	0.936
MB108A-C4-Z1-2	Ign (Sector)	TS	182537	31	5951	0.34179	0.00464	34.56047	1.07991	0.73336	0.02064	0.901
MB108A-C4-Z1-3	Ign (Core)	TS	326358	36	9143	0.31968	0.00369	30.26488	1.11236	0.68664	0.02396	0.949
MB108A-C5-Z1-2	Ign (Core)	TS	987545	65	15273	0.35096	0.00377	36.60383	1.02377	0.75643	0.01953	0.923
MB108A-C5-Z1-3	Ign (Core)	TS	636215	42	15112	0.35770	0.00376	37.28140	0.98747	0.75591	0.01838	0.918
MB108A-C5-Z1-4	Ign (Sector)	TS	112485	23	4853	0.35938	0.00383	35.77364	0.98790	0.72194	0.01839	0.922
MB108A-C5-Z1-5	Ign (Core)	TS	554399	38	14442	0.35625	0.00376	36.34671	1.02871	0.73996	0.01944	0.928
MB108A-C5-Z1-6	Ign (Sector)	TS	257853	50	5143	0.32212	0.00351	30.58655	0.86379	0.68867	0.01794	0.923
MB108A-C6-Z1-1	Amb	TS	813675	71	11515	0.33364	0.00405	33.09617	1.05724	0.71945	0.02126	0.925
MB108A-C6-Z1-2	Amb	TS	907351	48	18721	0.33646	0.00355	33.84541	0.97868	0.72956	0.01964	0.931
MB108A-C7-Z3-1	Ign (Sector)	TS	511990	37	14001	0.33284	0.00387	32.82659	1.08579	0.71531	0.02215	0.936

Appendix 1. LA-ICP-MS U-Pb Zircon Data

Sample Name	Zircon Phase	Format	^{206}Pb (cps)	^{204}Pb (cps)	$^{206}Pb/^{204}Pb$	$^{207}Pb/^{206}Pb$	2σ	$^{207}Pb/^{235}U$	2σ	$^{206}Pb/^{238}U$	2σ	ρ
MB108A-C7-Z3-2	Ign (Sector)	TS	534371	19	28406	0.31453	0.00337	30.10489	1.01506	0.69418	0.02219	0.948
MB108A-C7-Z3-3	Ign (Sector)	TS	401822	10	39723	0.34003	0.00390	33.01396	1.11608	0.70417	0.02239	0.941
MB108A-C7-Z1-1	Amb	TS	253240	12	21090	0.29123	0.00344	26.26360	0.93217	0.65407	0.02189	0.943
MB108A-C7-Z2-1	Ign (Sector)	TS	331524	6	52063	0.35561	0.00377	35.50289	1.16500	0.72409	0.02248	0.946
MB108A-C7-Z2-2	Ign (Sector)	TS	160990	11	14090	0.36035	0.00381	36.53470	1.32722	0.73533	0.02555	0.957
MB108A-C7-Z4-1	Amb	TS	457412	3	181370	0.35665	0.00376	36.12343	1.07951	0.73459	0.02054	0.936
MB108A-C7-Z4-2	Amb	TS	202685	3	67930	0.35843	0.00381	36.17507	1.10106	0.73200	0.02088	0.937
MB108A-C7-Z4-3	Amb	TS	786635	28	28394	0.35818	0.00379	37.33413	1.18837	0.75597	0.02270	0.943
MB108A-C7-Z4-4	Amb	TS	524517	20	26292	0.35580	0.00376	37.08220	1.19464	0.75588	0.02300	0.945
MB108A-C8-Z1-1	Ign (Sector)	TS	285645	3	81773	0.36076	0.00403	38.23049	1.34403	0.76858	0.02562	0.948
MB108A-C8-Z1-2	Ign (Sector)	TS	521264	4	143256	0.35746	0.00378	37.20244	1.11548	0.75481	0.02118	0.936
MB108A-C8-Z1-3	Ign (Sector)	TS	388882	5	80713	0.35737	0.00378	37.49715	1.10885	0.76099	0.02101	0.934
MB108A-C9-Z1-1	Ign (Sector)	TS	778984	5	154017	0.35105	0.00373	36.25886	1.14513	0.74911	0.02228	0.942
MB108A-C9-Z1-2	Ign (Sector)	TS	243741	4	67451	0.34900	0.00372	35.27988	1.27395	0.73315	0.02530	0.956
MB108A-C9-Z1-3	Ign (Sector)	TS	378374	1	742757	0.33939	0.00359	33.57398	1.12504	0.71748	0.02282	0.949
MB108A-C9-Z1-4	Ign (Sector)	TS	1083311	3	407836	0.35150	0.00369	37.26512	1.10807	0.76890	0.02139	0.936
MB108A-C10-Z1-1	Amb	TS	167210	2	82060	0.36012	0.00383	37.74322	1.32981	0.76013	0.02554	0.953
MB108A-C10-Z1-2	Amb	TS	121391	0	N/A	0.35928	0.00392	37.79998	1.57836	0.76305	0.03076	0.965
MB108A-C10-Z1-3	Amb	TS	293098	0	N/A	0.28596	0.00403	26.51642	0.85303	0.67252	0.01945	0.899
MB108A-C10-Z1-4	Amb	TS	186232	0	549721	0.34260	0.00425	35.20759	1.13702	0.74533	0.02222	0.923
MB108B1-C2-Z1	Amb	TS	2375726	143	16628	0.33956	0.00519	34.79619	1.59865	0.74322	0.03220	0.943
MB108B1-C2-Z1-B	Amb	TS	1967895	65	30392	0.34344	0.00401	35.72247	1.59098	0.75439	0.03242	0.965
MB108B1-C3-Z1A	Metamorphic	TS	1190105	300	3973	0.19175	0.00666	6.26891	0.43640	0.23711	0.01430	0.867
MB108B1-C3-Z2A	Metamorphic	TS	1652084	260	6357	0.24942	0.00884	15.79284	0.95133	0.45923	0.02237	0.809

Appendix 1. LA-ICP-MS U-Pb Zircon Data

Sample Name	Zircon Phase	Format	^{206}Pb (cps)	^{204}Pb (cps)	^{206}Pb/^{204}Pb	^{207}Pb/^{206}Pb	2σ	^{207}Pb/^{235}U	2σ	^{206}Pb/^{238}U	2σ	ρ
MB108B1-C4Z1A	Amb	TS	2000062	57	35066	0.34073	0.00375	34.42094	1.52585	0.73268	0.03146	0.969
MB108B1-C4Z1B	Amb	TS	1572780	61	25995	0.33384	0.00379	34.61141	1.46190	0.75194	0.03059	0.963
MB108B1-C5Z1A	Metamorphic	TS	3328344	489	6806	0.25314	0.00302	16.93181	0.69107	0.48510	0.01894	0.956
MB108B1-C5Z1B	Ign (Osc)	TS	1978959	285	6934	0.32587	0.00409	27.66313	1.19725	0.61568	0.02550	0.957
MB108B1-C5Z2A	Amb	TS	1562860	62	25128	0.33632	0.00374	32.62271	1.42245	0.70351	0.02966	0.967
MB108B1-C6Z1A	Amb	TS	562843	145	3889	0.33224	0.00380	30.21969	1.31050	0.65969	0.02759	0.965
MB108B1-C6Z2A	Amb	TS	1975917	189	10476	0.33135	0.00400	30.39649	1.22112	0.66533	0.02549	0.954
MB108B1-C6Z2B	Amb	TS	1525225	122	12485	0.34085	0.00375	34.53677	1.45140	0.73487	0.02981	0.965
MB108B1-C6Z3A	Metamorphic	TS	2445887	253	9653	0.24603	0.00473	17.68592	0.84706	0.52136	0.02287	0.916
MB108B1-C9Z2A	Ign (Core)	TS	1751128	93	18753	0.34243	0.00442	35.38475	1.52364	0.74944	0.03078	0.954
MB108B1-C9Z2B	Ign (Osc)	TS	1585108	95	16745	0.33394	0.00368	33.16132	1.35298	0.72022	0.02829	0.963
MB108B1-C9Z3A	Amb	TS	485753	112	4355	0.32412	0.00393	30.03975	1.47002	0.67219	0.03187	0.969
MB108B1-C9Z4A	Amb	TS	922229	141	6555	0.34427	0.00398	34.46319	1.42487	0.72603	0.02882	0.960
MB108B1-C9Z4B	Amb	TS	1401116	109	12868	0.34534	0.00390	36.38915	1.56609	0.76423	0.03174	0.965
MB108B1-C9Z5A	Amb	TS	378499	47	8101	0.32547	0.00405	33.29776	1.58452	0.74200	0.03408	0.965
MB108B1-C9Z5B	Amb	TS	2017217	82	24710	0.34909	0.00383	38.57287	1.62385	0.80138	0.03257	0.966
MB108B1-C9Z5C	Amb	TS	2452390	88	27985	0.34496	0.00382	37.27802	1.59480	0.78377	0.03239	0.966
MB108B1-C10Z1A	Ign (Core)	TS	2316016	101	22842	0.34089	0.00426	34.06085	1.42239	0.72466	0.02887	0.954
MB108B1-C10Z1B	Ign (Osc)	TS	1919333	130	14757	0.31387	0.00344	28.45586	1.23443	0.65754	0.02760	0.967
MB108B1-C11Z1	Ign (Core)	TS	1046671	86	12217	0.33453	0.00404	30.99326	1.43367	0.67194	0.03000	0.965
MB108B1-C11Z1B	Ign (Osc)	TS	2139889	142	15062	0.33905	0.00380	33.10869	1.48734	0.70824	0.03081	0.968
MB108B1-C11Z2A	Ign (Osc)	TS	794913	75	10644	0.31550	0.00368	30.61152	1.37778	0.70370	0.03059	0.966
MB108B1-C11Z2B	Ign (Core)	TS	2278145	92	24840	0.32990	0.00437	35.13508	1.62249	0.77242	0.03417	0.958
MB108B1-C11Z2C	Ign (Core)	TS	3350691	128	26113	0.33021	0.00566	33.56484	1.72782	0.73721	0.03578	0.943

Appendix 1. LA-ICP-MS U-Pb Zircon Data

Sample Name	Zircon Phase	Format	^{206}Pb (cps)	^{204}Pb (cps)	^{206}Pb/^{204}Pb	^{207}Pb/^{206}Pb	2σ	^{207}Pb/^{235}U	2σ	^{206}Pb/^{238}U	2σ	ρ
MB108B1-C13Z1A	Metamorphic	TS	211914	86	2466	0.25885	0.00404	21.83626	0.94516	0.61183	0.02470	0.933
MB108B1-C13Z2A	Ign (Core)	TS	1919435	81	23650	0.34101	0.00451	37.26636	1.74848	0.79259	0.03568	0.959
MB108B1-C13Z2B	Metamorphic	TS	3115604	163	19064	0.25800	0.00711	19.33502	1.10621	0.54354	0.02726	0.876
MB108B1-C13Z4A	Amb	TS	1908660	337	5671	0.32073	0.00419	30.62534	1.36947	0.69253	0.02962	0.956
MB108B1-C14Z1A	Ign (Osc)	TS	506319	107	4723	0.32993	0.00377	33.68437	1.46574	0.74047	0.03109	0.965
MB108B1-C15Z1A	Ign (Core)	TS	1548937	111	13946	0.33380	0.00380	35.53431	1.58020	0.77207	0.03319	0.967
MB108B1-C16Z1A	Amb	TS	2269758	164	13830	0.34529	0.00378	38.65021	1.67649	0.81183	0.03407	0.968
MB108B1-C16Z2A	Amb	TS	1559403	97	16157	0.33808	0.00373	36.63398	1.46675	0.78588	0.03025	0.961
MB108B1-C19Z1A	Ign (Core)	TS	3081949	175	17626	0.35210	0.00387	40.39524	1.70037	0.83207	0.03381	0.965
MB108B1-C19Z1B	Ign (Core)	TS	1816720	110	16464	0.34618	0.00378	39.05297	1.60482	0.81817	0.03241	0.964
MB108B1-C19Z1C	Ign (Core)	TS	2967311	124	23968	0.34398	0.00383	37.45443	1.55127	0.78970	0.03150	0.963
MB108B1-C20Z1A	Ign (Core)	TS	406939	106	3848	0.32620	0.00362	33.41735	1.54733	0.74299	0.03340	0.971
MB108B1-C20Z1B	Ign (Core)	TS	408676	201	2033	0.33724	0.00424	37.79832	2.22977	0.81290	0.04685	0.977
MB108B1-C21Z2A	Ign (Core)	TS	1778380	109	16316	0.34730	0.00391	38.15958	1.58993	0.79688	0.03197	0.963
MB108B1-4C	Ign (Core)	Mount	3083200	97	31901	0.35187	0.00337	35.06903	1.00095	0.72283	0.01943	0.942
MB108B1-4B	Ign (Core)	Mount	2742402	76	36012	0.35407	0.00361	36.20249	0.85626	0.74156	0.01582	0.902
MB108B1-4G	Ign (Core)	Mount	2550797	214	11914	0.35404	0.00536	37.25330	0.94730	0.76316	0.01559	0.804
MB108B1-5F	Ign (Core)	Mount	2557693	123	20718	0.35608	0.00352	36.19687	0.99772	0.73727	0.01897	0.933
MB108B1-5K	Amb	Mount	2380687	96	24758	0.34686	0.00353	35.01457	0.84225	0.73214	0.01596	0.906
MB108B1-5J	Ign (Core)	Mount	2900891	89	32526	0.34320	0.00330	33.85074	0.85221	0.71534	0.01664	0.924
MB108B1-5L	Ign (Core)	Mount	2464960	89	27638	0.35570	0.00353	37.45964	0.94442	0.76381	0.01770	0.919
MB108B1-6C	Ign (Core)	Mount	2269865	70	32261	0.33607	0.00337	32.64631	0.89957	0.70453	0.01808	0.931
MB108B1-7B	Ign (Core)	Mount	2069761	67	30873	0.34608	0.00343	35.39124	0.84618	0.74167	0.01614	0.910
MB108B1-8B	Ign (Core)	Mount	1904681	118	16205	0.32743	0.00319	32.53595	0.84865	0.72069	0.01744	0.927

Appendix 1. LA-ICP-MS U-Pb Zircon Data

Sample Name	Zircon Phase	Format	^{206}Pb (cps)	^{204}Pb (cps)	^{206}Pb/^{204}Pb	^{207}Pb/^{206}Pb	2σ	^{207}Pb/^{235}U	2σ	^{206}Pb/^{238}U	2σ	ρ
MB108B1-9C	Ign (Core)	Mount	2436644	130	18793	0.35155	0.00338	37.43254	0.97942	0.77225	0.01879	0.930
MB108B1-9D-1	Ign (Osc)	Mount	2021074	148	13670	0.35682	0.00341	38.08483	1.04898	0.77411	0.01999	0.938
MB108B1-9D-2	Ign (Core)	Mount	2083885	448	4655	0.36193	0.00346	38.84053	0.88603	0.77832	0.01612	0.908
MB108B1-9G	Metamorphic	Mount	590904	88	6739	0.27119	0.00266	23.08853	0.56694	0.61747	0.01390	0.917
MB108B1-9E2	Ign (Core)	Mount	2134110	101	21124	0.34356	0.00402	35.00006	1.14857	0.73886	0.02265	0.934
MB108B1-9C	Amb	Mount	2747693	164	16730	0.34411	0.00349	34.42823	0.93269	0.72562	0.01823	0.927
MB108B1-11A	Ign (Core)	Mount	2564306	124	20683	0.33752	0.00341	33.80600	0.95197	0.72643	0.01909	0.933
MB108B1-12E	Ign (Core)	Mount	2052205	127	16111	0.34242	0.00329	34.57869	0.98955	0.73240	0.01974	0.942
MB108B1-12E-2	Ign (Osc)	Mount	2917809	208	14056	0.34936	0.00335	35.13728	0.90123	0.72945	0.01735	0.927
MB108B1-13A	Ign (Osc)	Mount	2750210	210	13127	0.34728	0.00341	35.61522	0.86798	0.74380	0.01659	0.915
MB108B1-13A-2	Ign (Core)	Mount	3045301	138	21995	0.34790	0.00336	36.98226	0.93199	0.77098	0.01795	0.924
MB108B1-13C	Ign (Core)	Mount	2747808	134	20549	0.34995	0.00335	36.87428	0.98125	0.76421	0.01898	0.933
MB108B1-14A	Ign (Osc)	Mount	2044488	111	18498	0.35010	0.00340	37.12690	0.86257	0.76912	0.01623	0.908
MB108B1-14A-2	Metamorphic	Mount	3020441	266	11334	0.25989	0.00332	18.74622	0.61347	0.52315	0.01576	0.921
MB108B1-14B	Ign (Osc)	Mount	2753008	218	12625	0.31778	0.00358	26.81071	0.99349	0.61190	0.02160	0.953
MB108B1-15B	Ign (Core)	Mount	2443771	94	25943	0.33240	0.00323	34.34616	0.86878	0.74941	0.01750	0.923
MB108B1-16B	Ign (Osc)	Mount	320179	72	4465	0.32414	0.00314	31.17749	0.98474	0.69761	0.02097	0.952
MB108B1-16B-3	Ign (Osc)	Mount	366183	108	3375	0.31683	0.00339	28.18663	0.77305	0.64522	0.01630	0.921
MB108B1-16B-4	Ign (Core)	Mount	3236927	140	23077	0.33797	0.00356	33.98136	0.93204	0.72922	0.01847	0.923
MB108B1-17B	Ign (Osc)	Mount	3251756	295	11035	0.32306	0.00431	28.26478	0.66977	0.63455	0.01243	0.826
MB108B1-17H	Ign (Core)	Mount	2966527	143	20684	0.35006	0.00355	37.19247	0.94076	0.77057	0.01785	0.916
MB108B1-18F	Ign (Core)	Mount	1185644	85	13895	0.35342	0.00358	37.32157	0.86417	0.76589	0.01595	0.899
MB108B1-19C	Ign (Core)	Mount	2675315	149	17939	0.35791	0.00342	38.30036	0.96883	0.77613	0.01817	0.926
MB108B1-20B	Metamorphic	Mount	379014	81	4690	0.26410	0.00255	22.20324	0.62141	0.60974	0.01602	0.939

Appendix 1. LA-ICP-MS U-Pb Zircon Data

Sample Name	Zircon Phase	Format	^{206}Pb (cps)	^{204}Pb (cps)	$^{206}Pb/^{204}Pb$	$^{207}Pb/^{206}Pb$	2σ	$^{207}Pb/^{235}U$	2σ	$^{206}Pb/^{238}U$	2σ	ρ
MB108B1-20B-2	Metamorphic	Mount	1783046	115	15466	0.26531	0.00255	23.90269	0.60077	0.65343	0.01518	0.924
MB108B1-20D	Ign (Core)	Mount	4139745	167	24757	0.35223	0.00348	37.64675	0.92074	0.77518	0.01735	0.915
MB108B1-21D	Ign (Core)	Mount	3356957	151	22228	0.35272	0.00337	38.26634	0.87638	0.78685	0.01638	0.909
MB108B1-23A	Ign (Core)	Mount	3083793	136	22617	0.33142	0.00371	33.66847	0.76695	0.73680	0.01462	0.871
MB108B1-25A	Ign (Recryst)	Mount	237413	81	2919	0.34240	0.00340	34.20871	0.92484	0.72461	0.01822	0.930
MB108B1-28A	Ign (Core)	Mount	2742580	161	17074	0.34726	0.00346	37.34827	1.00208	0.78004	0.01943	0.929
MB108B1-30D	Ign (Core)	Mount	2784568	150	18575	0.34690	0.00339	36.92031	0.86901	0.77190	0.01653	0.910
MB108B1-30D-2	Ign (Osc)	Mount	3316898	204	16223	0.32636	0.00482	30.99838	0.80188	0.68888	0.01463	0.821
MB108B1-31-I	Ign (Osc)	Mount	2946260	172	17121	0.34616	0.00333	37.06670	0.90106	0.77662	0.01734	0.918
MB108B1-32H	Ign (Osc)	Mount	4142935	1206	3435	0.31312	0.00562	27.24230	1.07730	0.63101	0.02224	0.891
MB108B1-32C	Ign (Core)	Mount	2424016	160	15144	0.35370	0.00343	37.56718	0.89024	0.77033	0.01666	0.912
MB108B1-34F	Ign (Core)	Mount	2409007	171	14048	0.34999	0.00369	37.31236	1.11763	0.77321	0.02168	0.936
MB108B1-35K	Ign (Core)	Mount	2696789	160	16815	0.34596	0.00331	35.92541	0.92940	0.75314	0.01810	0.929
MB108B1-35E	Ign (Core)	Mount	3158510	158	19933	0.33909	0.00335	35.36605	0.78808	0.75643	0.01511	0.896
MB108B1-36D	Ign (Core)	Mount	1898300	309	6146	0.34811	0.00337	35.34433	0.82223	0.73637	0.01558	0.909
MB108B1-36A	Ign (Core)	Mount	2255595	122	18481	0.34236	0.00328	35.10277	0.95654	0.74363	0.01897	0.936
MB108B1-38J	Ign (Core)	Mount	2848084	149	19093	0.34711	0.00360	37.01590	0.98210	0.77342	0.01889	0.920
MB120S1-C0Z4	Metamorphic	TS	1086362	210	5181	0.24962	0.00294	20.25365	0.63502	0.58848	0.01710	0.927
MB120S1-C0Z4-2	Metamorphic	TS	1112490	93	11934	0.25796	0.00378	22.93506	0.49619	0.64483	0.01025	0.735
MB120S1-C2Z1	Metamorphic	TS	1066291	91	11749	0.27212	0.00288	24.97148	0.51669	0.66554	0.01183	0.859
MB120S1-C5Z1	Metamorphic	TS	1194322	89	13474	0.27008	0.00285	24.64308	0.47848	0.66176	0.01078	0.839
MB120S2-C0Z1-1	Metamorphic	TS	892097	84	10664	0.27416	0.00303	25.29168	0.71949	0.66906	0.01754	0.922
MB120S2-C4Z2-1	Metamorphic	TS	1098084	72	15347	0.25763	0.00274	22.91255	0.71545	0.64502	0.01894	0.940
MB120S2-C4Z2-2	Metamorphic	TS	1479933	80	18511	0.26100	0.00279	24.03019	0.63736	0.66774	0.01621	0.915

Appendix 1. LA-ICP-MS U-Pb Zircon Data

Sample Name	Zircon Phase	Format	^{206}Pb (cps)	^{204}Pb (cps)	^{206}Pb/^{204}Pb	^{207}Pb/^{206}Pb	2σ	^{207}Pb/^{235}U	2σ	^{206}Pb/^{238}U	2σ	ρ
MB120-11A1	Ign (Osc)	Mount	493752	87	5652	0.30971	0.00319	28.46450	0.71196	0.66658	0.01519	0.911
MB120-11A2	Ign (Osc)	Mount	435728	72	6081	0.30473	0.00293	28.74619	0.76362	0.68417	0.01694	0.932
MB120-11B2	Ign (Osc)	Mount	539247	72	7507	0.32201	0.00311	32.63830	0.86088	0.73512	0.01804	0.931
MB120-11C2	Metamorphic	Mount	3013899	1077	2800	0.27559	0.00270	22.56581	0.53535	0.59387	0.01283	0.911
MB120-11F1	Ign (Sector)	Mount	149302	67	2216	0.32045	0.00322	30.71724	0.78633	0.69522	0.01637	0.920
MB120-12C1	Metamorphic	Mount	948186	155	6125	0.27131	0.00276	24.40056	0.57842	0.65227	0.01397	0.903
MB120-12C2	Metamorphic	Mount	1064814	210	5076	0.25864	0.00253	23.22353	0.56781	0.65122	0.01459	0.917
MB120-12E1	Ign (Core)	Mount	1634935	141	11578	0.31882	0.00313	32.38981	0.91281	0.73683	0.01947	0.938
MB120-12F1	Ign (Core)	Mount	3493866	202	17287	0.30964	0.00403	28.57536	0.75303	0.66931	0.01534	0.870
MB120-13C1	Ign (Core)	Mount	109568	90	1217	0.32147	0.00321	30.86884	0.89533	0.69644	0.01896	0.939
MB120-13C2	Ign (Osc)	Mount	238761	96	2478	0.31413	0.00343	31.98530	1.06516	0.73847	0.02323	0.945
MB120-13E1	Ign (Osc)	Mount	620894	103	6009	0.31971	0.00310	32.37501	0.83007	0.73444	0.01743	0.926
MB120-13E2	Ign (Osc)	Mount	1075854	140	7703	0.32066	0.00311	32.20743	0.81557	0.72847	0.01704	0.924
MB120-15A1	Ign (Osc)	Mount	144060	99	1448	0.32231	0.00312	31.53395	0.85053	0.70958	0.01787	0.933
MB120-15A2	Metamorphic	Mount	1175246	165	7123	0.27117	0.00262	24.49051	0.69945	0.65502	0.01761	0.941
MB120-15B1	Ign (Core)	Mount	83192	92	905	0.32270	0.00323	31.15282	0.77261	0.70016	0.01588	0.915
MB120-15C1	Metamorphic	Mount	5035483	4541	1109	0.27338	0.00387	20.90131	0.55938	0.55450	0.01259	0.848
MB120-15C2	Metamorphic	Mount	2594482	837	3098	0.24185	0.00332	18.05842	0.43469	0.54153	0.01070	0.821
MB120-15B2	Ign (Osc)	Mount	940110	111	8432	0.31731	0.00307	31.50562	0.91142	0.72012	0.01963	0.942
MB120-15B3	Ign (Osc)	Mount	1333926	124	10760	0.30970	0.00299	29.76740	0.87204	0.69710	0.01928	0.944
MB138B2-2	Ign (Osc)	TS	3829210	547	6998	0.22666	0.00230	12.83349	0.27786	0.41065	0.00785	0.883
MB138B2-3	Ign (Osc)	TS	3857128	930	4150	0.20853	0.00594	8.54233	0.30609	0.29710	0.00647	0.608
MB138B2-6	Ign (Osc)	TS	3167819	910	3483	0.17105	0.00278	7.52598	0.33051	0.31910	0.01302	0.929
MB138B2-9A	Amb	TS	2745336	101	27293	0.32395	0.00310	33.43351	0.88207	0.74852	0.01840	0.932

Appendix 1. LA-ICP-MS U-Pb Zircon Data

Sample Name	Zircon Phase	Format	^{206}Pb (cps)	^{204}Pb (cps)	^{206}Pb/^{204}Pb	^{207}Pb/^{206}Pb	2σ	^{207}Pb/^{235}U	2σ	^{206}Pb/^{238}U	2σ	ρ
MB138B2-9B	Amb	TS	1593927	284	5620	0.31763	0.00305	32.15617	0.86395	0.73425	0.01843	0.934
MB138B2-12	Ign (Core)	TS	2169258	213	10178	0.38308	0.00367	42.31008	1.13866	0.80103	0.02015	0.935
MB138B2-14A	Metamorphic	TS	300715	69	4341	0.28995	0.00293	28.35137	0.78305	0.70916	0.01823	0.930
MB138B2-14B	Ign (Osc)	TS	2299519	395	5823	0.25274	0.00292	10.71725	0.34377	0.30754	0.00920	0.933
MB138B2-15	Ign (Core)	TS	3083487	1073	2873	0.27975	0.00273	18.42103	0.44947	0.47757	0.01068	0.917
MB138B2-15B	Ign (Core)	TS	1402978	1608	873	0.33185	0.00357	28.54571	0.74790	0.62387	0.01490	0.912
MB138B2-18B	Ign (Core)	TS	958183	122	7861	0.37933	0.00382	43.27316	1.39688	0.82738	0.02537	0.950
MB167S1-10	Ign (Osc)	TS	1191784	294	4053	0.27727	0.00302	22.29988	0.74901	0.58330	0.01853	0.946
MB167S1-C13	Ign (Core)	TS	1016191	40	25429	0.28368	0.00318	25.50073	0.79681	0.65197	0.01901	0.933
MB167S1-C14	Ign (Core)	TS	1247410	244	5114	0.27645	0.00345	22.49958	0.75777	0.59028	0.01846	0.929
MB167S1-A1	Metamorphic	TS	754791	232	3247	0.24319	0.00735	14.45255	0.70828	0.43103	0.01663	0.787
MB167S1-A2	Ign (Core)	TS	795872	55	14596	0.28069	0.00305	20.20953	0.62127	0.52218	0.01502	0.936
MB167S1-E	Metamorphic	TS	1723936	586	2941	0.22908	0.00301	12.39447	0.48489	0.39241	0.01446	0.942
MB167S1-J	Metamorphic	TS	1202548	58	20843	0.24128	0.01078	17.58154	1.23517	0.52849	0.02865	0.772
MB185-3A	Ign (Core)	TS	676180	135	4998	0.28142	0.00310	25.13196	0.55097	0.64769	0.01228	0.865
MB185-3B	Ign (Osc)	TS	2520469	85	29598	0.27828	0.00331	25.29519	0.62299	0.65925	0.01422	0.876
MB185-4-2	Ign (Core)	TS	880460	286	3076	0.28182	0.00316	23.69939	0.59572	0.60990	0.01372	0.895
MB185-7	Ign (Osc)	TS	631468	370	1709	0.28259	0.00495	22.68626	1.11886	0.58225	0.02684	0.935

Appendix 1. LA-ICP-MS U-Pb Zircon Data

Sample Name	Zircon Phase	Format	Age (Ma)						%
			$^{207}Pb^*/^{206}Pb^*$	2σ	$^{207}Pb^*/^{235}U$	2σ	$^{206}Pb^*/^{238}U$	2σ	Discordance
MB07-A	Ign (Core)	TS	3376	19	3373	32	3369	81	0
MB07-B1	Ign (Core)	TS	3374	17	3142	53	2793	124	21
MB07-B2	Ign (Osc)	TS	3363	17	3292	32	3176	77	6
MB07-C3-1A	Ign (Osc)	TS	3383	17	3372	28	3353	70	1
MB07-C3-1B	Ign (Core)	TS	3396	17	3146	47	2770	107	23
MB07-D1	Metamorphic	TS	3322	17	3165	39	2925	92	14
MB07-D2	Ign (Core)	TS	3367	17	3333	25	3278	60	3
MB07-C	Ign (Osc)	TS	3384	17	3432	29	3515	75	-4
MB07-I1	Metamorphic	TS	3297	19	3268	34	3220	83	2
MB07-I2	Ign (Core)	TS	3384	18	3364	29	3330	71	2
MB07-J	Ign (Core)	TS	3359	18	3247	30	3069	70	9
MB07-K	Ign (Core)	TS	3353	17	3363	29	3380	72	-1
MB07-O	Metamorphic	TS	3308	18	3305	27	3300	65	0
MB07-C6-1B	Ign (Core)	TS	3374	17	3387	27	3408	68	-1
MB07-U1	Ign (Core)	TS	3382	17	3395	26	3418	65	-1
MB07-C10-1A	Metamorphic	TS	3277	17	3161	25	2980	56	10
MB07-C10-1B	Ign (Core)	TS	3389	17	3383	34	3372	87	1
MB07-C9-1	Ign (Osc)	TS	3399	17	3364	51	3304	134	3
MB07-S	Ign (Core)	TS	3360	19	3294	30	3188	72	5
MB12S1-C2-Z2-1	Ign (Osc)	TS	3617	17	3472	54	3225	138	12
MB12S1-C6-Z1-1	Ign (Core)	TS	3597	16	3558	28	3488	71	3
MB12S1-C6-Z1-2	Ign (Core)	TS	3575	17	3532	37	3457	97	3
MB12S1-C7-Z2-1	Ign (Osc)	TS	3526	18	3469	24	3372	55	5
MB12S1-C7-Z1-1	Inherited (Core)	TS	3960	16	3930	29	3871	81	2
MB12S1-C14-Z1-1	Inherited (Core)	TS	3957	16	3920	26	3848	70	3

Appendix 1. LA-ICP-MS U-Pb Zircon Data

Sample Name	Zircon Phase	Format	Age (Ma)						%
			$^{207}Pb^*/^{206}Pb^*$	2σ	$^{207}Pb^*/^{235}U$	2σ	$^{206}Pb^*/^{238}U$	2σ	Discordance
MB12S2-C1Z1A	Ign (Core)	TS	3493	19	3356	51	3132	127	12
MB12S2-C1Z1B	Amb	TS	3515	22	3485	54	3433	144	2
MB12S2-C1Z1C	Amb (Recryst)	TS	3565	27	3417	57	3171	141	12
MB12S2-C3Z1A	Ign (Osc)	TS	3551	18	3493	51	3393	136	5
MB12S2-C3Z2A	Ign (Osc)	TS	3546	17	3445	49	3272	126	8
MB12S2-C14Z1A	Amb	TS	3580	18	3527	50	3435	134	4
MB12S2-C15Z1A	Ign (Osc)	TS	3609	17	3605	50	3599	137	0
MB12S2-C15Z1B	Ign (Osc)	TS	3627	17	3660	51	3721	144	-3
MB21B-C8Z1	Ign (Core)	TS	3553	16	3524	28	3473	72	2
MB21B-C1Z1	Amb	TS	3541	17	3538	31	3531	83	0
MB21B-C4Z1A	Ign (Core)	TS	3435	20	3031	57	2461	120	40
MB21B-C4Z1B	Ign (Osc)	TS	3473	19	3286	37	2988	88	16
MB21B-C6Z1	Ign (Core)	TS	3449	17	3054	36	2491	75	38
MB47B-C2Z1A	Ign (Osc)	TS	3578	16	3530	26	3448	66	4
MB47B-C2Z1B	Ign (Osc)	TS	3539	16	3561	29	3600	75	-2
MB47B-C2Z1C	Ign (Osc)	TS	3542	16	3499	26	3424	63	3
MB47B-C4Z1A	Metamorphic	TS	3406	28	3357	26	3277	51	4
MB47B-C4Z2A	Ign (Osc)	TS	3493	19	3432	33	3330	84	5
MB47B-C5Z1A	Ign (Osc)	TS	3548	16	3502	23	3423	55	4
MB47B-C8Z1A	Ign (Osc)	TS	3493	18	3243	29	2855	64	22
MB47B-C10Z1A	Ign (Osc)	TS	3523	19	3472	36	3383	92	4
MB47B-C11Z1A	Ign (Core)	TS	3442	18	3322	25	3125	58	10
MB47B-C13Z1B	Ign (Osc)	TS	3479	19	3225	28	2831	61	23
MB47B-C13Z1C	Ign (Core)	TS	3578	17	3546	30	3491	76	2
MB47B-C15Z1A	Metamorphic	TS	3301	20	3043	34	2669	73	24

Appendix 1. LA-ICP-MS U-Pb Zircon Data

Sample Name	Zircon Phase	Format	Age (Ma)						%
			$^{207}Pb^*/^{206}Pb^*$	2σ	$^{207}Pb^*/^{235}U$	2σ	$^{206}Pb^*/^{238}U$	2σ	Discordance
MB47B-C15Z1B	Ign (Osc)	TS	3477	34	3421	46	3326	111	5
MB47B-C16Z1A	Metamorphic	TS	3260	39	2918	44	2450	79	33
MB54B-4	Ign (Core)	TS	3547	15	3405	28	3169	68	12
MB54B-12	Metamict	TS	3422	25	3146	36	2731	75	25
MB54B-18	Ign (Core)	TS	3536	16	3457	24	3323	57	6
MB54B-25	Ign (Core)	TS	3540	15	3496	28	3421	72	3
MB54B-26	Ign (Core)	TS	3544	15	3447	22	3283	52	8
MB54B-32A	Ign (Osc)	TS	3469	17	3229	27	2857	58	21
MB54B-32B	Ign (Osc)	TS	3521	15	3362	23	3101	53	14
MB73A1-C2Z1A	Ign (Core)	TS	3525	18	3437	32	3289	79	7
MB73A1-C2Z1B	Ign (Core)	TS	3540	17	3543	33	3548	87	0
MB73A1-C4Z1A	Metamorphic	TS	3364	29	3197	34	2938	71	14
MB73A1-C4Z2A	Ign (Osc)	TS	3496	18	3424	33	3301	83	6
MB73A1-C8Z1A	Ign (Sector)	TS	3530	17	3470	33	3368	84	5
MB73A1-C8Z1B	Amb (Recryst)	TS	3481	18	3423	34	3325	85	5
MB73A1-C8Z1C	Amb (Recryst)	TS	3474	17	3442	32	3389	80	3
MB76C-C1-Z1-1	Metamict	TS	3241	31	3058	29	2787	52	16
MB76C-C2-Z1-1	Amb	TS	3466	42	3273	46	2967	95	17
MB76C-C4-Z1-1	Metamict	TS	3682	25	3542	35	3301	83	12
MB76C-C5-Z1	Amb	TS	3559	27	3484	34	3356	78	6
MB76C-C7-Z1	Amb	TS	3419	32	3169	34	2789	64	23
MB76C-C10-Z3-1	Amb	TS	3584	26	3539	31	3460	71	4
MB76C-C10-Z3-2	Amb	TS	3573	25	3528	29	3448	66	4
MB76C-C10-Z3-3	Amb	TS	3616	25	3493	28	3283	61	10
MB76C-C111-Z1-1	Amb	TS	3507	26	3466	30	3397	69	3

Appendix 1. LA-ICP-MS U-Pb Zircon Data

Sample Name	Zircon Phase	Format	Age (Ma)						%
			$^{207}Pb^*/^{206}Pb^*$	2σ	$^{207}Pb^*/^{235}U$	2σ	$^{206}Pb^*/^{238}U$	2σ	Discordance
MB76C-C111-Z1-2	Amb	TS	3314	27	3263	30	3182	66	4
MB76C-C111-Z1-3	Amb	TS	3415	26	3362	36	3273	85	4
MB103-C0Z1-1	Ign (Core)	TS	3713	16	3688	30	3642	80	2
MB103-C0Z1-2	Ign (Core)	TS	3694	17	3674	31	3637	81	2
MB103-C1Z1-1	Amb	TS	3688	16	3654	29	3593	77	3
MB103-C1Z1-2	Ign (Osc)	TS	3738	17	3717	30	3677	81	2
MB103-C1Z1-3	Ign (Sector)	TS	3635	18	3604	30	3550	76	2
MB103-C1Z1-4	Amb	TS	3696	17	3693	28	3687	75	0
MB103-C1Z1-5	Amb	TS	3713	16	3705	31	3691	82	1
MB103-C2Z1-1	Amb	TS	3694	25	3697	33	3701	82	0
MB103-C2Z1-2	Amb	TS	3591	34	3551	36	3481	80	3
MB103-C3Z1-1	Metamorphic	TS	3381	17	3338	30	3265	74	4
MB103-C3Z1-2	Metamorphic	TS	3298	17	3287	29	3269	72	1
MB103-C5Z1-1	Amb (Patchy)	TS	3747	26	3720	38	3669	99	2
MB103-C5Z1-2	Amb (Patchy)	TS	3726	18	3666	32	3558	83	5
MB103-C5Z1-3	Amb (Patchy)	TS	3734	16	3729	26	3720	70	0
MB103-C5Z1-4	Amb (Patchy)	TS	3643	22	3626	27	3594	66	1
MB103-C5Z1-5	Amb (Patchy)	TS	3732	16	3723	29	3707	79	1
MB103-C5Z1-6	Amb (Patchy)	TS	3730	16	3701	30	3647	81	2
MB103-C7Z1-1	Ign (Osc)	TS	3651	19	3555	28	3388	69	8
MB103-C7Z1-2	Ign (Sector)	TS	3644	20	3605	29	3535	74	3
MB103-C7Z1-3	Ign (Mixed)	TS	3583	18	3526	30	3426	77	5
MB103-C7Z1-4	Ign (Sector)	TS	3646	16	3581	31	3467	79	5
MB103-C7Z1-5	Ign (Sector)	TS	3648	17	3593	32	3494	82	4
MB103-C8Z1-1	Ign (Osc)	TS	3710	17	3677	34	3617	91	3

Appendix 1. LA-ICP-MS U-Pb Zircon Data

Sample Name	Zircon Phase	Format	Age (Ma)						%
			$^{207}Pb^*/^{206}Pb^*$	2σ	$^{207}Pb^*/^{235}U$	2σ	$^{206}Pb^*/^{238}U$	2σ	Discordance
MB103-C8Z1-2	Ign (Osc)	TS	3735	16	3726	31	3709	84	1
MB103-C8Z1-3	Ign (Osc)	TS	3725	16	3693	30	3635	80	2
MB103-C8Z1-5	Ign (Osc)	TS	3722	16	3682	32	3610	85	3
MB103-C9Z1-1	Ign (Osc)	TS	3754	17	3705	31	3615	83	4
MB103-C9Z1-2	Ign (Osc)	TS	3738	17	3728	32	3708	87	1
MB103-C9Z1-3	Ign (Osc)	TS	3754	37	3706	42	3618	97	4
MB103-C10Z1-1	Ign (Sector)	TS	3733	18	3668	31	3550	79	5
MB103-C10Z1-2	Ign (Sector)	TS	3715	17	3687	29	3634	76	2
MB103-C10Z1-3	Metamorphic	TS	3266	17	3234	29	3184	71	3
MB108A-C1-Z2-1	Amb	TS	3751	16	3725	31	3677	83	2
MB108A-C1-Z2-2	Amb	TS	3742	16	3724	33	3691	90	1
MB108A-C1-Z2-3	Amb	TS	3746	17	3689	32	3585	85	4
MB108A-C1-Z2-4	Amb	TS	3678	17	3620	35	3517	91	5
MB108A-C1-Z1-1	Amb	TS	3583	16	3585	32	3587	84	0
MB108A-C1-Z1-2	Amb	TS	3585	16	3557	30	3508	79	2
MB108A-C1-Z1-3	Amb	TS	3563	16	3580	43	3612	118	-1
MB108A-C1-Z1-4	Amb	TS	3445	16	3438	31	3425	79	1
MB108A-C1-Z3-1	Ign (Osc)	TS	3608	16	3560	32	3474	84	4
MB108A-C1-Z3-2	Ign (Osc)	TS	3558	17	3508	34	3420	89	4
MB108A-C1-Z3-3	Ign (Osc)	TS	3561	18	3522	31	3454	79	3
MB108A-C1-Z4-1	Ign (Osc)	TS	3545	17	3495	33	3409	84	4
MB108A-C1-Z4-2	Ign (Osc)	TS	3602	17	3548	33	3453	85	4
MB108A-C2-Z1-1	Amb	TS	3597	17	3560	34	3494	88	3
MB108A-C2-Z1-2	Ign (Osc)	TS	3671	16	3643	33	3592	90	2
MB108A-C2-Z1-3	Ign (Osc)	TS	3690	16	3636	33	3540	88	4

Appendix 1. LA-ICP-MS U-Pb Zircon Data

Sample Name	Zircon Phase	Format	Age (Ma)						%
			$^{207}Pb^*/^{206}Pb^*$	2σ	$^{207}Pb^*/^{235}U$	2σ	$^{206}Pb^*/^{238}U$	2σ	Discordance
MB108A-C2-Z1-4	Ign (Osc)	TS	3670	16	3661	34	3644	92	1
MB108A-C2-Z2-1	Amb	TS	3684	19	3662	38	3621	100	2
MB108A-C3-Z1-1	Ign (Osc)	TS	3706	17	3704	39	3700	108	0
MB108A-C3-Z1-2	Ign (Osc)	TS	3635	19	3615	42	3578	113	2
MB108A-C3-Z1-3	Ign (Osc)	TS	3711	16	3689	35	3649	95	2
MB108A-C3-Z2-1	Ign (Osc)	TS	3354	17	3306	29	3227	72	4
MB108A-C3-Z2-2	Ign (Osc)	TS	3464	17	3425	33	3359	85	3
MB108A-C3-Z2-3	Ign (Osc)	TS	3301	17	3261	29	3196	70	3
MB108A-C4-Z1-1	Ign (Sector)	TS	3636	20	3575	36	3465	92	5
MB108A-C4-Z1-2	Ign (Sector)	TS	3671	21	3626	30	3546	76	4
MB108A-C4-Z1-3	Ign (Core)	TS	3568	18	3495	35	3370	91	6
MB108A-C5-Z1-2	Ign (Core)	TS	3711	16	3683	27	3631	71	2
MB108A-C5-Z1-3	Ign (Core)	TS	3740	16	3701	26	3629	67	3
MB108A-C5-Z1-4	Ign (Sector)	TS	3747	16	3660	27	3503	68	7
MB108A-C5-Z1-5	Ign (Core)	TS	3734	16	3676	28	3570	72	5
MB108A-C5-Z1-6	Ign (Sector)	TS	3580	17	3506	27	3378	68	6
MB108A-C6-Z1-1	Amb	TS	3634	18	3583	31	3494	79	4
MB108A-C6-Z1-2	Amb	TS	3647	16	3606	28	3532	73	3
MB108A-C7-Z3-1	Ign (Sector)	TS	3630	18	3575	32	3478	83	4
MB108A-C7-Z3-2	Ign (Sector)	TS	3543	16	3490	33	3399	84	4
MB108A-C7-Z3-3	Ign (Sector)	TS	3663	17	3581	33	3436	84	7
MB108A-C7-Z1-1	Amb	TS	3424	18	3356	34	3244	85	6
MB108A-C7-Z2-1	Ign (Sector)	TS	3731	16	3653	32	3511	84	6
MB108A-C7-Z2-2	Ign (Sector)	TS	3751	16	3681	35	3553	94	6
MB108A-C7-Z4-1	Amb	TS	3736	16	3670	29	3550	76	5

Appendix 1. LA-ICP-MS U-Pb Zircon Data

Sample Name	Zircon Phase	Format	Age (Ma)						%
			$^{207}Pb^*/^{206}Pb^*$	2σ	$^{207}Pb^*/^{235}U$	2σ	$^{206}Pb^*/^{238}U$	2σ	Discordance
MB108A-C7-Z4-2	Amb	TS	3743	16	3671	30	3541	77	6
MB108A-C7-Z4-3	Amb	TS	3742	16	3702	31	3629	83	3
MB108A-C7-Z4-4	Amb	TS	3732	16	3696	31	3629	84	3
MB108A-C8-Z1-1	Ign (Sector)	TS	3753	17	3726	34	3676	93	2
MB108A-C8-Z1-2	Ign (Sector)	TS	3739	16	3699	29	3625	77	3
MB108A-C8-Z1-3	Ign (Sector)	TS	3739	16	3707	29	3648	76	2
MB108A-C9-Z1-1	Ign (Sector)	TS	3712	16	3674	31	3604	82	3
MB108A-C9-Z1-2	Ign (Sector)	TS	3703	16	3647	35	3545	93	4
MB108A-C9-Z1-3	Ign (Sector)	TS	3660	16	3598	33	3487	85	5
MB108A-C9-Z1-4	Ign (Sector)	TS	3714	16	3701	29	3677	77	1
MB108A-C10-Z1-1	Amb	TS	3750	16	3713	34	3645	93	3
MB108A-C10-Z1-2	Amb	TS	3747	16	3715	40	3655	111	3
MB108A-C10-Z1-3	Amb	TS	3396	22	3366	31	3316	75	2
MB108A-C10-Z1-4	Amb	TS	3674	19	3644	31	3590	82	2
MB108B1-C2-Z1	Amb	TS	3661	23	3633	44	3582	118	2
MB108B1-C2-Z1-B	Amb	TS	3678	18	3659	43	3624	118	2
MB108B1-C3-Z1A	Metamorphic	TS	2757	56	2014	59	1372	74	101
MB108B1-C3-Z2A	Metamorphic	TS	3181	55	2864	56	2436	98	31
MB108B1-C4Z1A	Amb	TS	3666	17	3622	43	3543	116	3
MB108B1-C4Z1B	Amb	TS	3635	17	3628	41	3615	112	1
MB108B1-C5Z1A	Metamorphic	TS	3205	19	2931	38	2549	82	26
MB108B1-C5Z1B	Ign (Osc)	TS	3598	19	3407	42	3093	101	16
MB108B1-C5Z2A	Amb	TS	3646	17	3569	42	3434	111	6
MB108B1-C6Z1A	Amb	TS	3627	17	3494	42	3266	106	11
MB108B1-C6Z2A	Amb	TS	3623	18	3500	39	3288	98	10

Appendix 1. LA-ICP-MS U-Pb Zircon Data

Sample Name	Zircon Phase	Format	Age (Ma)						%
			$^{207}Pb^*/^{206}Pb^*$	2σ	$^{207}Pb^*/^{235}U$	2σ	$^{206}Pb^*/^{238}U$	2σ	Discordance
MB108B1-C6Z2B	Amb	TS	3667	17	3625	41	3552	110	3
MB108B1-C6Z3A	Metamorphic	TS	3159	30	2973	45	2705	96	17
MB108B1-C9Z2A	Ign (Core)	TS	3674	20	3649	42	3605	112	2
MB108B1-C9Z2B	Ign (Osc)	TS	3635	17	3585	39	3497	105	4
MB108B1-C9Z3A	Amb	TS	3589	19	3488	47	3314	122	8
MB108B1-C9Z4A	Amb	TS	3682	18	3623	40	3519	107	5
MB108B1-C9Z4B	Amb	TS	3687	17	3677	42	3660	115	1
MB108B1-C9Z5A	Amb	TS	3596	19	3589	46	3578	125	1
MB108B1-C9Z5B	Amb	TS	3703	17	3735	41	3794	116	-2
MB108B1-C9Z5C	Amb	TS	3685	17	3701	41	3731	116	-1
MB108B1-C10Z1A	Ign (Core)	TS	3667	19	3612	40	3514	107	4
MB108B1-C10Z1B	Ign (Osc)	TS	3540	17	3435	42	3258	106	9
MB108B1-C11Z1	Ign (Core)	TS	3638	18	3519	45	3313	115	10
MB108B1-C11Z1B	Ign (Osc)	TS	3658	17	3584	43	3452	115	6
MB108B1-C11Z2A	Ign (Osc)	TS	3548	18	3507	43	3435	115	3
MB108B1-C11Z2B	Ign (Core)	TS	3617	20	3642	45	3690	123	-2
MB108B1-C11Z2C	Ign (Core)	TS	3618	26	3597	50	3560	131	2
MB108B1-C13Z1A	Metamorphic	TS	3240	24	3176	41	3077	98	5
MB108B1-C13Z2A	Ign (Core)	TS	3667	20	3701	45	3763	127	-3
MB108B1-C13Z2B	Metamorphic	TS	3235	43	3059	54	2798	113	16
MB108B1-C13Z4A	Amb	TS	3573	20	3507	43	3392	112	5
MB108B1-C14Z1A	Ign (Osc)	TS	3617	17	3601	42	3572	114	1
MB108B1-C15Z1A	Ign (Core)	TS	3635	17	3654	43	3688	120	-1
MB108B1-C16Z1A	Amb	TS	3686	17	3737	42	3831	120	-4
MB108B1-C16Z2A	Amb	TS	3654	17	3684	39	3738	108	-2

Appendix 1. LA-ICP-MS U-Pb Zircon Data

Sample Name	Zircon Phase	Format	Age (Ma)						%
			$^{207}Pb^*/^{206}Pb^*$	2σ	$^{207}Pb^*/^{235}U$	2σ	$^{206}Pb^*/^{238}U$	2σ	Discordance
MB108B1-C19Z1A	Ign (Core)	TS	3716	17	3780	41	3903	118	-5
MB108B1-C19Z1B	Ign (Core)	TS	3690	17	3747	40	3854	114	-4
MB108B1-C19Z1C	Ign (Core)	TS	3681	17	3706	40	3752	112	-2
MB108B1-C20Z1A	Ign (Core)	TS	3599	17	3593	45	3582	122	0
MB108B1-C20Z1B	Ign (Core)	TS	3650	19	3715	57	3835	164	-5
MB108B1-C21Z2A	Ign (Core)	TS	3695	17	3724	40	3778	114	-2
MB108B1-4C	Ign (Core)	Mount	3715	15	3641	28	3507	72	6
MB108B1-4B	Ign (Core)	Mount	3725	15	3672	23	3576	58	4
MB108B1-4G	Ign (Core)	Mount	3724	23	3700	25	3656	57	2
MB108B1-5F	Ign (Core)	Mount	3733	15	3672	27	3560	70	5
MB108B1-5K	Amb	Mount	3693	15	3639	23	3541	59	4
MB108B1-5J	Ign (Core)	Mount	3677	15	3606	25	3479	62	6
MB108B1-5L	Ign (Core)	Mount	3732	15	3706	25	3658	64	2
MB108B1-6C	Ign (Core)	Mount	3645	15	3570	27	3438	68	6
MB108B1-7B	Ign (Core)	Mount	3690	15	3650	23	3577	59	3
MB108B1-8B	Ign (Core)	Mount	3605	15	3567	25	3499	65	3
MB108B1-9C	Ign (Core)	Mount	3714	15	3705	26	3689	68	1
MB108B1-9D-1	Ign (Osc)	Mount	3736	14	3722	27	3696	72	1
MB108B1-9D-2	Ign (Core)	Mount	3758	14	3742	22	3711	58	1
MB108B1-9G	Metamorphic	Mount	3313	15	3231	24	3100	55	7
MB108B1-9E2	Ign (Core)	Mount	3679	18	3639	32	3566	83	3
MB108B1-9C	Amb	Mount	3681	15	3622	26	3517	68	5
MB108B1-11A	Ign (Core)	Mount	3652	15	3604	27	3520	71	4
MB108B1-12E	Ign (Core)	Mount	3674	15	3627	28	3542	73	4
MB108B1-12E-2	Ign (Osc)	Mount	3704	15	3643	25	3531	64	5

Appendix 1. LA-ICP-MS U-Pb Zircon Data

Sample Name	Zircon Phase	Format	Age (Ma)						%
			$^{207}Pb^*/^{206}Pb^*$	2σ	$^{207}Pb^*/^{235}U$	2σ	$^{206}Pb^*/^{238}U$	2σ	Discordance
MB108B1-13A	Ign (Osc)	Mount	3695	15	3656	24	3585	61	3
MB108B1-13A-2	Ign (Core)	Mount	3698	15	3693	25	3684	65	0
MB108B1-13C	Ign (Core)	Mount	3707	15	3690	26	3660	69	1
MB108B1-14A	Ign (Osc)	Mount	3707	15	3697	23	3678	59	1
MB108B1-14A-2	Metamorphic	Mount	3246	20	3029	31	2713	66	20
MB108B1-14B	Ign (Osc)	Mount	3559	17	3377	36	3078	86	16
MB108B1-15B	Ign (Core)	Mount	3628	15	3620	25	3605	64	1
MB108B1-16B	Ign (Osc)	Mount	3590	15	3525	31	3412	79	5
MB108B1-16B-3	Ign (Osc)	Mount	3555	16	3426	27	3210	64	11
MB108B1-16B-4	Ign (Core)	Mount	3654	16	3609	27	3531	68	3
MB108B1-17B	Ign (Osc)	Mount	3584	20	3428	23	3168	49	13
MB108B1-17H	Ign (Core)	Mount	3707	15	3699	25	3683	65	1
MB108B1-18F	Ign (Core)	Mount	3722	15	3702	23	3666	58	2
MB108B1-19C	Ign (Core)	Mount	3741	14	3728	25	3703	66	1
MB108B1-20B	Metamorphic	Mount	3271	15	3193	27	3069	64	7
MB108B1-20B-2	Metamorphic	Mount	3278	15	3264	24	3242	59	1
MB108B1-20D	Ign (Core)	Mount	3717	15	3711	24	3700	63	0
MB108B1-21D	Ign (Core)	Mount	3719	14	3727	22	3742	59	-1
MB108B1-23A	Ign (Core)	Mount	3624	17	3600	22	3559	54	2
MB108B1-25A	Ign (Recryst)	Mount	3674	15	3616	26	3513	68	5
MB108B1-28A	Ign (Core)	Mount	3695	15	3703	26	3717	70	-1
MB108B1-30D	Ign (Core)	Mount	3693	15	3691	23	3688	60	0
MB108B1-30D-2	Ign (Osc)	Mount	3600	22	3519	25	3378	56	7
MB108B1-31-I	Ign (Osc)	Mount	3690	15	3695	24	3705	63	0
MB108B1-32H	Ign (Osc)	Mount	3536	27	3392	38	3154	87	12

Appendix 1. LA-ICP-MS U-Pb Zircon Data

Sample Name	Zircon Phase	Format	Age (Ma)						%
			$^{207}Pb^*/^{206}Pb^*$	2σ	$^{207}Pb^*/^{235}U$	2σ	$^{206}Pb^*/^{238}U$	2σ	Discordance
MB108B1-32C	Ign (Core)	Mount	3723	15	3709	23	3682	60	1
MB108B1-34F	Ign (Core)	Mount	3707	16	3702	29	3692	78	0
MB108B1-35K	Ign (Core)	Mount	3689	15	3664	25	3619	66	2
MB108B1-35E	Ign (Core)	Mount	3659	15	3649	22	3631	55	1
MB108B1-36D	Ign (Core)	Mount	3699	15	3648	23	3557	58	4
MB108B1-36A	Ign (Core)	Mount	3673	15	3642	27	3584	70	2
MB108B1-38J	Ign (Core)	Mount	3694	16	3694	26	3693	68	0
MB120S1-C0Z4	Metamorphic	TS	3182	19	3104	30	2983	69	7
MB120S1-C0Z4-2	Metamorphic	TS	3234	23	3224	21	3208	40	1
MB120S1-C2Z1	Metamorphic	TS	3318	16	3307	20	3289	46	1
MB120S1-C5Z1	Metamorphic	TS	3307	16	3294	19	3274	42	1
MB120S2-C0Z1-1	Metamorphic	TS	3330	17	3320	27	3302	67	1
MB120S2-C4Z2-1	Metamorphic	TS	3232	17	3223	30	3209	74	1
MB120S2-C4Z2-2	Metamorphic	TS	3253	17	3270	26	3297	62	-1
MB120-11A1	Ign (Osc)	Mount	3519	16	3435	24	3293	59	7
MB120-11A2	Ign (Osc)	Mount	3494	15	3445	26	3360	65	4
MB120-11B2	Ign (Osc)	Mount	3579	15	3570	26	3552	67	1
MB120-11C2	Metamorphic	Mount	3338	15	3208	23	3005	52	11
MB120-11F1	Ign (Sector)	Mount	3572	15	3510	25	3403	62	5
MB120-12C1	Metamorphic	Mount	3314	16	3285	23	3237	54	2
MB120-12C2	Metamorphic	Mount	3238	15	3236	24	3233	57	0
MB120-12E1	Ign (Core)	Mount	3564	15	3562	27	3559	72	0
MB120-12F1	Ign (Core)	Mount	3519	20	3439	26	3303	59	7
MB120-13C1	Ign (Core)	Mount	3577	15	3515	28	3407	72	5
MB120-13C2	Ign (Osc)	Mount	3541	17	3550	32	3565	86	-1

Appendix 1. LA-ICP-MS U-Pb Zircon Data

Sample Name	Zircon Phase	Format	Age (Ma)						%
			$^{207}Pb^*/^{206}Pb^*$	2σ	$^{207}Pb^*/^{235}U$	2σ	$^{206}Pb^*/^{238}U$	2σ	Discordance
MB120-13E1	Ign (Osc)	Mount	3568	15	3562	25	3550	64	1
MB120-13E2	Ign (Osc)	Mount	3573	15	3557	25	3528	63	1
MB120-15A1	Ign (Osc)	Mount	3581	15	3536	26	3457	67	4
MB120-15A2	Metamorphic	Mount	3313	15	3288	27	3248	68	2
MB120-15B1	Ign (Core)	Mount	3583	15	3524	24	3421	60	5
MB120-15C1	Metamorphic	Mount	3326	22	3134	26	2844	52	17
MB120-15C2	Metamorphic	Mount	3132	22	2993	23	2790	45	12
MB120-15B2	Ign (Osc)	Mount	3557	15	3535	28	3496	73	2
MB120-15B3	Ign (Osc)	Mount	3519	15	3479	28	3410	73	3
MB138B2-2	Ign (Osc)	TS	3029	16	2668	20	2218	36	37
MB138B2-3	Ign (Osc)	TS	2894	45	2290	32	1677	32	73
MB138B2-6	Ign (Osc)	TS	2568	27	2176	39	1785	63	44
MB138B2-9A	Amb	TS	3589	15	3593	26	3602	67	0
MB138B2-9B	Amb	TS	3558	15	3555	26	3549	68	0
MB138B2-12	Ign (Core)	TS	3844	14	3826	26	3793	72	1
MB138B2-14A	Metamorphic	TS	3417	16	3431	27	3455	68	-1
MB138B2-14B	Ign (Osc)	TS	3202	18	2499	29	1729	45	85
MB138B2-15	Ign (Core)	TS	3362	15	3012	23	2517	46	34
MB138B2-15B	Ign (Core)	TS	3626	16	3438	25	3125	59	16
MB138B2-18B	Ign (Core)	TS	3829	15	3849	32	3886	89	-1
MB167S1-10	Ign (Osc)	TS	3348	17	3197	32	2962	75	13
MB167S1-C13	Ign (Core)	TS	3383	17	3328	30	3236	74	5
MB167S1-C14	Ign (Core)	TS	3343	19	3206	32	2991	74	12
MB167S1-A1	Metamorphic	TS	3141	47	2780	46	2310	74	36
MB167S1-A2	Ign (Core)	TS	3367	17	3101	29	2708	63	24

Appendix 1. LA-ICP-MS U-Pb Zircon Data

Sample Name	Zircon Phase	Format	Age (Ma)						%
			$^{207}Pb^*/^{206}Pb^*$	2σ	$^{207}Pb^*/^{235}U$	2σ	$^{206}Pb^*/^{238}U$	2σ	Discordance
MB167S1-E	Metamorphic	TS	3046	21	2635	36	2134	67	43
MB167S1-J	Metamorphic	TS	3128	69	2967	65	2735	120	14
MB185-3A	Ign (Core)	TS	3371	17	3313	21	3219	48	4.7
MB185-3B	Ign (Osc)	TS	3353	18	3320	24	3264	55	2.7
MB185-4-2	Ign (Core)	TS	3373	17	3256	24	3070	55	9.9
MB185-7	Ign (Osc)	TS	3377	27	3214	47	2958	108	14.2

Appendix 2. LA-ICP-MS Secondary Reference Material Data Tables

Sample Name		^{206}Pb (cps)	^{204}Pb (cps)	$^{206}Pb/^{204}Pb$	$^{207}Pb/^{206}Pb$	2σ	$^{207}Pb/^{235}U$	2σ	$^{206}Pb/^{238}U$	2σ	ρ
MB07	OG1-1	189929	9	20109	0.29897	0.00332	29.68724	0.83782	0.72018	0.01869	0.91941
MB07	OG1-2	153613	7	22005	0.29816	0.00350	28.50646	0.77101	0.69341	0.01689	0.90072
MB07	OG1-3	251167	12	20570	0.29789	0.00343	28.94756	0.90386	0.70477	0.02046	0.92974
MB07	OG1-4	435224	0	1187643	0.29646	0.00330	29.83668	0.90624	0.72993	0.02063	0.93061
MB167	OG1-1	756249	68	11102	0.29913	0.00324	29.19910	0.96819	0.70795	0.02218	0.94499
MB167	OG1-2	277845	13	21642	0.29868	0.00325	28.99326	0.89445	0.70402	0.02033	0.93593
MB185	OG1-1	258418	0		0.29923	0.00328	29.39225	0.69600	0.71240	0.01496	0.88662
MB185	OG1-2	325919	1	401287	0.29910	0.00325	29.33694	0.65636	0.71137	0.01392	0.87429
MB185	OG1-3	637230	1	750181	0.29659	0.00321	29.28775	0.68406	0.71618	0.01483	0.88641
MB12S1	OG1-1	297312	11	27969	0.30099	0.00319	28.95522	0.97529	0.69772	0.02230	0.94905
MB12S1	OG1-2	274333	12	22794	0.30076	0.00318	29.02089	0.89696	0.69983	0.02033	0.93975
MB12S1	OG1-3	353697	7	52730	0.29831	0.00315	29.06269	0.92226	0.70660	0.02115	0.94310
MB12S1	OG1-4	348731	1	606738	0.29849	0.00312	29.26818	0.87004	0.71115	0.01979	0.93593
MB12S2	OG1-1	214776	33	6419	0.29936	0.00350	29.87191	1.56016	0.72371	0.03684	0.97467
MB12S2	OG1-2	312035	36	8738	0.29742	0.00333	29.42613	1.50307	0.71755	0.03576	0.97569
MB12S2	OG1-3	263205	19	13834	0.29684	0.00330	29.10506	1.51147	0.71112	0.03607	0.97683
MB47B	OG1-1	264856	14	18318	0.29895	0.00322	29.12306	0.66668	0.70653	0.01428	0.88260
MB47B	OG1-2	205606	19	10691	0.29870	0.00326	29.38680	0.85579	0.71353	0.01927	0.92716
MB47B	OG1-3	245637	20	12137	0.29687	0.00321	28.80088	0.64914	0.70362	0.01392	0.87770
MB54B	OG1-1	495786	41	12018	0.29140	0.00286	25.01299	0.57573	0.62255	0.01296	0.90463
MB54B	OG1-2	351310	38	9137	0.29971	0.00289	29.03732	0.73794	0.70268	0.01653	0.92543
MB54B	OG1-3	429871	53	8157	0.30047	0.00288	29.28514	0.85517	0.70689	0.01950	0.94448
MB54B	OG1-4	671046	54	12357	0.29987	0.00287	29.16065	0.73793	0.70527	0.01652	0.92563
MB54B	OG1-5	449081	49	9099	0.29896	0.00289	29.20255	0.77814	0.70845	0.01760	0.93209
MB73A1	OG1-1	279593	22	12823	0.30041	0.00335	29.43023	0.95984	0.71053	0.02178	0.93975
MB73A1	OG1-2	239678	22	10710	0.29843	0.00334	29.19800	0.92748	0.70959	0.02109	0.93585

Appendix 2. LA-ICP-MS Secondary Reference Material Data Tables

Sample Name		^{206}Pb (cps)	^{204}Pb (cps)	$^{206}Pb/^{204}Pb$	$^{207}Pb/^{206}Pb$	2σ	$^{207}Pb/^{235}U$	2σ	$^{206}Pb/^{238}U$	2σ	ρ
MB76C	OG1-1	502036	124	4050	0.29778	0.00500	28.55340	1.06261	0.69545	0.02309	0.89228
MB76C	OG1-2	403714	105	3829	0.29612	0.00501	28.50606	0.98147	0.69818	0.02094	0.87111
ID	OG1-1	178394	102	1755	0.29790	0.00321	28.67886	0.74178	0.69822	0.01642	0.90930
ID	OG1-2	209375	90	2327	0.29801	0.00317	28.81239	0.84802	0.70121	0.01925	0.93251
MB103	OG1-3	453679	165	2741	0.29741	0.00317	29.11745	0.85401	0.71006	0.01941	0.93183
MB103	OG1-4	441095	59	7482	0.29701	0.00315	28.85320	0.78821	0.70456	0.01774	0.92179
MB103	OG1-5	270822	48	5656	0.29910	0.00316	29.57640	0.82286	0.71719	0.01846	0.92524
MB103	OG1-6	473727	37	12663	0.29718	0.00313	29.51846	0.83846	0.72040	0.01901	0.92890
MB103	OG1-7	155639	6	26460	0.29846	0.00317	27.96928	0.78753	0.67965	0.01773	0.92635
MB120S2	OG1-8	196623	9	21280	0.29704	0.00318	23.13769	0.73756	0.56495	0.01696	0.94203
MB120S2	OG1-9	295282	49	6008	0.29962	0.00316	29.33236	0.82258	0.71003	0.01845	0.92648
AG2	OG1-10	221751	128	1735	0.30244	0.00325	29.00671	0.78895	0.69560	0.01738	0.91860
AG2	OG1-11	239140	62	3846	0.29616	0.00314	24.99543	1.00048	0.61211	0.02362	0.96425
AG2	OG1-12	293328	46	6428	0.29891	0.00317	30.22775	0.90415	0.73344	0.02051	0.93492
AG2	OG1-15	211261	67	3145	0.29870	0.00318	29.70674	0.77510	0.72131	0.01718	0.91311
MB21B	OG-1-16	494441	57	8637	0.29502	0.00343	28.84628	1.31177	0.70915	0.03118	0.96682
MB21B	OG1-1	321960	159	2030	0.30042	0.00332	28.97937	0.86369	0.69962	0.01937	0.92875
MB21B	OG1-2	339355	16	20881	0.29697	0.00314	28.78407	0.83663	0.70298	0.01903	0.93128
MB120S1	OG1-3	386163	55	6971	0.29631	0.00314	29.07157	0.84686	0.71157	0.01931	0.93143
MB120S1	OG1-4	166828	110	1513	0.29903	0.00319	28.77305	0.81690	0.69786	0.01837	0.92695
MB120S1	OG1-5	269996	37	7330	0.29728	0.00314	28.63310	0.83392	0.69854	0.01896	0.93201
MB108A	OG1-1	328529	60	5489	0.29982	0.00323	29.22990	0.94596	0.70706	0.02158	0.94313
MB108A	OG1-2	312904	51	6149	0.29987	0.00318	29.55547	0.88202	0.71483	0.01994	0.93465
MB108A	OG1-3	307929	109	2821	0.29990	0.00331	29.67916	0.82188	0.71774	0.01823	0.91728
MB108A	OG1-4	425272	111	3838	0.29803	0.00321	28.91483	0.98220	0.70367	0.02267	0.94827
MB108A	OG1-5	411173	16	25111	0.29854	0.00316	29.51610	0.97369	0.71706	0.02240	0.94700

Appendix 2. LA-ICP-MS Secondary Reference Material Data Tables

Sample Name		^{206}Pb (cps)	^{204}Pb (cps)	$^{206}Pb/^{204}Pb$	$^{207}Pb/^{206}Pb$	2σ	$^{207}Pb/^{235}U$	2σ	$^{206}Pb/^{238}U$	2σ	ρ
MB108A	OG1-6	620424	8	77253	0.29869	0.00315	29.37511	0.87775	0.71327	0.01994	0.93558
MB108B1 TS	OG1-1	246058	46	5400	0.30048	0.00336	29.06145	1.19417	0.70146	0.02773	0.96221
MB108B1 TS	OG1-2	290144	95	3050	0.29835	0.00335	27.94139	1.15651	0.67922	0.02706	0.96239
MB108B1 TS	OG1-3	298229	152	1957	0.29152	0.00357	28.41425	1.28808	0.70691	0.03086	0.96285
MB108B1 TS	OG1-4	534360	89	6006	0.29467	0.00325	28.86106	1.18401	0.71036	0.02807	0.96326
MB108B1 TS	OG1-5	303945	231	1313	0.29825	0.00329	29.75979	1.42142	0.72367	0.03363	0.97293
MB108B1 TS	OG1-6	300572	107	2818	0.29749	0.00332	29.85935	1.22090	0.72795	0.02863	0.96199
MB108B1 Mount	OG1-1	439322	40	11117	0.30075	0.00290	29.31048	0.87009	0.70684	0.01984	0.94577
MB108B1 Mount	OG1-2	350697	48	7311	0.30056	0.00290	29.26454	0.80631	0.70618	0.01822	0.93650
MB108B1 Mount	OG1-3	393608	56	7002	0.29930	0.00288	29.01484	0.80283	0.70310	0.01824	0.93769
MB108B1 Mount	OG1-4	372592	70	5319	0.29752	0.00286	28.74606	0.75219	0.70074	0.01705	0.92990
MB108B1 Mount	OG1-5	322338	69	4648	0.29746	0.00289	29.13567	0.82214	0.71038	0.01882	0.93900
MB108B1 Mount	OG1-6	204855	82	2506	0.29886	0.00295	29.71847	0.78731	0.72121	0.01773	0.92775
MB120 Mount	OG-1	322461	58	5547	0.29968	0.00291	28.42417	0.72086	0.68791	0.01611	0.92361
MB120 Mount	OG1-2	434611	72	6024	0.29952	0.00292	28.55659	0.78188	0.69149	0.01770	0.93462
MB120 Mount	OG1-3	325956	66	4938	0.29867	0.00291	28.50532	0.74325	0.69219	0.01674	0.92769
MB120 Mount	OG1-4	438237	85	5168	0.29691	0.00289	28.16551	0.74359	0.68800	0.01689	0.92968
MB120 Mount	OG1-5	337830	67	5014	0.29831	0.00287	28.60687	0.71459	0.69551	0.01603	0.92266
MB138B2	OG1-1	545562	43	12546	0.29899	0.00289	29.62338	0.72994	0.71858	0.01629	0.91983
MB138B2	OG1-2	598684	57	10545	0.29492	0.00288	28.79489	0.70317	0.70813	0.01585	0.91641
MB138B2	OG1-3	387857	55	7088	0.29879	0.00288	29.45469	0.76117	0.71498	0.01714	0.92766
MB138B2	OG1-4	484549	64	7552	0.29706	0.00289	29.21580	0.70907	0.71329	0.01586	0.91631

Appendix 2. LA-ICP-MS Secondary Reference Material Data Tables

Sample Name		Age (Ma)						%
		$^{207}Pb^*/^{206}Pb^*$	2σ	$^{207}Pb^*/^{235}U$	2σ	$^{206}Pb^*/^{238}U$	2σ	Discordance
MB07	OG1-1	3465	17	3477	27	3497	70	-0.9
MB07	OG1-2	3461	18	3437	26	3396	64	1.9
MB07	OG1-3	3459	18	3452	30	3439	77	0.6
MB07	OG1-4	3452	17	3481	29	3533	76	-2.3
MB167	OG1-1	3466	17	3460	32	3451	83	0.4
MB167	OG1-2	3463	17	3453	30	3436	76	0.8
MB185	OG1-1	3466	17	3467	23	3468	56	0.0
MB185	OG1-2	3466	17	3465	22	3464	52	0.1
MB185	OG1-3	3453	17	3463	23	3482	55	-0.8
MB12S1	OG1-1	3475	16	3452	33	3412	84	1.9
MB12S1	OG1-2	3474	16	3454	30	3420	77	1.6
MB12S1	OG1-3	3461	16	3456	31	3446	79	0.5
MB12S1	OG1-4	3462	16	3463	29	3463	74	0.0
MB12S2	OG1-1	3467	18	3483	50	3510	136	-1.2
MB12S2	OG1-2	3457	17	3468	49	3487	133	-0.9
MB12S2	OG1-3	3454	17	3457	50	3463	134	-0.3
MB47B	OG1-1	3465	17	3458	22	3445	54	0.6
MB47B	OG1-2	3464	17	3467	28	3472	72	-0.2
MB47B	OG1-3	3454	17	3447	22	3434	52	0.6
MB54B	OG1-1	3425	15	3309	22	3120	51	9.8
MB54B	OG1-2	3469	15	3455	25	3431	62	1.1
MB54B	OG1-3	3473	15	3463	28	3447	73	0.8
MB54B	OG1-4	3470	15	3459	25	3441	62	0.8
MB54B	OG1-5	3465	15	3460	26	3453	66	0.4
MB73A1	OG1-1	3472	17	3468	32	3460	82	0.3
MB73A1	OG1-2	3462	17	3460	31	3457	79	0.1

Appendix 2. LA-ICP-MS Secondary Reference Material Data Tables

Sample Name		Age (Ma)						%
		$^{207}Pb^*/^{206}Pb^*$	2σ	$^{207}Pb^*/^{235}U$	2σ	$^{206}Pb^*/^{238}U$	2σ	Discordance
MB76C	OG1-1	3459	26	3438	36	3403	87	1.6
MB76C	OG1-2	3450	26	3437	33	3414	79	1.1
ID	OG1-1	3459	17	3443	25	3414	62	1.3
ID	OG1-2	3460	16	3447	28	3425	73	1.0
MB103	OG1-3	3457	16	3457	28	3459	73	-0.1
MB103	OG1-4	3455	16	3449	26	3438	67	0.5
MB103	OG1-5	3466	16	3473	27	3486	69	-0.6
MB103	OG1-6	3456	16	3471	28	3498	71	-1.2
MB103	OG1-7	3462	16	3418	27	3343	68	3.6
MB120S2	OG1-8	3455	16	3233	31	2887	70	19.7
MB120S2	OG1-9	3468	16	3465	27	3459	69	0.3
AG2	OG1-10	3483	17	3454	26	3404	66	2.3
AG2	OG1-11	3450	16	3308	38	3078	94	12.1
AG2	OG1-12	3465	16	3494	29	3546	76	-2.3
AG2	OG1-15	3463	16	3477	25	3501	64	-1.1
MB21B	OG-1-16	3444	18	3448	44	3455	117	-0.3
MB21B	OG1-1	3472	17	3453	29	3419	73	1.6
MB21B	OG1-2	3454	16	3446	28	3432	72	0.7
MB120S1	OG1-3	3451	16	3456	28	3464	72	-0.4
MB120S1	OG1-4	3465	16	3446	27	3413	69	1.5
MB120S1	OG1-5	3456	16	3441	28	3415	72	1.2
MB108A	OG1-1	3469	17	3461	31	3447	81	0.6
MB108A	OG1-2	3470	16	3472	29	3477	75	-0.2
MB108A	OG1-3	3470	17	3476	27	3488	68	-0.5
MB108A	OG1-4	3460	17	3451	33	3435	85	0.7
MB108A	OG1-5	3463	16	3471	32	3485	84	-0.6

Appendix 2. LA-ICP-MS Secondary Reference Material Data Tables

Sample Name		Age (Ma)						%
		$^{207}Pb^*/^{206}Pb^*$	2σ	$^{207}Pb^*/^{235}U$	2σ	$^{206}Pb^*/^{238}U$	2σ	Discordance
MB108A	OG1-6	3463	16	3466	29	3471	75	-0.2
MB108B1 TS	OG1-1	3473	17	3456	40	3426	104	1.4
MB108B1 TS	OG1-2	3462	17	3417	40	3341	103	3.6
MB108B1 TS	OG1-3	3426	19	3433	44	3447	115	-0.6
MB108B1 TS	OG1-4	3442	17	3449	39	3460	105	-0.5
MB108B1 TS	OG1-5	3461	17	3479	46	3510	125	-1.4
MB108B1 TS	OG1-6	3457	17	3482	39	3526	106	-1.9
MB108B1 Mount	OG1-1	3474	15	3464	29	3447	75	0.8
MB108B1 Mount	OG1-2	3473	15	3462	27	3444	68	0.8
MB108B1 Mount	OG1-3	3467	15	3454	27	3432	69	1.0
MB108B1 Mount	OG1-4	3457	15	3445	25	3423	64	1.0
MB108B1 Mount	OG1-5	3457	15	3458	27	3460	71	-0.1
MB108B1 Mount	OG1-6	3464	15	3478	26	3501	66	-1.0
MB120 Mount	OG-1	3469	15	3434	25	3375	61	2.8
MB120 Mount	OG1-2	3468	15	3438	27	3388	67	2.3
MB120 Mount	OG1-3	3463	15	3437	25	3391	63	2.1
MB120 Mount	OG1-4	3454	15	3425	26	3375	64	2.3
MB120 Mount	OG1-5	3461	15	3440	24	3404	61	1.7
MB138B2	OG1-1	3465	15	3474	24	3491	61	-0.7
MB138B2	OG1-2	3444	15	3447	24	3451	60	-0.2
MB138B2	OG1-3	3464	15	3469	25	3477	64	-0.4
MB138B2	OG1-4	3455	15	3461	24	3471	59	-0.5

Appendix 2.1 LA-ICP-MS Secondary reference material figures

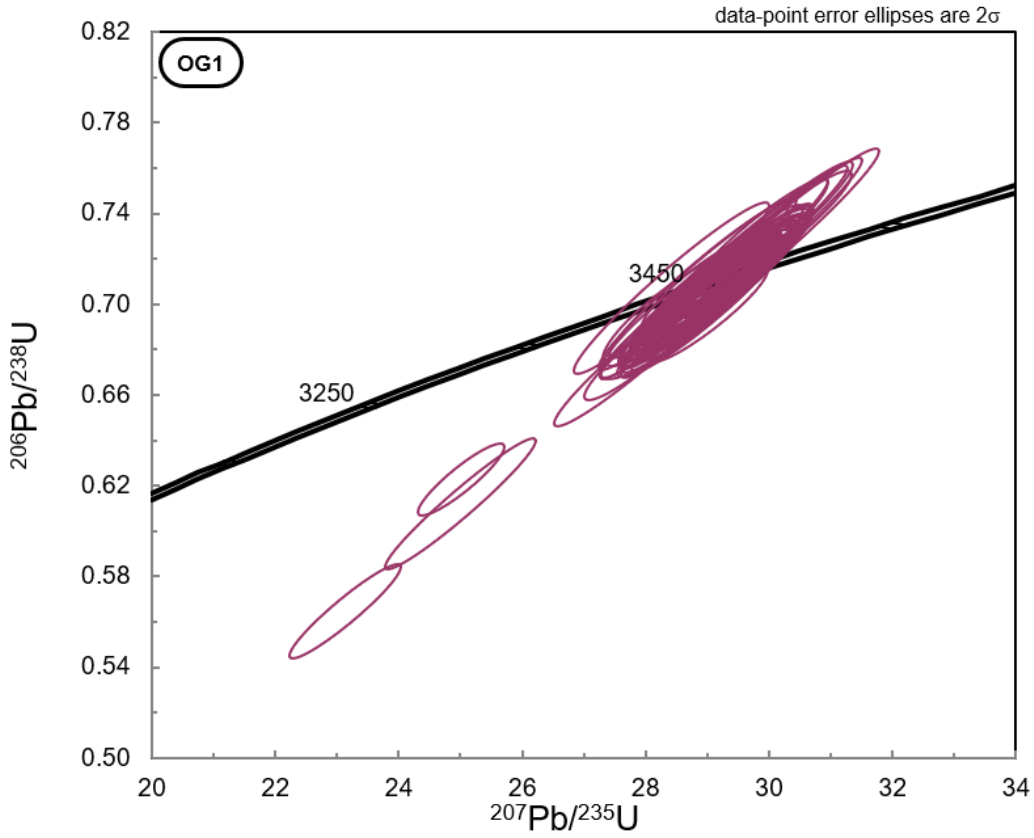

Appendix 2.1 LA-ICP-MS Secondary reference material figures

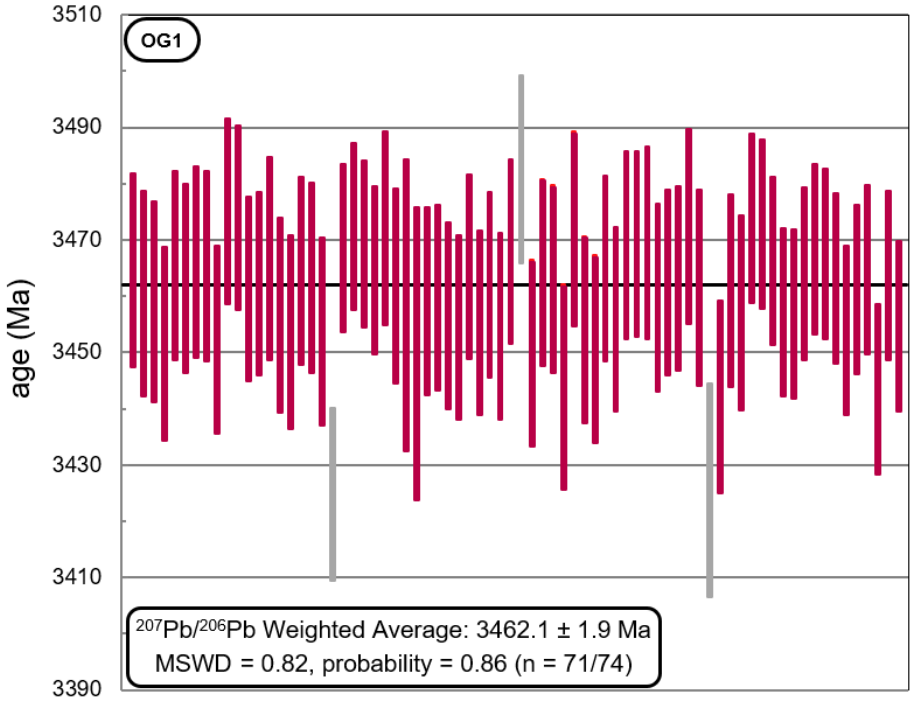

Appendix 3. LASS Data Tables

Grain Spot	Zirc. Phase	$^{206}Pb/^{204}Pb$	$^{207}Pb/^{235}U$	2σ	$^{206}Pb/^{238}U$	2σ	ρ	Age (Ma)						%
								$^{207}Pb/^{206}Pb$	2σ	$^{207}Pb/^{235}U$	2σ	$^{206}Pb/^{238}U$	2σ	Disc.
108A_13A - 1	ign	1956	38.4	1.6	0.784	0.031	0.93	3739	14	3730	40	3730	110	0.0
108A_13A - 2	amb	7582	41.3	1.7	0.838	0.034	0.98	3743	13	3798	41	3919	120	-3.1
108A_14B - 1	amb	5507	28.5	1.2	0.689	0.026	0.92	3473	17	3434	40	3378	98	1.7
108A_14B - 2	amb	6884	28.4	1.1	0.682	0.025	0.73	3486	18	3432	40	3351	98	2.4
108A_14B - 3	amb	8086	34.7	1.4	0.729	0.027	0.84	3693	13	3629	39	3528	100	2.9
108A_15B - 1	Ign	2063	33.3	1.3	0.724	0.028	0.59	3636	15	3588	40	3509	100	2.2
108A_15B - 2	ign	4476	34.8	1.4	0.747	0.028	0.87	3658	15	3630	40	3596	100	0.9
108A_16B - 1	ign	2817	33.0	1.3	0.722	0.028	0.93	3636	14	3582	39	3499	110	2.4
108A_16C - 1	ign	3739	36.6	1.5	0.753	0.029	0.94	3723	14	3679	40	3616	110	1.7
108A_19C - 1	ign	4059	35.0	1.4	0.733	0.027	0.90	3701	13	3639	39	3544	100	2.7
108A_19C - 2	meta	5375	27.8	1.1	0.682	0.025	0.70	3459	14	3412	39	3351	97	1.8
108A_19C - 3	ign	4019	33.1	1.3	0.737	0.027	0.90	3608	13	3585	41	3558	100	0.8
108A_21B - 1	ign	5085	37.9	1.5	0.776	0.029	0.93	3736	13	3717	39	3702	110	0.4
108A_21C - 1	ign	6031	37.5	1.5	0.762	0.028	0.32	3746	13	3706	39	3651	100	1.5
108A_21C - 2	ign	5077	33.8	1.3	0.721	0.027	0.89	3673	13	3604	39	3497	100	3.1
108A_22B - 1	ign	6486	36.3	1.4	0.757	0.028	0.78	3705	14	3675	39	3633	100	1.2
108A_23B - 1	ign	5563	36.8	1.5	0.748	0.028	0.94	3747	13	3687	40	3598	110	2.5
108A_23B - 2	amb	5508	37.8	1.5	0.767	0.028	0.89	3747	13	3715	39	3670	100	1.2
108A_23C - 1	ign	2932	36.5	1.4	0.769	0.029	0.78	3694	14	3680	39	3677	100	0.1
108A_23C - 2	amb	7453	34.9	1.4	0.738	0.028	0.91	3683	13	3635	39	3563	100	2.0
108A_27A - 1	ign	5952	29.3	1.2	0.677	0.026	0.79	3542	17	3461	40	3334	98	3.8
108A_27A - 2	ign	6561	36.7	1.5	0.765	0.028	0.90	3700	13	3684	39	3666	110	0.5
108A_36E - 1	ign	2469	36.3	1.4	0.749	0.028	0.79	3717	14	3675	39	3604	100	2.0
108A_36E - 2	ign	2555	38.0	1.5	0.769	0.029	0.43	3745	13	3720	39	3677	100	1.2
108A_36E - 3	ign	6352	37.2	1.5	0.766	0.029	0.91	3727	13	3701	41	3666	100	0.9
108A_38B - 1	ign	2819	35.0	1.4	0.756	0.030	0.95	3649	14	3637	39	3625	110	0.3

Appendix 3. LASS Data Tables

Grain Spot	Zirc. Phase	$^{206}Pb/^{204}Pb$	$^{207}Pb/^{235}U$	2σ	$^{206}Pb/^{238}U$	2σ	ρ	Age (Ma)						%
								$^{207}Pb/^{206}Pb$	2σ	$^{207}Pb/^{235}U$	2σ	$^{206}Pb/^{238}U$	2σ	Disc.
108A_38B - 2	ign	2943	36.7	1.5	0.765	0.029	0.79	3701	14	3686	39	3663	100	0.6
108A_40B - 1	ign	4486	37.2	1.5	0.765	0.030	0.96	3718	14	3697	40	3662	110	1.0
108A_40B - 2	ign	5636	36.8	1.5	0.743	0.028	0.82	3750	14	3689	39	3579	100	3.1
108A_42B - 1	ign	3522	34.0	1.4	0.730	0.028	0.88	3645	16	3610	40	3533	110	2.2
108A_42B - 2	ign	4682	36.0	1.4	0.748	0.028	0.64	3698	16	3667	39	3600	100	1.9
108A_46B - 1	ign	5667	37.1	1.5	0.753	0.028	0.85	3738	13	3695	39	3619	100	2.1
108A_46B - 2	ign	7239	37.6	1.5	0.769	0.028	0.76	3732	13	3710	39	3677	100	0.9
108A_46B - 3	ign	5994	34.2	1.5	0.762	0.031	0.94	3596	17	3611	43	3646	110	-1.0
108A_50C - 1	ign	4720	37.8	1.5	0.779	0.029	0.60	3717	13	3713	40	3716	100	-0.1
108A_50C - 2	ign	6027	37.6	1.5	0.767	0.028	0.80	3732	13	3709	39	3668	100	1.1
108A_50C - 3	ign	9067	36.5	1.4	0.751	0.028	0.84	3721	13	3680	39	3610	100	1.9
108A_50C - 4	ign	3251	37.0	1.5	0.768	0.029	0.91	3704	13	3692	39	3674	100	0.5
108A_51B - 1	amb	1533	34.5	1.4	0.736	0.028	0.73	3664	16	3624	40	3553	100	2.0
108A_51B - 2	amb	8281	37.8	1.5	0.771	0.028	0.89	3733	13	3715	39	3684	100	0.8
108A_53A - 1	ign	3013	36.2	1.4	0.752	0.028	0.76	3700	13	3671	39	3614	100	1.6
108A_60C - 1	ign	3161	35.0	1.5	0.743	0.032	0.96	3661	15	3638	41	3577	120	1.7
108A_60C - 2	ign	3662	36.0	1.4	0.749	0.028	0.88	3701	13	3667	39	3603	100	1.8
108A_61A - 1	ign	4574	37.3	1.5	0.765	0.028	0.82	3721	13	3702	39	3662	100	1.1
108A_61A - 2	ign	7825	37.7	1.5	0.772	0.029	0.89	3720	13	3711	39	3686	110	0.7
108A_61B - 1	meta	7232	35.4	1.4	0.747	0.028	0.88	3675	14	3649	39	3596	100	1.5
108A_65C - 1	ign	3525	34.8	1.5	0.752	0.029	0.93	3638	17	3629	42	3615	110	0.4
108A_67C - 1	ign	2481	39.0	1.6	0.815	0.032	0.66	3691	15	3742	42	3838	110	-2.5
108A_67C - 2	ign	2449	38.4	1.5	0.790	0.030	0.92	3714	14	3730	40	3753	110	-0.6
108A_67C - 3	amb	5456	33.1	1.3	0.725	0.028	0.92	3617	13	3582	39	3513	100	2.0
108A_68A - 1	ign	3745	37.5	1.5	0.764	0.029	0.86	3732	13	3707	39	3656	100	1.4
108A_69A - 1	amb	4444	34.2	1.4	0.754	0.029	0.96	3607	13	3614	39	3622	110	-0.2

Appendix 3. LASS Data Tables

Grain Spot	Zirc. Phase	$^{206}Pb/^{204}Pb$	$^{207}Pb/^{235}U$	2σ	$^{206}Pb/^{238}U$	2σ	ρ	Age (Ma)						%
								$^{207}Pb/^{206}Pb$	2σ	$^{207}Pb/^{235}U$	2σ	$^{206}Pb/^{238}U$	2σ	Disc.
108A_69A - 2	amb	5589	33.4	1.3	0.713	0.027	0.94	3657	13	3592	40	3468	100	3.6
108A_14C - 1	ign	7321	34.7	1.4	0.721	0.027	0.79	3689	15	3630	39	3500	100	3.7
108A_11B - 1	meta	2668	36.6	1.7	0.757	0.033	0.97	3695	17	3675	44	3627	120	1.3
108A_31A - 1	meta	9273	32.8	1.3	0.708	0.027	0.78	3633	13	3575	40	3450	100	3.6
108A_31A - 2	ign	1864	36.1	1.4	0.740	0.029	0.80	3718	18	3670	39	3571	110	2.8
108A_46A - 1	amb	2529	37.0	1.5	0.756	0.029	0.91	3722	17	3690	39	3629	100	1.7
108A_46A - 2	meta	37675	36.3	1.4	0.749	0.028	0.56	3706	15	3674	39	3603	100	2.0
108A_46A - 3	amb	8247	38.0	1.5	0.767	0.028	0.90	3742	13	3720	39	3668	100	1.4

Appendix 3. LASS Data Tables

Grain Spot	Zirc. Phase	$^{176}Hf/^{177}Hf$	2σ	$^{176}Lu/^{177}Hf$	2σ	$^{176}Yb/^{177}Hf$	2σ	$^{176}Hf/^{177}Hf_i$	$2\sigma_i$	εHf_0	$2\sigma_0$	εHf_i	$2\sigma_i$	Assigned Age	2σ	Th/U
108A_13A - 1	ign	0.280283	0.000042	0.000490	0.000110	0.0159	0.0038	0.280291	0.000043	-88.2	1.5	-3.5	1.6	3740.7	2.3	0.42
108A_13A - 2	amb	0.280328	0.000065	0.001600	0.000110	0.0549	0.0044	0.280335	0.000065	-86.6	2.3	-4.8	2.4	3740.7	2.3	0.83
108A_14B - 1	amb	0.280293	0.000043	0.001472	0.000028	0.0485	0.0008	0.280301	0.000043	-87.8	1.6	-5.7	1.6	3740.7	2.3	0.73
108A_14B - 2	amb	0.280296	0.000038	0.001260	0.000110	0.0415	0.0035	0.280304	0.000039	-87.7	1.4	-5.1	1.4	3740.7	2.3	0.70
108A_14B - 3	amb	0.280326	0.000044	0.001380	0.000120	0.0470	0.0042	0.280334	0.000045	-86.7	1.6	-4.3	1.7	3740.7	2.3	0.75
108A_15B - 1	Ign	0.280261	0.000043	0.000560	0.000100	0.0180	0.0035	0.280269	0.000044	-89.0	1.6	-4.5	1.6	3740.7	2.3	0.42
108A_15B - 2	ign	0.280262	0.000046	0.000590	0.000110	0.0190	0.0036	0.280270	0.000047	-88.9	1.7	-4.5	1.7	3740.7	2.3	0.46
108A_16B - 1	ign	0.280313	0.000055	0.001070	0.000230	0.0351	0.0077	0.280322	0.000057	-87.1	2.0	-3.9	2.1	3740.7	2.3	0.53
108A_16C - 1	ign	0.280211	0.000040	0.000319	0.000018	0.0098	0.0007	0.280219	0.000040	-90.7	1.5	-5.7	1.5	3740.7	2.3	0.22
108A_19C - 1	ign	0.280332	0.000058	0.001004	0.000030	0.0335	0.0010	0.280340	0.000058	-86.5	2.1	-3.1	2.1	3740.7	2.3	0.71
108A_19C - 2	meta	0.280258	0.000046	0.000585	0.000020	0.0174	0.0005	0.280267	0.000046	-89.0	1.7	-4.6	1.7	3740.7	2.3	0.31
108A_19C - 3	ign	0.280246	0.000036	0.000462	0.000012	0.0147	0.0005	0.280255	0.000036	-89.5	1.3	-4.7	1.4	3740.7	2.3	0.44
108A_21B - 1	ign	0.280329	0.000050	0.001430	0.000110	0.0485	0.0035	0.280339	0.000051	-86.5	1.8	-4.3	1.9	3740.7	2.3	0.79
108A_21C - 1	ign	0.280343	0.000061	0.002000	0.000140	0.0687	0.0056	0.280353	0.000062	-86.0	2.2	-5.2	2.2	3740.7	2.3	0.82
108A_21C - 2	ign	0.280345	0.000046	0.001756	0.000036	0.0589	0.0017	0.280355	0.000046	-85.9	1.7	-4.5	1.7	3740.7	2.3	0.74
108A_22B - 1	ign	0.280272	0.000049	0.001040	0.000083	0.0358	0.0034	0.280282	0.000049	-88.5	1.8	-5.3	1.8	3740.7	2.3	0.65
108A_23B - 1	ign	0.280329	0.000044	0.001140	0.000075	0.0375	0.0024	0.280339	0.000044	-86.5	1.6	-3.5	1.6	3740.7	2.3	0.69
108A_23B - 2	amb	0.280283	0.000053	0.001440	0.000100	0.0484	0.0032	0.280293	0.000053	-88.1	1.9	-5.9	2.0	3740.7	2.3	0.77
108A_23C - 1	ign	0.280245	0.000054	0.000429	0.000019	0.0134	0.0007	0.280255	0.000054	-89.5	1.9	-4.7	2.0	3740.7	2.3	0.43
108A_23C - 2	amb	0.280335	0.000051	0.001364	0.000038	0.0463	0.0011	0.280346	0.000051	-86.2	1.8	-3.8	1.9	3740.7	2.3	0.76
108A_27A - 1	ign	0.280311	0.000052	0.001125	0.000034	0.0326	0.0010	0.280322	0.000052	-87.1	1.9	-4.1	1.9	3740.7	2.3	0.36
108A_27A - 2	ign	0.280300	0.000050	0.001640	0.000220	0.0530	0.0071	0.280311	0.000052	-87.5	1.8	-5.8	1.9	3740.7	2.3	0.64
108A_36E - 1	ign	0.280267	0.000047	0.000919	0.000019	0.0304	0.0006	0.280278	0.000047	-88.7	1.7	-5.1	1.7	3740.7	2.3	0.63
108A_36E - 2	ign	0.280284	0.000043	0.000870	0.000099	0.0287	0.0032	0.280295	0.000044	-88.1	1.6	-4.4	1.6	3740.7	2.3	0.58
108A_36E - 3	ign	0.280298	0.000058	0.000990	0.000072	0.0328	0.0022	0.280309	0.000058	-87.6	2.1	-4.2	2.1	3740.7	2.3	0.62
108A_38B - 1	ign	0.280241	0.000048	0.000717	0.000025	0.0235	0.0008	0.280252	0.000048	-89.6	1.7	-5.5	1.8	3740.7	2.3	0.51

Appendix 3. LASS Data Tables

Grain Spot	Zirc. Phase	$^{176}Hf/^{177}Hf$	2σ	$^{176}Lu/^{177}Hf$	2σ	$^{176}Yb/^{177}Hf$	2σ	$^{176}Hf/^{177}Hf_i$	$2\sigma_i$	εHf_0	$2\sigma_0$	εHf_i	$2\sigma_i$	Assigned Age	2σ	Th/U
108A_38B - 2	ign	0.280288	0.000052	0.000736	0.000039	0.0234	0.0013	0.280300	0.000052	-87.9	1.9	-3.9	1.9	3740.7	2.3	0.46
108A_40B - 1	ign	0.280305	0.000052	0.001040	0.000110	0.0357	0.0038	0.280316	0.000053	-87.3	1.9	-4.1	1.9	3740.7	2.3	0.73
108A_40B - 2	ign	0.280302	0.000051	0.001120	0.000160	0.0379	0.0054	0.280314	0.000052	-87.4	1.8	-4.3	1.9	3740.7	2.3	0.71
108A_42B - 1	ign	0.280258	0.000059	0.000795	0.000063	0.0269	0.0019	0.280270	0.000059	-88.9	2.1	-5.1	2.2	3740.7	2.3	0.60
108A_42B - 2	ign	0.280256	0.000049	0.000689	0.000085	0.0227	0.0026	0.280268	0.000049	-89.0	1.8	-4.9	1.8	3740.7	2.3	0.51
108A_46B - 1	ign	0.280312	0.000058	0.001580	0.000220	0.0529	0.0074	0.280325	0.000060	-87.0	2.1	-5.1	2.2	3740.7	2.3	0.72
108A_46B - 2	ign	0.280267	0.000043	0.001470	0.000260	0.0491	0.0088	0.280280	0.000047	-88.6	1.6	-6.5	1.7	3740.7	2.3	0.69
108A_46B - 3	ign	0.280246	0.000047	0.000870	0.000160	0.0282	0.0055	0.280259	0.000048	-89.3	1.7	-5.7	1.8	3740.7	2.3	0.45
108A_50C - 1	ign	0.280279	0.000053	0.000998	0.000069	0.0335	0.0026	0.280292	0.000053	-88.2	1.9	-4.8	1.9	3740.7	2.3	0.64
108A_50C - 2	ign	0.280321	0.000055	0.001660	0.000140	0.0560	0.0052	0.280334	0.000056	-86.7	2.0	-5.0	2.0	3740.7	2.3	0.79
108A_50C - 3	ign	0.280239	0.000030	0.000381	0.000059	0.0122	0.0021	0.280252	0.000030	-89.6	1.1	-4.6	1.2	3740.7	2.3	0.24
108A_50C - 4	ign	0.280292	0.000041	0.000627	0.000038	0.0203	0.0015	0.280306	0.000041	-87.7	1.5	-3.4	1.5	3740.7	2.3	0.50
108A_51B - 1	amb	0.280231	0.000055	0.000493	0.000008	0.0158	0.0004	0.280244	0.000055	-89.9	2.0	-5.2	2.0	3740.7	2.3	0.45
108A_51B - 2	amb	0.280299	0.000046	0.002830	0.000220	0.0966	0.0073	0.280313	0.000049	-87.4	1.7	-8.8	1.8	3740.7	2.3	0.97
108A_53A - 1	ign	0.280336	0.000032	0.000974	0.000031	0.0316	0.0009	0.280351	0.000032	-86.1	1.2	-2.6	1.2	3740.7	2.3	0.64
108A_60C - 1	ign	0.280269	0.000054	0.000980	0.000110	0.0315	0.0036	0.280284	0.000055	-88.4	1.9	-5.1	2.0	3740.7	2.3	0.45
108A_60C - 2	ign	0.280291	0.000043	0.000982	0.000078	0.0331	0.0028	0.280306	0.000043	-87.7	1.6	-4.3	1.6	3740.7	2.3	0.61
108A_61A - 1	ign	0.280283	0.000039	0.001461	0.000041	0.0492	0.0012	0.280298	0.000039	-87.9	1.4	-5.8	1.5	3740.7	2.3	0.75
108A_61A - 2	ign	0.280344	0.000050	0.001392	0.000050	0.0469	0.0014	0.280359	0.000050	-85.8	1.8	-3.4	1.8	3740.7	2.3	0.73
108A_61B - 1	meta	0.280252	0.000034	0.000229	0.000001	0.0071	0.0001	0.280267	0.000034	-89.0	1.3	-3.7	1.3	3740.7	2.3	0.15
108A_65C - 1	ign	0.280247	0.000054	0.001210	0.000260	0.0391	0.0085	0.280262	0.000057	-89.2	1.9	-6.4	2.1	3740.7	2.3	0.56
108A_67C - 1	ign	0.280263	0.000037	0.000412	0.000044	0.0129	0.0014	0.280278	0.000037	-88.7	1.4	-3.8	1.4	3740.7	2.3	0.33
108A_67C - 2	ign	0.280237	0.000034	0.000522	0.000040	0.0169	0.0014	0.280253	0.000034	-89.5	1.3	-5.0	1.3	3740.7	2.3	0.46
108A_67C - 3	amb	0.280256	0.000048	0.000685	0.000057	0.0223	0.0018	0.280272	0.000048	-88.9	1.7	-4.7	1.8	3740.7	2.3	0.51
108A_68A - 1	ign	0.280252	0.000051	0.000874	0.000052	0.0272	0.0015	0.280268	0.000051	-89.0	1.8	-5.3	1.9	3740.7	2.3	0.40
108A_69A - 1	amb	0.280301	0.000053	0.000750	0.000110	0.0246	0.0039	0.280317	0.000054	-87.3	1.9	-3.3	2.0	3740.7	2.3	0.55

Appendix 3. LASS Data Tables

Grain Spot	Zirc. Phase	$^{176}Hf/^{177}Hf$	2σ	$^{176}Lu/^{177}Hf$	2σ	$^{176}Yb/^{177}Hf$	2σ	$^{176}Hf/^{177}Hf_i$	$2\sigma_i$	εHf_0	$2\sigma_0$	εHf_i	$2\sigma_i$	Assigned Age	2σ	Th/U
108A_69A - 2	amb	0.280278	0.000057	0.001236	0.000062	0.0405	0.0020	0.280295	0.000057	-88.1	2.1	-5.3	2.1	3740.7	2.3	0.63
108A_14C - 1	ign	0.280274	0.000072	0.001400	0.000170	0.0482	0.0051	0.280290	0.000073	-88.2	2.6	-5.9	2.6	3740.7	2.3	0.67
108A_11B - 1	meta	0.280297	0.000057	0.000660	0.000110	0.0222	0.0038	0.280314	0.000058	-87.4	2.1	-3.2	2.1	3740.7	2.3	0.22
108A_31A - 1	meta	0.280252	0.000056	0.000376	0.000003	0.0106	0.0001	0.280269	0.000056	-89.0	2.0	-4.0	2.0	3740.7	2.3	0.14
108A_31A - 2	ign	0.280222	0.000058	0.000458	0.000037	0.0146	0.0011	0.280239	0.000058	-90.0	2.1	-5.3	2.1	3740.7	2.3	0.42
108A_46A - 1	amb	0.280267	0.000044	0.000578	0.000069	0.0188	0.0024	0.280284	0.000044	-88.4	1.6	-4.0	1.6	3740.7	2.3	0.46
108A_46A - 2	meta	0.280221	0.000055	0.000241	0.000001	0.0073	0.0001	0.280238	0.000055	-90.1	2.0	-4.8	2.0	3740.7	2.3	0.15
108A_46A - 3	amb	0.280314	0.000061	0.001392	0.000084	0.0473	0.0024	0.280331	0.000061	-86.8	2.2	-4.4	2.2	3740.7	2.3	0.75

Appendix 4. LASS Secondary Reference Material Data Table

Grain Spot	$^{206}Pb/^{204}Pb$	$^{207}Pb/^{235}U$	2σ	$^{206}Pb/^{238}U$	2σ	ρ	Age (Ma)						%
							$^{207}Pb/^{206}Pb$	2σ	$^{207}Pb/^{235}U$	2σ	$^{206}Pb/^{238}U$	2σ	Disc.
MUN-1 - 1	N/A	N/A	N/A	N/A	N/A	N/A	N/A	N/A	N/A	N/A	N/A	N/A	N/A
MUN-1 - 2	N/A	N/A	N/A	N/A	N/A	N/A	N/A	N/A	N/A	N/A	N/A	N/A	N/A
MUN-1 - 3	N/A	N/A	N/A	N/A	N/A	N/A	N/A	N/A	N/A	N/A	N/A	N/A	N/A
MUN-1 - 4	N/A	N/A	N/A	N/A	N/A	N/A	N/A	N/A	N/A	N/A	N/A	N/A	N/A
MUN-1 - 5	N/A	N/A	N/A	N/A	N/A	N/A	N/A	N/A	N/A	N/A	N/A	N/A	N/A
MUN-1 - 6	N/A	N/A	N/A	N/A	N/A	N/A	N/A	N/A	N/A	N/A	N/A	N/A	N/A
MUN-1 - 7	N/A	N/A	N/A	N/A	N/A	N/A	N/A	N/A	N/A	N/A	N/A	N/A	N/A
MUN-3 - 1	N/A	N/A	N/A	N/A	N/A	N/A	N/A	N/A	N/A	N/A	N/A	N/A	N/A
MUN-3 - 2	N/A	N/A	N/A	N/A	N/A	N/A	N/A	N/A	N/A	N/A	N/A	N/A	N/A
MUN-3 - 3	N/A	N/A	N/A	N/A	N/A	N/A	N/A	N/A	N/A	N/A	N/A	N/A	N/A
MUN-3 - 4	N/A	N/A	N/A	N/A	N/A	N/A	N/A	N/A	N/A	N/A	N/A	N/A	N/A
MUN-3 - 5	N/A	N/A	N/A	N/A	N/A	N/A	N/A	N/A	N/A	N/A	N/A	N/A	N/A
MUN-3 - 6	N/A	N/A	N/A	N/A	N/A	N/A	N/A	N/A	N/A	N/A	N/A	N/A	N/A
MUN-3 - 7	N/A	N/A	N/A	N/A	N/A	N/A	N/A	N/A	N/A	N/A	N/A	N/A	N/A
OG1_1 - 1	13000	29.0	1.2	0.695	0.028	0.95	3470	14	3451	42	3401	110	1.5
OG1_1 - 2	26125	29.3	1.2	0.702	0.028	0.95	3484	15	3462	40	3428	100	1.0
OG1_1 - 3	59333	28.3	1.1	0.683	0.026	0.90	3472	14	3429	39	3355	100	2.2
OG1_1 - 4	12281	27.2	1.1	0.663	0.026	0.98	3460	13	3388	41	3277	100	3.4
OG1_1 - 5	9801	28.7	1.1	0.696	0.026	0.87	3464	13	3444	38	3406	98	1.1
OG1_1 - 6	6432	27.6	1.1	0.675	0.025	0.79	3448	14	3404	40	3324	98	2.4
OG1_1 - 7	12968	28.6	1.1	0.693	0.026	0.92	3465	13	3439	39	3392	99	1.4
R33 - 1	447	0.5	0.0	0.065	0.003	0.18	431	33	410	14	407	15	0.8
R33 - 3	395	0.5	0.0	0.063	0.002	0.34	441	38	400	14	394	14	1.5
R33 - 4	361	0.5	0.0	0.063	0.002	0.06	451	36	401	14	396	14	1.5
R33 - 5	780	0.5	0.0	0.064	0.002	0.46	450	33	405	14	398	14	1.9
R33 - 6	433	0.5	0.0	0.064	0.002	0.28	477	37	412	14	403	15	2.4

Appendix 4. LASS Secondary Reference Material Data Table

Grain Spot	$^{206}Pb/^{204}Pb$	$^{207}Pb/^{235}U$	2σ	$^{206}Pb/^{238}U$	2σ	ρ	Age (Ma)						%
							$^{207}Pb/^{206}Pb$	2σ	$^{207}Pb/^{235}U$	2σ	$^{206}Pb/^{238}U$	2σ	Disc.
R33 - 7	661	0.5	0.0	0.065	0.002	0.30	450	31	410	14	403	15	1.8
R33 - 8	418	0.5	0.0	0.064	0.002	0.38	474	35	412	14	402	15	2.3
R33 - 9	482	0.5	0.0	0.065	0.002	0.07	476	40	418	15	405	15	3.2
R33 - 10	523	0.5	0.0	0.064	0.002	0.44	405	32	402	13	401	15	0.4
R33 - 11	610	0.5	0.0	0.064	0.002	0.53	390	28	399	13	399	14	-0.1
R33 - 12	642	0.5	0.0	0.064	0.002	0.63	405	29	401	13	399	14	0.6
R33 - 13	612	0.5	0.0	0.063	0.002	0.08	410	36	400	14	396	15	1.0
R33 - 14	1624	0.5	0.0	0.064	0.002	0.13	412	33	404	14	399	15	1.1
Plesovice - 1	4606	0.4	0.0	0.055	0.002	0.63	324	22	341	11	343	12	-0.5
Plesovice - 2	2900	0.4	0.0	0.054	0.002	0.64	317	22	338	11	340	12	-0.8
Plesovice - 3	4236	0.4	0.0	0.052	0.002	0.64	352	21	331	11	329	12	0.4
Plesovice - 4	4430	0.4	0.0	0.052	0.002	0.69	369	22	332	11	328	12	1.2
Plesovice - 5	3071	0.4	0.0	0.053	0.002	0.57	338	23	331	11	332	12	-0.2
Plesovice - 6	2723	0.4	0.0	0.053	0.002	0.41	376	24	335	11	330	12	1.3
Plesovice - 7	3664	0.4	0.0	0.053	0.002	0.66	346	24	334	11	332	12	0.5
Plesovice - 8	2724	0.4	0.0	0.053	0.002	0.66	368	24	336	11	332	12	1.3
Plesovice - 9	3123	0.4	0.0	0.053	0.002	0.51	361	26	338	11	334	12	1.3
Plesovice - 10	2366	0.4	0.0	0.053	0.002	0.52	339	22	334	11	335	12	-0.1
Plesovice - 11	3318	0.4	0.0	0.054	0.002	0.57	315	22	337	11	340	12	-0.9
Plesovice - 12	2782	0.4	0.0	0.053	0.002	0.54	314	24	334	11	335	12	-0.4
Plesovice - 13	3707	0.4	0.0	0.052	0.002	0.69	340	24	329	11	327	12	0.6
Plesovice - 14	3255	0.4	0.0	0.052	0.002	0.20	312	23	328	11	330	12	-0.4
91500 - 1	1325	1.8	0.1	0.177	0.007	0.35	1055	23	1053	25	1050	36	0.3
91500 - 2	1119	1.8	0.1	0.170	0.006	0.28	1076	22	1030	26	1014	35	1.6
91500 - 3	2333	1.8	0.1	0.173	0.006	0.41	1044	22	1032	26	1027	35	0.4
91500 - 4	1552	1.8	0.1	0.174	0.007	0.41	1071	24	1046	26	1037	36	0.9

Appendix 4. LASS Secondary Reference Material Data Table

Grain Spot	$^{206}Pb/^{204}Pb$	$^{207}Pb/^{235}U$	2σ	$^{206}Pb/^{238}U$	2σ	ρ	Age (Ma)						%
							$^{207}Pb/^{206}Pb$	2σ	$^{207}Pb/^{235}U$	2σ	$^{206}Pb/^{238}U$	2σ	Disc.
91500 - 5	1023	1.8	0.1	0.173	0.007	0.59	1053	20	1038	26	1030	35	0.8
91500 - 6	1918	1.8	0.1	0.174	0.007	0.59	1046	22	1038	26	1031	36	0.7
91500 - 7	1257	1.8	0.1	0.170	0.006	0.50	1054	22	1027	26	1013	35	1.3
91500 - 7	2865	1.8	0.0	0.176	0.003	0.83	1060	32	1048	13	1042	14	0.6

Appendix 4. LASS Secondary Reference Material Data Table

Grain Spot	$^{176}Hf/^{177}Hf$	2σ	$^{176}Lu/^{177}Hf$	2σ	$^{176}Yb/^{177}Hf$	2σ	$^{176}Hf/^{177}Hf_i$	$2\sigma_i$	εHf_0	$2\sigma_0$	εHf_i	$2\sigma_i$	Assigned Age	2σ	Th/U
MUN-1 - 1	0.282153	0.000032	0.000393	0.000002	0.0128	0.0003	0.282161	0.000032	-22.1	1.2	N/A	N/A	0.0	0.0	N/A
MUN-1 - 2	0.282145	0.000034	0.000322	0.000004	0.0101	0.0001	0.282154	0.000034	-22.3	1.3	N/A	N/A	0.0	0.0	N/A
MUN-1 - 3	0.282118	0.000038	0.000534	0.000048	0.0185	0.0024	0.282129	0.000038	-23.2	1.4	N/A	N/A	0.0	0.0	N/A
MUN-1 - 4	0.282188	0.000041	0.000708	0.000028	0.0230	0.0008	0.282200	0.000041	-20.7	1.5	N/A	N/A	0.0	0.0	N/A
MUN-1 - 5	0.282122	0.000036	0.000414	0.000018	0.0128	0.0005	0.282137	0.000036	-22.9	1.3	N/A	N/A	0.0	0.0	N/A
MUN-1 - 6	0.282130	0.000030	0.000386	0.000004	0.0123	0.0002	0.282146	0.000030	-22.6	1.1	N/A	N/A	0.0	0.0	N/A
MUN-1 - 7	0.282106	0.000040	0.000490	0.000018	0.0156	0.0007	0.282124	0.000040	-23.4	1.5	N/A	N/A	0.0	0.0	N/A
MUN-3 - 1	0.282160	0.000043	0.002572	0.000004	0.0846	0.0009	0.282168	0.000043	-21.8	1.6	N/A	N/A	0.0	0.0	N/A
MUN-3 - 2	0.282150	0.000073	0.002493	0.000004	0.0808	0.0007	0.282159	0.000073	-22.1	2.6	N/A	N/A	0.0	0.0	N/A
MUN-3 - 3	0.282113	0.000073	0.002616	0.000009	0.0849	0.0005	0.282123	0.000073	-23.4	2.6	N/A	N/A	0.0	0.0	N/A
MUN-3 - 4	0.282116	0.000064	0.002625	0.000003	0.0844	0.0007	0.282128	0.000064	-23.2	2.3	N/A	N/A	0.0	0.0	N/A
MUN-3 - 5	0.282162	0.000054	0.002656	0.000002	0.0856	0.0008	0.282176	0.000054	-21.5	1.9	N/A	N/A	0.0	0.0	N/A
MUN-3 - 6	0.282122	0.000056	0.002979	0.000010	0.0992	0.0005	0.282138	0.000056	-22.9	2.0	N/A	N/A	0.0	0.0	N/A
MUN-3 - 7	0.282135	0.000049	0.002497	0.000004	0.0810	0.0005	0.282153	0.000049	-22.3	1.8	N/A	N/A	0.0	0.0	N/A
OG1_1 - 1	0.280610	0.000057	0.000657	0.000029	0.0176	0.0007	0.280617	0.000057	-76.7	2.1	1.2	2.1	3465.4	1.9	0.54
OG1_1 - 2	0.280590	0.000045	0.000779	0.000027	0.0215	0.0012	0.280599	0.000045	-77.3	1.6	0.3	1.7	3465.4	1.9	0.66
OG1_1 - 3	0.280597	0.000061	0.000704	0.000018	0.0200	0.0009	0.280608	0.000061	-77.0	2.2	0.8	2.2	3465.4	1.9	0.75
OG1_1 - 4	0.280645	0.000047	0.001011	0.000041	0.0280	0.0019	0.280658	0.000047	-75.2	1.7	1.8	1.7	3465.4	1.9	0.67
OG1_1 - 5	0.280694	0.000040	0.001398	0.000086	0.0418	0.0035	0.280708	0.000040	-73.4	1.5	2.7	1.5	3465.4	1.9	0.70
OG1_1 - 6	0.280614	0.000044	0.000872	0.000046	0.0244	0.0022	0.280630	0.000044	-76.2	1.6	1.2	1.6	3465.4	1.9	0.73
OG1_1 - 7	0.280658	0.000041	0.001089	0.000075	0.0325	0.0030	0.280676	0.000041	-74.6	1.5	2.3	1.5	3465.4	1.9	0.76
R33 - 1	0.282726	0.000048	0.001195	0.000045	0.0392	0.0016	0.282733	0.000048	-1.8	1.7	6.8	1.7	402.2	1.6	0.56
R33 - 3	0.282738	0.000044	0.000993	0.000076	0.0323	0.0025	0.282747	0.000044	-1.3	1.6	7.4	1.6	402.2	1.6	0.48
R33 - 4	0.282747	0.000036	0.001372	0.000051	0.0453	0.0020	0.282756	0.000036	-1.0	1.3	7.6	1.3	402.2	1.6	0.59
R33 - 5	0.282703	0.000049	0.001343	0.000052	0.0444	0.0018	0.282714	0.000049	-2.5	1.8	6.1	1.8	402.2	1.6	0.59

Appendix 4. LASS Secondary Reference Material Data Table

Grain Spot	$^{176}Hf/^{177}Hf$	2σ	$^{176}Lu/^{177}Hf$	2σ	$^{176}Yb/^{177}Hf$	2σ	$^{176}Hf/^{177}Hf_i$	$2\sigma_i$	εHf_0	$2\sigma_0$	εHf_i	$2\sigma_i$	Assigned Age	2σ	Th/U
R33 - 6	0.282735	0.000043	0.001299	0.000051	0.0430	0.0018	0.282746	0.000043	-1.4	1.6	7.2	1.6	402.2	1.6	0.59
R33 - 7	0.282721	0.000049	0.001559	0.000070	0.0513	0.0030	0.282733	0.000049	-1.8	1.8	6.7	1.8	402.2	1.6	0.60
R33 - 8	0.282701	0.000046	0.001576	0.000062	0.0520	0.0026	0.282713	0.000046	-2.5	1.7	6.0	1.7	402.2	1.6	0.61
R33 - 9	0.282770	0.000044	0.001541	0.000053	0.0511	0.0022	0.282785	0.000044	0.0	1.6	8.6	1.6	402.2	1.6	0.60
R33 - 10	0.282680	0.000047	0.001359	0.000056	0.0441	0.0021	0.282695	0.000047	-3.2	1.7	5.4	1.7	402.2	1.6	0.55
R33 - 11	0.282707	0.000047	0.001490	0.000046	0.0484	0.0017	0.282723	0.000047	-2.2	1.7	6.4	1.7	402.2	1.6	0.56
R33 - 12	0.282733	0.000035	0.001602	0.000057	0.0527	0.0019	0.282750	0.000035	-1.2	1.3	7.3	1.3	402.2	1.6	0.59
R33 - 13	0.282707	0.000051	0.001335	0.000053	0.0447	0.0019	0.282725	0.000051	-2.1	1.8	6.5	1.8	402.2	1.6	0.57
R33 - 14	0.282733	0.000045	0.001591	0.000057	0.0531	0.0024	0.282751	0.000045	-1.2	1.6	7.3	1.6	402.2	1.6	0.61
Plesovice - 1	0.282473	0.000037	0.000163	0.000001	0.0076	0.0001	0.282480	0.000037	-10.8	1.4	-3.3	1.4	337.1	0.4	0.09
Plesovice - 2	0.282480	0.000030	0.000157	0.000001	0.0073	0.0000	0.282487	0.000030	-10.5	1.1	-3.1	1.1	337.1	0.4	0.09
Plesovice - 3	0.282516	0.000029	0.000152	0.000002	0.0070	0.0000	0.282525	0.000029	-9.2	1.1	-1.7	1.1	337.1	0.4	0.09
Plesovice - 4	0.282477	0.000028	0.000155	0.000001	0.0072	0.0001	0.282485	0.000028	-10.6	1.1	-3.1	1.1	337.1	0.4	0.09
Plesovice - 5	0.282460	0.000034	0.000153	0.000002	0.0071	0.0000	0.282470	0.000034	-11.1	1.3	-3.7	1.3	337.1	0.4	0.09
Plesovice - 6	0.282476	0.000035	0.000157	0.000001	0.0073	0.0001	0.282487	0.000035	-10.5	1.3	-3.1	1.3	337.1	0.4	0.09
Plesovice - 7	0.282472	0.000032	0.000155	0.000002	0.0072	0.0000	0.282484	0.000032	-10.6	1.2	-3.2	1.2	337.1	0.4	0.09
Plesovice - 8	0.282461	0.000033	0.000155	0.000001	0.0072	0.0001	0.282473	0.000033	-11.0	1.2	-3.6	1.2	337.1	0.4	0.09
Plesovice - 9	0.282475	0.000034	0.000156	0.000001	0.0073	0.0000	0.282489	0.000034	-10.5	1.3	-3.0	1.3	337.1	0.4	0.09
Plesovice - 10	0.282505	0.000029	0.000152	0.000001	0.0070	0.0001	0.282519	0.000029	-9.4	1.1	-1.9	1.1	337.1	0.4	0.09
Plesovice - 11	0.282499	0.000032	0.000150	0.000001	0.0070	0.0001	0.282514	0.000032	-9.6	1.2	-2.1	1.2	337.1	0.4	0.09
Plesovice - 12	0.282477	0.000043	0.000155	0.000001	0.0072	0.0000	0.282492	0.000043	-10.4	1.6	-2.9	1.6	337.1	0.4	0.09
Plesovice - 13	0.282458	0.000033	0.000153	0.000001	0.0071	0.0000	0.282475	0.000033	-11.0	1.2	-3.5	1.2	337.1	0.4	0.09
Plesovice - 14	0.282492	0.000029	0.000154	0.000001	0.0071	0.0000	0.282509	0.000029	-9.8	1.1	-2.3	1.1	337.1	0.4	0.09
91500 - 1	0.282325	0.000051	0.000360	0.000001	0.0115	0.0001	0.282332	0.000051	-16.0	1.8	7.6	1.8	1065.4	5.8	0.32
91500 - 2	0.282293	0.000065	0.000358	0.000001	0.0114	0.0001	0.282302	0.000065	-17.1	2.3	6.6	2.3	1065.4	5.8	0.33
91500 - 3	0.282369	0.000049	0.000359	0.000001	0.0113	0.0001	0.282380	0.000049	-14.3	1.8	9.3	1.8	1065.4	5.8	0.33

Appendix 4. LASS Secondary Reference Material Data Table

Grain Spot	$^{176}Hf/^{177}Hf$	2σ	$^{176}Lu/^{177}Hf$	2σ	$^{176}Yb/^{177}Hf$	2σ	$^{176}Hf/^{177}Hf_i$	$2\sigma_i$	εHf_0	$2\sigma_0$	εHf_i	$2\sigma_i$	Assigned Age	2σ	Th/U
91500 - 4	0.282278	0.000056	0.000362	0.000001	0.0114	0.0001	0.282290	0.000056	-17.5	2.0	6.1	2.0	1065.4	5.8	0.33
91500 - 5	0.282270	0.000055	0.000364	0.000001	0.0115	0.0001	0.282284	0.000055	-17.7	2.0	5.9	2.0	1065.4	5.8	0.33
91500 - 6	0.282321	0.000073	0.000363	0.000001	0.0115	0.0001	0.282337	0.000073	-15.8	2.6	7.8	2.6	1065.4	5.8	0.32
91500 - 7	0.282248	0.000055	0.000365	0.000001	0.0117	0.0001	0.282266	0.000055	-18.4	2.0	5.3	2.0	1065.4	5.8	0.32
91500 - 7	0.282284	0.000046	0.000315	0.000003	0.0096	0.0001	0.282301	0.000046	-17.1	1.7	6.5	1.7	1065.4	5.8	0.35

Appendix 4.1 LASS Secondary Reference Material Figures

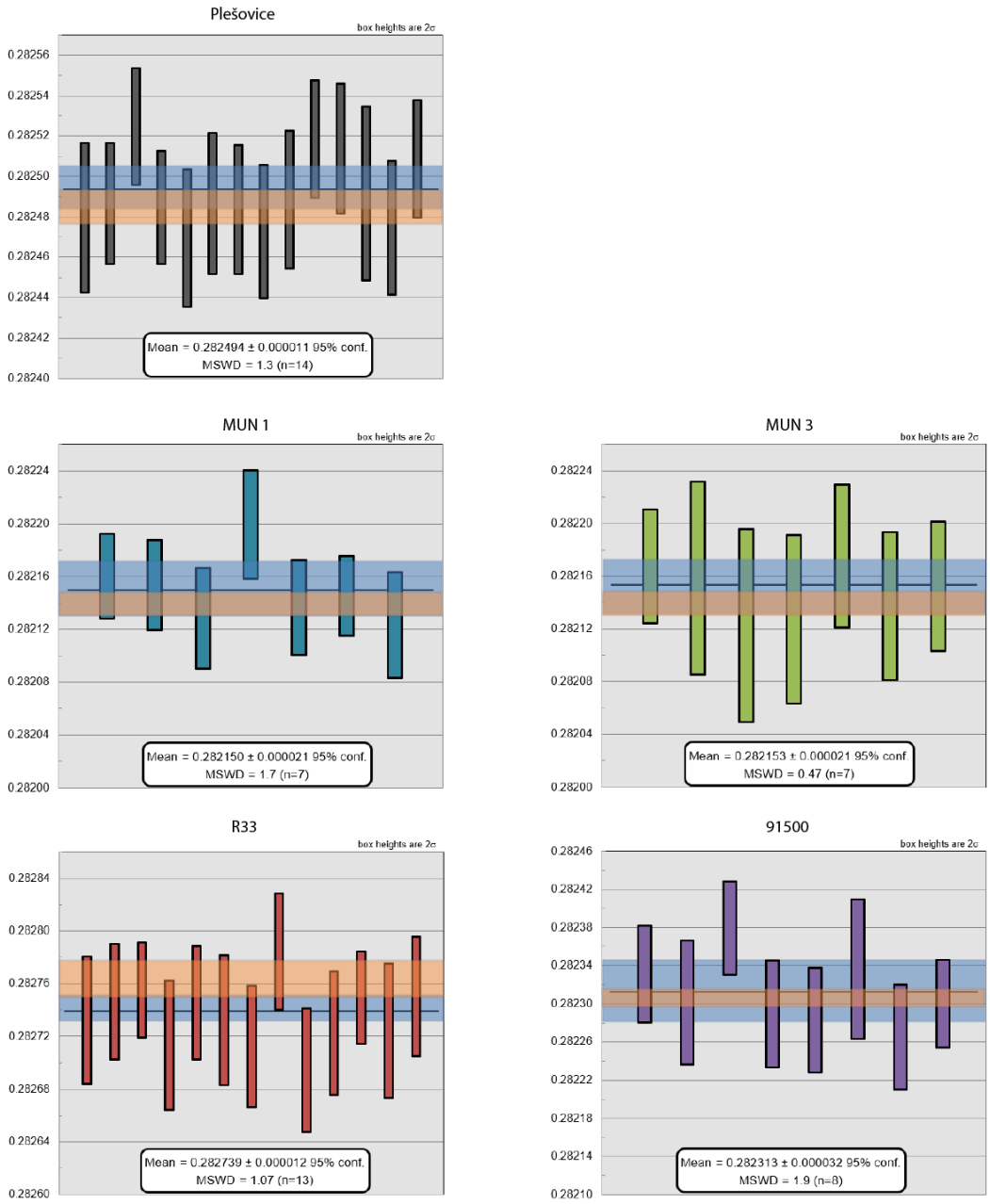

Appendix 4.1. Secondary Reference Material results for measured $^{176}Hf/^{177}Hf$. Shaded orange area represents accepted $^{176}Hf/^{177}Hf$ ratios and their errors. Shaded blue areas represent standards measured in this study with their associated errors.

Appendix 4.1 LASS Secondary Reference Material Figures

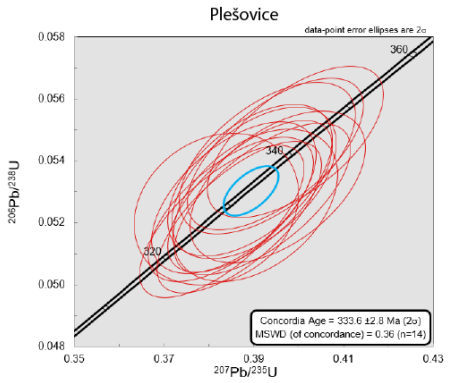

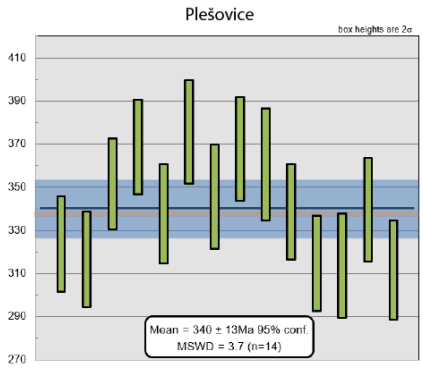

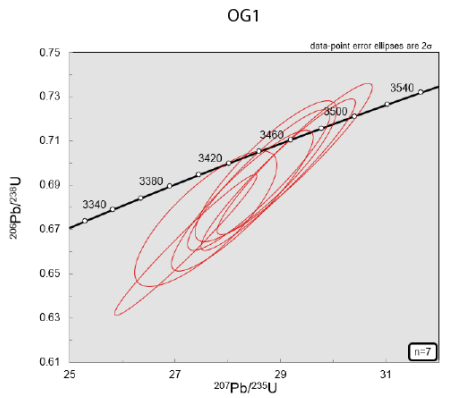

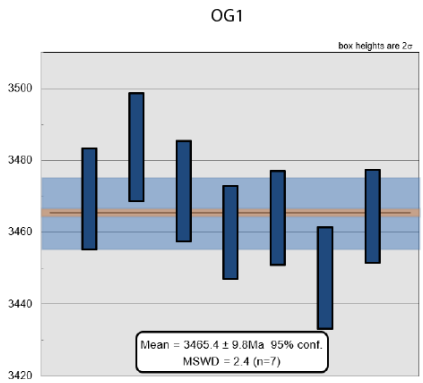

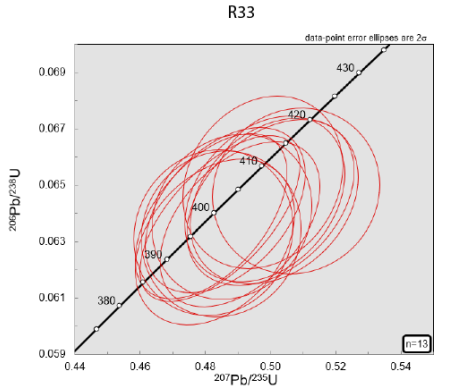

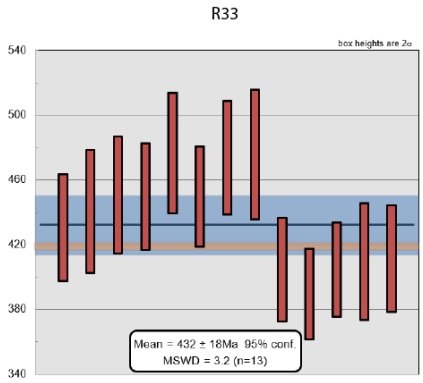

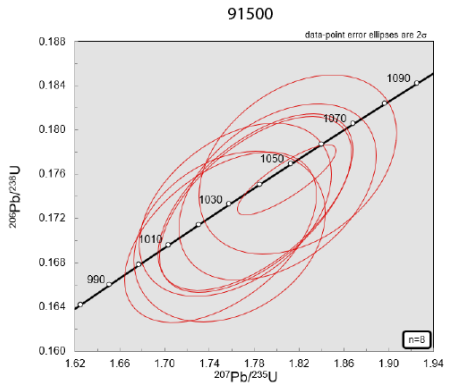

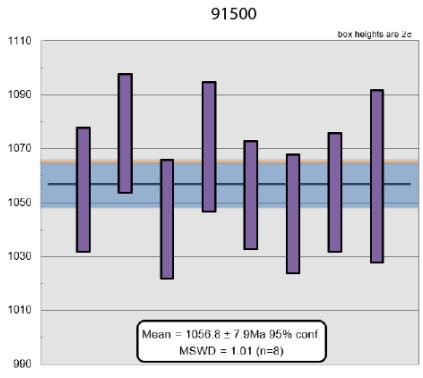

Appendix 5. Representative Zircon Images

Foliated Granite (~3375Ma, BSE, Spots are 25µm, $^{207}Pb/^{206}Pb$ Ages)

MB07

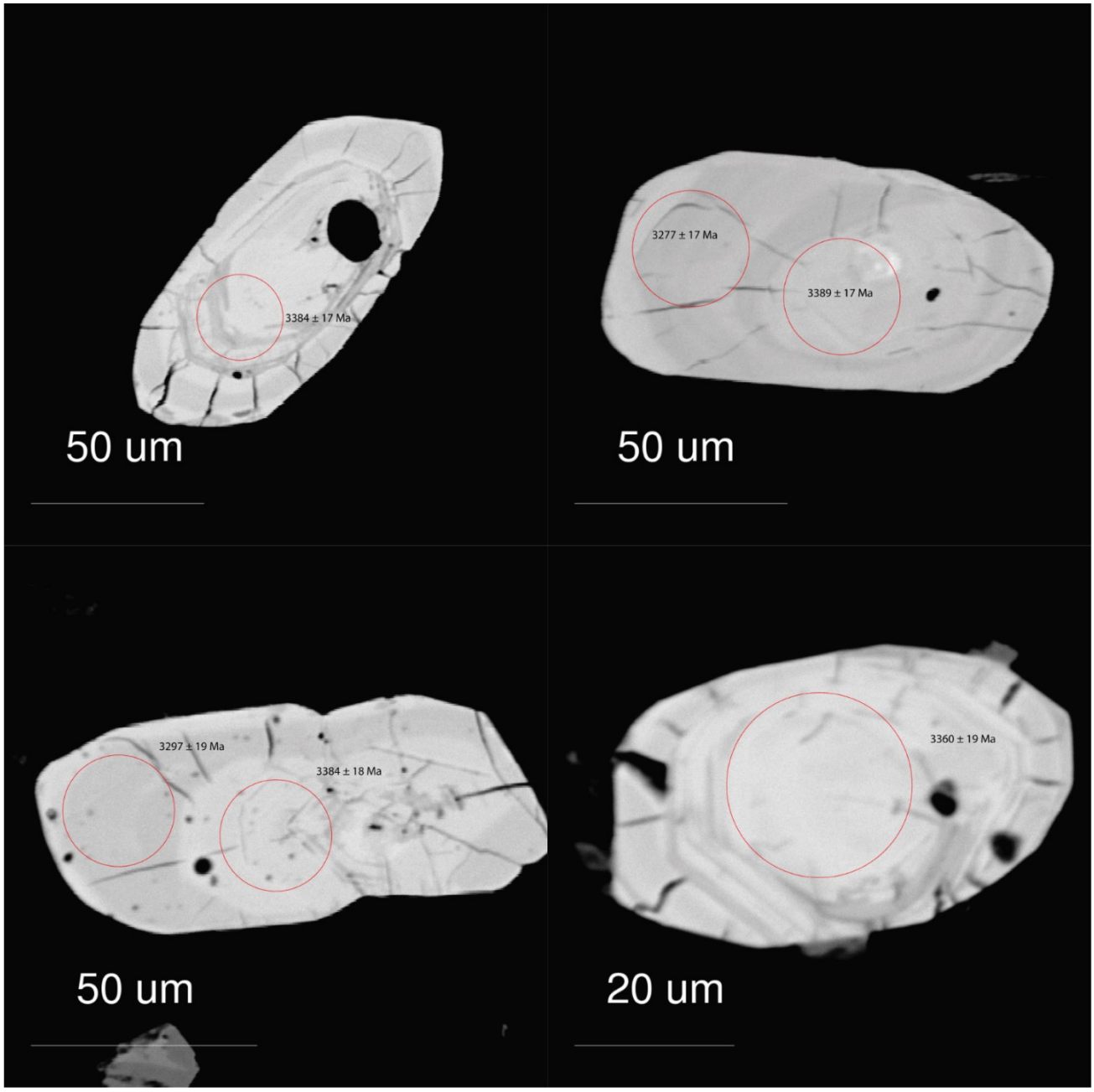

Foliated Granite (~3375Ma, BSE, Spots are 25µm, $^{207}Pb/^{206}Pb$ Ages)

MB167

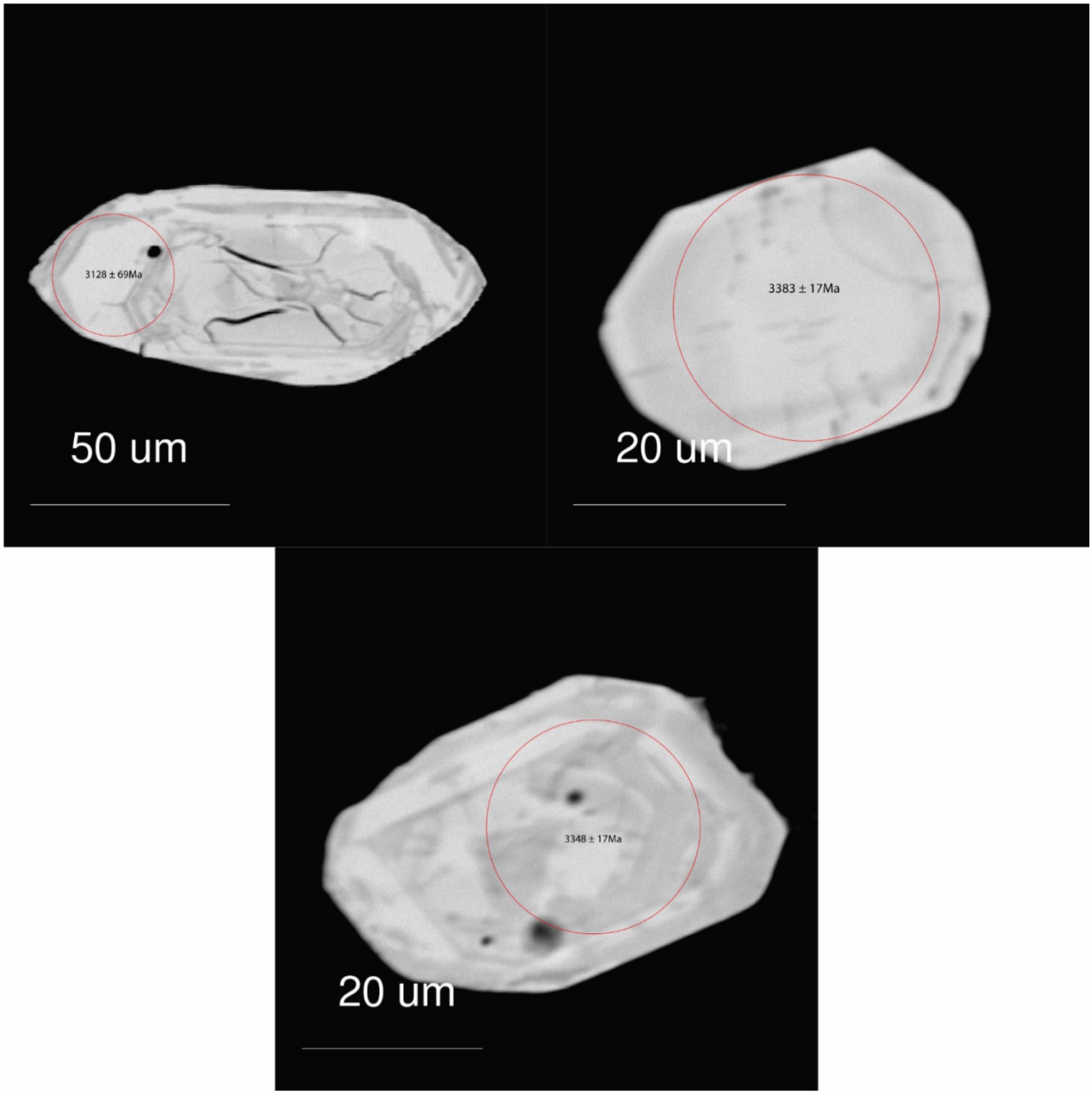

Foliated Granite (~3375Ma, BSE, Spots are 25µm, $^{207}Pb/^{206}Pb$ Ages)

MB185

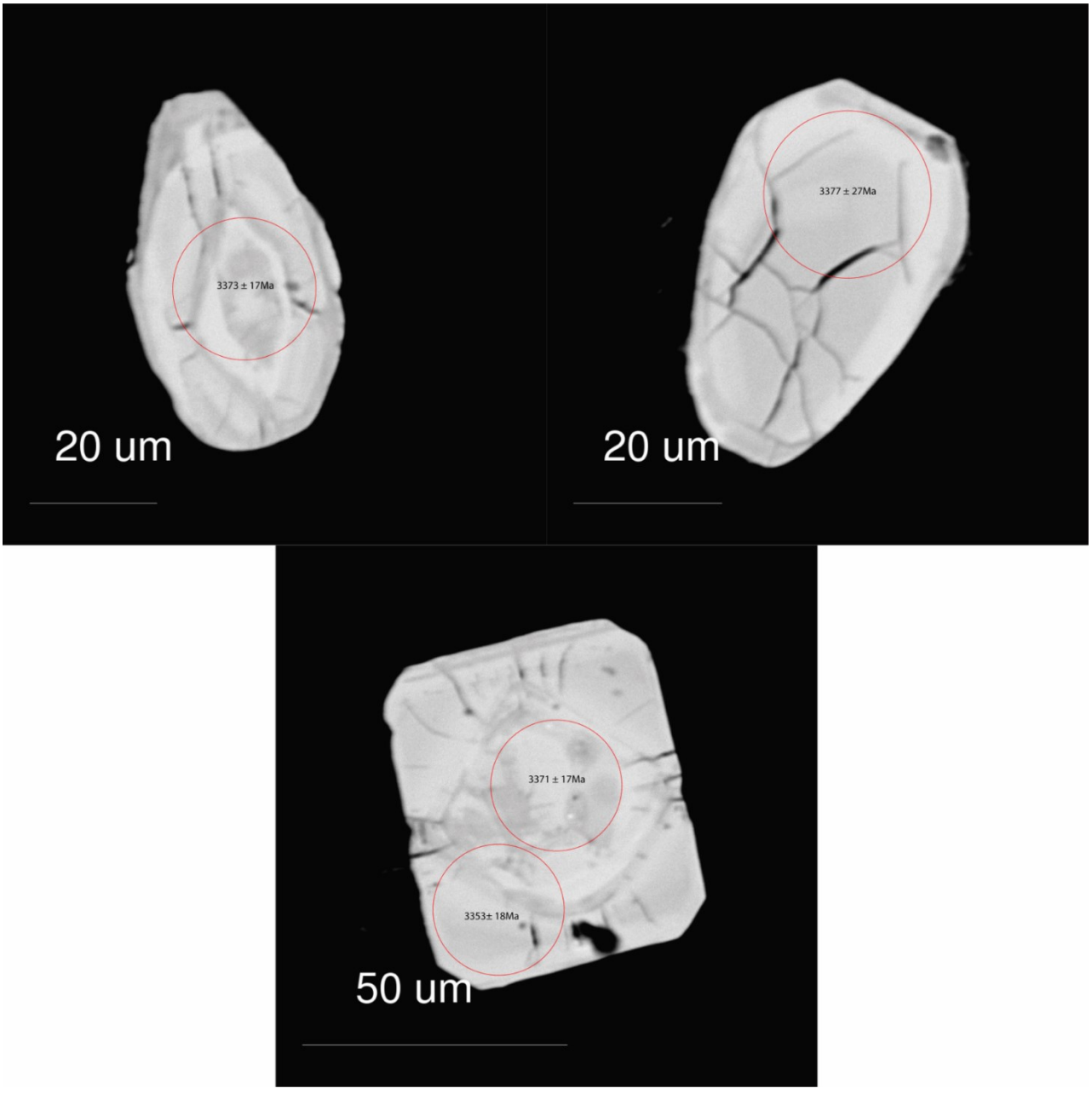

Felsic-Intermediate Gneiss Series (BSE, Spots are 25µm, $^{207}Pb/^{206}Pb$ Ages)

MB12 (~3500-3600Ma Crystallization, Inherited 3958±11Ma)

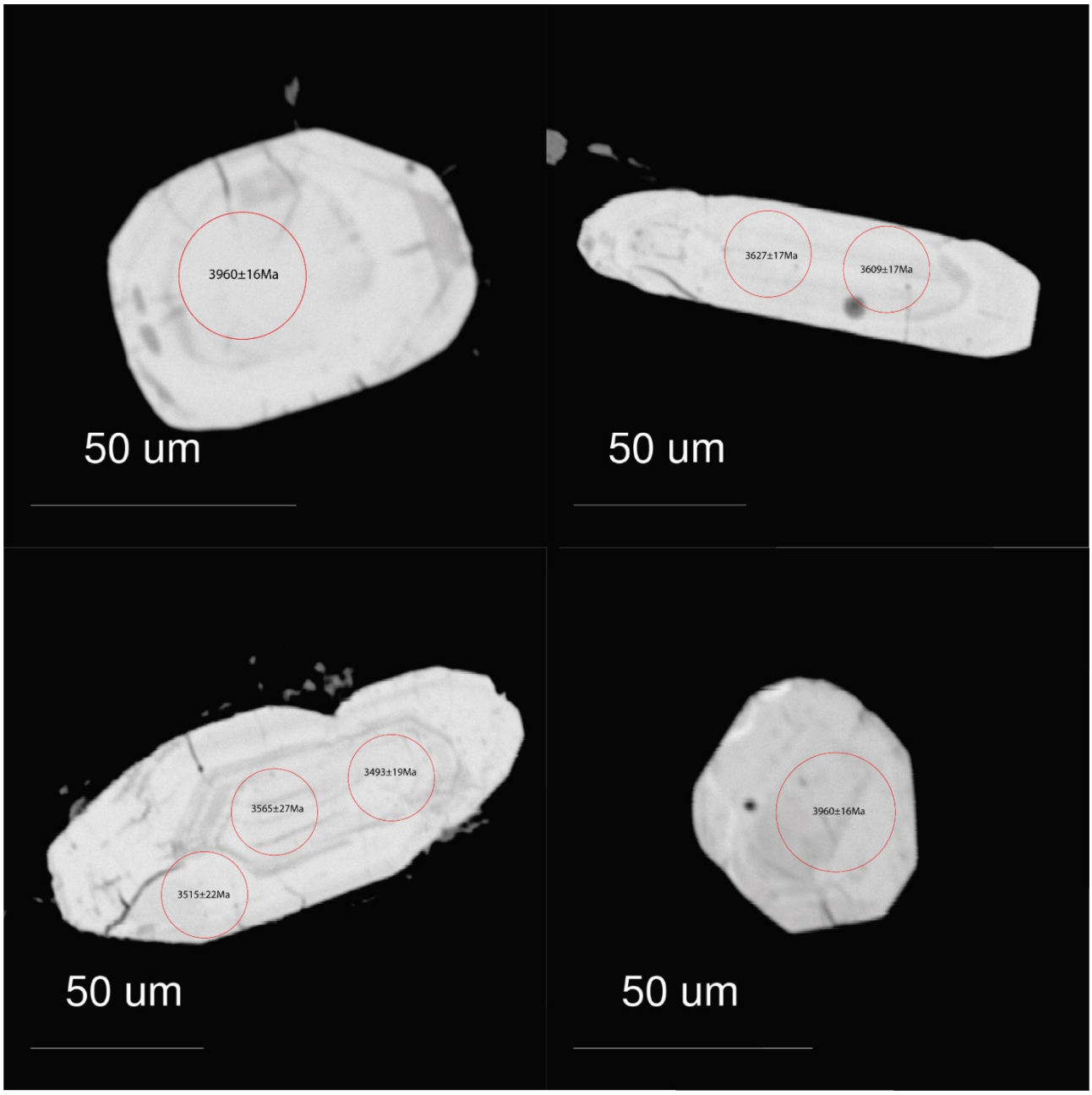

Felsic-Intermediate Gneiss Series (BSE, Spots are 25µm, $^{207}Pb/^{206}Pb$ Ages)

MB21B (~3546±38Ma)

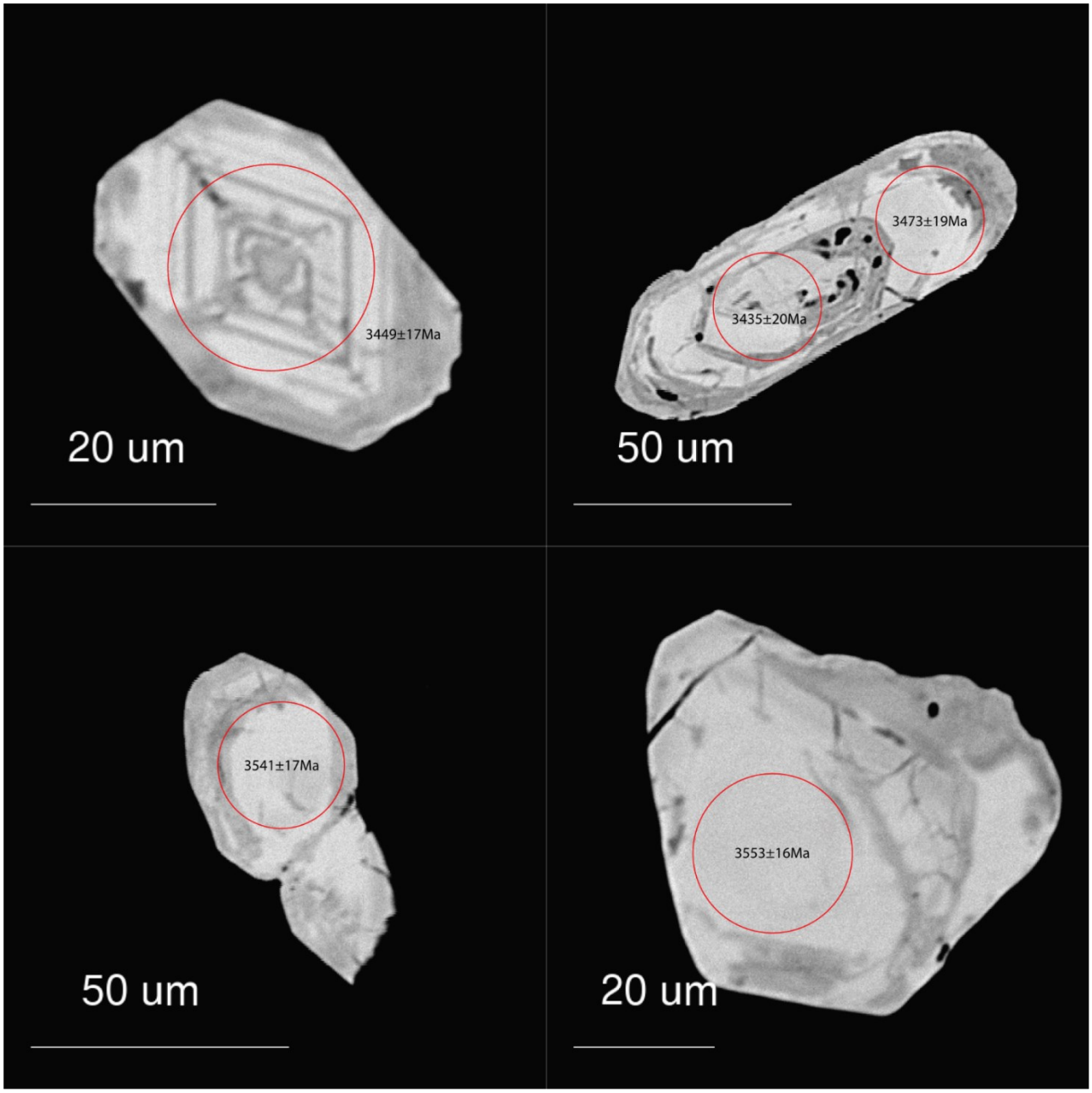

Felsic-Intermediate Gneiss Series (BSE, Spots are 25µm, $^{207}Pb/^{206}Pb$ Ages)

MB47B (~3500-3570Ma)

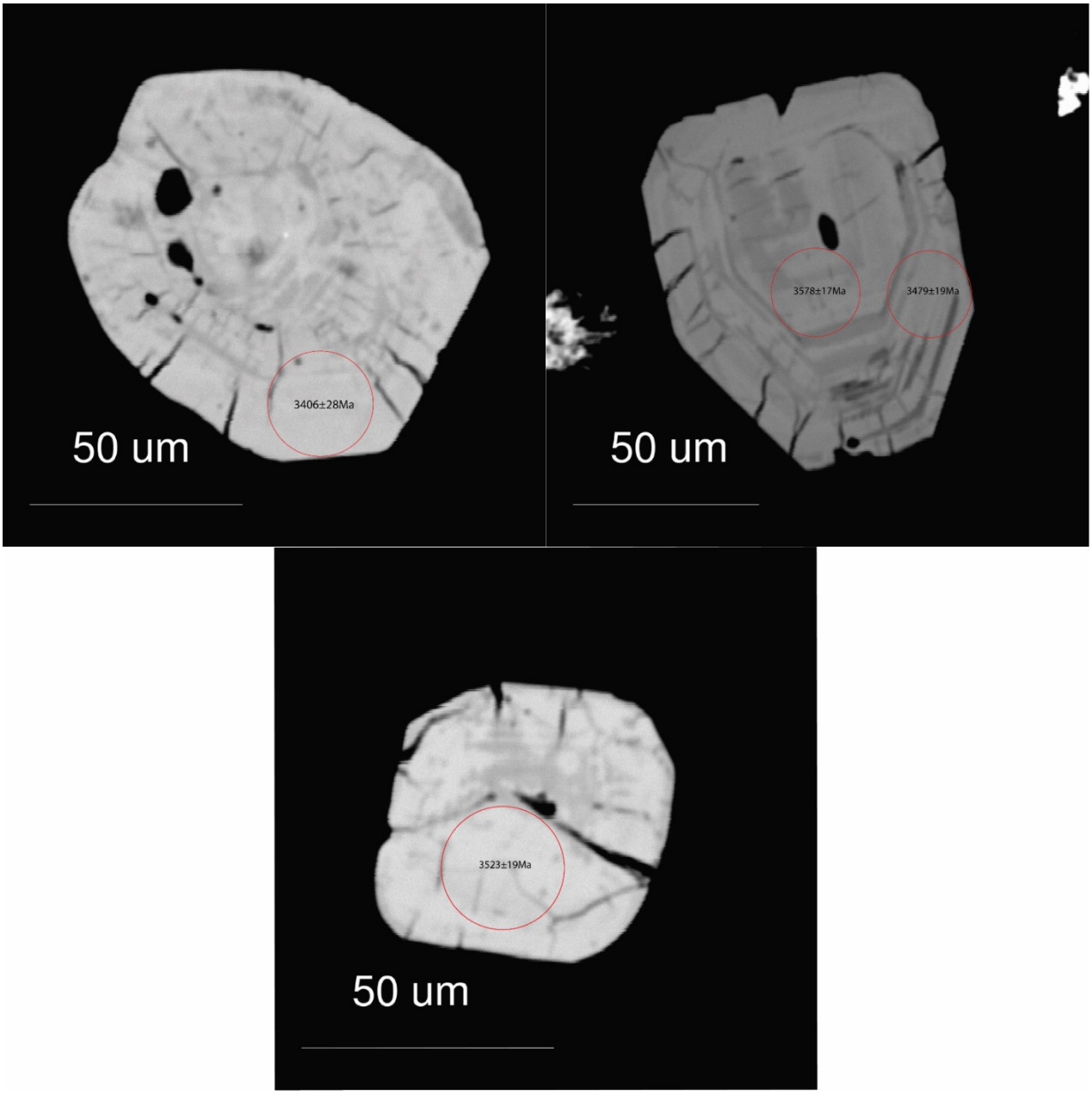

Felsic-Intermediate Gneiss Series (BSE, Spots are 25µm, $^{207}Pb/^{206}Pb$ Ages)

MB54B (3578±35Ma)

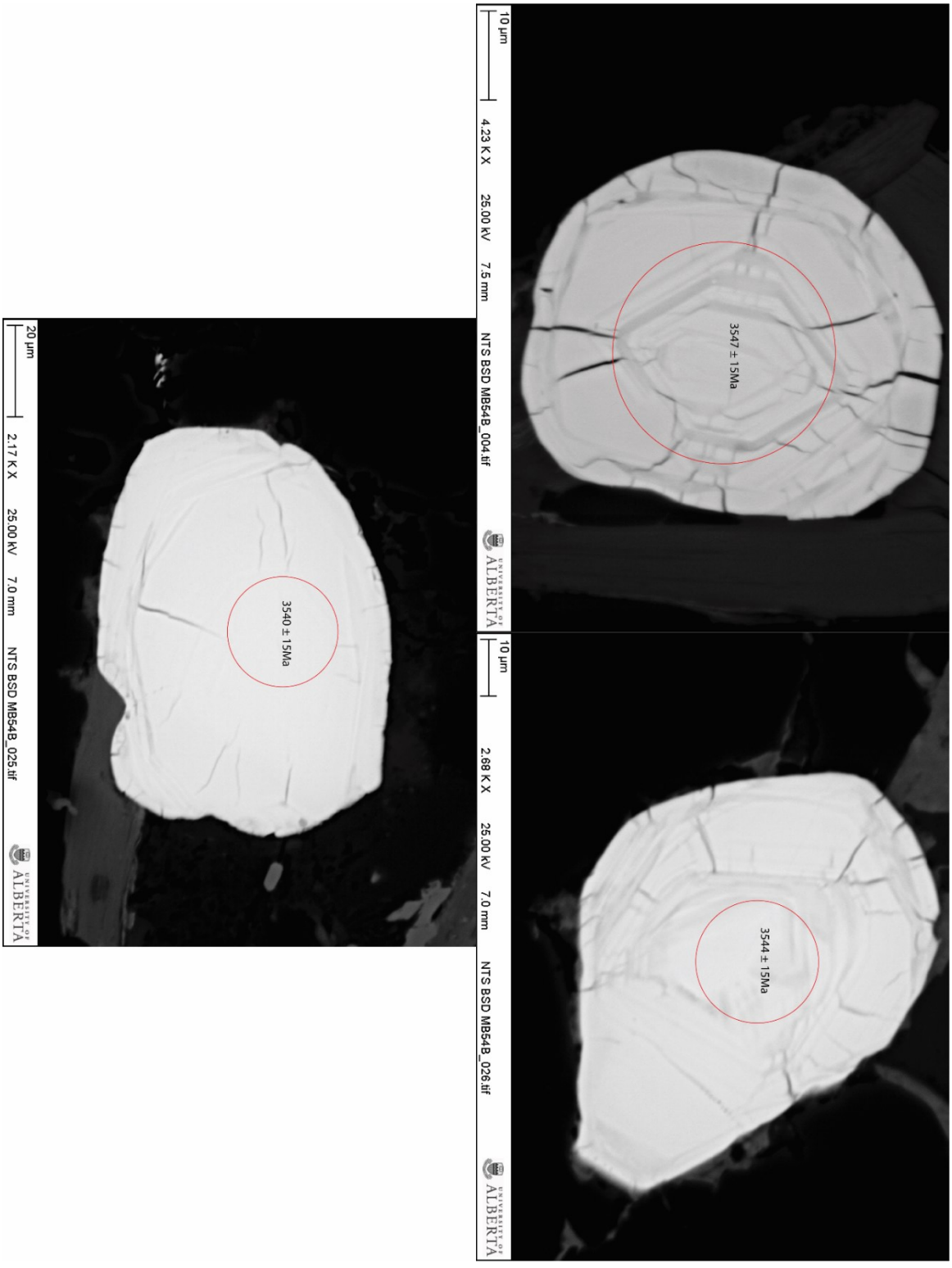

Felsic-Intermediate Gneiss Series (CL, Spots are 25µm, $^{207}Pb/^{206}Pb$ Ages)

MB120 (3571±7Ma)

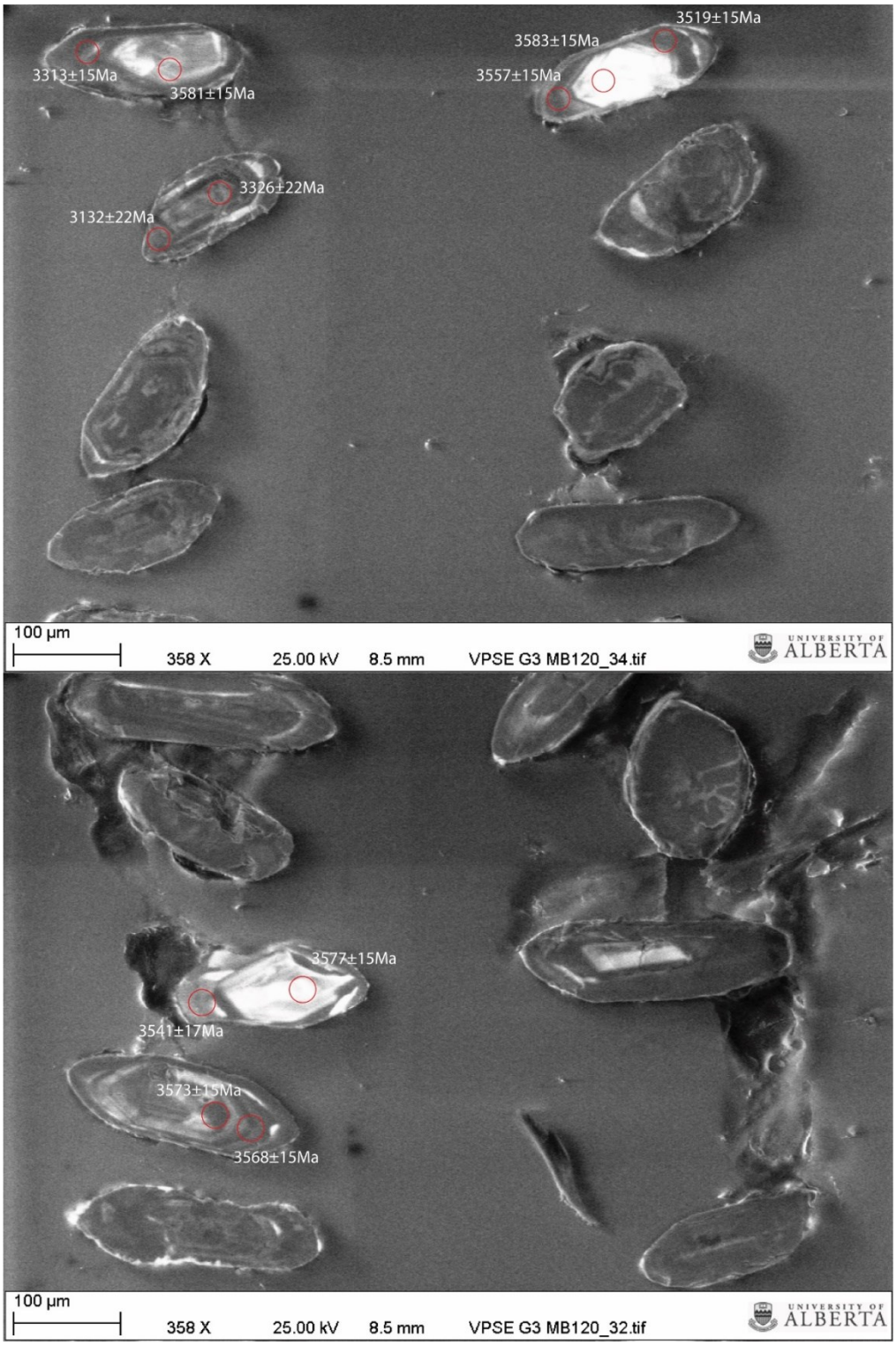

Mixed Gneiss Series (BSE, Spots are 25µm, $^{207}Pb/^{206}Pb$ Ages)

MB73A1 (~3480-3570Ma)

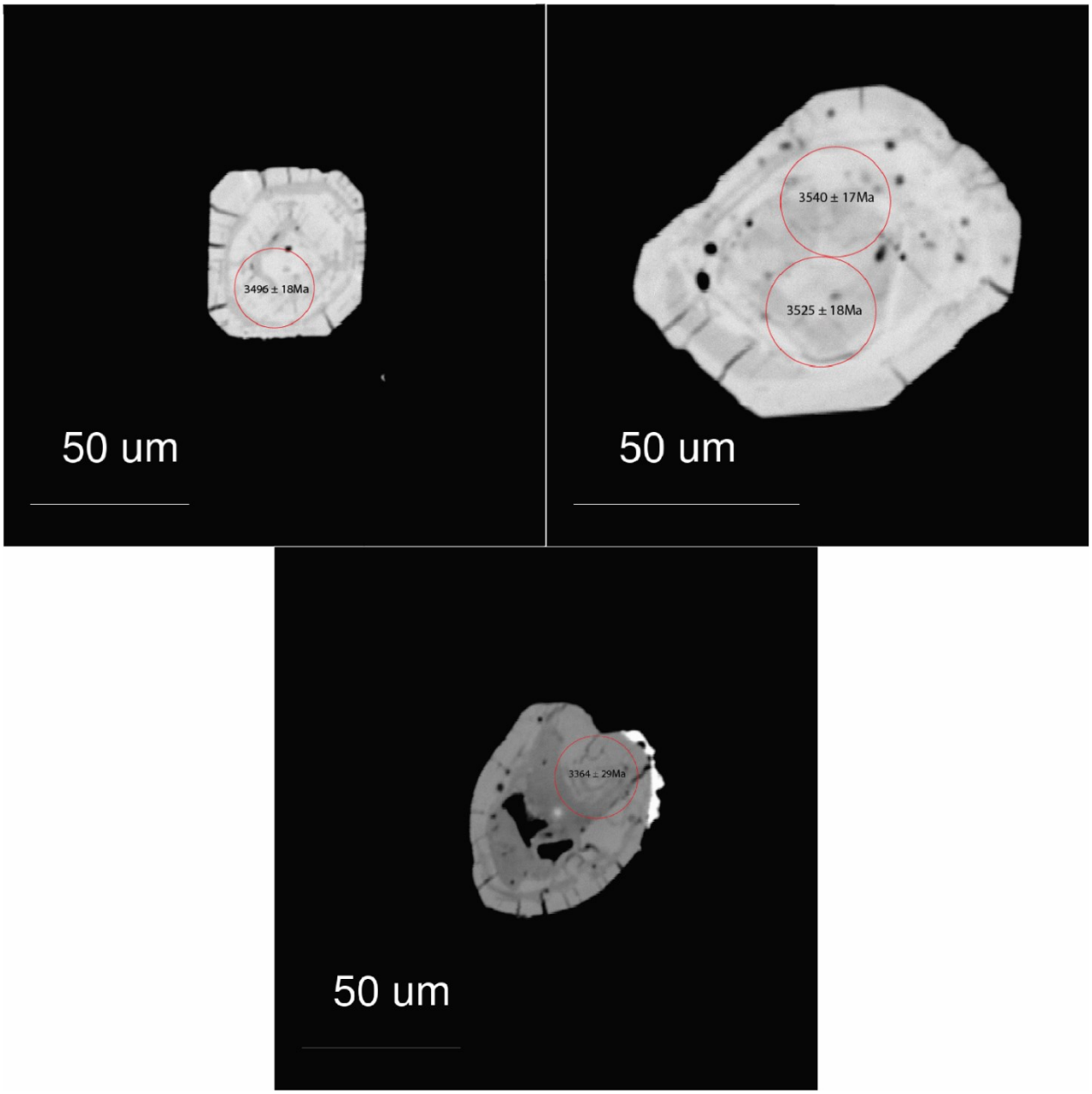

Mixed Gneiss Series (CL, Spots are 25µm, $^{207}Pb/^{206}Pb$ Ages)

MB108B1 (~3650-3750Ma)

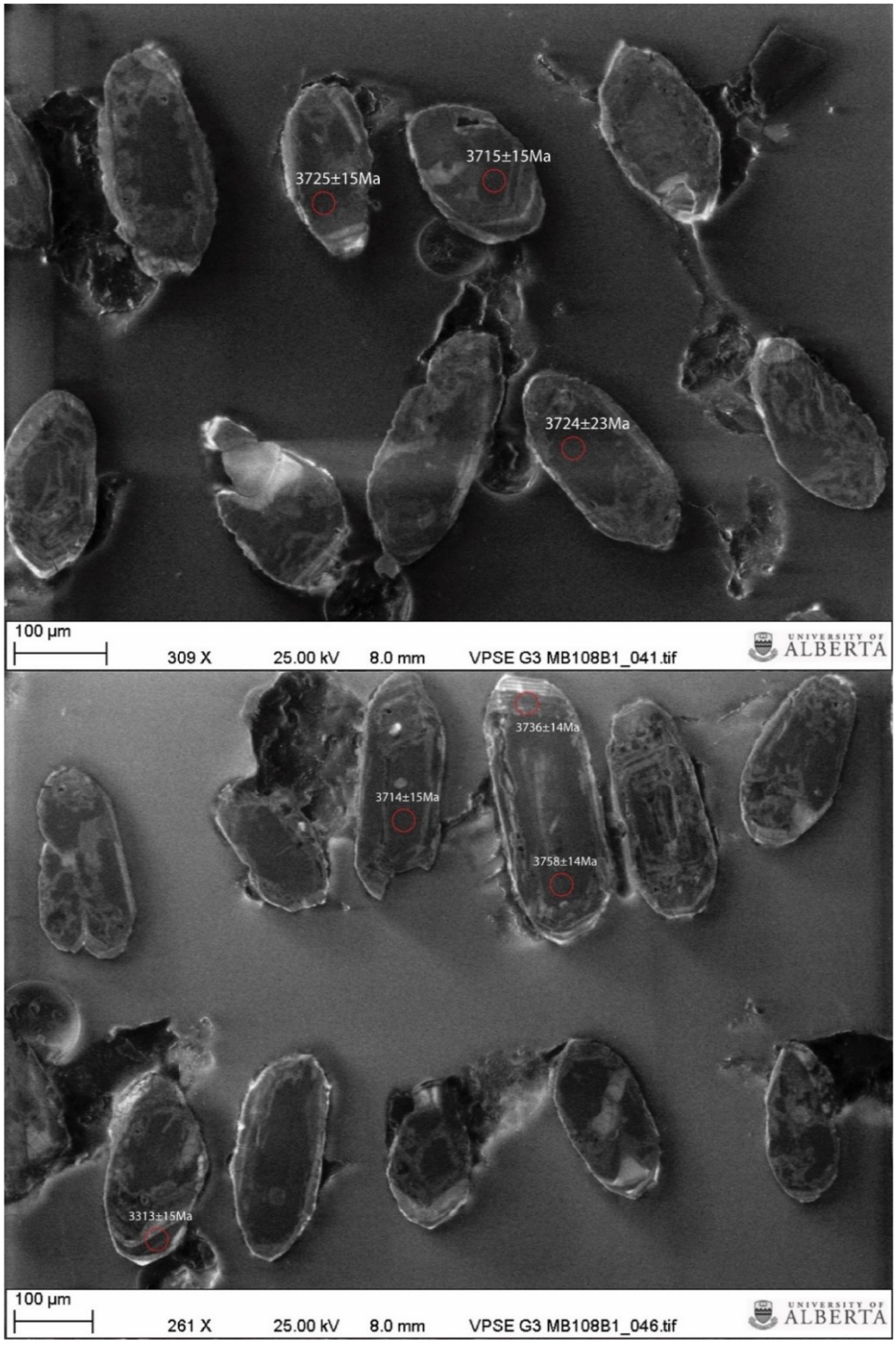

Mixed Gneiss Series (BSE, Spots are 25µm, $^{207}Pb/^{206}Pb$ Ages)

MB138B2 (Unknown Crystallization Age)

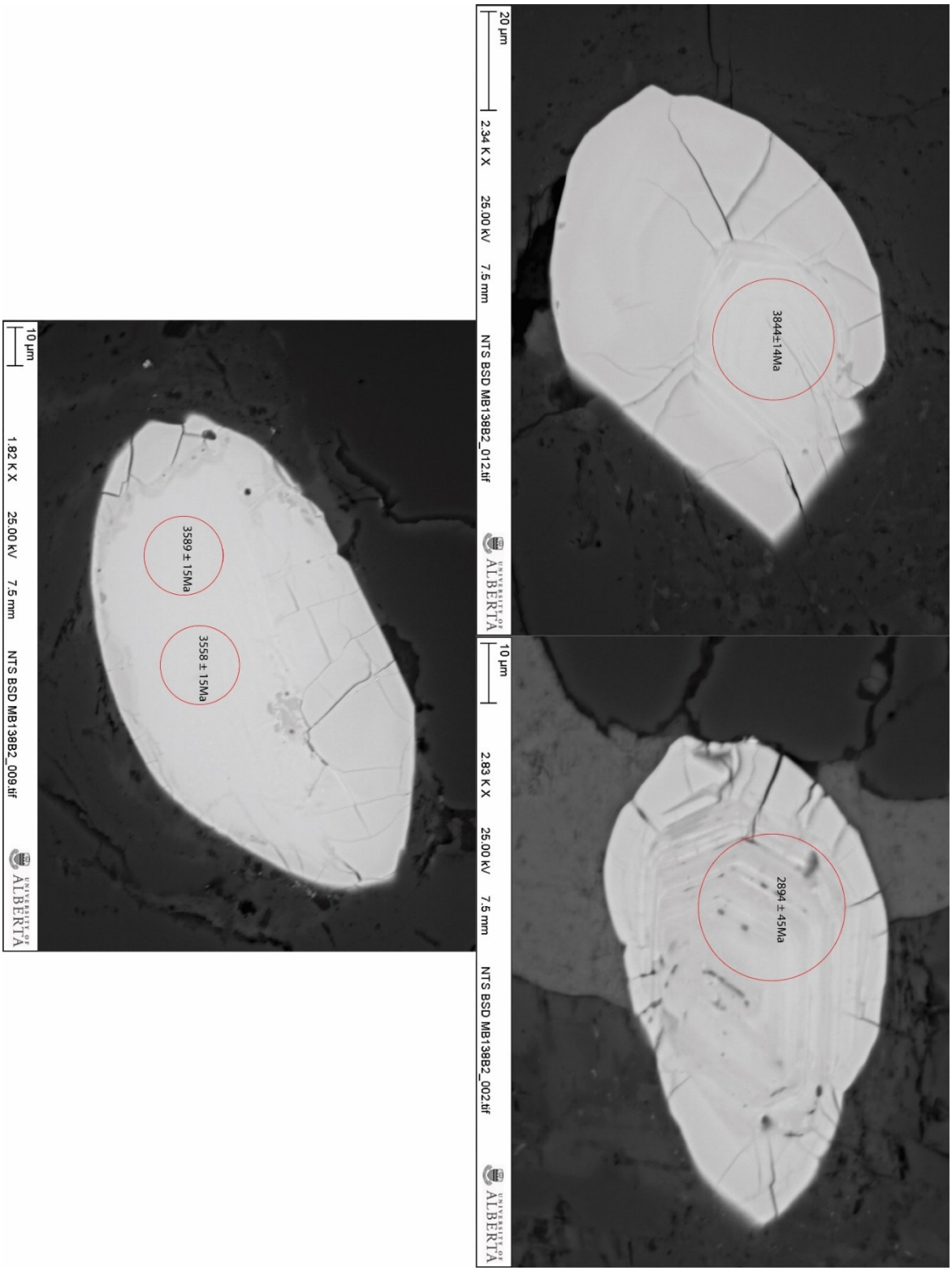

Metagabbro (3740.7±2.3Ma, BSE, Spots are 25µm, $^{207}Pb/^{206}Pb$ Ages)

MB103 (3737.4±5.5Ma)

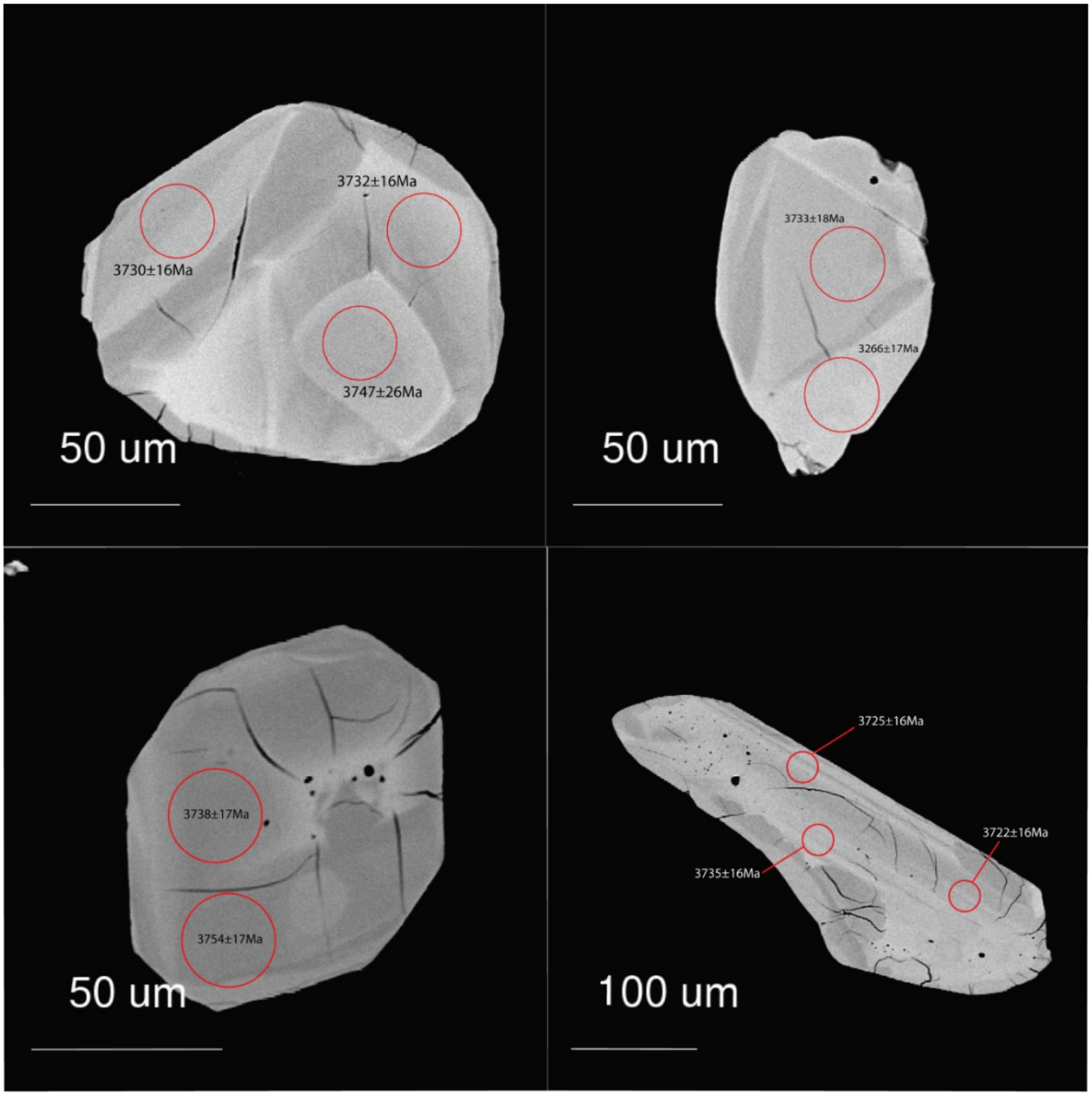

Metagabbro (3740.7±2.3Ma, BSE, Spots are 25µm, $^{207}Pb/^{206}Pb$ Ages)

MB108A (3741.2±2.6Ma)

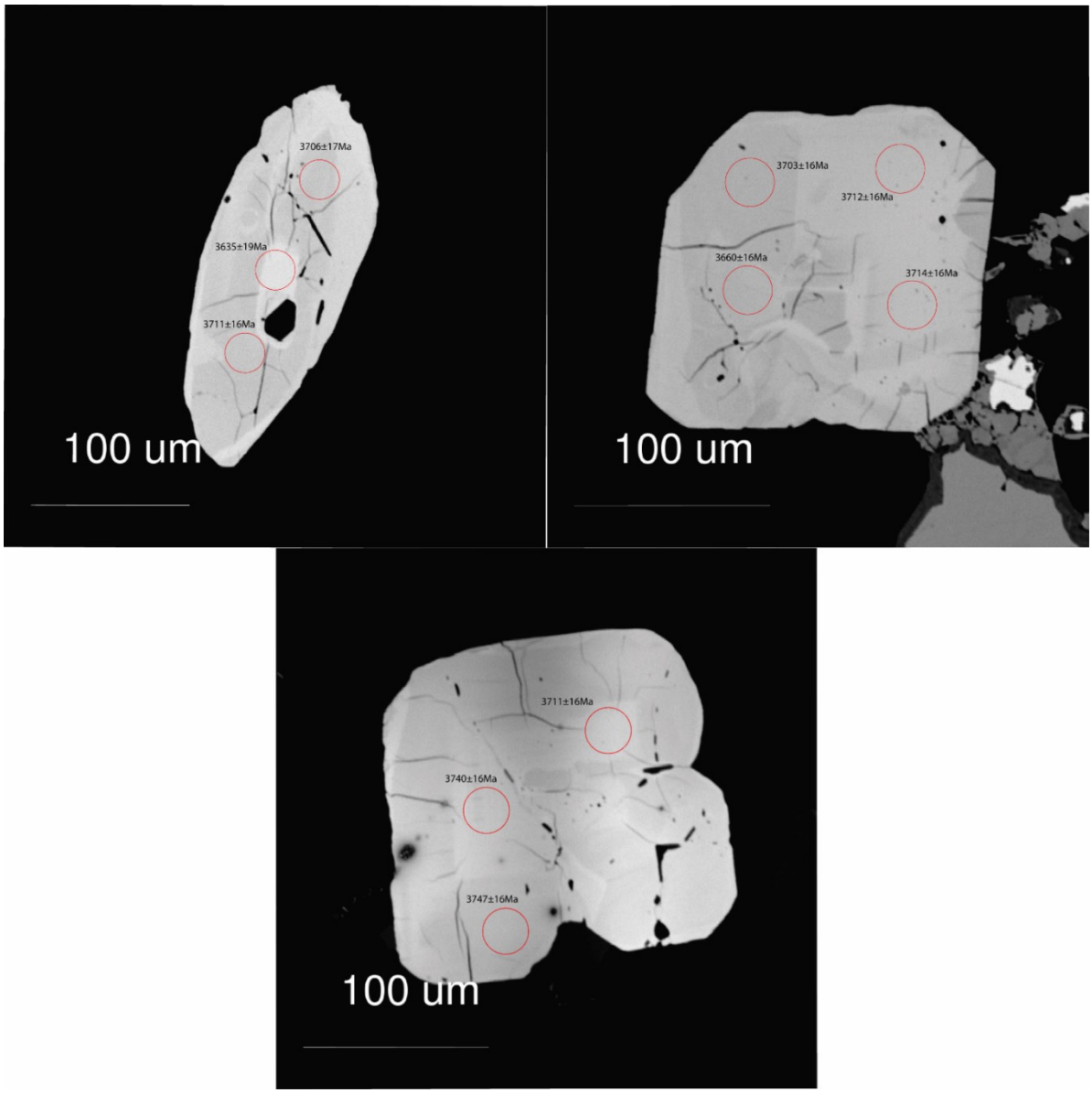

Metagabbro (CL, Spots are 33µm, $^{207}Pb/^{206}Pb$ Ages, εHf calculated using age of 3740.7±2.3Ma)

MB108A

Metagabbro (CL, Spots are 33µm, $^{207}Pb/^{206}Pb$ Ages, εHf calculated using age of 3740.7±2.3Ma)

MB108A

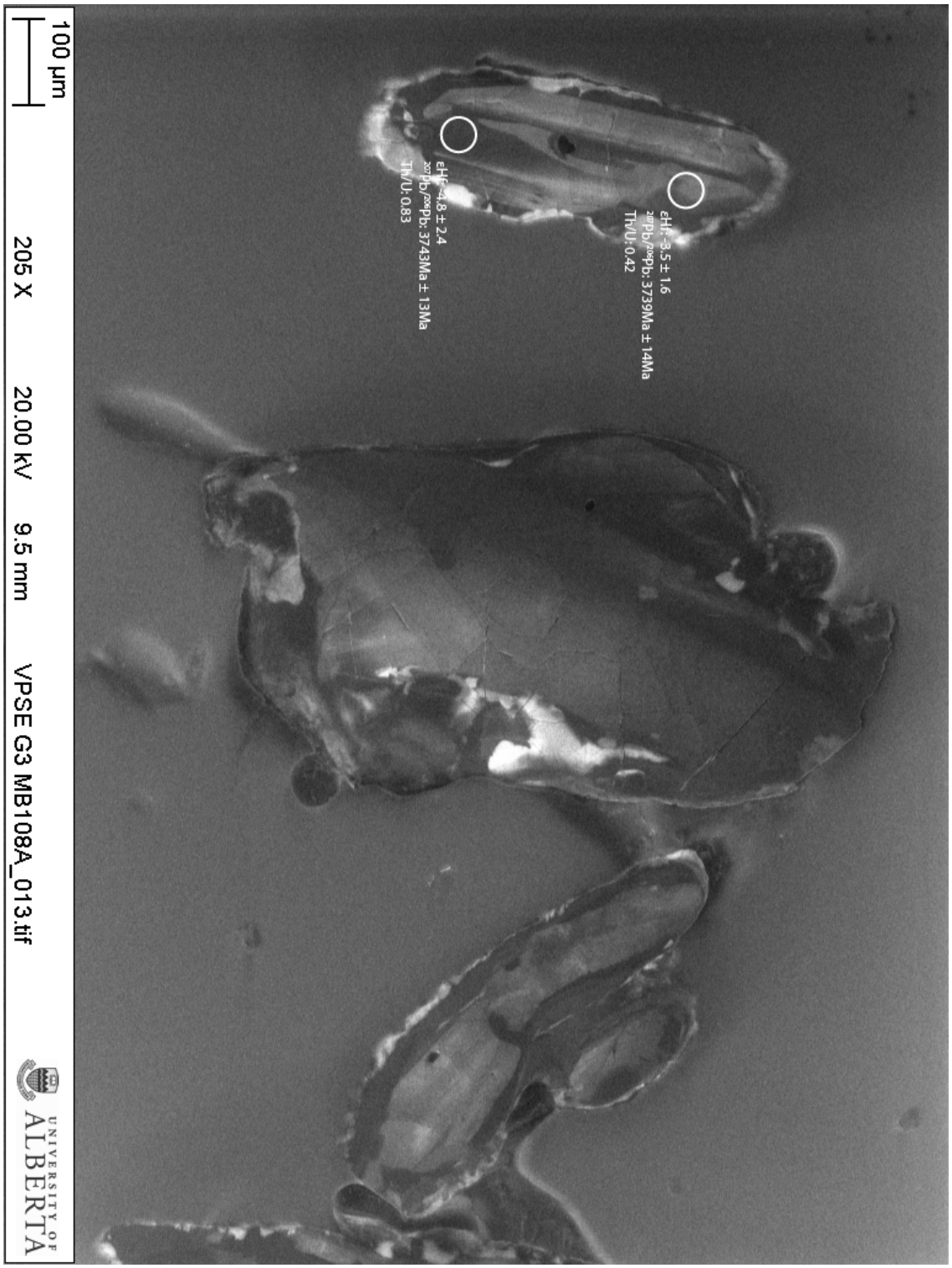

Metagabbro (CL, Spots are 33µm, $^{207}Pb/^{206}Pb$ Ages, εHf calculated using age of 3740.7±2.3Ma)

MB108A

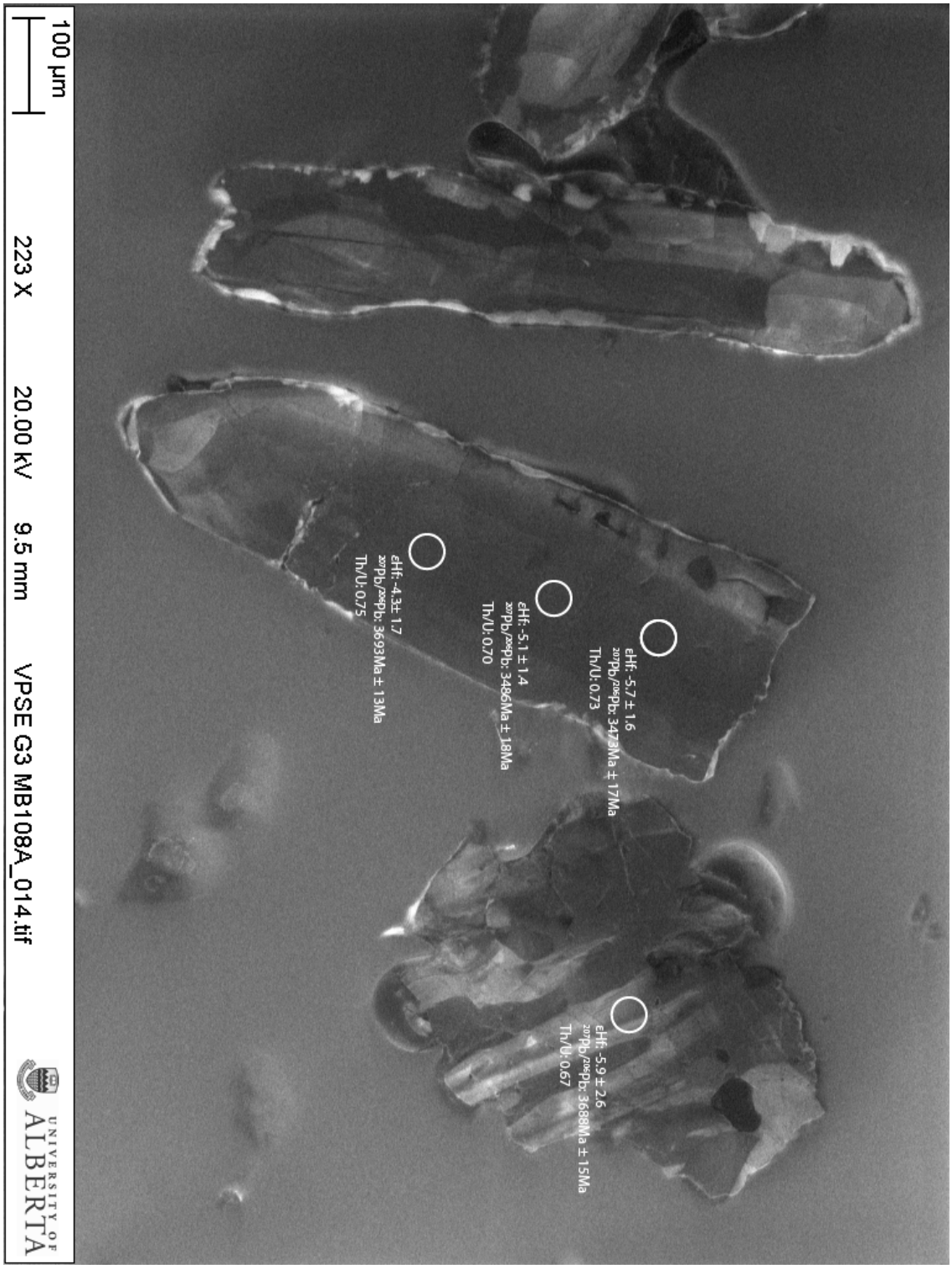

Metagabbro (CL, Spots are 33µm, $^{207}Pb/^{206}Pb$ Ages, εHf calculated using age of 3740.7±2.3Ma)

MB108A

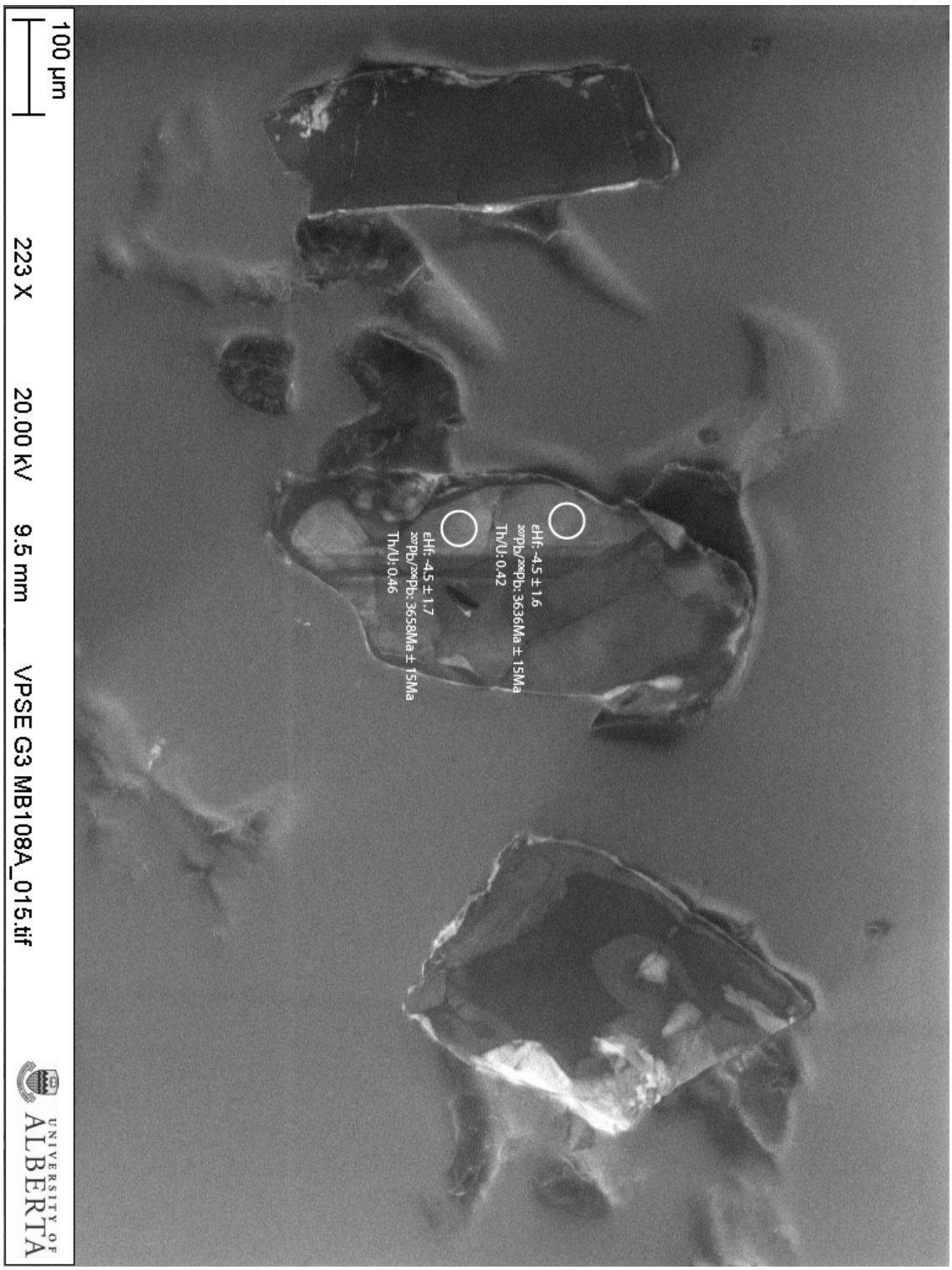

Metagabbro (CL, Spots are 33µm, $^{207}Pb/^{206}Pb$ Ages, εHf calculated using age of 3740.7±2.3Ma)

MB108A

Metagabbro (CL, Spots are 33µm, $^{207}Pb/^{206}Pb$ Ages, εHf calculated using age of 3740.7±2.3Ma)

MB108A

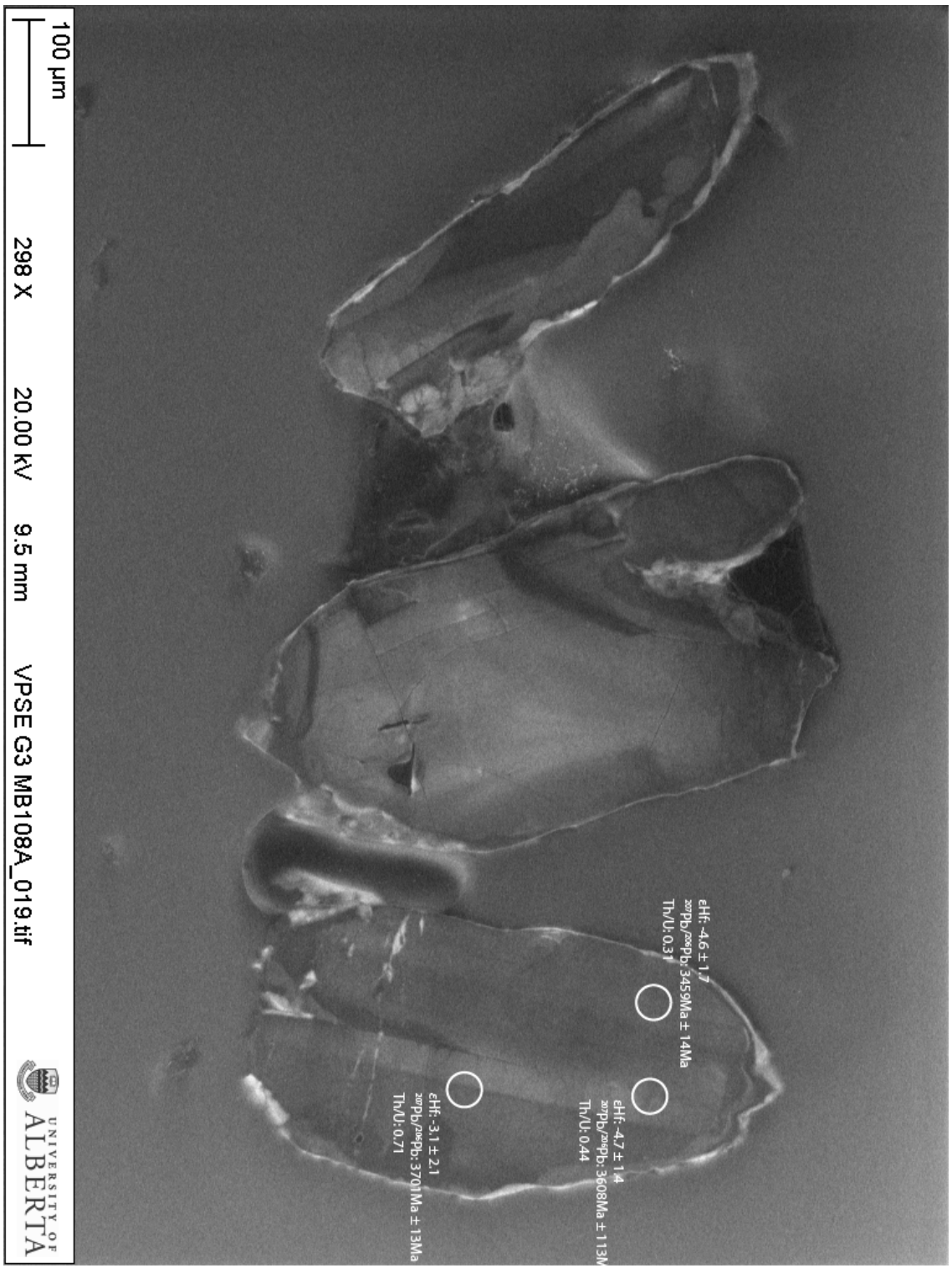

Metagabbro (CL, Spots are 33µm, $^{207}Pb/^{206}Pb$ Ages, εHf calculated using age of 3740.7±2.3Ma)

MB108A

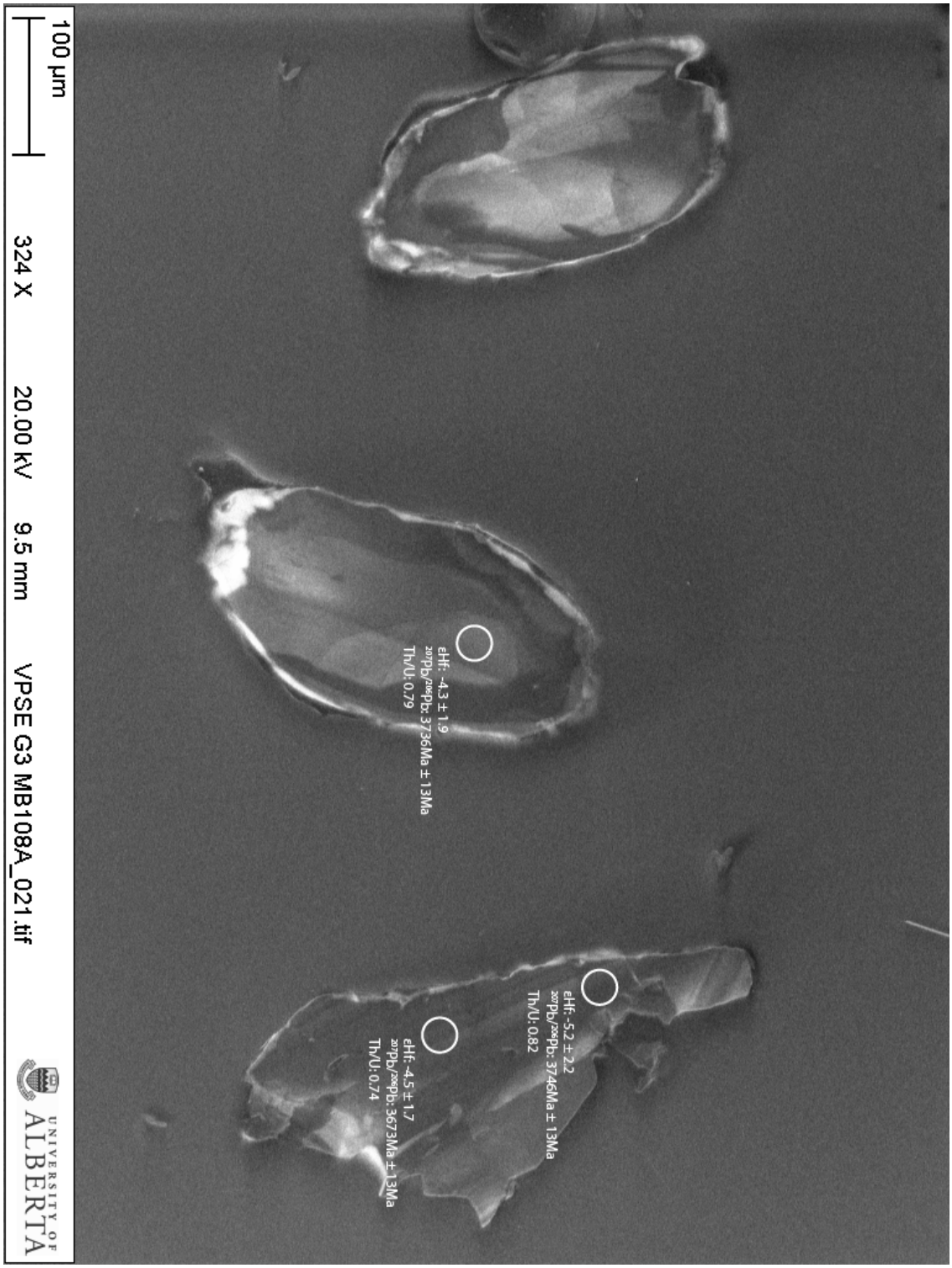

Metagabbro (CL, Spots are 33µm, $^{207}Pb/^{206}Pb$ Ages, εHf calculated using age of 3740.7±2.3Ma)

MB108A

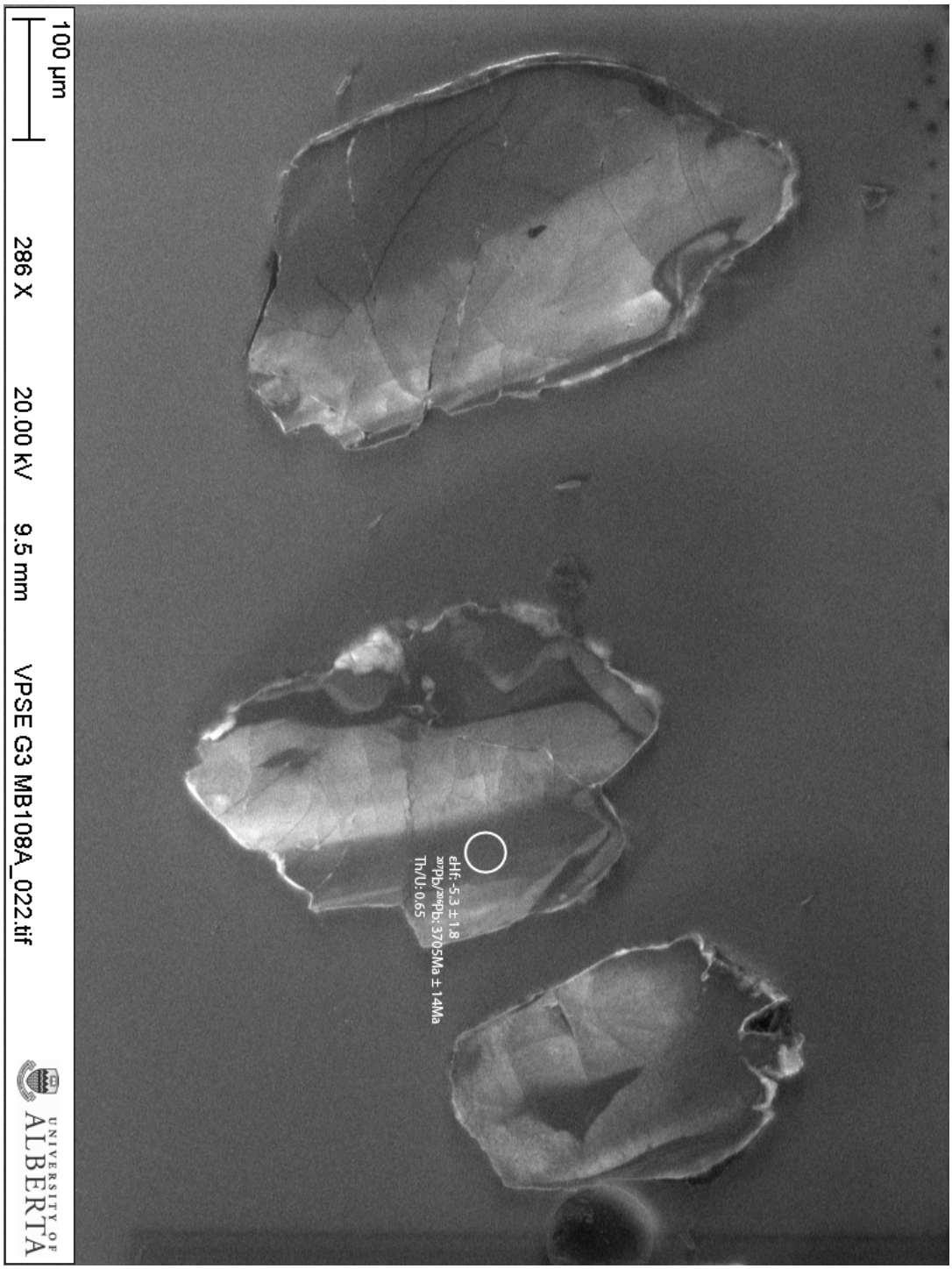

Metagabbro (CL, Spots are 33µm, $^{207}Pb/^{206}Pb$ Ages, εHf calculated using age of 3740.7±2.3Ma)

MB108A

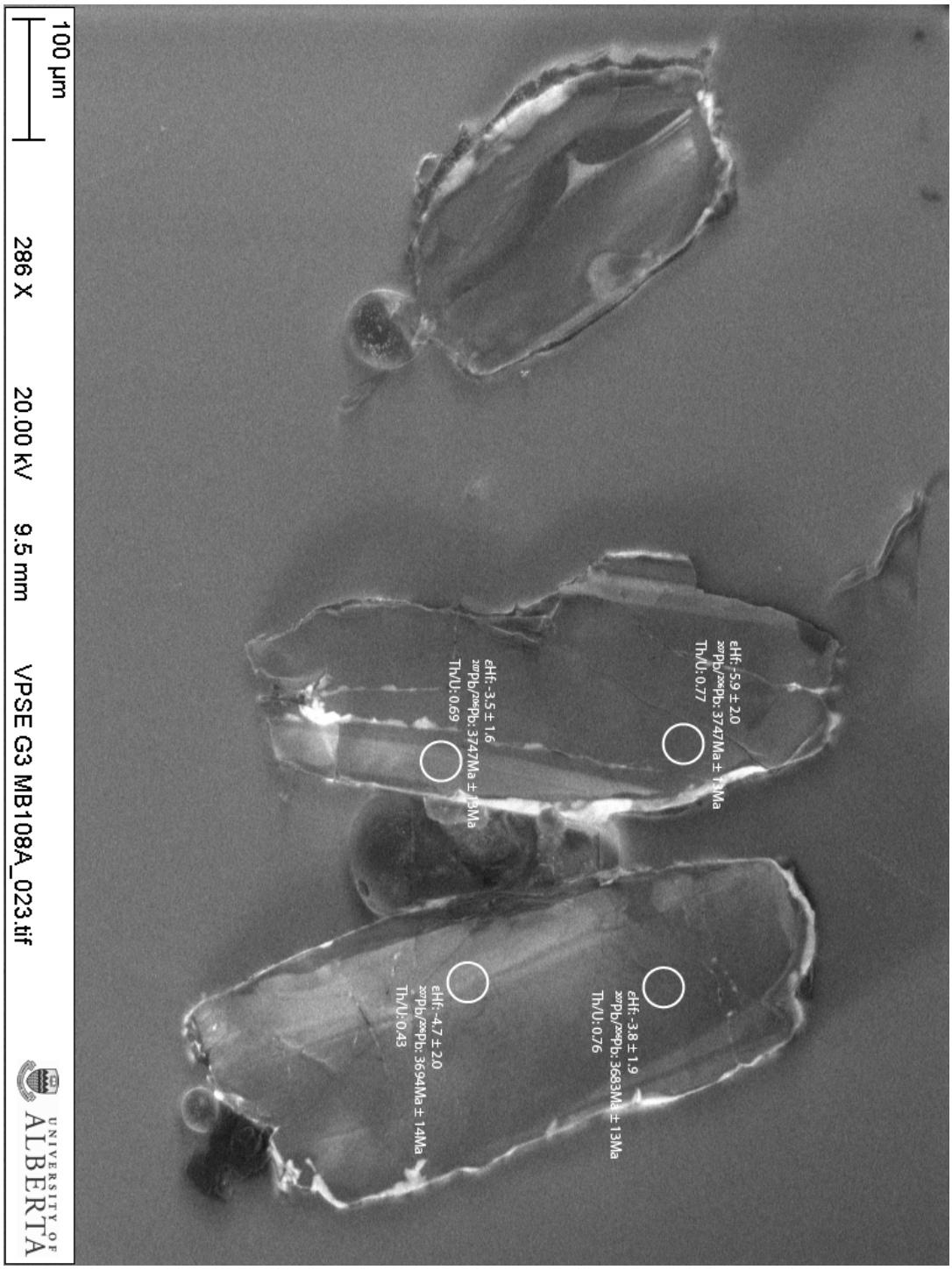

Metagabbro (CL, Spots are 33µm, $^{207}Pb/^{206}Pb$ Ages, εHf calculated using age of 3740.7±2.3Ma)

MB108A

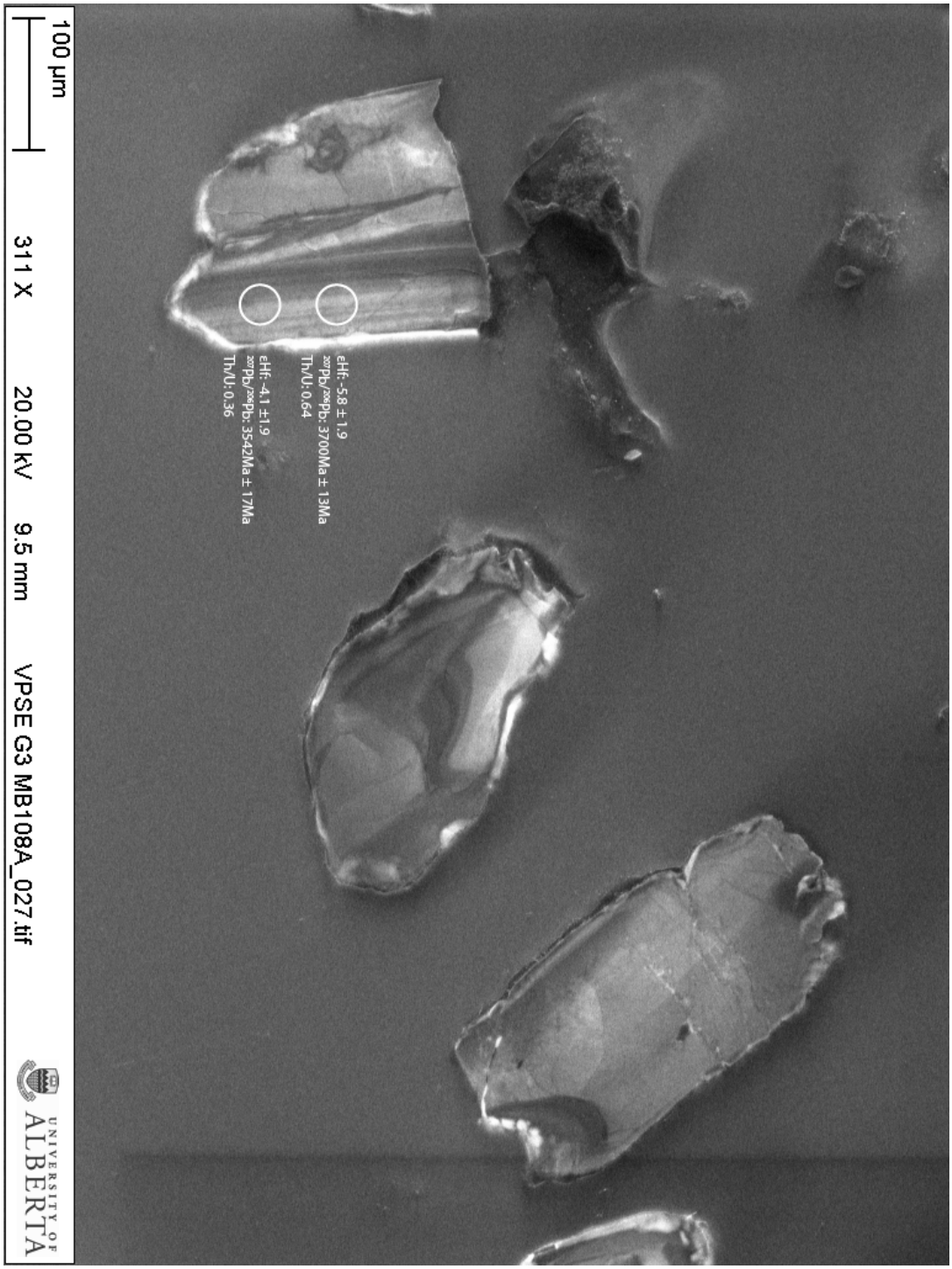

Metagabbro (CL, Spots are 33µm, $^{207}Pb/^{206}Pb$ Ages, εHf calculated using age of 3740.7±2.3Ma)

MB108A

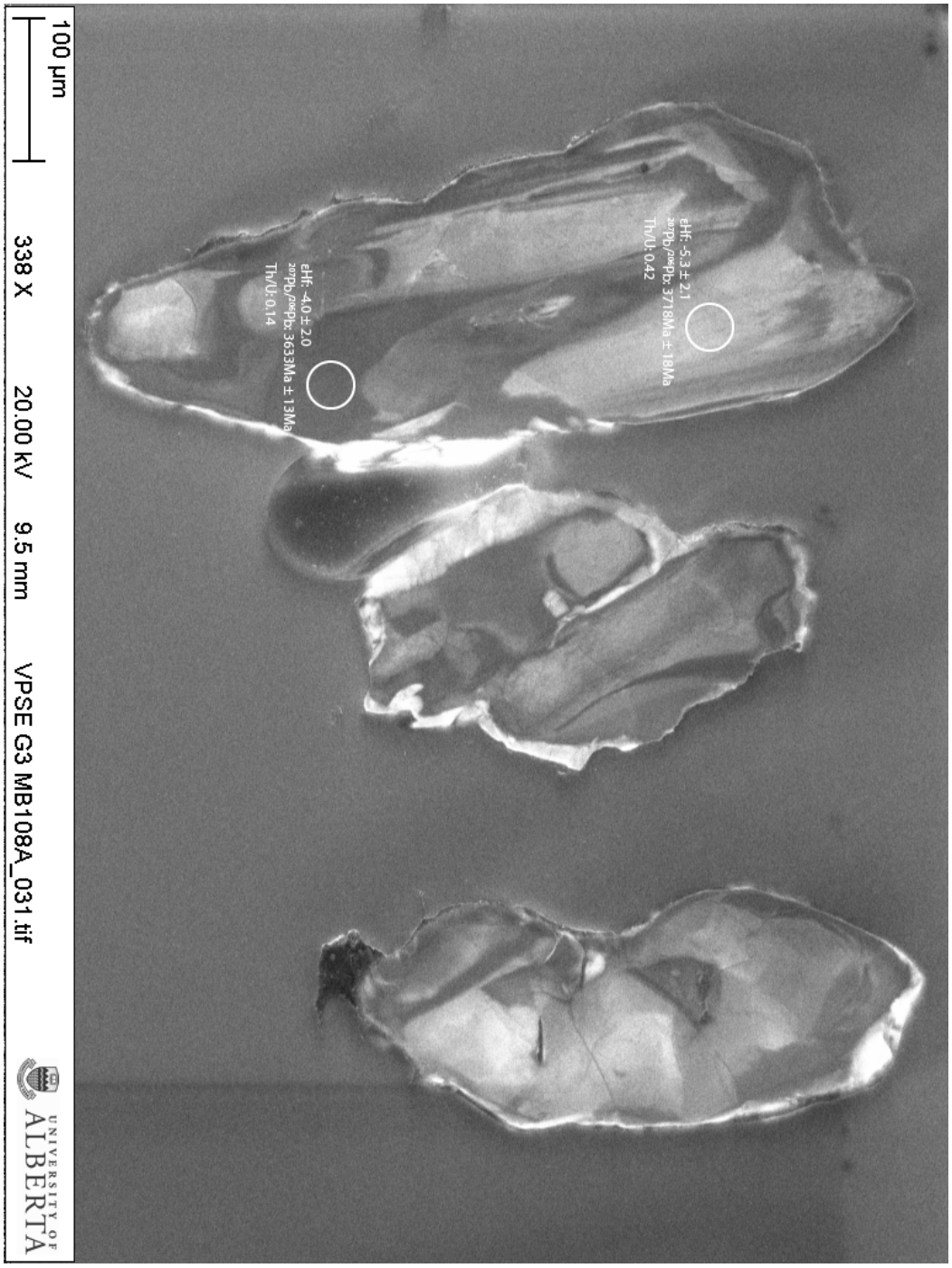

Metagabbro (CL, Spots are 33µm, $^{207}Pb/^{206}Pb$ Ages, εHf calculated using age of 3740.7±2.3Ma)

MB108A

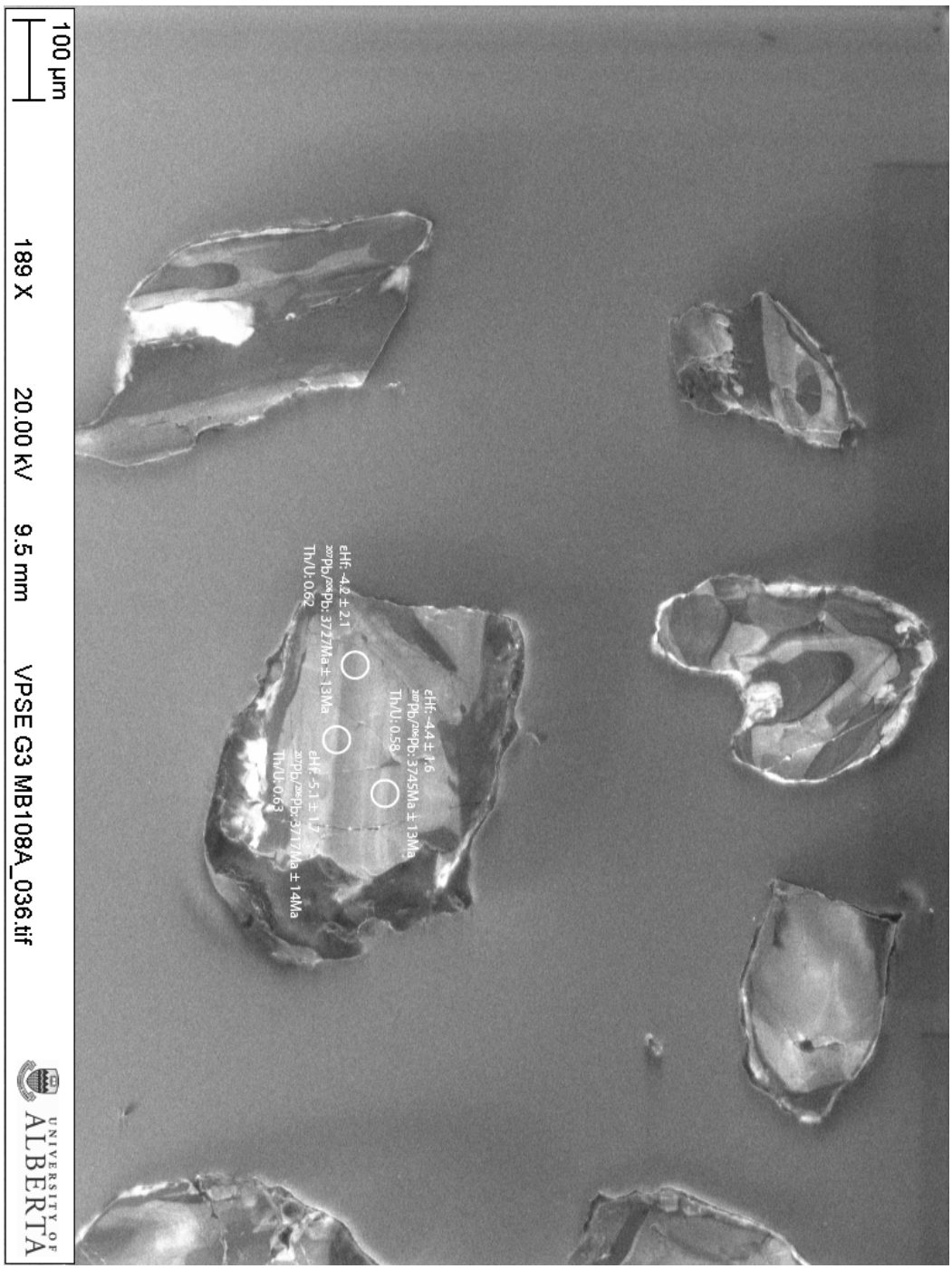

Metagabbro (CL, Spots are 33µm, $^{207}Pb/^{206}Pb$ Ages, εHf calculated using age of 3740.7±2.3Ma)

MB108A

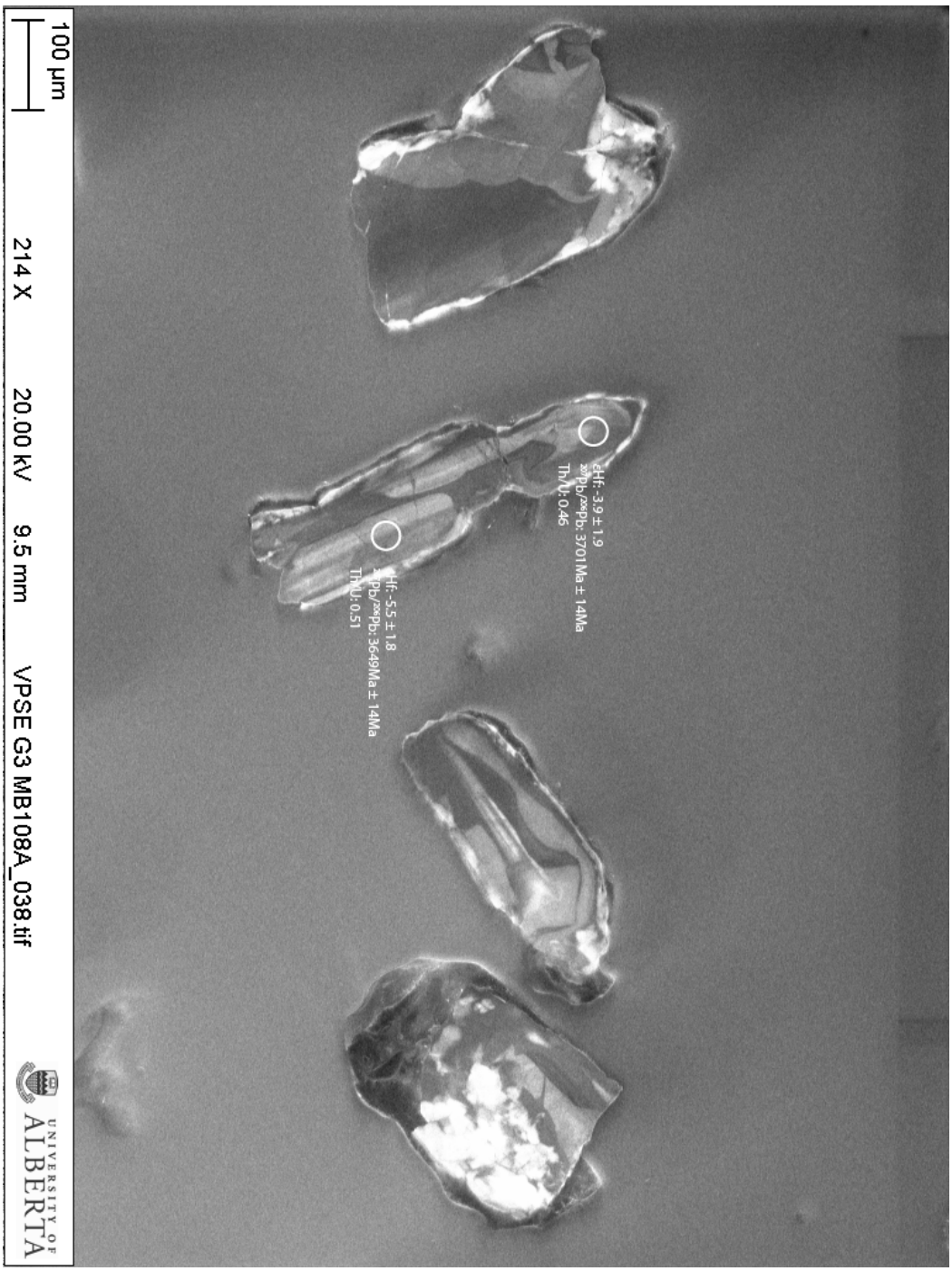

Metagabbro (CL, Spots are 33µm, $^{207}Pb/^{206}Pb$ Ages, εHf calculated using age of 3740.7±2.3Ma)

MB108A

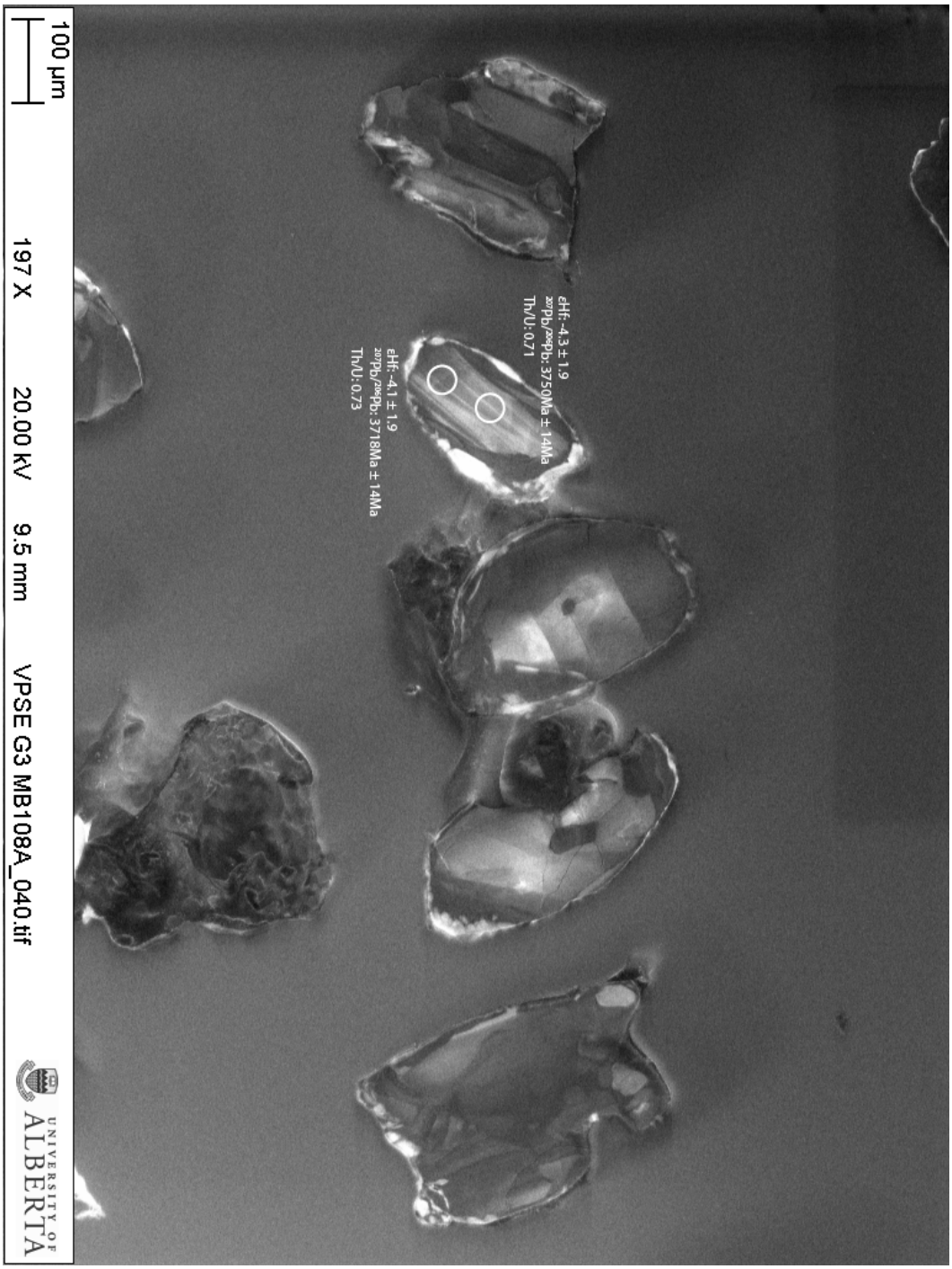

Metagabbro (CL, Spots are 33µm, $^{207}Pb/^{206}Pb$ Ages, εHf calculated using age of 3740.7±2.3Ma)

MB108A

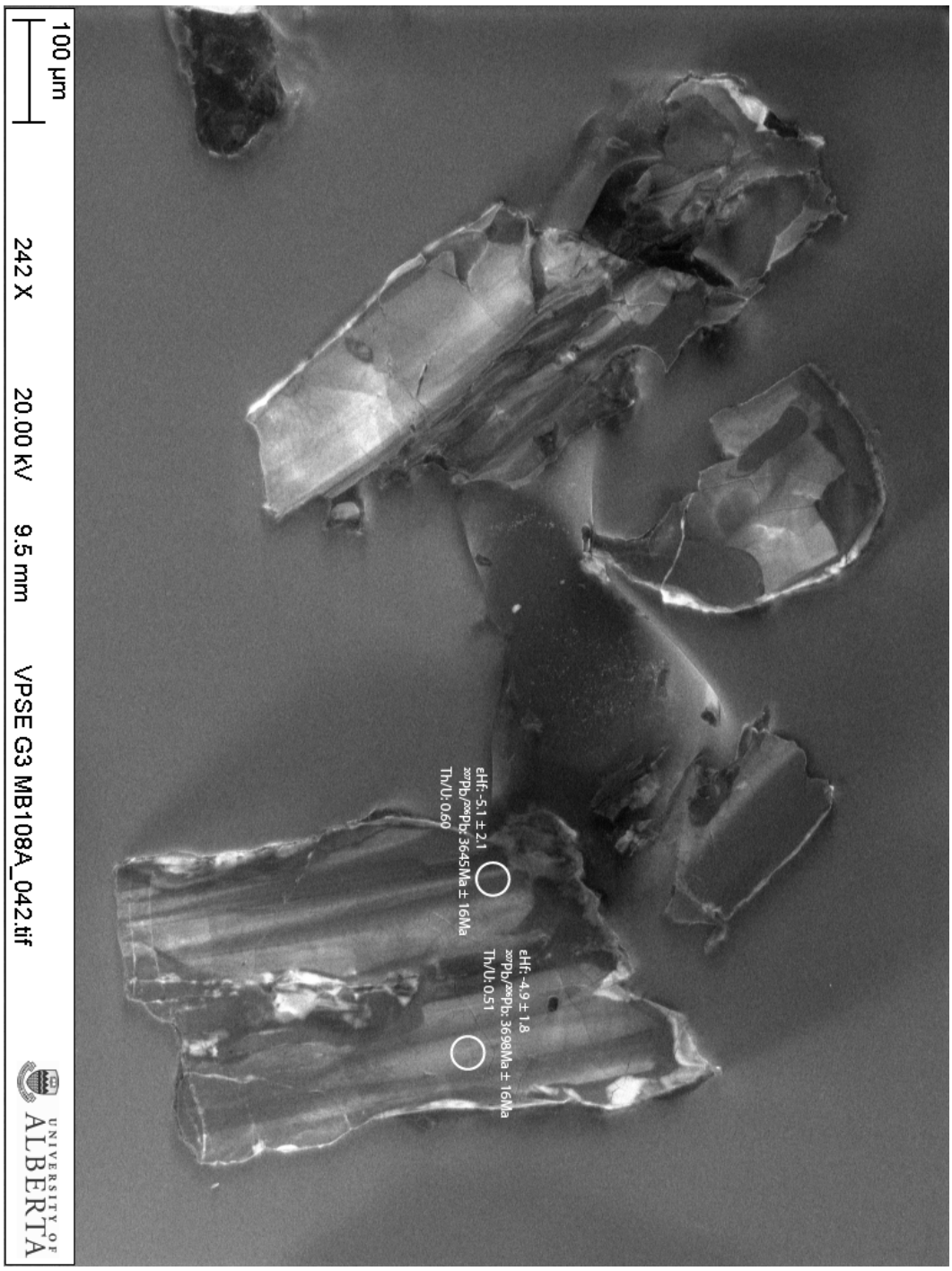

Metagabbro (CL, Spots are 33µm, $^{207}Pb/^{206}Pb$ Ages, εHf calculated using age of 3740.7±2.3Ma)

MB108A

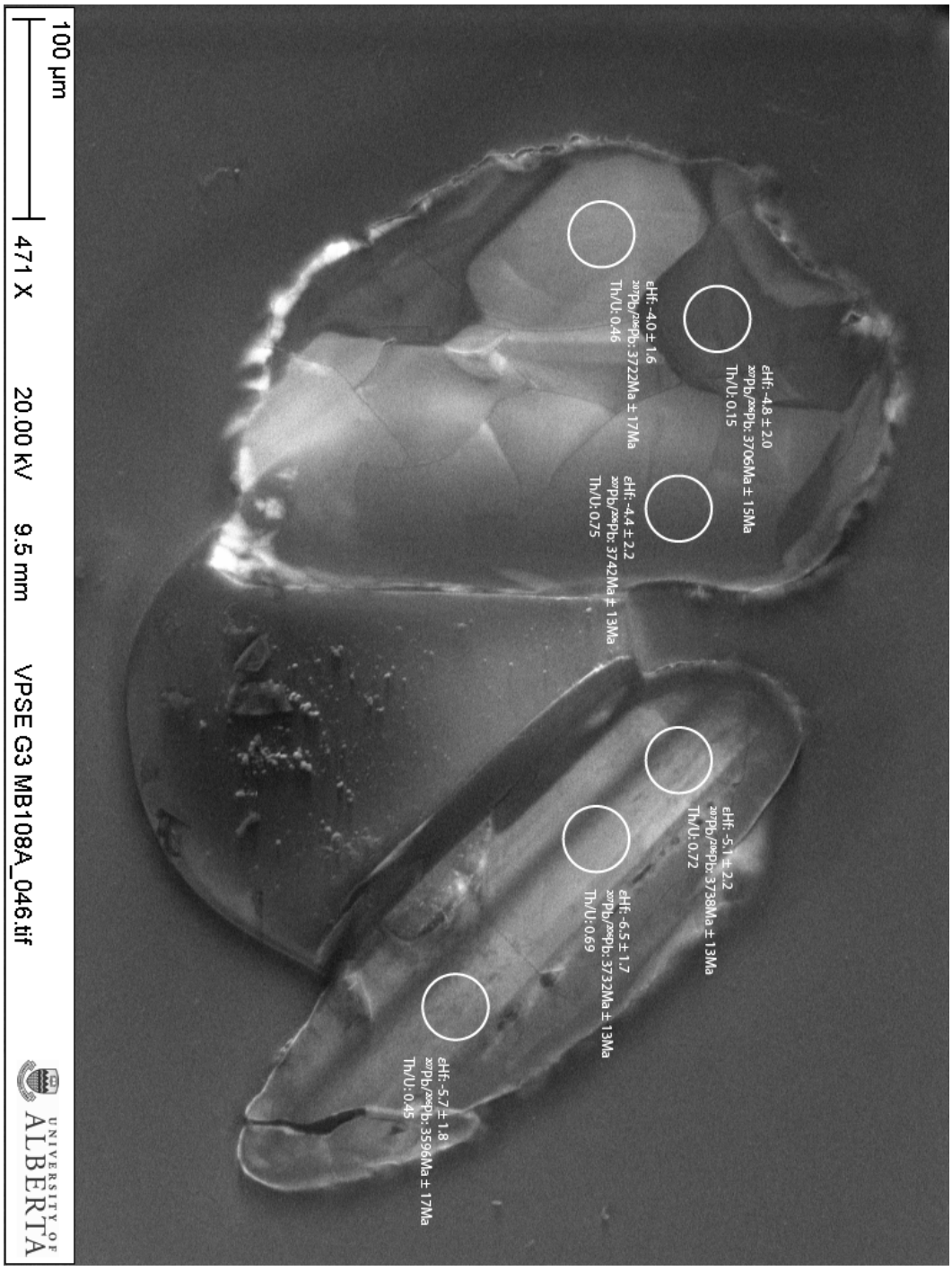

Metagabbro (CL, Spots are 33µm, $^{207}Pb/^{206}Pb$ Ages, εHf calculated using age of 3740.7±2.3Ma)

MB108A

Metagabbro (CL, Spots are 33µm, $^{207}Pb/^{206}Pb$ Ages, εHf calculated using age of 3740.7±2.3Ma)

MB108A

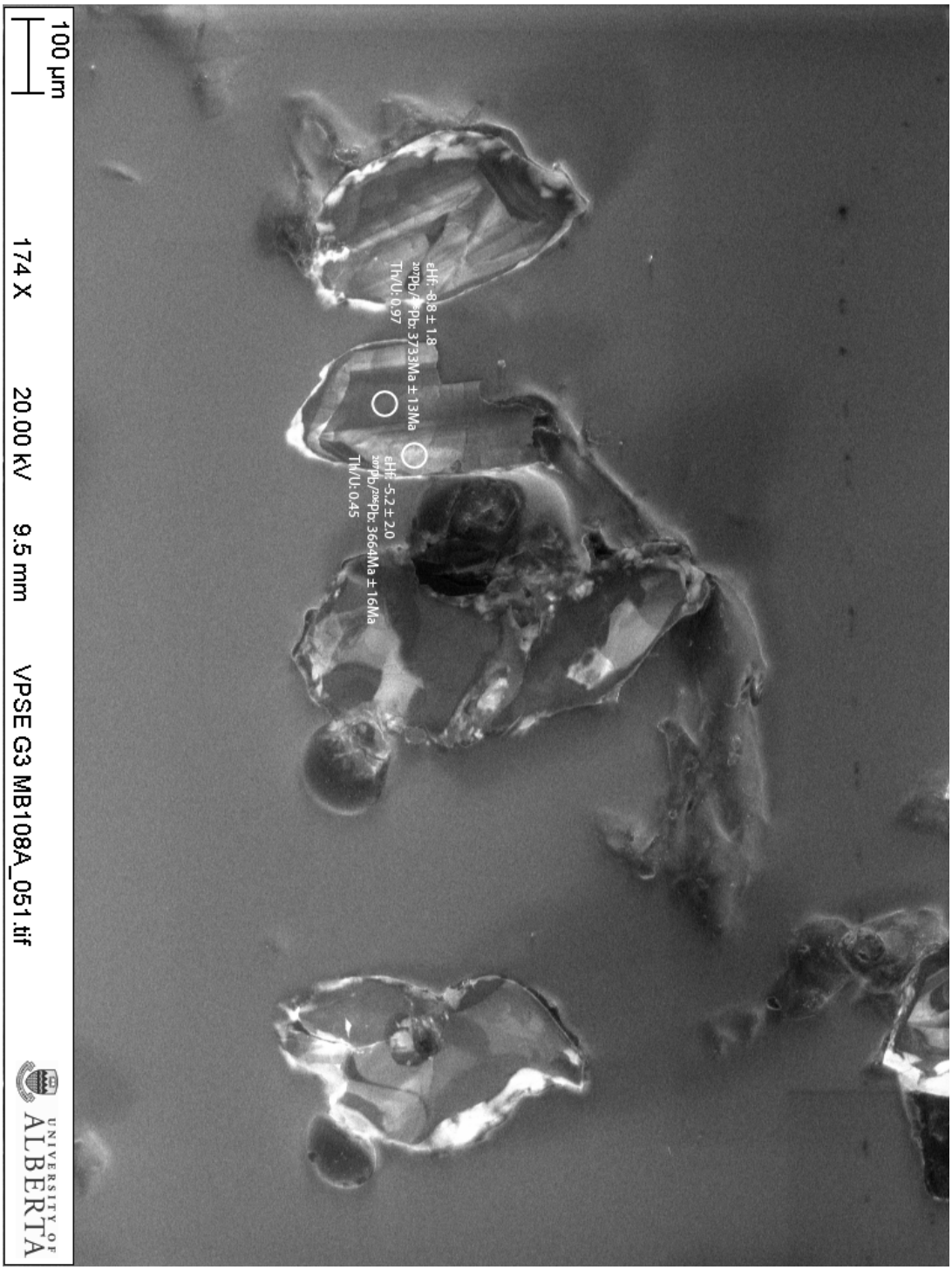

Metagabbro (CL, Spots are 33µm, $^{207}Pb/^{206}Pb$ Ages, εHf calculated using age of 3740.7±2.3Ma)

MB108A

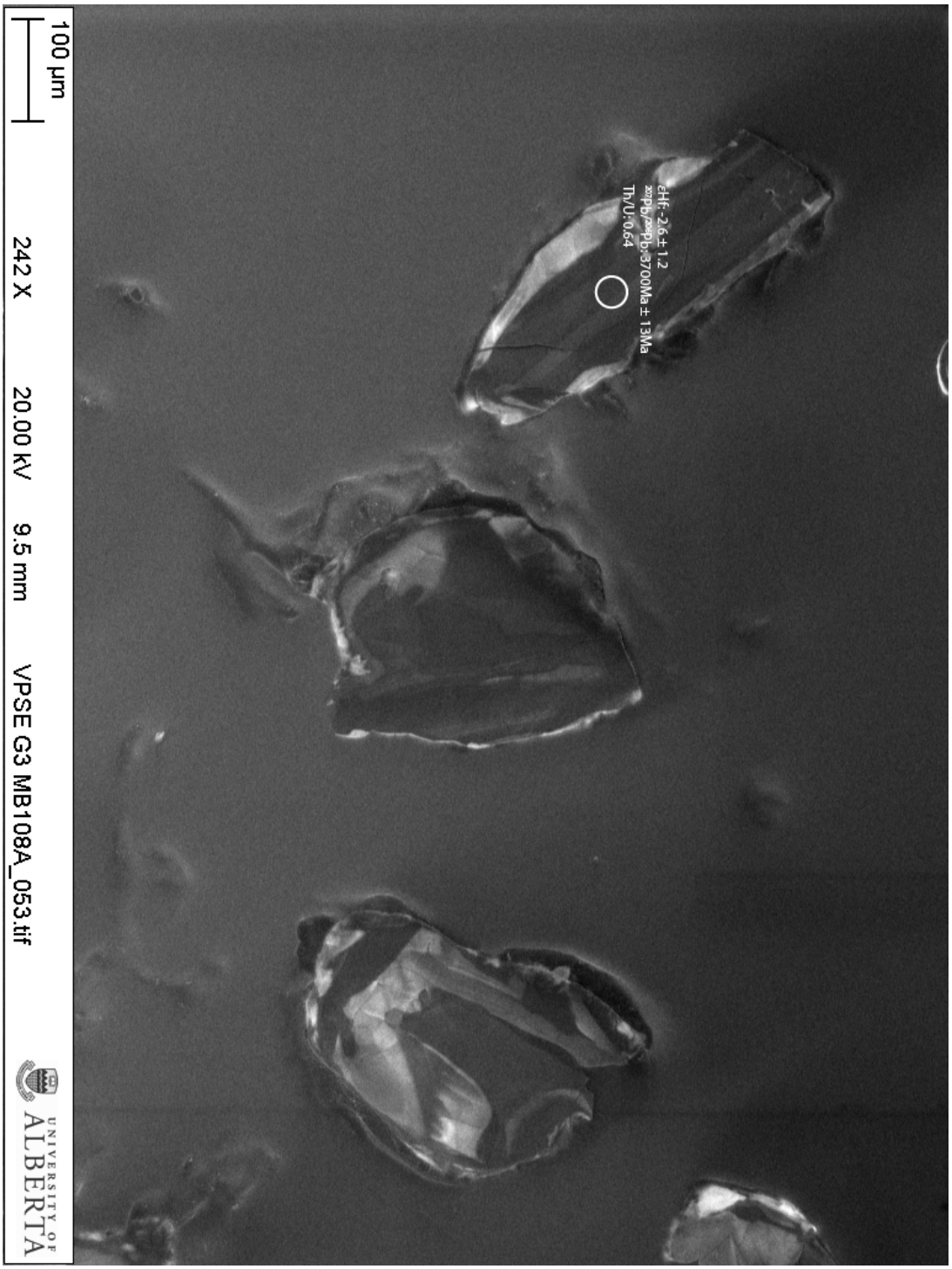

Metagabbro (CL, Spots are 33µm, $^{207}Pb/^{206}Pb$ Ages, εHf calculated using age of 3740.7±2.3Ma)

MB108A

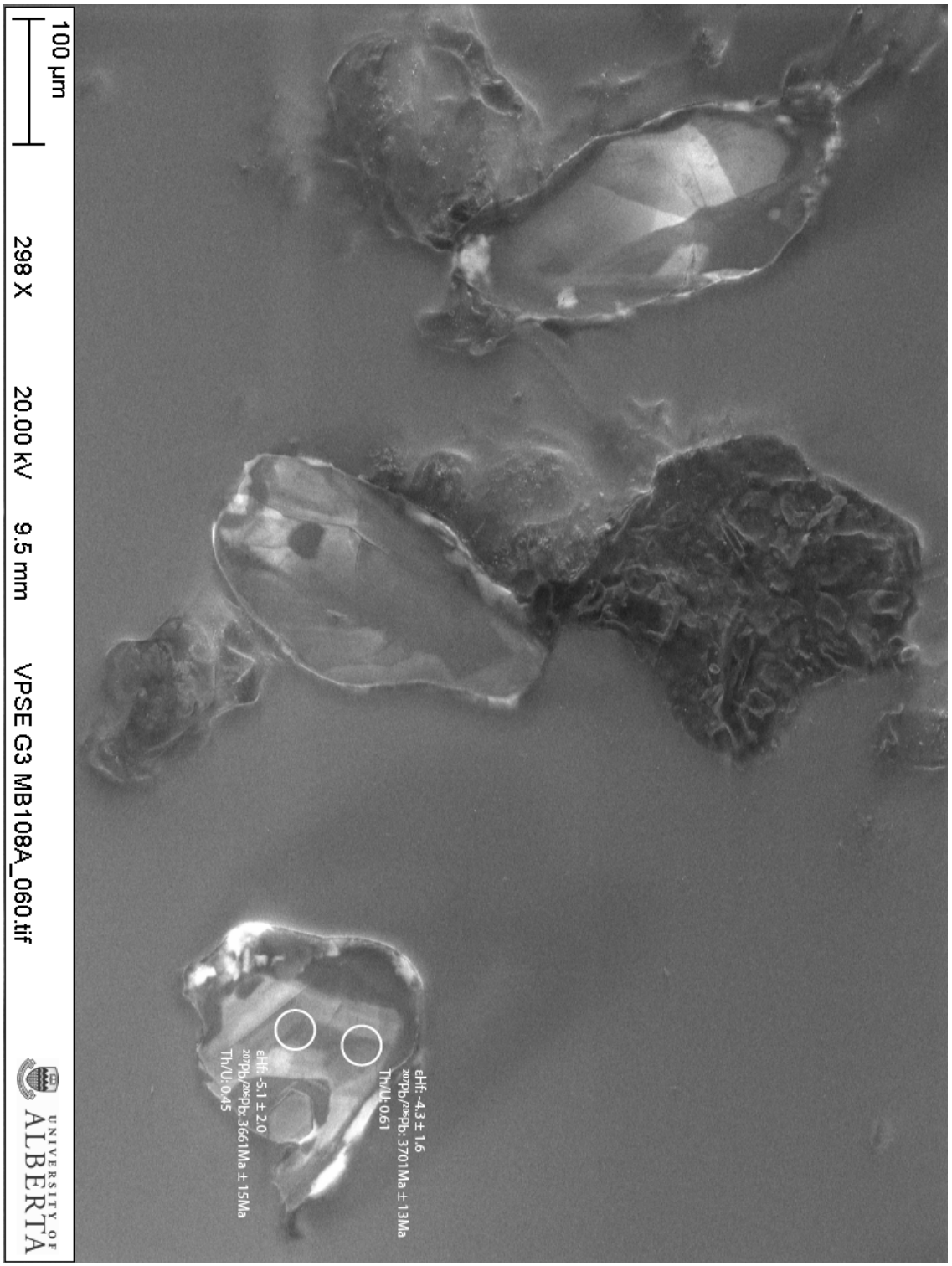

Metagabbro (CL, Spots are 33µm, $^{207}Pb/^{206}Pb$ Ages, εHf calculated using age of 3740.7±2.3Ma)

MB108A

Metagabbro (CL, Spots are 33µm, $^{207}Pb/^{206}Pb$ Ages, εHf calculated using age of 3740.7±2.3Ma)

MB108A

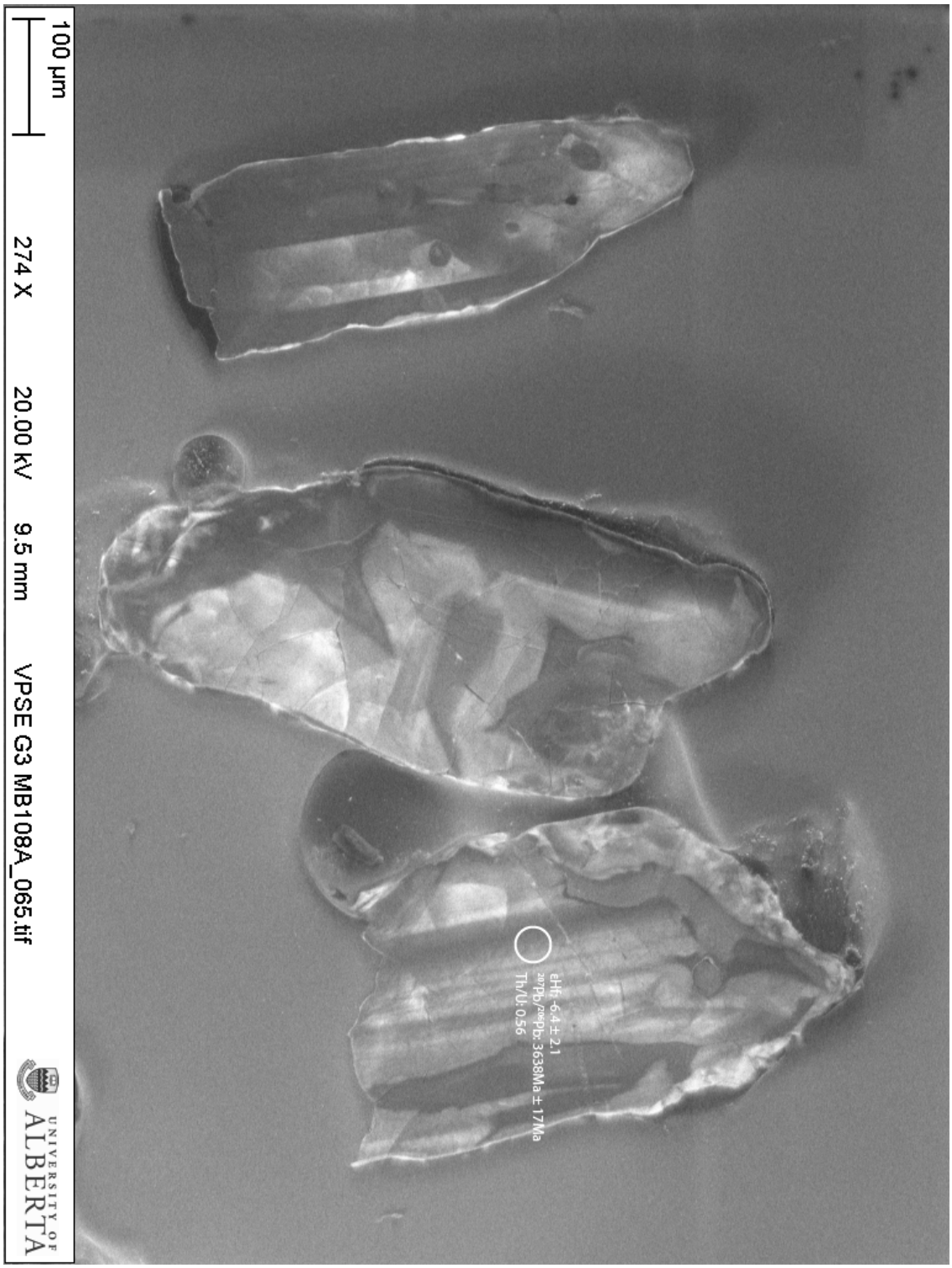

Metagabbro (CL, Spots are 33µm, $^{207}Pb/^{206}Pb$ Ages, εHf calculated using age of 3740.7±2.3Ma)

MB108A

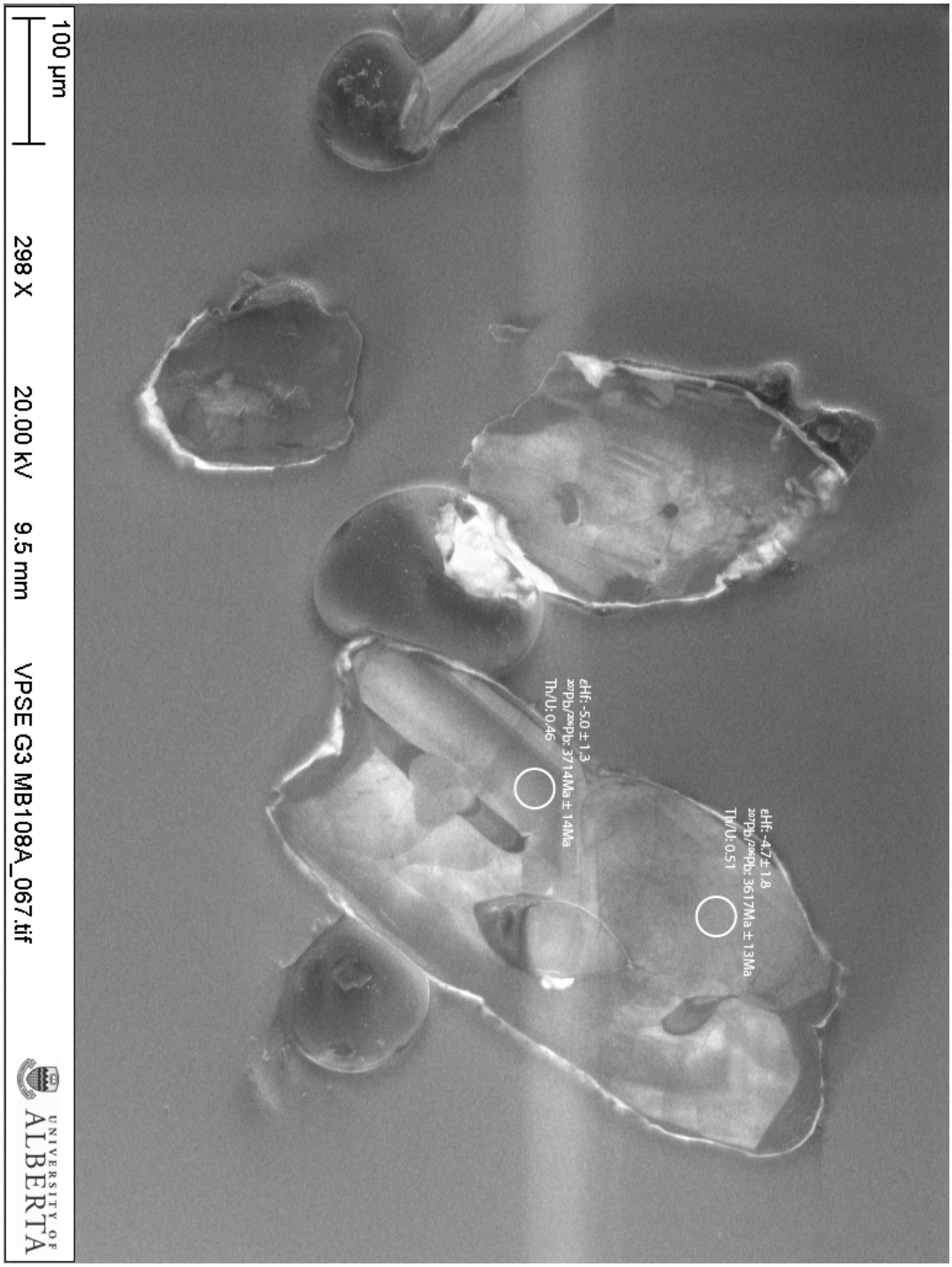

Metagabbro (CL, Spots are 33µm, $^{207}Pb/^{206}Pb$ Ages, εHf calculated using age of 3740.7±2.3Ma)

MB108A

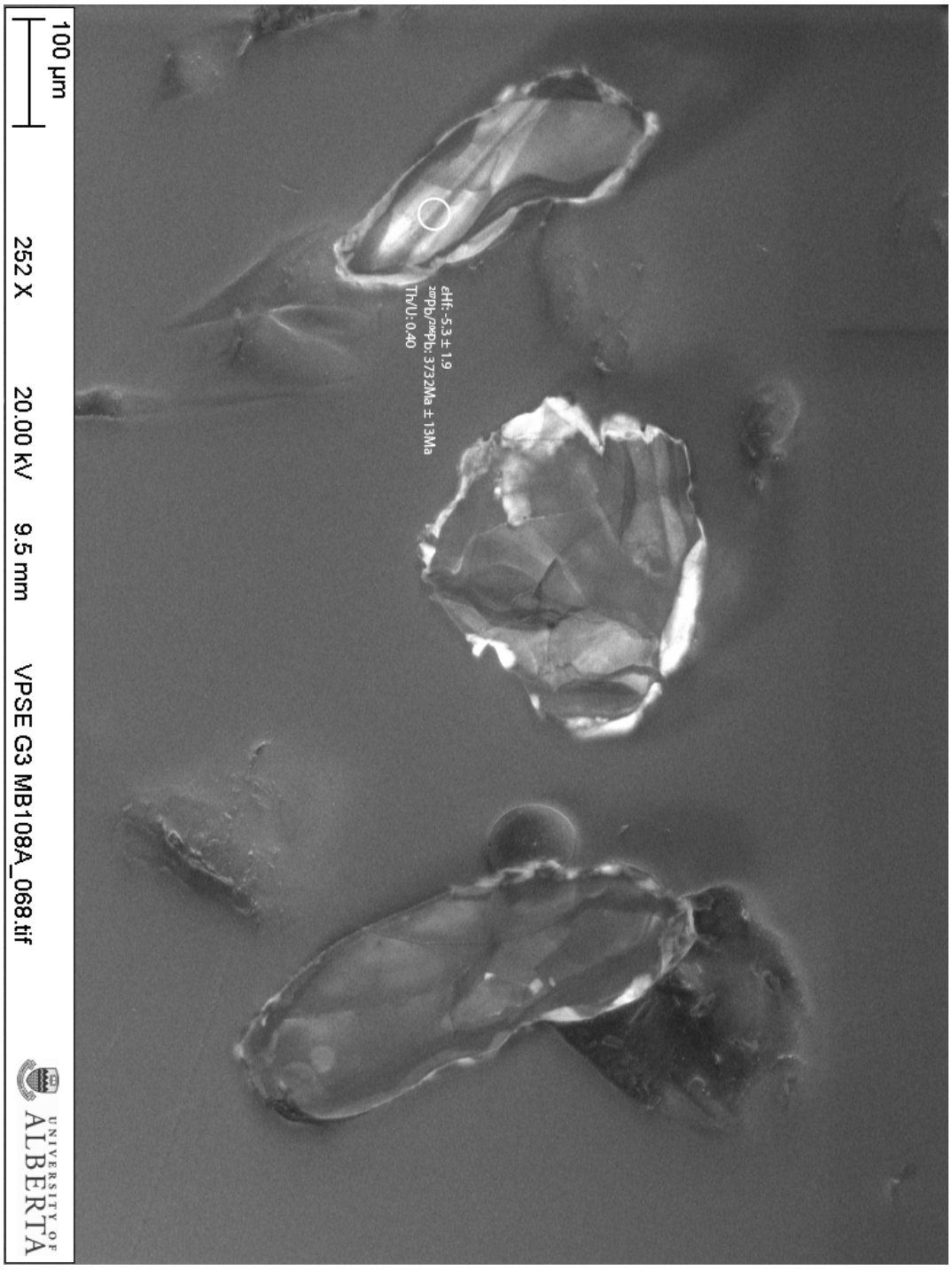

Metagabbro (CL, Spots are 33µm, $^{207}Pb/^{206}Pb$ Ages, εHf calculated using age of 3740.7±2.3Ma)

MB108A

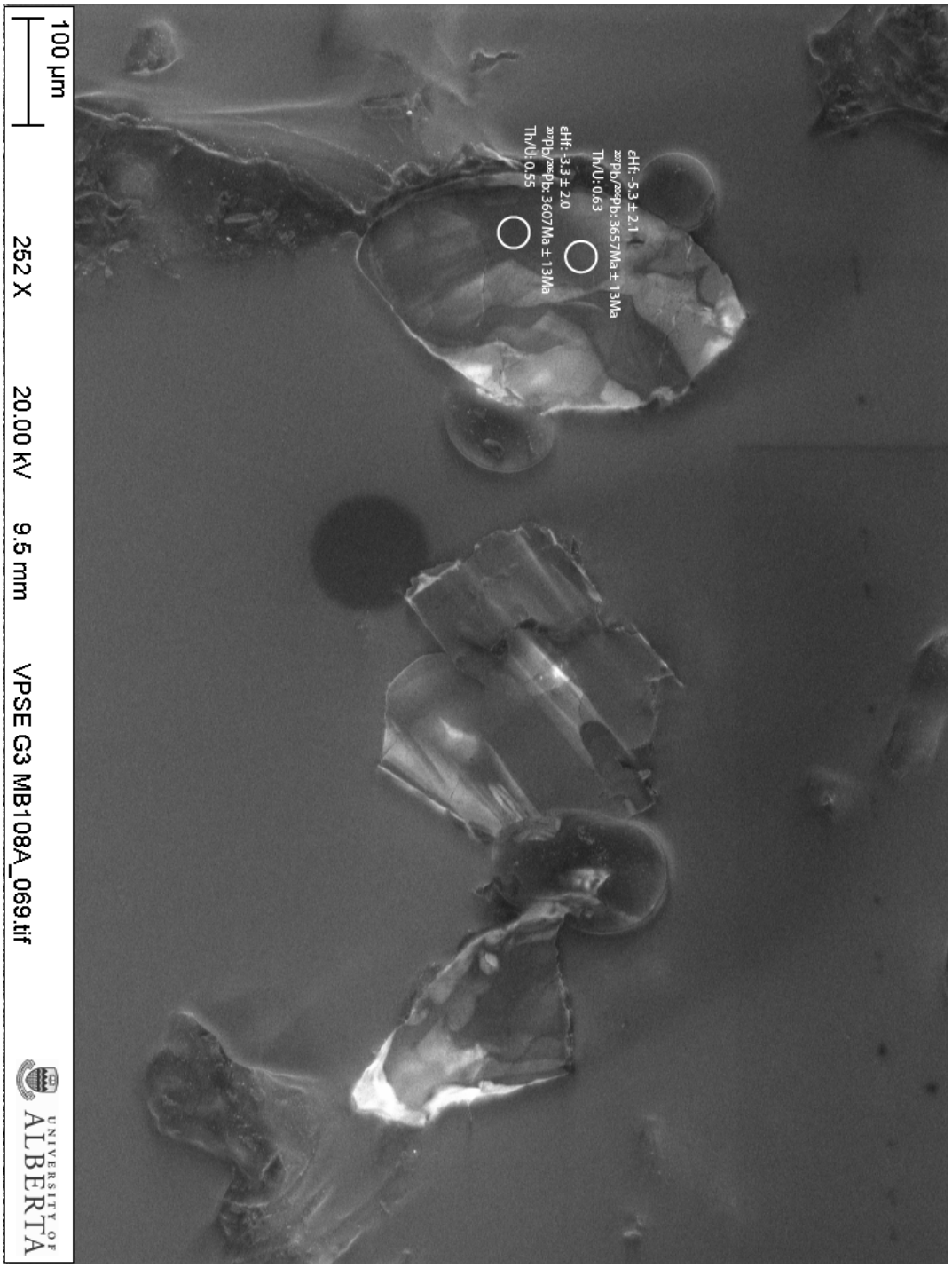

Appendix 6. Sample Locations

Sample Name	Zone	Easting	Northing	Unit name
MB04	11W	560871	7220587	Foliated Granite
MB07	11W	560338	7221165	Foliated Granite
MB12	11W	561209	7220239	Tonalitic-Granodioritic Gneiss
MB13	11W	561170	7220152	Pegmatitic Pink Granitoid
MB14	11W	561049	7220125	Tonalitic-Granodioritic Gneiss
MB15	11W	560931	7220091	Amphibolite
MB16	11W	560841	7219922	Amphibolite
MB17	11W	560777	7219929	Amphibolite
MB21A	11W	560743	7219573	Tonalitic-Granodioritic Gneiss
MB21B	11W	560743	7219573	Tonalitic-Granodioritic Gneiss
MB32	11W	561541	7219961	Mafic Dyke
MB47A	11W	561259	7219174	Pegmatitic Pink Granitoid
MB47B	11W	561259	7219174	Tonalitic-Granodioritic Gneiss
MB54A	11W	561478	7220009	Mafic Dyke
MB54B	11W	561478	7220009	Tonalitic-Granodioritic Gneiss
MB72A1	11W	562444	7220540	Ultramafic
MB72A2	11W	562444	7220540	Ultramafic
MB72B	11W	562444	7220540	Metagabbro
MB73A1	11W	562472	7220549	Tonalitic-Granodioritic Gneiss
MB73A2	11W	562472	7220549	Tonalitic-Granodioritic Gneiss
MB76A	11W	562602	7220245	Biotite Gneiss
MB76B1	11W	562602	7220245	Biotite Gneiss
MB76B2	11W	562602	7220245	Biotite Gneiss
MB76C	11W	562602	7220245	Biotite Gneiss
MB91	11W	562642	7220733	Biotite Gneiss
MB91B	11W	562642	7220733	White late-stage Intrusive Granitoid
MB92	11W	562747	7220781	White late-stage Intrusive Granitoid
MB93	11W	562793	7220829	Pegmatitic Pink Granitoid
MB98A1	11W	563275	7220687	Metagabbro
MB98A2	11W	563275	7220687	Metagabbro
MB98B	11W	563275	7220687	Pegmatitic Pink Granitoid
MB103	11W	563806	7220110	Metagabbro
MB108A	11W	563540	7219480	Metagabbro
MB108B	11W	563540	7219480	Tonalitic-Granodioritic Gneiss
MB114	11W	563217	7220187	Metagabbro
MB116A	11W	563115	7220286	Supracrustals (Iron Formation)
MB116B	11W	563115	7220286	Supracrustals (Garnetite)

Appendix 6. Sample Locations

Sample Name	Zone	Easting	Northing	Unit name
MB120	11W	562053	7221400	Tonalitic-Granodioritic Gneiss
MB130	11W	562195	7221349	Metagabbro
MB132	11W	5624797	7220685	White late-stage Intrusive Granitoid
MB138A	11W	563710	7221341	White late-stage Intrusive Granitoid
MB138B1	11W	563710	7221341	Tonalitic-Granodioritic Gneiss
MB138B2	11W	563710	7221341	Tonalitic-Granodioritic Gneiss
MB141	11W	563933	7221239	Ultramafic
MB167	11W	560580	7219905	Foliated Granite
MB169	11W	560665	7219815	Amphibolite
MB170A	11W	560813	7219737	Tonalitic-Granodioritic Gneiss
MB170B	11W	560813	7219737	White late-stage Intrusive Granitoid
MB185	11W	560725	7221306	Foliated Granite

***UTM Coordinates based off of the NAD83 geometric datum**